Discovery and characterization of the binary system LSI +61°303 in very high energy gamma-rays with MAGIC

Ph.D. Dissertation
by
Núria Sidro Martín

supervised by
Juan Cortina Blanco & F. Javier Rico Castro

Institut de Física d'Altes Energies
Universitat Autònoma de Barcelona

Barcelona, June 5th 2008

Núria Sidro Martín
Institut de Física d'Altes Energies
Universitat Autònoma de Barcelona
E-08291 Barcelona
nsidro@ifae.es

Contents

Chapter 1

Introduction

The window of very high energy (VHE) gamma-ray astrophysics was opened less than two decades ago, when the Crab Nebula was detected for the first time, with photon energies from 100 GeV to 100 TeV. After several years of development, the technique used by imaging atmospheric Čerenkov telescopes is now allowing to conduct sensitive observations in the VHE γ-ray regime. The instruments detect cosmic γ-rays by the detection of secondary showers produced by interactions of primary γ-rays with Earth's atmosphere, seen either directly (shower arrays) or through their Čerenkov radiation (Imaging Atmospheric Čerenkov telescopes – IACTs).

In this short time, the field evolved fast, and several extragalactic and galactic source classes have been established as TeV emitters, showing a variety of interesting phenomena that are boosting theory in VHE γ-ray astrophysics.

The Major Atmospheric Gamma Imaging Čerenkov (MAGIC) telescope is currently the largest single dish IACT, characterized by a 17 m diameter reflector. Located on La Palma (Spain), it features the lowest energy threshold IACT nowadays, allowing the reconstruction of γ-rays with energies from 60 GeV to 10 TeV. It combines a huge, ultralight reflector with a large number of technical innovations. The camera has a total field of view of about 3.5°.

When this work was started in 2004, no stellar X-ray binary object was known to emit VHE γ-rays, although theoretical predictions for theses systems were promising. Among them, LSI +61°303 is a peculiar binary, characterized by a variable radio emission, modulated with a $\sim$ 26.5 days orbital period. The source was also known to be periodic in infrared, optical and X-ray bands. LSI +61°303 was initially proposed as a possible counterpart of the high-energy COS B γ-ray source, which was also detected by EGRET above 100 GeV (3EG J0241+6103). However, the association was unclear due to the low angular resolution of EGRET. This possible association together with the fact that jet flows were claimed from radio interferometric observations, made LSI +61°303 a promising microquasar candidate.

The detection and detailed study of LSI +61°303 at VHE γ-rays with MAGIC was proposed as the main objective of this thesis, as an attempt to better understand the nature and physical properties of this peculiar system.

This thesis is structured as follows.

- In chapter 2, I give an overview of the production mechanisms and sources of VHE γ-ray. I describe the physics of the extended air showers produced by the cosmic rays entering in the atmosphere and the techniques developed to detect them.

- In chapter 3, the MAGIC telescope is presented. I will introduce in detail the remote camera control software, since is the part of the detector in which I contributed technically.

- The analysis chain of the MAGIC data is explained in chapter 4: from the reconstruction of the image recorded by the telescope of the air shower produced by the cosmic ray in the atmosphere to the selection of the γ-ray candidates among these recorded images. And the final reconstruction of the physical physical quantities, which finally yields

the γ-ray estimated energy and incident direction, the significance of the γ-ray source detection, the lightcurve and the energy spectrum.

- The LSI +61°303 X-ray binary, its physical properties and phenomenology are presented in chapter 5. There I also review the theoretical models of VHE γ-ray production.

- In chapter 6, I present the results of the analysis of LSI +61°303 observations with MAGIC during years 2005 and 2006. I report on the discovery of VHE γ-rays from the direction of LSI +61°303. The position, extension, energy spectra and differential fluxes of this source are presented. The flux variations with time are studied in detail, which yields a periodic γ-ray signal, that points to the mechanism for VHE emission being related to the orbital period of the system.

- The conclusions of the results of my analysis are the subject of chapter 7.

At the time of writing this dissertation, there are already 4 galactic γ-ray binary objects: LS 5039, PSR B1259-63, Cyg X1 and LSI +61°303 that are detected at VHEs and established as a new category named γ-ray binaries.

Chapter 2

Very High Energy Gamma Ray Astronomy

In this chapter we review the physical mechanisms by which very high energy γ-rays are produced, and the astrophysical objects where these mechanisms may take place. We move on to describe the Čerenkov technique used by Imaging Air Čerenkov Telescopes to indirectly detect γ-rays entering the Earth atmosphere by means of the Čerenkov light which they produce. For that purpose, the main features of extended air showers are reviewed, with emphasis on the difference between Extended Air Shower (EAS) induced by primary γ-rays and the more numerous EAS induced by charged cosmic ray nuclei (which represent the main source of background for these telescopes)

2.1 Cosmic rays

Since antiquity and until the 19th century, astronomical observations were made in the visible domain. But nowadays the sky is studied in an broad band of the electromagnetic spectrum: Gamma-rays (γ-rays) , X-rays, ultraviolet (UV), visible, infrared (IR), millimeter and submillimeter domain, radio, ... Observations in all these wavelengths enable the study of different astrophysical phenomena, which improves our global understanding of the Universe. This thesis is developed within the framework of the γ-ray astronomy, which is closely connected to the search for the origin of the cosmic rays, subject which we introduce in the following paragraphs.

Cosmic rays (CR) have a long history, starting in 1912 when Victor Hess lifted electroscopes in balloons to 5-km altitudes and detected a mysterious ionizing radiation coming constantly from space. Early cosmic ray physicists used this natural flux of high energy protons to discover a number of elementary particles (as the positron, muon or pion) by observing them in cloud chambers and photographic emulsions at high altitudes, where the flux at high energies is less attenuated. In 1938, Pierre Auger showed that very high energy cosmic rays generate extensive air showers in Earth's atmosphere, distributing the original energy among billions of lower-energy particles which arrive almost simultaneously to the ground.

Different techniques are employed to detect cosmic rays from energies from 10^9 to 10^{20} eV [1]. Up to 10^{14} eV, direct detection is feasible with balloon and space experiments. Above this energy, the flux is too low for space-based detectors, and cosmic rays are studied by observing their air-shower development.

Direct CR detection shows that at low energies the CR flux is modulated by the solar wind, which shields the solar system from charged particles below about 10^9 eV. From a few GeV to a few PeV (1PeV = 10^{15} eV), the CR spectrum is well described by a power law of spectral index 2.7, i.e., the number of CR arriving on Earth per unit time, area, solid angle, and kinetic energy E is $F(E) \propto E^{-2.7}$. At higher energies, the spectrum steepens to $F(E) \propto E^{-3}$ and the transition region is called the *knee*. At about 10^{18} eV the spectrum hardens again, giving rise to a feature named the *ankle*. Finally, at about 10^{20} eV, the *cosmologically meaningful*

termination or *GZK cut-off* predicted by Greisen, Zatsepin, and Kuzmin [2, 3] is expected as these ultra-high energy CRs lose energy through pion production in interactions with the cosmic microwave background radiation.

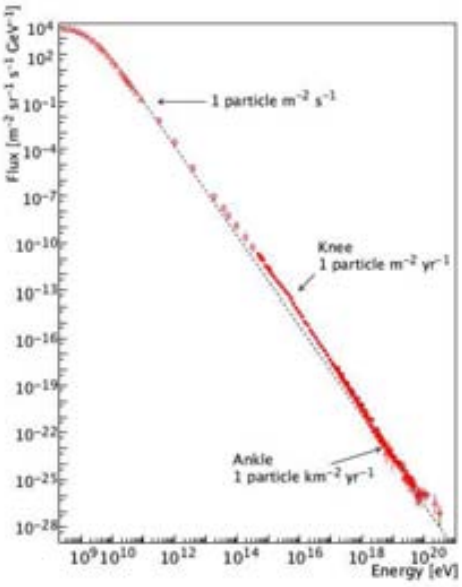

Figure 2.1: Cosmic ray spectrum, extending over more than 13 orders of magnitude, with fluxes dropping from 1 particle $\mathrm{cm}^{-2}\mathrm{s}^{-1}$ at around 100 MeV to less than 0.01 particle $\mathrm{km}^{-2}\mathrm{century}^{-1}$ for the highest observed energies.

The cosmic ray composition has been measured directly at low energies (up to the knee): about 79% of the primary nucleons are protons and the remainder are helium and a small fraction of heavier elements (1% C,N,O,Fe). Less than 1% consists of electrons and positrons, and only a tiny fraction is made up of γ**-rays**. While the origin of a significant part of the low-energy Cosmic rays (below 10 GeV) can be traced back to the Sun, the high-energy part ranging up to the knee is believed to originate mostly from galactic accelerators. The region between the knee and the ankle is still under debate, while at higher energies the particles are generally believed to have an extragalactic origin.

Recently, the Pierre Auger experiment reported evidence for anisotropy in the arrival directions of the cosmic rays with the highest energies, which are correlated with the positions of relatively nearby active galactic nuclei[1] (AGN) [4]. The correlation has a maximum significance for CR with energy greater than $\sim 6\times10^{19}$ eV and AGNs at a distance less than 75 Mpc. This correlation favours the hypothesis that the highest energy CRs originate from extragalactic sources close enough so that their flux is not significantly attenuated by interaction with the cosmic background radiation (GZK effect).

For CR with energies below the knee, different sources have been suggested:

- Galactic sources of CR: supernova remnants (shell type), plerions, pulsars, microquasars and X-ray binary systems, young stars and young open clusters.

- Extragalactic sources of CR: AGNs (in the beamed regions, jet), gamma ray bursts, starburst galaxies and clusters of galaxies.

These sources are reviewed in detail in Sec. 2.3.

Cosmic rays emitted by a diversity of astrophysical objects can reach the Earth. On their way they interact with the interstellar and intergalactic medium and charged CRs are quickly deflected by galactic and intergalactic magnetic fields. Therefore, the distribution of CR incident directions is isotropic, with the exception of the small flux of (neutral) γ-rays and neutrinos, which points back to their origin. The most energetic (> 1 GeV) among these CRs can interact with nuclei in the atmosphere and create extended air showers, that develop in the atmosphere. The detection of this EAS is the base of the imaging atmospheric Čerenkov telescopes, and will be described in Sec. 2.4.4.

[1] The Pierre Auger data do not identify AGN as the sources of cosmic rays unambiguously. Other candidate sources which follow the same distribution of nearby AGN cannot be ruled out.

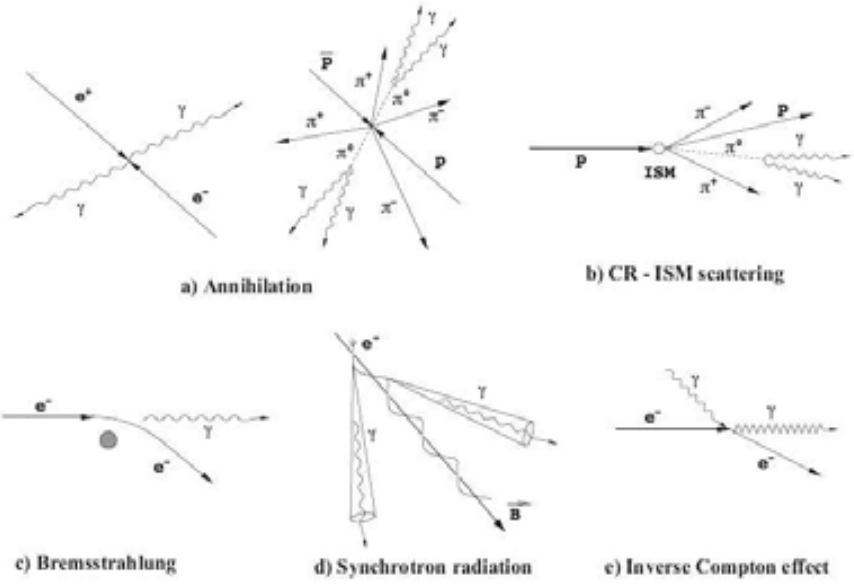

Figure 2.2: Schematic illustration of the main mechanisms of γ-ray production. The Interstellar Medium or cosmic ray particles can be protons or heavy ions.

2.2 Mechanisms of γ-ray production

Astronomical objects release energy in different types of processes. Most of the energy is emitted thermally, and can be described in first approximation with a black-body spectrum. The effective temperatures typically range from 3000 K (red stars) to $> 10^6$ K (X-ray binaries accretion disks, white dwarfs). The hottest objects radiate thermally X-rays up to a few keV energy band.

Gamma-rays are produced by non-thermal processes. The most relevant processes responsible of producing γ-rays are shown in Fig. 2.2 and are briefly explained in the following paragraphs. For a more extensive review, the reader is referred to Longair (1992) [5].

- Electron-positron annihilation (Fig. 2.2, a): Whenever electrons and positrons coexist locally, they rapidly annihilate into two photons $e^+e^- \rightarrow \gamma\gamma$. The process results in a spectral line at 511 keV$= m_e c^2$, if the system e^+e^- is at rest. Thermalized positrons interacting with cold electrons can produce 3γ. The γ-ray spectrum appears as a continuum in the MeV range, as described in [6], with the same spectrum of the parent positrons, but steeper.

- π^0 decay (Fig. 2.2, b): High energy protons interact with matter and γ radiation and produce a variety of hadronic particles. About 30% of these particles are π^0, which decay after a very short time into two γ-rays with a branching ratio around 99%.

- Particles through electromagnetic fields: Charged particles, usually electrons or protons, are accelerated in the electric field produced by a nucleus or ion. When the particles is de-accelerated, radiation is emitted. The effect is called *Bremsstrahlung* (Fig. 2.2, c). High energy relativistic electrons produce *Synchrotron radiation* (Fig. 2.2, d) when in presence of magnetic fields. The emitted photons energy has a peak, whose position is proportional to the transverse component of the magnetic field B_G and to the electron Lorentz factor $\gamma_e \equiv 1/\sqrt{1-\beta^2}$ (where β is the electron velocity in terms of c) and is given by

$$E_{\max} = 5 \times 10^{-9} B_G \gamma_e^2 \,\mathrm{eV} \tag{2.1}$$

  According to eq. 2.1, in order to get high energy photons directly from synchrotron process, relativistic CRs (electrons or protons) and strong magnetic fields are required.

Moreover, synchrotron emission provides the seed photon field for inverse Compton scattering.

- Inverse Compton (IC) scattering (Fig. 2.2, d): When relativistic electrons (or positrons) scatter off low energy photons, they transfer part of their energy, resulting in high energy γ-rays. Depending on the incident electron (E_e) and photon ($E_{\gamma,i}$) energies, one distinguishes two different regimes: the *Thomson limit* if $E_e E_{\gamma,i} \ll m_e^2 c^4$ and the *Klein-Nishina limit* if $E_e E_{\gamma,i} \gg m_e^2 c^4$, where m_e is the electron mass. The average energy of the photon after the scattering process is

$$\langle E_{\gamma,f} \rangle \approx \begin{cases} \frac{4}{3}\langle E_{\gamma,i}\rangle \gamma_e^2 & \text{Thomson limit} \\ \frac{1}{2}\langle E_e \rangle & \text{Klein-Nishina limit} \end{cases} \tag{2.2}$$

  where γ_e is the electron Lorentz factor. Typical target photon fields in IC-scattering are the 2.7 K cosmic microwave background radiation, synchrotron radiation and thermally generated photons from stars or clouds.
  In the Thomson regime, the emitted photons follow the spectral shape of the seed photons, while in the Klein-Nishina regime, the resulting spectrum has a sharp cut-off, which is determined by the maximum energy of the participating electrons.

2.3 Sources of VHE γ-rays

In this section we will review the major classes of VHE γ-ray emitters. Some of them are already detected at those energies, some are still potential candidates (see figure 2.3).

Extragalactic sources:

Active galactic nuclei (AGN) are galaxies where most of the radiation comes from their innermost region, commonly interpreted as a black hole (BH) of mass between $10^6 - 10^{10} M_\odot$. The BH is accreting surrounding material forming a highly relativistic rotating accretion disk, which radiates thermal emission in the UV and visible domains. Perpendicular to the disk, two plasma jets are generated. The jets may carry away part of the angular momentum of the accreted material and extend up to several Mpc distance from the central BH. The radio emission is related to synchrotron radiation produced by relativistic particles in the jet. It is believed that the VHE radiation is produced by energetic electrons when interact with soft photons inside the jet (inverse Compton process) or by protons which generate hadronic cascades.
AGNs include a variety of objects with different spectral features, such as quasars, Seyfert galaxies and radio galaxies. In the unified scheme, the difference between the observable properties of these objects depends on their orientation with respect to the observer. The class of galaxies with the jet pointing towards the Earth are called BL Lacs or blazars. Currently all but two extragalactic objects detected in VHE γ-rays are blazars (the exceptions are the radio galaxy M87 [7] and the flat spectrum radio quasar 3C 279 [8]).

Starburst galaxies are galaxies in which star formation is taking place on an unusually large or rapid scale. Such bursts of star formation may take place after a collision with another galaxy. There are theoretical models predicting that the high supernova rate could provide shocks which are strong enough to accelerate charged particles to the highest energies.

Gamma-ray bursts (GRB) are the most energetic and violent short term phenomena in the universe. They last from tens of milliseconds to a few hundred of seconds, with a large diversity of temporal profiles. These phenomena are detected isotropically in the sky, at a rate of about 1 per day.

The fast and precise observations at X-rays by the BeppoSAX instrument, allowed counterpart observations by optical telescopes, which detected the GRB afterglows. These measurements could determine the redshift of some GRB host galaxies (centered around redshift $z \sim 1$), proving the their extragalactic origin [9].
Gamma-ray bursts are separated into two classes: short-duration bursts, lasting from a few milliseconds to 2 s, and long-duration bursts, from 2 s to a few hundreds of seconds. Short GRBs are thougt to be the result of binary mergers, involving the collision and coalescence of compact objects such as neutron stars, although other possibilities exist. On the other side, the most widely accepted interpretation of the phenomena of long-duration GRBs is that they are asymmetric supernova or hypernova explosions. In the fireball model [10], the explosion produces an ultrarelativistic outflow of an optically thick plasma shell, which produces the GRB as soon as it becomes optically thin. Because of the short duration and fast rise of the γ-ray flux, the sources must be compact. Since they are at cosmological distances, they must be extremely luminous, releasing about 10^{52} erg of γ-rays in less than 1 s. GeV photons can, in principle, be produced via synchrotron and inverse Compton processes by accelerated electrons in internal shocks.
The first significant detections in the GeV to TeV regime were made by EGRET, which could observe 7 GRBs between 100 MeV and 18 GeV [11]. So far (early 2008) the MAGIC telescope observed about 10 GRBs just seconds after the alert was given. And for the first time an atmospheric Čerenkov telescope was able to perform direct rapid observations of the prompt emission phase of GRBs. These observations were triggered by alerts from Swift, HETE-II, and Integral experiments. No evidence for γ-ray signals was found, and upper limits for the flux were derived for all them [12]. Bursts discovered by Swift have mean red shift of $z \sim 2$, thus their observability with ground based experiments is strongly limited due to absorption of VHE γ-rays through pair production with photons of the extragalactic background light, when traveling long distances. As a result, the number of GRBs that MAGIC can detect is estimated to 0.2-0.7 per year. This number can be expected to increase again with GRB monitoring by GLAST, AGILE and Swift altogether.

Galactic sources:

Supernova remnant (SNR) is the structure resulting from a supernova explosion, occurring at the end of the life of massive stars. When a star finishes burning its fuel and its mass is high enough, the internal pressure is no longer able to sustain the gravitational pressure and it collapses. The result is a huge explosion. The external shells are ejected forming a nebula, and the core becomes a compact object, a neutron star or a black hole, depending on the mass. There are two types of supernova remnants:

- *Shell type*, where only the expanding outer structure of ejected material radiates. A shock wave travels out ahead of the ejected material, plows into the surrounding interstellar medium, heats it and causes it to emit thermal X-rays. Particles accelerate in the shocks by means of collissionless interaction of the particles with magnetic clouds in the interstellar medium (Fermi acceleration). Accelerated electrons emit synchrotron radiation at radio wavelengths and Inverse Compton radiations at γ-ray energies. Accelerated protons may generate γ-rays through hadronic cascading.
  SNRs have already been detected at VHE γ-rays, as Cas A [13]. The morphology of the shell at TeV energies have been also mapped, as in the cases of RX J1713.7 − 3946 [14] or RX J0852.0 − 4622 [15].
- *Pulsar wind nebulae* (PWNe) or *plerions* emit the bulk of their radiation from within the expanding shell because of the presence of a fast rotating magnetized neutron star (pulsar, see below). The rotational energy of the neutron star is converted into a relativistic stream of particles (mostly electrons and positrons).

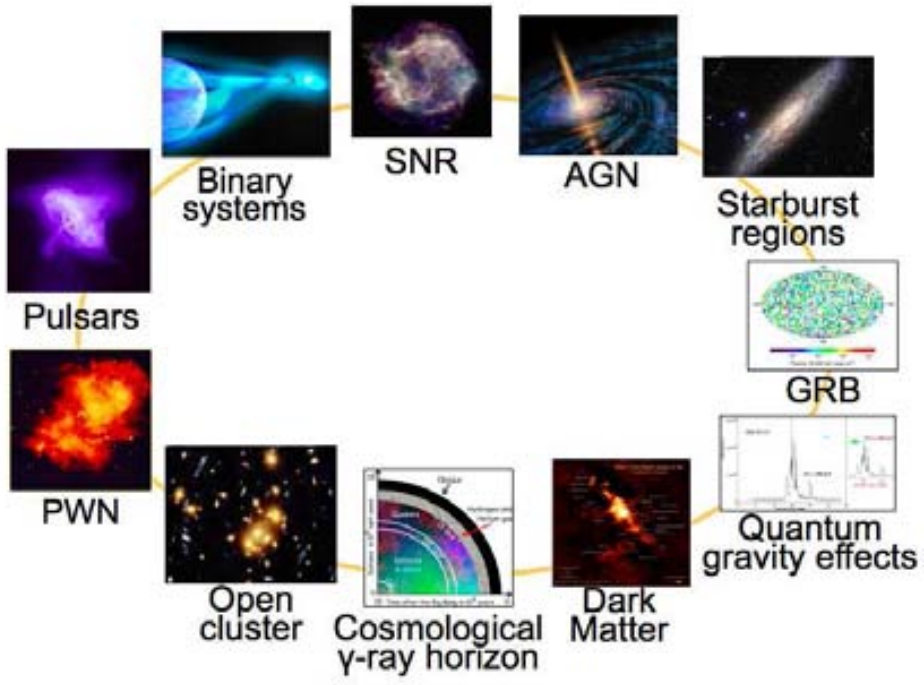

Figure 2.3: Illustration of the main scientific targets of VHE γ-ray astrophysics addressed by current ground based γ-ray experiments such as MAGIC.

This pulsar wind terminates in a shock when it encounters the ambient medium, which is often composed of ejecta from the supernova explosion. The accelerated electrons of the PWN are an efficient source of VHE γ-rays, by IC up-scattering of ambient photons, for example those of the microwave background. Compared to the case of shell-type remnants, the up-scattering process is very efficient in generating γ-rays, which explains the abundance of pulsar wind nebulae detected in high energy gamma rays. The most famous and best studied PWN is the Crab Nebula (or M1) that, being a bright VHE γ-ray emitter, is considered the GeV-TeV standard candle for γ-ray astronomy.

Pulsars are strongly magnetized (up to 10^{12} G fields) and very fast rotating neutron stars, with periods between a few milliseconds up to a few seconds. Intense radiation is beamed along the magnetic poles forming jets. Since the magnetic axis is not aligned with the rotation axis, the emitted beam sweeps through the sky, resulting in a periodic signal if the beam hits the Earth. Six pulsars have been detected at 100 MeV-10 GeV energies, but none has been detected so far at VHEs. The emission mechanism at the highest energies is not yet completely understood: it could be synchrotron emission near the polar caps of the pulsar or IC scattering in the outer regions (outer gaps) of the magnetosphere. The emission can be also a mixture of both mechanisms.
Besides Crab, three millisecond pulsars have been already observed by MAGIC: PSR B1957+20, PSR J0218+4232, and PSR B1951+32 [16, 17] and upper limits to the steady and pulsed emission have been derived for them.

Microquasars and X-ray binary systems Compact stellar objects like white dwarfs, neutron stars and black holes may produce HE and VHE γ-rays when they accrete matter. In binary systems, the process of accretion may occur in two ways: the transfer of matter can be through the stellar wind of the companion star, making the accretion close to spherical; or the transfer occurs when the compact object meets the decretion disk of the companion star, forming an accretion disk and relativistic jets of matter. Among them, MAGIC observed the black hole binary Cyg X-1 in a flare state [18]. Also HESS

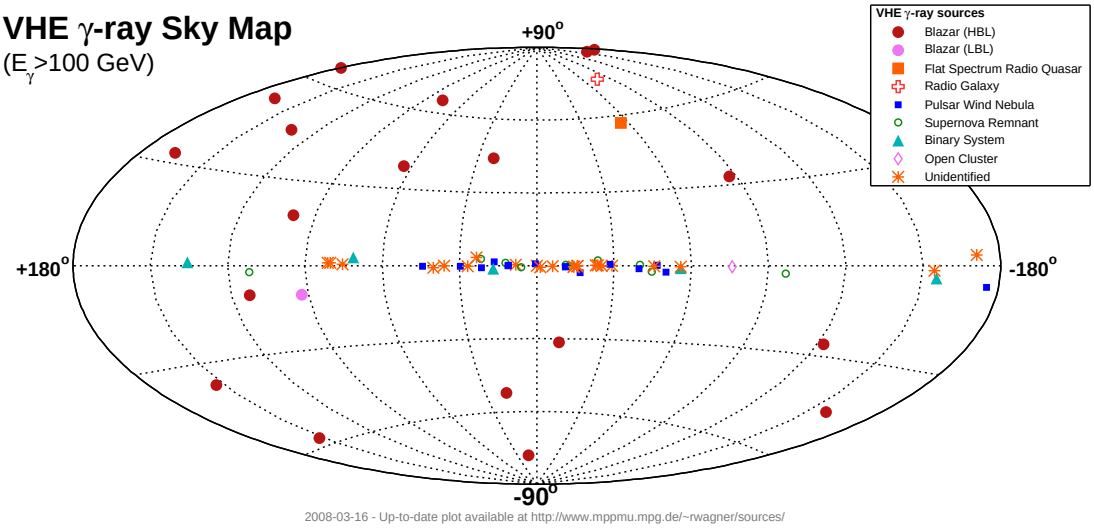

Figure 2.4: A sky map of the VHE γ-ray sources in galactic coordinates as of March 2008 (from R. Wagner in *http://www.mppmu.mpg.de/ rwagner/sources*).

reported the detection of the X-ray binary [19].
These objects are described in detail in Chapter 5, since LSI +61°303, the main topic of this thesis, belongs to this group.

Young open star clusters It has been suggested that the collision between winds of young massive stars could create shocks, which could accelerate particles to extreme energies. A VHE γ-ray signal associated with the open cluster Westerlund 2 has been detected by HESS [20], establishing a new class of galactic VHE γ-ray emitters.

Galactic center The Galactic center has been found to emit steady VHE γ-ray signal up to 10 TeV as reported by the CANGAROO [21], HESS. [22], VERITAS [23], and the MAGIC [24] collaborations. However, the interpretation of the emission mechanism is difficult since the region hosts different potential sources, and the angular resolution of the current instruments is insufficient to pinpoint the exact location of the VHE source. Most probable scenarios involve emission due to a pulsar wind nebula or a closeby supernova remnant.

Unidentified sources Some of the detected galactic VHE γ-ray sources do not have any obvious wavelength counterpart. Mostly they are sources detected by EGRET. The first unidentified VHE source was TeV J2032+4130, which was discovered by HEGRA [25] and later confirmed by MAGIC [26]. HESS also detected several sources with no clear counterpart (as HESS J1427-608, for instance) [27]. The GLAST experiment, with about 20 times better sensitivity than EGRET, will help to clarify some of the possible associations.

Diffuse emission EGRET and HESS experiments observed a diffuse high energy γ-ray excess in the galactic plane region after subtracting point sources [28, 29]. The most likely scenario is hadronic collision of cosmic rays with dense molecular clouds and dust in the galactic plane creating among other particles π^0's which subsequently decay into VHE γ-rays. Spatial agreement between the observed VHE γ-ray excess and distribution of molecular clouds supports this hypothesis.

Nowadays, several galactic and extragalactic source classes are established as TeV γ-ray emitters. The current sky map of VHE γ-ray sources is shown in figure 2.4.

Fundamental Physics: In addition to the aforementioned sources, there are some fundamental questions that γ-ray astronomy may help to understand.

Dark matter The nature of dark matter is still an ongoing discussion. One of the proposed candidates for dark matter is the neutralino, which, being itself its anti-particle, can undergo a self-annihilation into quarks or into two γ-rays. Quarks in turn convert into hadrons, among them π^0's, which decay emitting γ-rays. These γ-rays can be then detected confirming the existence of the neutralino, in case other γ-ray production mechanisms can be ruled out. Since the rest mass of the neutralino is uncertain, it is also the γ-ray energy. However, some of the dark matter models predict a rest mass above 50 GeV, which allows for VHE γ-ray signals.
Several locations, where an observable flux of γ-ray arising from neutralino annihilation is expected, have been targeted with Čerenkov telescopes, like e.g. the Galactic Center, but only upper limits have been derived [30]. Draco is a dwarf spheroidal galaxy at a distance of about 82 kpc. It has been also observed with MAGIC, and upper limits on the γ-ray flux have been derived [31]. A comparison with predictions from supersymmetric models shows that this limit does not constrain the phase parameter space, but a very high flux enhancement can be excluded.

Quantum gravity effects might become apparent when measuring time differences as a function of the energy, when observing short flares from distant sources. In fact, data from a well known TeV blazar, Mkn 501, were recently analyzed for energy-dependent differences in arrival time. This source showed flux variations in a time scale as short as 2 minutes. The timing analysis of these flares allows to set some of the most stringent constraints to quantum gravity theories predicting violation of Lorentz Invariance close to the Planck scale [32].

Gamma-ray horizon The γ-rays travelling from far away extragalactic objects can interact with the diffuse extragalactic background fields (EBL) producing e^+e^- pairs. The higher the energy of the γ-ray, the lower the energy of the EBL photon can be resulting in a higher absorption probability of the γ-ray. A given EBL density leads to a maximum distance beyond with a γ-ray source cannot be seen any more, the so-called γ-ray horizon.
The measurements of the γ-ray horizon for sources at several redshifts will open the possibility to obtain constraints in some fundamental cosmological parameters (such as the Hubble constant) or EBL models (see [33] for details).

2.4 Detection techniques

2.4.1 Direct detections

Cosmic rays at GeV energies can be detected directly from satellites, using different techniques. For instance, γ-rays can be detected when interacting with a scintillator material. This interaction produces some low-energy light (typically visual) which is then collected by a photomultiplier tube. Also Compton scattering can be used to detect γ-rays. For instance, in a two level telescope, composed of scintillator materials. The incoming gamma ray Compton scatters off an electron in the top level. The scattered photon travels into the lower level where it is absorbed. Phototubes viewing both levels determine the interaction points and the energy deposited in the two layers. From this, the energy and direction of the incoming γ-ray can be determined.

Gamma rays with energies greater than 30 MeV can lead to pair production when they interact with materials. An instrument using this technique is usually composed of layers of converter material interleaved with tracking material. An incoming gamma ray will interact with one of the converter layers to produce a pair. The trackers become ionized as the pair passes through them, leaving a trail of sparks. By recording the trails through the tracker, we can reconstruct a 3-dimensional picture of the pair as it travels through the chamber. The paths of the pair through the tracker allows determination of the direction of the incoming photon and the energy of the electron and positron give the energy of the incoming photon.

The EGRET satellite experiment, onboard the Compton Gamma-Ray Observatory (CGRO), was operated from 1991 to 2000 [34]. With a detector area of 0.1 m^2, it was able to measure γ-rays up to 30 GeV. This instrument conducted the first all sky survey above 100 MeV, detecting about 270 sources, 170 of which were unidentified.

Satellites with larger detector areas are necessary to reach higher energies, due to the relatively low flux of CRs above GeV energies. The AGILE (acronym for Astro-rivelatore Gamma a Immagini LEggero) was launched in May 2007. It has three instruments, which will cover the energy range from tens of KeV to 50 GeV, producing simultaneous detections in the X-ray and γ-ray band. The GLAST experiment is planned to be launched in May 2008. It will explore the energy range from 30 MeV to 100 GeV with 10% energy resolution between 100 MeV and 10 GeV. The LAT (Large Area Telescope), the main instruments on-board GLAST has a field of view about twice as wide (more than 2.5 steradians), and sensitivity at least about 50 times as large, as that of EGRET at 100 MeV, a comparison that improves at higher energies. Its two year sensitivity limit for source detection in an all-sky survey is 2.4×10^{-9}cm^{-2} s^{-1}(at energies above 100 MeV). GLAST will be able to locate sources to positional accuracies from 30 arc seconds to 5 arc minutes, given a much better point spread function, what would allow better searches of counterparts at other frequencies. After 1 year of survey, several thousand sources are expected to be detected with unprecedented resolution. However, still it will need several years of observation time to deliver a γ-ray spectrum of the Crab Nebula above 50 GeV.

2.4.2 Indirect detections: Extended air showers

Instruments with larger sensitive area can only be built on the ground, but the Earth's atmosphere is not transparent to CRs and VHE γ-rays. Thus detection is done indirectly: from the effects that CRs produce when entering in the atmosphere.

When an energetic enough cosmic ray (energy > 1 GeV) hits the atmosphere, an extended air shower develops, as illustrated in Fig. 2.5. The physics of EAS is reviewed in detail by [5, 35] among others. An EAS consists of the particles produced after the interaction of the primary CR on top of the atmosphere ($\sim$ 25 km above sea level). The CR interacts with a molecule of the atmosphere, generating several secondary particles. The secondary products subsequently interact and generate new particles, and, as this process repeats, an EAS is generated. At the beginning of the process the number of particles in the shower rapidly grows. But, since the energy of the primary particle is distributed over all the generated particles, at some point their energy falls below the threshold for production of further particles.

In the following, we describe first the physics of the electromagnetic and hadronic showers, and afterwords the techniques developed to detect them.

Electromagnetic EAS High energy γ-rays or electrons enter the atmosphere, interact with nuclei of the air molecules and develop an electromagnetic EAS. Primary γ-ray interacts with the strong Coulomb field of an atmospheric nucleus and generate an electron-positron pair. If the energy of the resulting $e^{\pm}$ is sufficient, they will be accelerated in the presence of the Coulomb field of other atmospheric nuclei. As a result of this acceleration, a fraction of their kinetic energy is emitted in the form of real photons, i.e., they undergo bremsstrahlung radiation. If the energy of the secondary γ-rays is still higher than 1.022 MeV, they produce again $e^{\pm}$ pairs, which in turn can suffer further bremsstrahlung processes. The result of this recursive process is an avalanche of photons, electrons and positrons, which roughly follow the direction of the original γ-ray and share its total energy. A sketch of an electromagnetic EAS is shown in Fig. 2.5 left.

On the other hand, if a cosmic electron is the primary particle, an electromagnetic cascade, analogous to the one described but starting with bremsstrahlung emission, develops. Electron-induced EASs are in fact an irreducible background for ground-based γ-ray detectors although their flux is much lower than that of hadronic CRs.

In electromagnetic showers there is also a muonic and hadronic component. They are

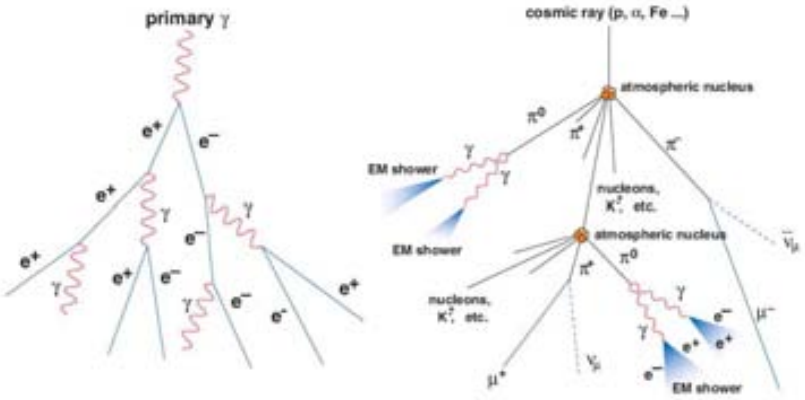

Figure 2.5: Sketch of the development of an EAS induced by a γ-ray (left) and by a charged cosmic nucleus (right).

produced by $\mu^{\pm}$ pair production and by hadronic photo-production ($\gamma + nucleus \rightarrow hadrons$). Nevertheless, none of these contributions are expected to be significant in electromagnetic showers, since the cross section of these reactions (about 1.5 mb for hadronic photo-production in air) are much smaller than that of bremsstrahlung and $e^{\pm}$ pair production (about 500 mb).

The result of the whole process is a shower of photons, electrons and positrons. And all of these particles are strongly collimated along the incident direction of the primary γ-ray.

As the EAS develops, the energy per particle reaches a critical energy, at which the energy losses of electrons and positrons by ionization and by bremsstrahlung are equal, about 86 MeV for e^- in air [37]. At lower energies, the losses by ionization become dominant and the shower dies out.

The height above the sea level where the number of particles in the shower is highest is called shower maximum. The higher the energy of the primary particle, the deeper is the shower maximum due to a longer cascade until the critical energy is reached. The depth of the shower maximum is proportional to the logarithm of the primary energy. The shower maximum is at about 13 to 7 km above sea level for energies of the primary γ-rays between 20 GeV and 10 TeV.

Hadronic EAS Hadronic showers are induced by high energy cosmic nuclei (mostly protons and helium nuclei) hitting an atmospheric nucleus and developing a shower with a hadronic core of pions (π^0, π^+ and π^- in roughly equal proportions), kaons and lighter nucleons (see Fig. 2.5). Hadrons and pions give rise to hadronic cascades through further collisions, resulting in photons, electrons, positrons and muons, that develop electromagnetic sub-showers. The following processes are involved in hadronic shower:

$$\begin{aligned} \pi^0 &\longrightarrow \gamma + \gamma \\ \pi^{\pm} &\longrightarrow \mu^{\pm} + \nu_{\mu}(\bar{\nu}_{\mu}) \\ K^{\pm} &\longrightarrow \mu^{\pm} + \nu_{\mu}(\bar{\nu}_{\mu}) \\ K^{\pm} &\longrightarrow \pi^{\pm} + \pi^0 \\ \mu^{\pm} &\longrightarrow e^{\pm} + \nu_e(\bar{\nu}_e) + \bar{\nu}_{\mu}(\nu_{\mu}) \end{aligned} \tag{2.3}$$

The muon lifetime ($\tau = 2.2 \times 10^{-6}$ s) is about two orders of magnitude higher than that of the pion and kaon ($\tau \sim 10^{-8}$ s), and, as many muons are produced with very high energy in the upper layers of the atmosphere, frequently they have high enough Lorentz factors to reach the Earth surface before decaying, and can also be detected by ground base experiments.

A hadronic shower grows until the energy per nucleon is below the pion production threshold (about 1 GeV). A hadronic shower with a primary proton with energy 100 GeV is shown

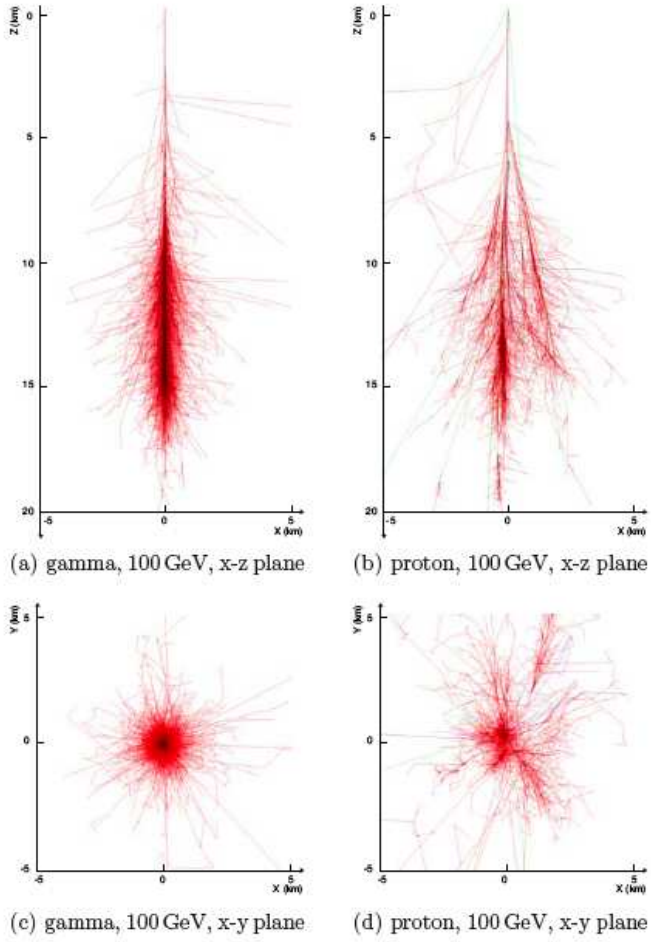

Figure 2.6: Simulated longitudinal (top) and lateral (bottom) developments of an electromagnetic (left) and hadronic (right) shower with initial energy 100 GeV. Plots adapted from [36].

in Fig. 2.6. A lateral view of the simulated hadronic EAS illustrates the fact that hadronic showers are broader, much wider and irregular than electromagnetic EAS.

Indirect techniques In the last 40 years, several techniques have been developed to detect CRs and VHE γ-rays from the ground:

Particle counter Shower particles can be directly detected with particle counters on the ground. As only showers produced by high energy primary particles reach the ground level, this technique works only for primary energies above $\sim 10^{13}$ eV (threshold that can be lowered building the detectors at high altitude). One technique is to detect high energy particles is through their direct interaction with water tanks. These energetic particles are traveling faster than the speed of light in water when they reach the detectors; therefore, their electromagnetic shock waves produce Čerenkov light that can be measured by photomultiplier tubes mounted on the tanks. This principle is used by experiments as MILAGRO, AGASA, Auger, HEGRA or KASKADE.

Fluorescence A small fraction of the shower energy is transferred to the atmospheric nitrogen molecules and excites them. The de-excitation has distinct spectrum lines in the near UV. Detectable fluorescence light is produced for primary particles above 10^{15} eV. This technique is also used in the Auger or HiRes experiments.

Radio emission Shower detection in radio wavelengths has also been investigated [38]. The

mechanism for the radio emission of air showers was recently proposed to be coherent *geosynchrotron* emission: Secondary electrons and positrons produced in the particle cascade travel with velocities close to the speed of light through the Earth's magnetic field and are deflected. As in synchrotron radiation, this produces dipole radiation that is relativistically beamed into the forward direction. The shower front emitting the radiation has a thickness that is comparable to (or less than) a wavelength for radio emission below $\sim$ 100 MHz. Hence the emission is expected to be coherent to a large extent, which greatly amplifies the signal. This method becomes feasible for energies above 10^{17} eV.

Čerenkov light Charged particles emit Čerenkov light when their speed in a medium is higher than the speed of light in the medium. This technique, that is the base for the MAGIC telescope, will be developed in following section 2.4.3.

2.4.3 Čerenkov light from EAS

Whenever a charged particle travels through a medium with a speed that exceeds the speed of light in that medium, it emits light. This light is called Čerenkov radiation [39]. The Čerenkov effect works as follows: when a charged particle particle travels in a medium, it disrupts the local electromagnetic field, polarizing it. As the electric dipoles depolarize, spherical electromagnetic waves are emitted along the track of the relativistic particle (Fig. 2.7).

This process is similar to the one produced by supersonic objects travelling in the air, where the sonic waves that travel slower than the supersonic body. The superposition of the spherical waves results in a shock front. In an equivalent way, the Čerenkov emission produces a shock-wave behind the charged particle as it crosses the medium. The wavefront propagates at a fixed angle $\theta_{\check{c}}$ with respect to the trajectory of the particle, due to the fact that the light emitted from different points along the particle trajectory add coherently just for this certain angle (see sketch figure 2.7).

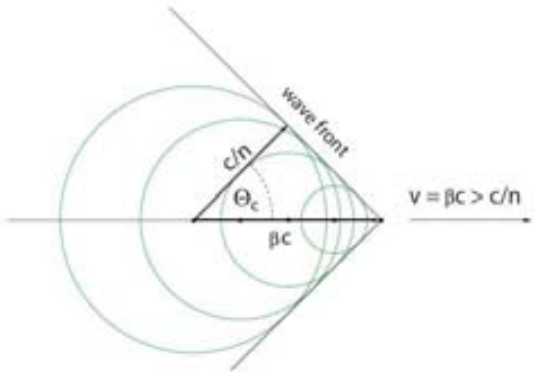

Figure 2.7: Sketch for the propagation of Čerenkov light. The radiation emitted by a charged particle moving in a medium, travelling faster than the light in these medium, causes constructive interferences that generate a shock wave. From [40].

The speed of light in a medium with refractive index n is $c' = c/n$, where c is the speed of light in the vacuum. Then, the Čerenkov angle can be deduced from geometrical considerations:

$$\cos\theta_{\check{c}} = \frac{c'}{v} = \frac{c/n}{\beta c} = \frac{1}{\beta n}\,, \tag{2.4}$$

where $v = \beta c$ is the speed of the charged particle. The speed of light in the air depends on the pressure and therefore on the height above the sea level. At sea level it has a value of 99.97% of the speed of light in the vacuum. Due to the fact that β is (by definition) smaller than 1, the maximum angle of Čerenkov emission given by

$$\cos\theta_{\check{c}}^{max} = \frac{1}{n}\,. \tag{2.5}$$

The minimum energy of a particle moving in a medium to emit Čerenkov radiation is thus given by

$$E_{\check{c}}^{thr} = \frac{m_0 c^2}{\sqrt{1-\beta_{min}^2}} = \frac{m_0 c^2}{\sqrt{1-(1/n)^2}}\,, \tag{2.6}$$

where m_0 is the rest mass of the charged particle.

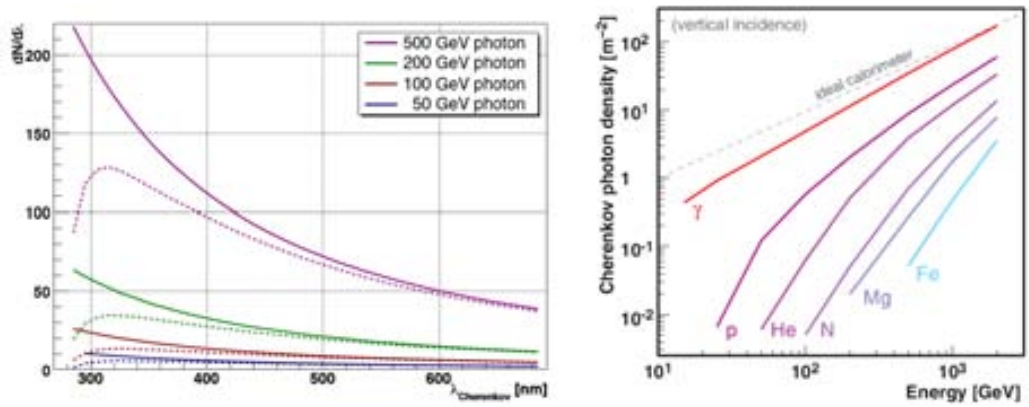

Figure 2.8: Left: Čerenkov photon spectra from vertical γ-ray showers of different primary energies, emitted at 10 km above sea level (solid lines) and detected at 2 km (dashed lines) after suffering absorption in the Ozone layer and Rayleigh and Mie scattering. Right: Čerenkov photon density at 2 km height above sea level and within a radius of 125 m from the shower core, for different type of vertically incident primary particles, as a function of their energies. From [42].

Due to the linear dependence on the particle's mass m_0, low mass particles such as electrons dominate the Čerenkov emission. The number of photons emitted per unit length l and per unit wavelength λ can be calculated using the Frank-Tamm equation [41]:

$$\frac{dN^2}{dxd\lambda} = \frac{2\pi\alpha Z^2}{\lambda^2}\left(1 - \frac{1}{\beta^2 n^2(\lambda)}\right) \tag{2.7}$$

where α is the fine structure constant and Z the particle's charge. Due to the $1/\lambda^2$-dependence of the number of photons emitted, the peak of the spectral intensity distribution lies in the UV region, as shown in Fig. 2.8 (left panel). In the same figure we show that due to strong absorption processes of UV radiation in the atmosphere, the spectrum observed at ground level is quite different from the emitted one, and lead to a maximum number of Čerenkov photons emitted in the blue region of the electromagnetic spectrum, at about 330 nm. The most important attenuation processes that Čerenkov photons suffer in the atmosphere are:

- Absorption in the Ozone layer ($O_3 + \gamma \rightarrow O_2 + O$), mainly in the upper part ($\gtrsim$ 10 km) of the atmosphere. Practically all photons with wavelength lower than 290 nm are absorbed through this process.
- Rayleigh scattering, which occurs on polarizable molecules with sizes smaller than the photon wavelength. If the atmospheric conditions are good, this is the process responsible for most of the Čerenkov light attenuation from 15 to 2 km above sea level, with a cross section $\propto \lambda^4$.
- Mie scattering, which takes place on polarizable molecules with sizes comparable or larger than the photon wavelength, basically aerosol particles present in the atmosphere. Its effect is especially important when atmospheric conditions are not optimal, i.e., if there is dust, pollution, clouds, fog, etc. The spectral dependence of the cross section is $\propto \lambda^a$, with $1 \lesssim a \lesssim 1.5$.
- Absorption by H_2O and CO_2 molecules, only important for photon wavelengths above 800 nm. These wavelengths are outside the sensitive range of the photo-sensors which are typically used for Čerenkov detection.

The light yield of EAS initiated by different incident particle species is shown in Fig. 2.8 (right panel). For an electromagnetic shower, the summed track length of all charged shower

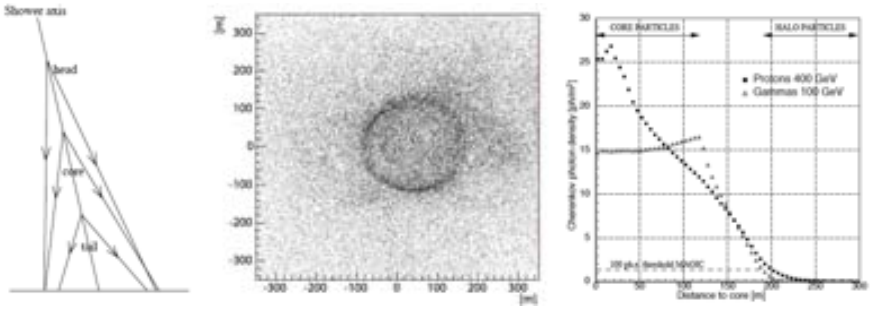

Figure 2.9: Left: Schematic view of an atmospheric γ-ray shower showing different Čerenkov angles at different altitudes. Middle: Čerenkov photon distribution for the shower with initial energy 50 GeV. Right: Simulation of the lateral distribution of Čerenkov photon densities for 100 GeV γ-ray and 400 GeV proton induced showers. The γ-ray density is practically constant out to a radius of a hundred meters, where the hump occurs, and then decays rapidly for larger radii. From [43].

particles is in first order proportional to the energy of the primary particle. The number of emitted Čerenkov photons is proportional to the number of shower particles. Therefore, the total Čerenkov light yield is proportional in first order to the energy of the primary particle. This means that the atmosphere behaves almost like an ideal calorimeter for γ-ray-initiated showers.

When travelling through the atmosphere, shower particles cross a medium that continuously changes its refraction index n. Under the very simplified assumption of an isothermic atmosphere, the refraction index is given by

$$n(h) = 1 + n_0 e^{-h/h_0} \quad n_0 = 0.00029\,, h_0 = 7.1\text{km} \tag{2.8}$$

where h is the height above the sea level. With decreasing height, the refraction index n of the air increases due to the increasing density and therefore the emission angle θ of the Čerenkov light increases according to equation 2.8. This dependence of the angle on height is responsible for the fact that the light emitted by the shower electrons and positrons at a range of different heights reaches the ground at approximately the same distance from the axis of the shower, an effect that produces a characteristic enhancement of the Čerenkov light density. This effect is illustrated in figure 2.9. This ring, also called hump, typically occurs for a radius between 100 and 130 m from the center of the Čerenkov light pool. The Čerenkov light at the ground is the superposition of all the light emitted in cones integrated over the whole shower longitudinal path. However, in a real EAS, due to multiple scattering the trajectories of secondary $e^{\pm}$ are slightly deviated from the track of the incoming primary γ-ray, and consequently, the ideal ring gets smeared.

2.4.4 Čerenkov telescopes

Solar heliostat telescopes A possible method to detect the Čerenkov light emitted by an EAS is the use of solar panels. A large field of solar heliostats can be used as a primary collection mirrors of the telescope. Although the heliostats have been designed for the collection and concentration of sunlight for solar energy research, it is also possible to use them at night to collect the quick flashes of Čerenkov light that result from a γ-ray air showers. The Čerenkov light is collected onto a secondary mirror, which focus it onto a camera of photomultiplier tubes, which turns the light into a measurable electric signal. This concept is illustrated in figure 2.10. Experiments as CELESTE (see [44] for an status review), STACEE [45], and CACTUS use this technique.

Imaging Atmospheric Čerenkov telescopes Present instruments in the field of ground-based γ-ray astronomy are sensitive to photons with energies above ∼50-100 GeV. The most

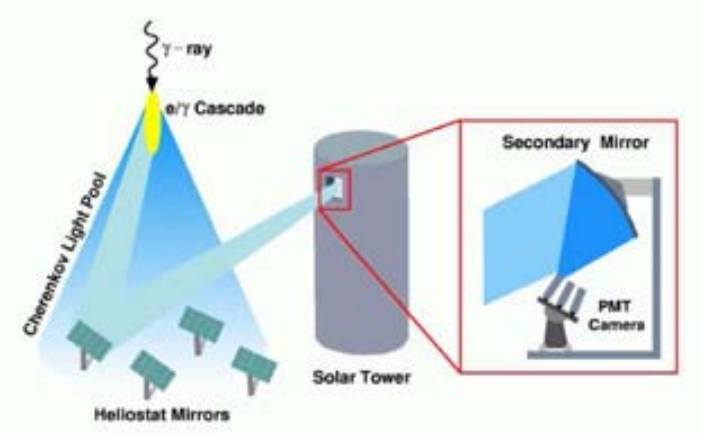

Figure 2.10: The solar heliostats collect the Čerenkov light produced by γ-ray air showers. The light is reflected onto secondary mirrors on the solar tower, which focus it onto a photomultiplier tube camera. From [46].

sensitive of these instruments are Imaging Atmospheric Čerenkov Telescopes. The pioneering experiment in this field was the Whipple telescope [47], which in 1989 detected the first gamma-ray signal from the Crab Nebula. Significant improvement was afterwards achieved by HEGRA [48] through the introduction of stereoscopy, i.e. the simultaneous imaging of the same shower with multiple Čerenkov telescopes.

An IACT consists of

1. a mechanical system, which counteracts the Earth rotation to track an astrophysical object in the sky,

2. a collecting surface, which gathers and focuses the incident light, and

3. a receiver element, which converts the collected light in a recordable image of the shower.

The principle of the IACT is shown in figure 2.11. The EAS is measured indirectly by generating an image of its Čerenkov light against the night-sky. A mirror surface collects a fraction of the Čerenkov light pool and a set of light detectors at the focal plane converts the incident Čerenkov photons into electric pulses which conform an image of the EAS.

The wide spread of the Čerenkov light has two counteracting consequences. On one hand, the light spread allows the IACT to detect EASs over a large range of impact parameters[2], from $\sim$ 30 to $\sim$ 150 m. This provides IACTs with huge collection areas (of the order of $10^5 \mathrm{m}^2$) which results in high sensitivities in comparison with γ-ray detectors mounted on satellites, whose dimensions are limited by space-launching requirements to $\sim 0.01 - 1\mathrm{m}^2$. On the other hand, the dilution of the Čerenkov radiation over the large light pool makes its detection more difficult, forcing to use large mirror areas and high sensitivity photodetectors.

The image formed in the camera of photo-sensors, generally photomultiplier tubes (PMT)[3],is a geometrical projection of the atmospheric shower: a symmetrical ellipsoid in the atmosphere causes an elliptical image in the camera.

Čerenkov photons emitted at different heights reach the telescope mirror dish with different angles and, therefore, are focused on different positions in the camera of the telescope. Therefore the image contains information of the longitudinal development of the EAS, i.e., the number of particles emitting Čerenkov light as a function of the height in the atmosphere.

[2]Although the efficiency of detection of showers with impact parameters larger than $\sim$ 150m is quite low, the large amount of showers arriving with these larger impact distances makes them to be still a significant fraction of the total amount of detected showers.

[3]Higher sensitivity light detectors such as Hybrid PhotoDetectors (HPD), Avalanche PhotoDiodes (APD), or Silicon Photomultipliers (SiPM) have also been studied, and are proposed for the next generation of IACTs.

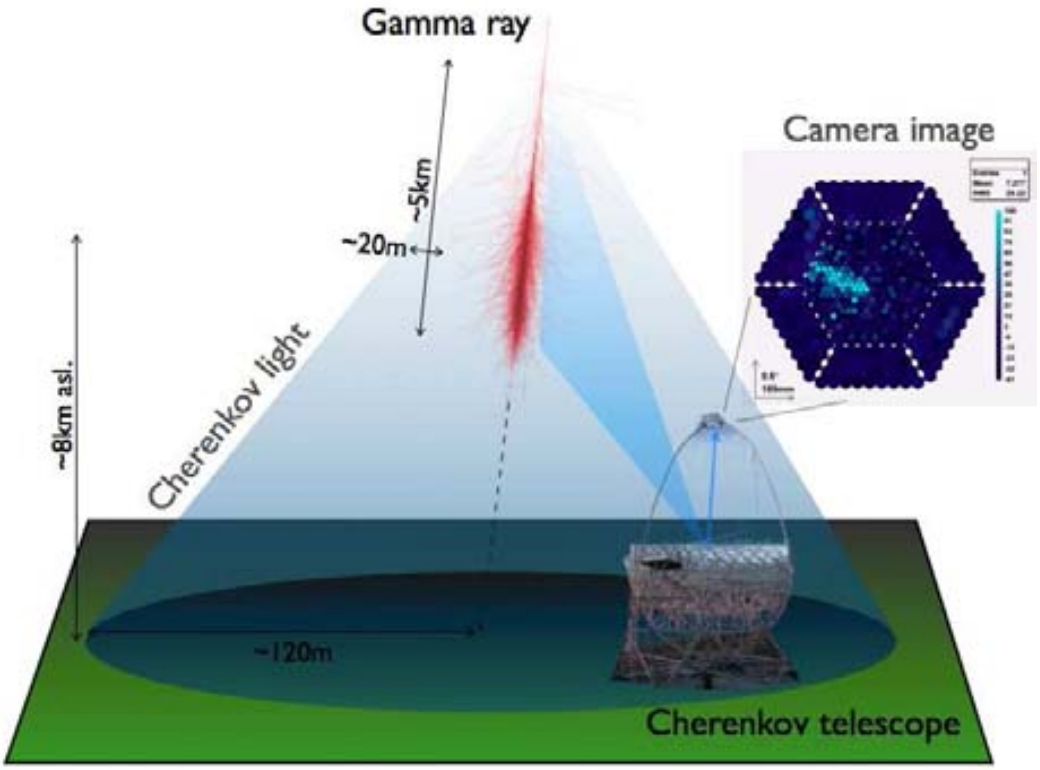

Figure 2.11: Sketch of the detection principle of an IACT telescope, through the formation of an image of the EAS in a pixelized camera. The numbers in the figure correspond to a typical 1 TeV γ-ray induced shower.

Light coming from the upper part of the shower, where the secondary particles are more energetic, arrives at a smaller angle and is mapped onto a region close to the camera center, whereas light emitted from the last stages of the shower, from less energetic secondary charged particles, has larger angles and is mapped further away from the camera enter.

The Čerenkov technique relies on the information that is contained in the images formed in the telescope to infer the characteristics of the primary particle that originated the EAS, as will be explained in more detail in section 4.2.4. On one hand, the total amount of light contained in the image is the main estimator of the energy of the primary particle. This is true because, although the fraction of initial energy which is lost in form of Čerenkov radiation is about 3 orders of magnitude smaller than the energy which is lost through ionization, the ratio between the two energy losses is, in first order constant. Therefore, the amount of Čerenkov light provides a good estimation of the energy absorbed in the atmosphere, that is, the atmosphere itself acts a calorimeter. On the other hand, the orientation and shape of the image are indicators of the nature and the incoming direction of the primary particle.

To characterize an IACT, two important parameters are required, namely the sensitivity and the energy threshold. The sensitivity of an IACT is defined as the minimum detectable γ-ray flux in a given number of observation hours. The energy threshold of the telescope is the minimum energy of the primary particle for which the telescope is able to disentangle the signal from the background. Both parameters are not constant for a given telescope, because they are strongly influenced by the amount of dispersion (i.e. density) of the Čerenkov light at the observation ground level. Observational conditions as the zenith angle of the observed source produce a change in the light density at ground. Although an equivalent amount of light is produced for vertical and slant cascades, the light spreads over a larger area in the ground, and the resulting photon density is lower. Although the sensitivity of IACT grows when observing at high zenith angles due to the increase on collection area, their energy

threshold moves to higher energies, as the Čerenkov light spreads in a larger area.

The conventional definition of the energy threshold E_{th} for IACTs is the energy for which the differential γ-ray rate distribution peaks. As this definition makes the E_{th} dependent on the slope of the γ-ray spectrum coming from the source, a reference object or standard candle is used for an unambiguous definition. For Northern hemisphere IACTs, the source widely chosen as reference is the Crab Nebula.

IACT experiments The first reliable VHE gamma-ray signal from an astronomical object, the Crab Nebula, was detected using the IACT technique in the late 1980s by the Whipple 10-m-diameter telescope located on Mt. Hopkins, Arizona [47]. Over the next 15 years, major efforts to detect γ-rays were made by the Čerenkov Array at Themis (CAT), the Gamma-Ray Observatory in the Outback (CANGAROO), High-Energy Gamma-Ray Astronomy (HEGRA) and other groups. HEGRA pioneered the use of stereoscopic arrays, consisting of two or more 10-m-diameter class telescopes observing the flashes simultaneously from different directions, which represented a significant improvement in sensitivity. They managed to detect about 10 VHE γ-ray sources, in particular they discovered γ-rays from blazars [49].

The turn of the century brought about a new generation of telescopes and arrays of telescopes which are equipped with larger dishes and higher pixelization cameras, and bring the energy threshold down to $\sim$ 100 GeV. The first such instrument was the High-Energy Stereoscopic System (HESS), an array of four 13 m diameter IACTs equipped with $\sim 5^o$ field of view cameras, located in Namibia. It was completed in 2004 and covers an energy band from 100 GeV to 100 TeV with an angular resolution of around 0.07°.

The 17 meter diameter single MAGIC Telescope [43] was commissioned one year later in La Palma, Spain. MAGIC is the lowest energy threshold IACT in the world. It combines a huge ultralight reflector with a large number of technical innovations. The camera has a total field of view of about 3.5°. The design of the telescope was optimized for fast repositioning to perform follow-up observations of the prompt emission of Gamma-Ray Bursts. Whereas HESS observes sources mainly from the Southern Hemisphere of the sky, MAGIC targets the Northern Hemisphere.

The Very Energetic Radiation Imaging Telescope Array System (VERITAS) is a stereoscopic array consisting of four 12-m diameter IACTs, located in Southern Arizona [50] which started fully operation in 2007.

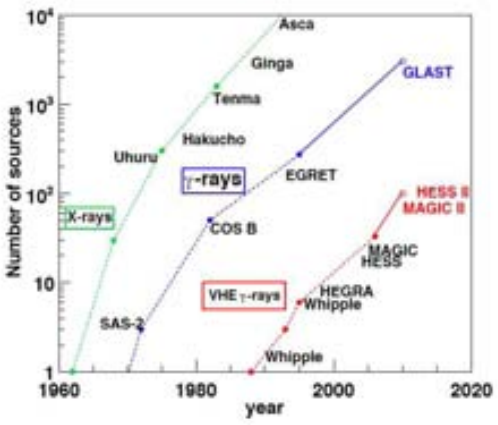

Figure 2.12: Number of established sources as a function of time (the so-called *Kifune-plot*) in the X-ray, GeV γ-ray and VHE γ-ray domains. From J. Hinton in the rapporteur talk at the 30th International Cosmic Ray Conference (2007) [51].

Both HESS and MAGIC have already started their upgrade: HESS is building a single 28 m diameter telescope at the center of the existing array and MAGIC is installing a second 17 m telescope to be operated in coincidence with the first one. It will be commissioned in Autumn 2008.

With this new generation of instruments, the current number of TeV γ-ray sources (as reported in the 2007 International Cosmics Rays Conference) is about 70 and is continuously growing. The development of the TeV field is compared with the development of the X-ray and GeV γ-ray fields of astronomy in figure 2.12 (an updated version of the so-called *Kifune-plot*).

This thesis makes use of the MAGIC installations for the specific observations on the galactic source LSI +61°303. Thus the MAGIC telescope will be described in detail in the next Chapter.

Chapter 3

The MAGIC Telescope

The MAGIC Telescope, the detector on which the experimental part of this Thesis is based on, is introduced. The MAGIC group at IFAE was responsible for building the camera and calibration system, writing the software to control them, and the software to centrally control all telescope systems. In particular, the author of this Thesis was responsible for the development and maintenance of the control software for the camera and calibration systems, which are treated in detail in this chapter.

The Major Atmospheric Gamma Imaging Čerenkov Telescope belongs to the latest generation of Čerenkov telescopes. It is located on the Canary island of La Palma (28.8°N, 17.9°W) at the Roque de los Muchachos Observatory (2200 m a.s.l.). This is the same location where the HEGRA[1] stereoscopic system of Imaging Atmospheric Čerenkov Telescopes was installed. This observatory is rated among the best observation sites in the Northern Hemisphere[2].

The initial ideas of the project came with a "Letter of Intent" in 1995 [52]. A detailed Technical Design Report was completed in 1998 [43]. The construction started in September 2001 and the commissioning phase finished in Fall 2004. Since then, regular observations are carried out.

Building the MAGIC telescope represented a challenge due to the numerous technological innovations and the introduction of new techniques never tried before in IACTs. The commitment to technological improvement was forced by the goal of the experiment: to push down the energy threshold as much as possible, below the values achieved by Whipple[3], and almost cover, with the highest sensitivity possible, the still unexplored energy gap between 10 GeV and 300 GeV. With a high conversion efficiency from Čerenkov photons to photoelectrons (phe) and its large collecting mirror area (17 m Ø), an energy threshold (E_{th}) close to 30 GeV is the ultimate target for MAGIC.

Other key elements are the fast movement of the telescope to any position in the sky to observe prompt emission of γ-ray bursts and the capability to operate under moderate moonshine conditions, increasing the duty cycle by a factor 1.5.

In the following sections, the most relevant elements of the MAGIC telescope are described (see Fig. 3.1), with emphasis in the technological innovations with respect to previous IACTs. We pay special attention to the description of the telescope camera and calibration system, and in particular their slow control software, since it is the part of the detector in which the author of this Thesis contributed technically.

[1] HEGRA stands for High Energy Gamma-Ray Astronomy, and its description can be found in [48].

[2] In fact, due to good atmospheric quality, low human-made light background and good weather, it became the European Northern Observatory (ENO).

[3] A recent review of the Whipple telescope, based at the Fred Lawrence Whipple Observatory in Southern Arizona (U.S.) can be found in [47].

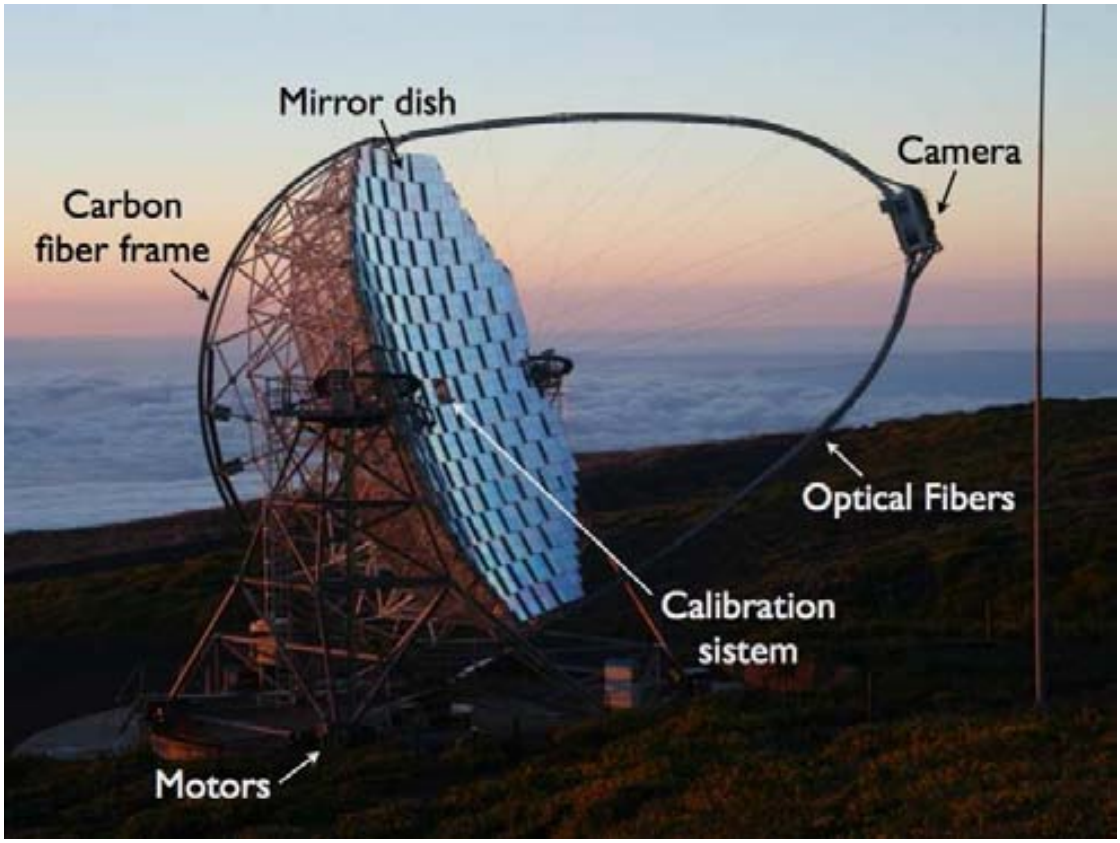

Figure 3.1: Photograph of the MAGIC telescope with main elements labelled.

3.1 The telescope frame, mirror dish and drive system

One of the unique feature of the MAGIC telescope was its ability to reposition to any direction of the sky in a matter of a few seconds, with an eye on observing the prompt emission of GRBs. To achieve this goal, the weight of the moving parts of the telescope is required to be as low as possible.

The telescope has an alt-azimuth-mount placed on a circular rail. The frame is made of carbon fiber-epoxy composite tubes which are especially light-weight. The rest of the support is made of aluminum. The total weight is about 64 tons [53]. The signal transmission cables from the camera to the control house imposes a mechanical constraint on the movement: from $-80°$ to $105°$ in zenith and $400°$ in azimuth. It is moved by two 11 kW azimuth and a single 11 kW zenith motor. The repositioning times ranges from 0 to 40 seconds depending on the angular distance the telescope has to slew, whereas the mean slewing time is about 30 seconds. In the first two years of operation of the MAGIC telescope about 10 GRBs were observed seconds after the alert was given, but no VHE γ-ray signal was found so far [12].

The angular position is controlled by 14-bit shaft encoders with an accuracy of $0.022°$. By using a high sensitivity CCD camera mounted on the mirror dish center, the precision of the tracking system can be verified by the simultaneous monitoring of a set of reference LEDs installed in the camera frame and background stars (Starguider System). With this star-field tracking monitor system it has been measured that the telescope tracks better than a 1/10 of a pixel size [54].

Reflectors of Čerenkov telescopes follow either a *Davies-Cotton* [55] or a *parabolic* layout. In the first case, all reflector facets have the same focal length f, which in turn is the same of the telescope as a whole, and are arranged on a sphere of radius equal to f. This mount is designed to reduce Coma aberrations. Whereas in the parabolic layout, the spherical mirror

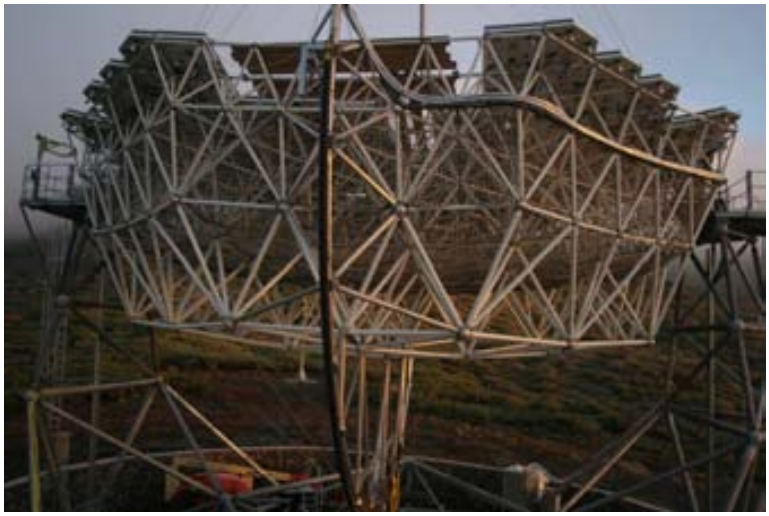

Figure 3.2: MAGIC telescope pointing upwards. In this position, the carbon fiber frame are clearly visible. Mirrors were partially installed.

facets are arranged on a paraboloid, and the focal length of the individual mirrors varies with the distance from the optical axis. Both approaches provide (for small and perfect mirror facets) a point-like focus for light rays parallel to the optical axis.

The parabolic layout is isochronous, i.e. a plane incident wavefront results in practically no spread in the photon arrival time distribution at the focal plane. As it is important to keep the Čerenkov time distribution narrow to minimize the effect of the Night Sky Background, in order to minimize the spread in the arrival times at the camera plane, the overall curvature of the reflector area is parabolic[4]. The focal length to diameter ratio $f/D = 1$ is one of the smallest among the currently operating IACTs (the smaller the f/D value the larger the coma aberration) and it is a consequence of the light structure of the telescope and the limited cost[5].

The telescope reflector is composed of 964 octagonal mirror elements of 49.5×49.5 cm^2 area each, grouped in 4-element panels[6]. Each panel is equipped with an internal heating system to prevent dew and ice formation. Due to the overall parabolic shape of the reflector, their focal length gradually increases (from 17 to 18 m) with the distance to the optical axis. The construction of these individual mirror elements is another of the technical innovations adopted by the MAGIC telescope. An aluminum box filled by an aluminum honeycomb structure, which is light but rigid enough, constitutes the base of each mirror element. A 5 mm thick AlMgSi1.0 alloy front plate is glued to the honeycomb. The front plate surface is diamond-milled to its final shape and then quartz coated to protect it against aging and scratches. The final mirror element weight less than 4 kg. The advantages of this mirror structure with respect to the conventional glass mirrors typically used by IACTs are: light weight, longer life, and fast and cost effective production.

The mean reflectivity in the range of interest ($\sim 300 - 650$ nm) is about 85% and the roughness of the mirror surface is below 10 nm. 90% of the light of a parallel incident beam is collected in an area smaller than a small pixel of the MAGIC camera [56].

Another novel technique related to the reflector surface has been introduced in the MAGIC telescope. The frame structure still suffers residual deformations when changing elevation.

[4]The side effect of the parabolic dish is the coma aberration, which makes the images to look extended if looking off-axis. In case of the MAGIC reflector, coma aberration effect amounts to 7%.

[5]A larger f/D value could mean that the camera has to be larger and placed further away from the reflector than 17 m, which would necessitate both, a much heavier camera and supporting structure.

[6]Due to an originally too tight mount between the panels, a staggering or *chessboard* structure of the panels was introduced in 2005. This step of about 6 cm between mirrors leads to a small difference in the photon arrival times at the PMT camera of up to 0.6 ns, which is still below a possible signal resolution of the PMTs (1-2 ns).

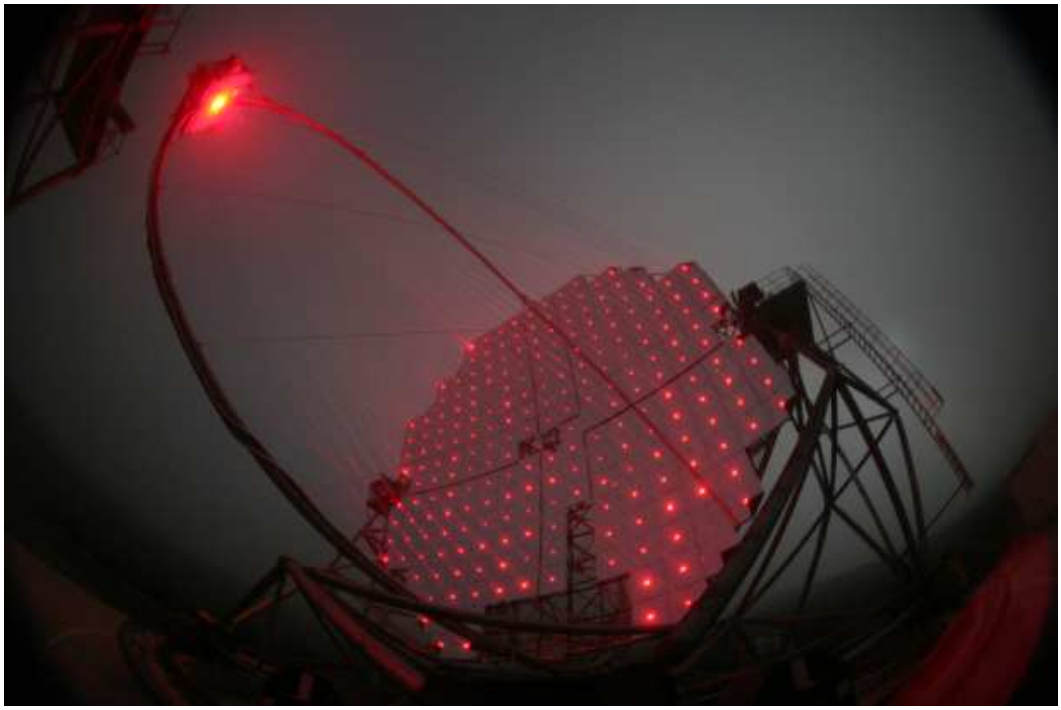

Figure 3.3: Mirror panel lasers switched on during re-alignment procedure. Not all mirror panels were installed at the time of the photograph.

To correct for them, an Active Mirror Control (AMC) system has been developed [57]. Each 1×1 m^2 mirror panel is equipped with a switchable laser pointer (see Fig. 3.3). The spot that this laser makes on the camera lids is monitored by a CCD camera and used as a reference for the original position of the mirror panel. Two stepping motors can tilt the panel in two perpendicular directions to adjust its position until the laser spot shifts to its nominal position (defined by 4 reference LEDs located in the camera lids). The whole reflector can be re-adjusted remotely in less than 3 minutes.

The Point Spread Function (PSF) of the reflector can be measured using a dedicated CCD camera, from the width of the rings produced by individual muons or from the comparison of Hillas parameters in real and Monte-Carlo data. The reflector is usually focused to 10 km because this corresponds to the typical height of the maximum of a 100 GeV γ-ray induced shower at low zenith angle. After AMC adjustment, a point-like light source at this distance produces a Gaussian image at the camera plane with $\sigma = 10.5$ mm, which corresponds to 0.035°.

3.2 The camera

The MAGIC camera captures the Čerenkov light showers using photomultiplier tubes (PMTs), converts the light into an electric signal and the transmits it to the control house.

The camera is designed to improve the γ-ray sensitivity and to reduce the energy threshold. Over the last decades, IACT cameras developed from a single PMT to arrays of hundreds of pixels. The finer the camera is pixelized, the better it discriminates γ-ray and background cosmic ray showers. A small pixel size also helps reducing the integrated background from the light of the night sky (LONS), which allows to reduce the trigger threshold at the discriminator level, resulting in a reduction in the energy threshold.

The images produced by low energy γ-ray induced showers ($\leq$100 GeV) are rather small (angular size $\sim0.3^\circ$) and lie close to the camera center. This requires a fine pixelization close to the camera center. On the other hand, the images of higher energy showers are more extended (up to 1.5°). So only a $\sim 4^\circ$ field of view (FOV) camera ensures full containment

Figure 3.4: Front view of the MAGIC telescope camera. The plexiglas window protects the camera interior where the light concentrators collect the incident light onto the camera photosensors.

of the higher energy showers images (shower energies ≤ 10 TeV).

The final pixel layout represents a trade off between the aforementioned requirements and the cost of the PMT array. The MAGIC camera was built with two pixel sizes: an inner hexagonal array composed of 397 inner PMTs[7] of 1″ diameter (0.1° FOV), surrounded by 180 outer PMTs of 1.5″ diameter (0.2° FOV). The whole camera FOV is $3.5 - 3.8°$ in diameter. A scheme of the MAGIC camera is shown in figure 3.5.

The photosensor used for all pixels are PMTs. Although their quantum efficiency (QE) is typically lower than the one achieved by hybrid photo-multipliers and avalanche photodiodes, the latter were too expensive and their active area was limited. The PMTs were carefully selected to comply with the following requirements:

- Low gain ($\lesssim 2 \times 10^4$) compared to typical PMTs to avoid that moonlight induces anode currents in excess of some tens of μA.
- Good time resolution with a pulse full width half maximum (FWHM) close to 1 ns in order to exploit the structure of the Čerenkov flashes, to reduce the coincidence trigger window and to efficiently suppress accidental triggers produced by LONS.
- Wide dynamic range up to 5×10^3 to detect the largest expected signals ($\sim 5 \times 10^3$ phe per pixel for a $\sim$ 10 TeV γ-induced shower), and at the same time resolve signals of just a few phe.
- Good QE in the range of wavelengths of the showers Čerenkov light (between ∼300-600 nm). Moreover, PMTs are coated by a scattering layer and a wavelength shifter mixture that convert the photons in the near-UV range into photons in a range where the PMT have a higher QE. This technique enhance the average QE of the PMTs in $\sim 20\%$ [58].
- Low afterpulse rate to avoid limiting the minimum trigger threshold setting for individual PMTs.

The PMTs have a hemispherical bialcali photocathode and 6 dynodes, studied in detail in [59]. The first five amplification stages are powered through the main HV power supply.

[7]The central pixel is equipped with a higher sensitive photodetector, devoted to optical observations. Such observations are useful for searches for pulsed γ-ray emission from objects which have a corresponding optical pulsation (as the Crab Nebula).

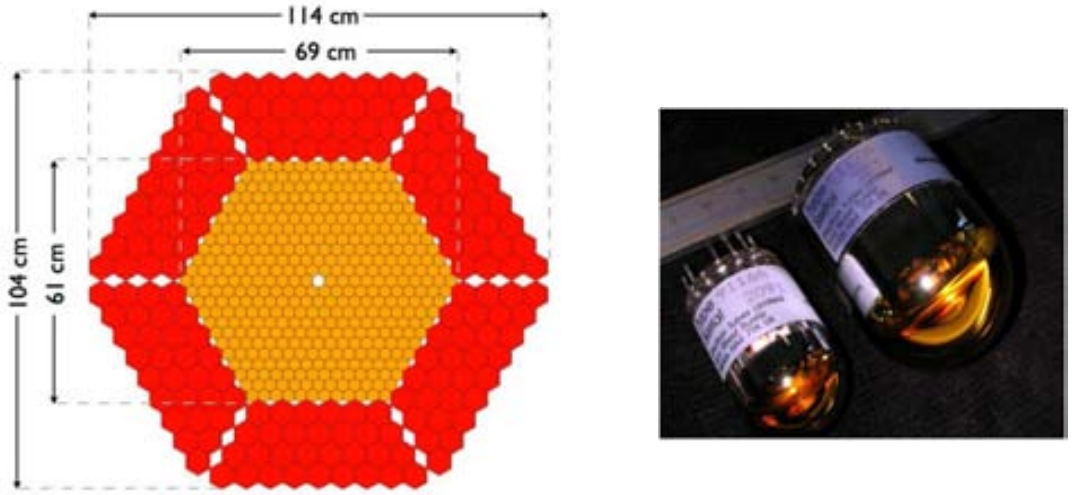

Figure 3.5: Left: Scheme of the MAGIC camera. The inner region (in orange) is equipped with 397 0.1° Ø FOV pixels to get a better sampling of the low energy showers. The outer region (in red) is composed of 180 0.2° Ø FOV pixels. The total size of the camera is 1.5 m, corresponding to a FOV of $3.5 - 3.8°$ in diameter. Right: The two pixel sizes in the MAGIC telescope's camera (without coating).

The first dynode is fixed by a Zener diode to 360 V. The voltage drops in the successive dynodes 2, 3 and 4 are equal, but can be regulated for each pixel. The last two dynodes, 5 and 6, need an independent power supply on account of the high current. They are fixed to a -360 V and -175 V with respect to the anode. The total voltage drop in each individual photomultipliers is regularly adjusted (*flat-fielding* process) such that a pulsed light source generates the same charge in ADC counts for all pixels. Inner pixels are usually run at $\sim$ 1200 V (voltage drop from cathode to anode) while outer pixels run at $\sim$ 975 V. These HVs and the anode currents are monitored at a rate of 2-3 Hz using 12 bit ADCs, multiplexed in groups of 96.

A plate of light guides is coupled to the front of the PMTs (see figure 3.4). Light collectors, common in IACTs, concentrate the light entering a hexagonal grid onto a circular photocathode and reject the background light coming from outside reflector (such as back-scattered light from the ground, during moonshine, distant light from human installations or cars). The concentrators are especially designed to maximize the probability of *double crossing*: for some incident angles photons can cross twice the photocathode, hence the effective QE increases. The MAGIC light collectors are made of aluminized Mylar foil with $\sim$ 85% reflectivity and allow an increment of the photon detection efficiency by $\sim$ 20%.

Finally, a front cover made by UV transmitting plexiglas protects the PMTs and light collectors from the environmental conditions and hermetically seals the electronic sensors and camera elements from humidity and dust. It has an uniform transmission (from 300 to 800 nm) of about 92%.

The design of the camera aimed at the lowest possible weight. Therefore, most of the trigger and readout electronics is not included in the camera housing, but in a central data acquisition building, located 150 m away from the telescope. The total size of the camera is 1.5 m in diameter and it weights 500 kg.

But the decision of housing the main readout electronics outside the camera implied a major challenge: the attenuation and distortion of analogue PMT signals during the transmission to the acquisition building. A distortion of a few ns of the fast Čerenkov optical flashes (which last 2-3 ns) caused by coaxial long cables can reduce the efficiency of the time coincidence based trigger. To minimize the pulse degradation, optical fibers are used instead to transfer the PMT signals. Using optical fibers we ensure that there is no crosstalk between

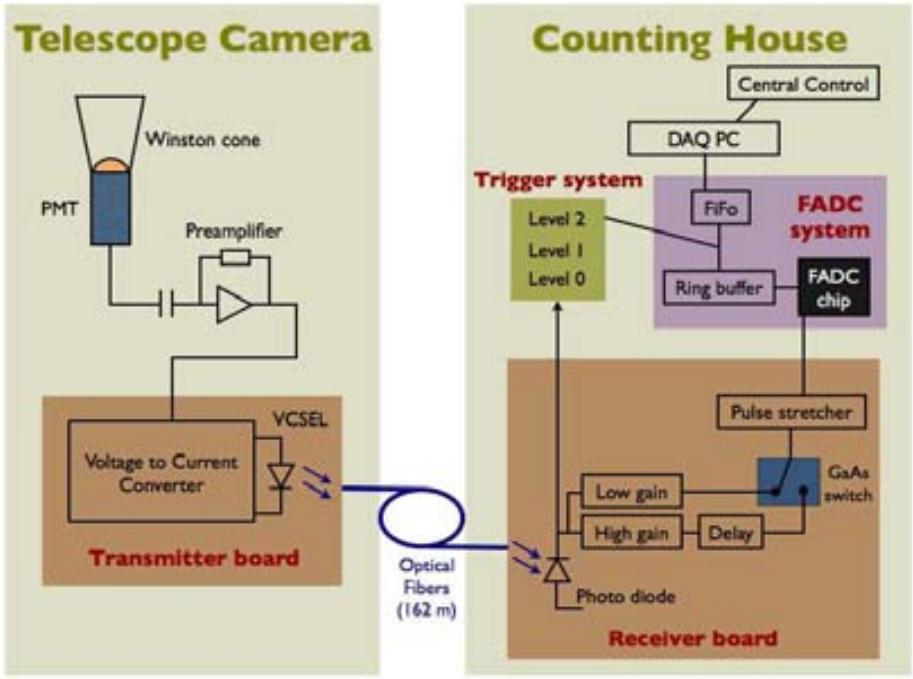

Figure 3.6: A flow diagram of the MAGIC readout chain. PMT signals are reconverted into optical pulses and sent to the counting house. There the pulses are digitized and, in Case a trigger condition is fulfilled, recorded on disc.

different channels so they can be packed more compactly, signals are not affected by external electromagnetic interferences and cables are light. The use of optical fibers implies that the electrical PMT pulses have to be converted into light pulses, which is done by means of an optical link system with VCSEL (Vertical Cavity Surface Emitting Laser) drivers, specially adapted to have low instabilities [58].

3.3 Trigger and data acquisition systems

Once the signal is in the control house, the so-called *receiver board* transforms the optical pulses back to electrical pulses. A scheme of the data readout can be seen in Fig. 3.6. The signal in the receiver board is split into two branches. The first one, the *trigger signal*, goes to a discriminator with an adjustable threshold that indicates the presence of a significant signal above the noise level. This first stage is called *Level Trigger 0* (LT0). The fact that the discriminator threshold can be changed remotely during data taking according to the needs of the observation, allows the observation with different LONS conditions (galactic or extragalactic sources or observations with moderate moon light).

For each one of the innermost 325 pixels, a digital signal reaches the trigger system, which is split in a first LT1 and second LT2 level triggers. The LT1 stage applies tight time coincidences and an N-next-neighbour logic to the LT0 outputs in any of the 19 superimposed macro-cells (Fig. 3.7). In the case that N compact nearest neighbouring pixels show a signal exceeding an adjustable threshold in a tight coincidence time interval of 5 ns, the LT1 outputs a trigger signal. LT2 level uses a fast programmable electronics, where a pattern recognition is applied to select events by topological information. For the time being, the LT2 is just an inclusive `or` of the 19 macrocells.

The second branch of the analog signal coming from each pixel, goes to the fast analog-to-digital converter (FADC) system, where electric pulses are digitized. But still in the receiver board, the analog FADC signal is again duplicated into a high and a low-gain channels. The high-gain is amplified by a factor of 10 whereas the low-gain is delayed by 50 ns. If the

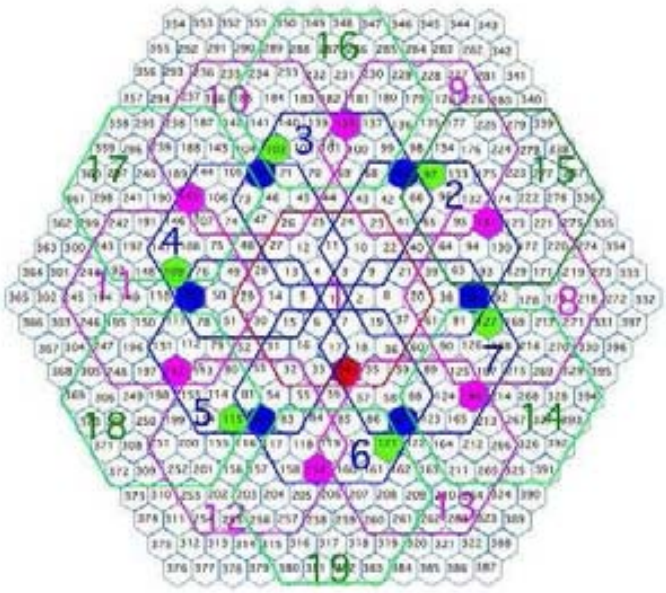

Figure 3.7: Schema of the trigger macrocells in the inner region of the MAGIC camera.

high-gain exceeds a pre-set threshold, a switch is actuated and the delayed low-gain is added right afterwards the high-gain. The combination of both signals with different gains is then digitized by the same FADC channel. This procedure substantially extends the dynamic range of the 8-bit FADCs.

The LT2 directly communicates with the FADC system and enables the acquisition of the data whenever an event passes all the trigger system levels. This LT2 has a prescaler board to scale down the number of triggers in order not to overcome the maximum continuous acquisition rate of 1 kHz allowed by the data acquisition system (DAQ). Since the digitization speed is limited to 300 MSamples/s, the analog signals are stretched to $\sim$ 6 ns FWHM in the receiver board[8] (so that at least 4 points can be measured for each pulse and the pulse shape can be reconstructed). The FADC chips continuously digitize the analog signals of each pixel and store them into an intermediate ring buffer. When the trigger signal arrives to the FADC modules, the FADC chip stops digitizing, the position of the pulse in the ring buffer is determined, and 30 time slices (15 for high and 15 for low-gain) are written into the FiFo buffer for each pixel.

Finally, the digitized pulse is formatted into the standard raw event data format, saved to disk, and in a few hours-days written to tape. Up to 150 GBytes of raw data can be generated in one data taking night.

3.4 The calibration system

The final output of the readout chain is given in FADC counts by the DAQ system. The integrated charge expressed in counts has no physical meaning and cannot be directly used for the description of the shower image. Hence FADC counts must be converted into photoelectrons which have physical connection with the EAS produced by the primary particle. In order to reconstruct the number of photoelectrons from the digital information it is necessary to calibrate the camera and the readout chain with respect to the incident light flux.

The calibration system consists of very fast (3-4 ns FWHM) and powerful (10^8-10^{10} photons/ns/sr) LEDs in three different wavelengths (370, 460 and 520 nm) and different intensities. The LEDs are installed at the center of the mirror dish and illuminate the camera

[8]This 300 MSamples/s system was used until April 2007, when it was upgraded to a 2 GSamples/s FADC system [60].

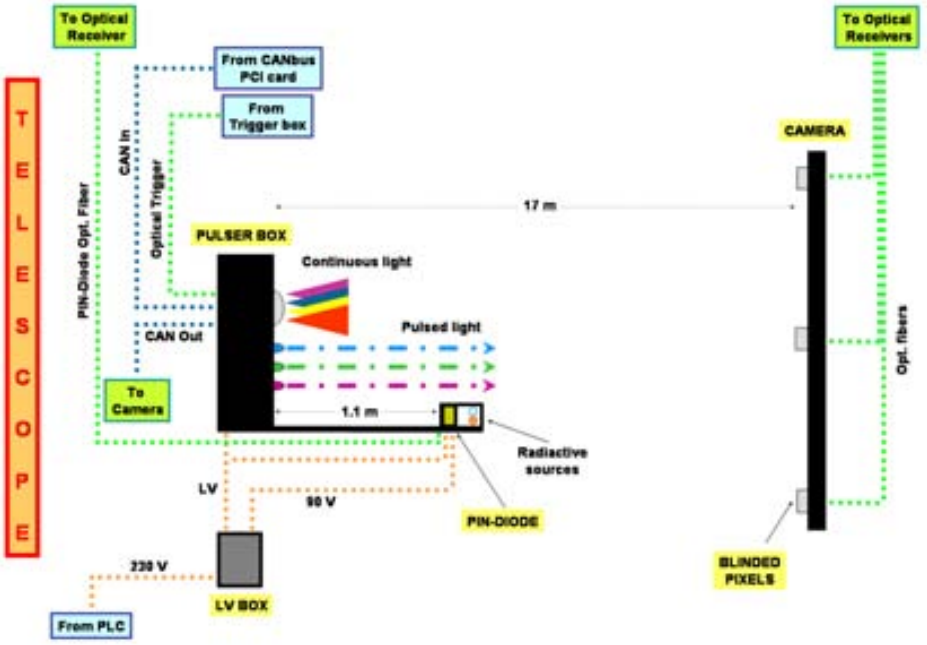

Figure 3.8: Schema of the calibration system elements installed in the telescope: pulser box, calibration LV box, PIN-diode and blinded pixels (from [61]).

homogeneously. The light intensity is variable in the range of 4 to 700 phe per inner pixel. This enables to check the linearity of the readout chain and calibrate the whole dynamic range.

The absolute camera response to the calibration light can be obtained using a calibrated PIN diode (photodiode that exhibits an increase on its electrical conductivity as a function of the intensity and wavelength of the incident light) and three blinded camera pixels (with attenuated illumination using filters) which measure the absolute calibration light flux. In addition, there are continuous light sources in four different colours and variable intensities to simulate the camera response to different background light conditions (as the presence of star in the FOV or moonlight). Figure 3.8 shows the elements of the MAGIC calibration system.

A complementary method to calibrate the signal in phe is the so-called *Excess Noise Factor* or *F-Factor* method. The method is based on the fact that for a given calibration light pulse, the output pulses of the PMT are approximately normally distributed with a Gaussian width given by the square root of the number of photoelectrons at the photocathode, with only a small excess noise F:

$$\frac{\sigma_Q}{< Q >} = F \frac{1}{\sqrt{N_{phe}}} \,. \tag{3.1}$$

The F-Factor of any electronic device is simply defined as:

$$F = \frac{(\text{Signal/Noise})_{\text{input}}}{(\text{Signal/Noise})_{\text{output}}} \,, \tag{3.2}$$

being therefore a numerical value which account for the additional noise introduced by the readout and amplification chain, assuming it is independent on the signal intensity. From the knowledge of the F-Factor of the PMTs and the analysis of the output signal of each pixel, one can extract the average number of phe impinging on the first dynode of each PMT. In the case of the PMTs of the MAGIC camera, the F-Factor has been measured for a sample of 20 PMTs [58] giving a value of 1.15 ± 0.02. Further details on the usage of this method are given in Chapter 4, where the data analysis procedure used for this thesis is described.

The advantage of the F-Factor method is its simplicity and robustness. Its disadvantage is that it does not implicitly include the QE and phe collection efficiency of the PMTs (which can vary from one PMT to another) nor the transmission efficiency of the light guides, whereas the Blind Pixel and the PIN-diode methods do. Therefore, the F-Factor method measures the number of phes arriving to the first dynode of the PMTs and the other two methods measure the photon flux. Currently, although both the blind pixel and the PIN diode are operative, the F-Factor method is the calibration procedure followed in the MAGIC data analysis.

In dedicated calibration runs, the MAGIC camera is illuminated by calibration LED flashes and read out using the standard DAQ chain. Moreover, using an external calibration trigger, it is possible to take calibration events interlaced with normal data taking at a rate of 50 Hz, to correct for PMT gain variations on short time scales.

3.5 The slow control

The MAGIC telescope is controlled from a central PC. The control system is split up into functional units which correspond to the independent subsystems of the telescope already described (DAQ, camera, AMC, $\cdots$). A Central Control (CeCo) computer coordinates all the subsystems, which have no intercommunication, and provides the user graphical interface during normal data taking. The operator has access to all the subsystem functionalities from the CeCo program, which is written in Labview 6.0.2. All subsystem PCs and the CeCo communicate with each other via standard TCP/IP[9] socket connections.

Another dedicated control program is the Camera Control (CaCo) program (dubbed *La Guagua*) which steers the camera of the telescope and offers the shifters an independent user interface with more detailed information about the camera status. It is implemented to allow *stand alone* run mode, without communication with CeCo or any other subsystem. It is based in the same concept of the CeCo: every functionality in the camera is controlled by independent camera and calibration subsystems, which are managed by a central decision manager. The CaCo consists of *two layers of software* developed using different programming languages:

- C/C++ *Subsystem drivers* developed to communicate with the hardware [62].
- Labview 6.0.2 for the graphical user interface (GUI) (figure 3.9) and *stat-machine decision manager*.

The author of this work has been the co-responsible for the development and maintenance of the control software for the camera and calibration systems, which are described in more detail in what follows.

3.5.1 Camera subsystems and drivers

The *Subsystem Drivers* are the programs which drive the hardware and provide proper initialization to enable the communication. The camera and calibration control subsystem are controlled by drivers, which can be divided into those controlled using the CANbus (Controller Area Network serial bus) and those controlled by RS-485 (Recommended Standard 485) communication lines (see schema in figure 3.10):

- Two CANbus lines of about 200 m long with a total of 16 nodes and an RS-232 linked to the CANbus via CANtoSerial adaptor.
- Two RS-485 bus lines (also $\sim$200 m long) are used to communicate the camera control program with two autonomous Programmable Logic Controllers (PLCs) [63], through a standard protocol over RS-485 called MODbus.

[9]TCP/IP stand for Transmission Control Protocol and the Internet Protocol, which are communications protocols on which the internet and most commercial networks run.

The drivers allow the communication with the hardware. The following subsystems are controlled or motorized by the camera slow control:

- High voltage power supply (HVPS): The high voltage for the camera PMT is provided by an external power supply located at the control house. The HV is transported to the camera through coaxial cables. Their control is done via RS-232. The hardware offers a display and some functionalities to manually control the HV. In case of an emergency, a procedure to manually ramp down the HVs can be performed.

- Camera high voltage: The total high voltage provided by the HVPS is regulated through 8 *HV masters* per each of the 6 camera sectors. Each master hosts 12 *HV regulators* (so, one regulator per pixel) which vary the output voltage from 0 to 2000 V. Each regulator has a monitor card, with a low voltage output proportional to the output voltage, which is used to monitor the HV applied for each pixel.

- Camera DC: Each sector is equipped with 12 monitor cards to digitize every pixel anode DC current. H/DC separated monitor boards prevents loosing part of the pixel information in case of damages in one of the cards. The communication between the camera and the CaCo system is done through two separate CanBus lines (see Fig. 3.10).

- Active Loads: An Active Load power supply (360 V) and an independent power supply (175 V) are used to fix the last two PMT dynodes (5th and 6th). Their voltage and intensity values are monitorized by the CaCo.

- Lids: Camera lids can be access remotely through the same PLC that controls the Cooling system.

- Cooling: The camera cooling system is controlled by an autonomous PLC. Their initial parameters and the monitored values can be sent and received by the CaCo through the ModBus line.

- Low voltage (LV): The Low voltage supply powers the electronics in the monitoring digital cards, the cooling sensors and most of the camera electronics. It is controlled by a second PLC.

- Star guider and AMC LEDs: used as reference for the Star guider CCD camera and as reference for mirror panels re-alignment procedure, respectively. They can be independently switched on/off and are operated by the LV PLC.

- Central pixel: is a special pixel located at the center of the camera and intended to analyze fast optical signals coming from pulsed γ-ray sources, as pulsars. Its voltage can be switched on/off from the LV PLC. An independent read-out system is implemented.

- Calibration pulser box: The pulsed and continuous LEDs can be switched on and off via CanBus.

- Calibration LV: The calibration pulser box is powered by an independent LV power supply box (located near the pulser box). The LV box is fed by a 230 V line taken from the cooling box below the telescope, which is switched on/off by the PLC and from the remote control system.

- Calibration IO (Trigger): An optical trigger carries the calibration trigger pattern to fire the LEDs from the control house to the pulser box. It is directly controlled by an I/O PCI card installed in the CaCo computer.

Each CaCo subsystem has its own driver with its own function libraries. These functions implement all the possible hardware tasks. Many subsystems controlled by independent drivers share common resources, in particular the communication buses. The drivers are multi-threading programs. All drivers which share the same bus are implemented as independent threads in a unique program. When a driver (a thread) needs to access the bus,

it freezes the other drivers using *semaphores*. As soon as the driver stops using the bus, it unfreezes the rest of threads.

Internal sockets named *pipes* are used to deal between the central decision manager and the subsystem drivers. *Pipes* can be opened by multiple processes for reading or writing purposes. Two types of separate *pipe* channels are used: one to send commands from the CaCo to the Drivers (specific actions to be executed), named `subsys_cmd`; and another to send reports on the opposite direction (monitoring the executed actions), named `subsys_report`.

The main software piece, which enables the communication between the decision manager and the subsystem drivers, is the `ListenFromDevice` method. When an object of this type is created, the program is able to wait and receive commands through the *pipes* in order to process an action. Once the communication is enabled, the subsystem is always pulling into the *pipe* to check if there is a command to be processed. When a command is received, it is processed and the Driver sends a report to the decision manager. This assures that the latest command has always been properly executed. Semaphores are implemented to avoid losing any action if the system is busy processing another action.

The driver sends its status report to the decision manager every few seconds, even when no action is requested. Contents of the subsystem reports are shown in Table 3.1. Besides some parameters for status, error flags, and timestamps, which are common for all subsystems, the reported values and commands are different for each subsystem. These, and the most important commands are listed in Appendix B.

Subsystem	Contents of the report
HV PS	HVs and currents of the two camera power supplies
HV	All 577 pixel monitored high voltages
DC Currents	All 577 pixel monitored anode DC currents
Active Loads	Voltages and currents provided by the +350 V and +175 V power supplies
LV	Voltage and current of the camera +5 V, +12 V and -12 V power supplies, and Optical Transmitters +12 V power supply. Temperature and Relative Humidity.
Lids	Motor status and monitored normal/safety switches values
Cooling	Temperature of sensors located on camera Wall, Center and Optical Transmitters. Temperature of the water on tank. Relative humidity values for camera wall and center. Pressure sensors, pump, refrigerator, valve, resistor and fans status

Table 3.1: Values reported by the subsystems (through `subsys_report` pipe).

3.5.2 State-machine decision manager

One of the tasks of the CaCo is to provide the user with a simple user interface to control the camera and the calibration systems. The most important concept behind this control system in the so-called *state-machine*: the program evaluates the status of every controlled subsystem through the driver regular reports. Reports from the drivers are automatically received by the CaCo at a given periodicity. And the program updates a state table whenever a report from a subsystem arrives.

Using the individual subsystem states, a *global state* for the whole CaCo system is evaluated. This global state is the input for the *decision manager*. It is an autonomous decision-making system, able to deal with situations where rapid actions are needed (e.g. some risk in the hardware). The global state also defines when some actions are permitted or forbidden. Figure 3.11 shows all possible subsystem and global states.

Under special circumstances, the camera enters into a state such that no actions coming from CeCo or user are allowed. This is the so-called global *blocked* state, which occurs when

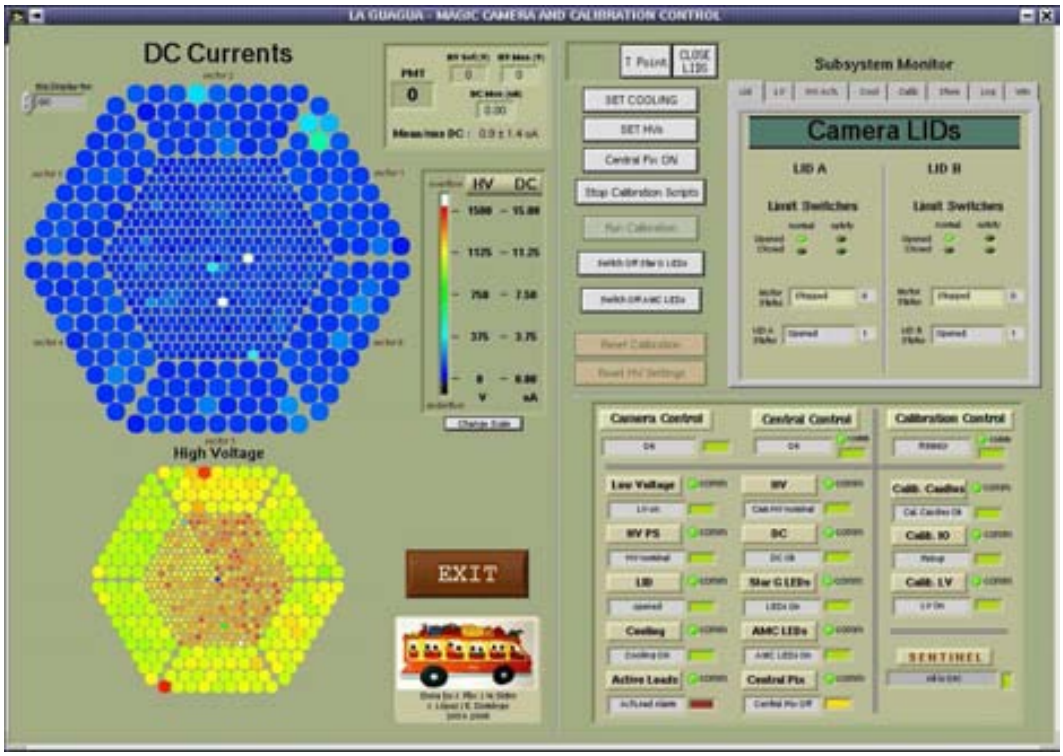

Figure 3.9: Screen shot of the GUI for the Camera and Calibration Control (La Guagua).

an emergency happens. CaCo takes automatic control over the whole system and ramps down the pixel High Voltages or close the camera lids if necessary. These emergencies can be related to, for instance, with bad atmospheric conditions, timeout of an important camera subsystem, etc... All possible subsystems states which drive the camera into *blocked* state are displayed in red in Fig. 3.11.

Any subsystem under alarm conditions fires the camera global *alarm* state. This happens, for example if one of the lids has reached a safety limit and cannot be closed remotely. These subsystem conditions are displayed in orange in Fig. 3.11.

The global state *hot* is fired when one or more pixels have too high DC level. This may happen e.g. if a bright star is present in the FOV. In such a state, the CaCo reduces automatically the high voltage of the affected pixels (in steps of 5%) to assure that they stay into a safe anode DC region.

Sentinel routine as security manager A routine called *Sentinel* protects the camera against dangerous situations, like the system operation during daytime. Sentinel uses tables with the position of the sun (created with *XEphem*) and checks regularly the MAGIC weather station solar irradiation monitor. Moreover, the operation is not allowed either in case of bad atmospheric conditions, determined by the weather station as well. In all these situations, the CaCo goes to *blocked* state, in which CeCo or users cannot operate the camera nor the calibration systems[10].

The sentinel routine allows to switch on the camera two hours before dusk, in order to warm up the camera. In such *warm-up mode*, until it is completely dark, the sentinel does not allow to open the lids. Only low voltage is present in the camera, which is enough for the cooling system to reach a stable and proper working temperature. Ramping up the pixel high voltages is allowed 1 hour before dusk time, complemeting the *warm-up* stage.

[10]Only experts are allowed to bypass Sentinel for tests and checks of the system.

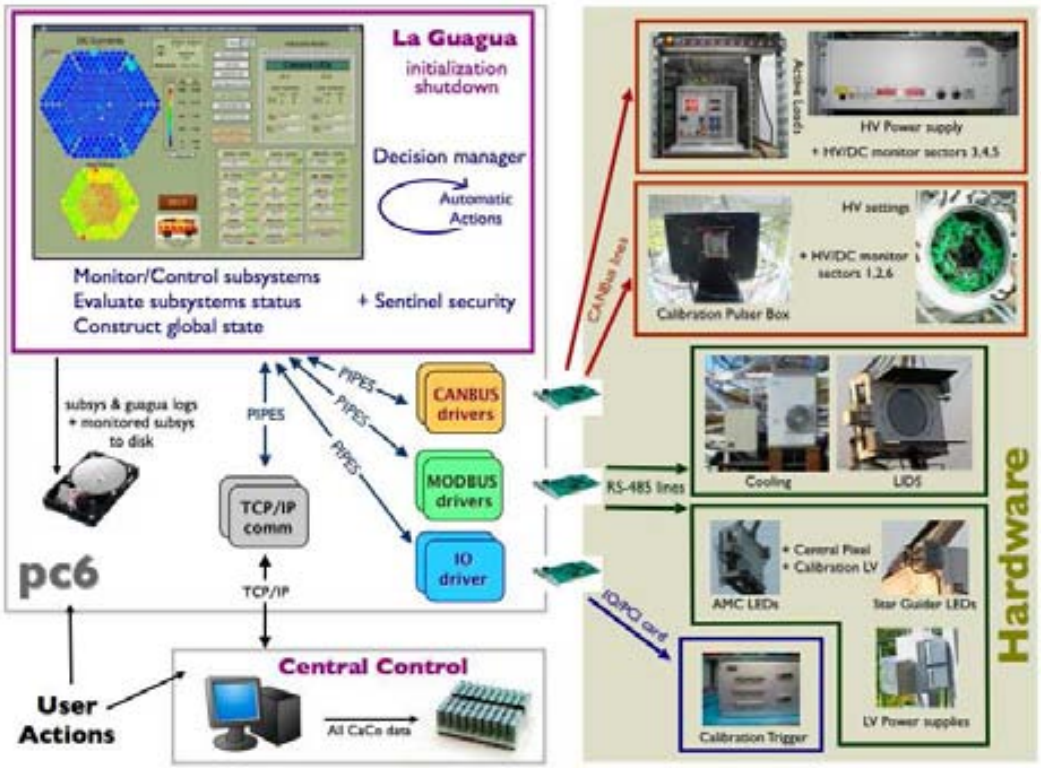

Figure 3.10: Camera and Calibration slow control: schematic view of the CaCo software architecture and its relation with the CeCo and the camera hardware.

CaCo start-up At start-up, all subsystems enter into an Initialization phase in which the different subsystems are driven to be ready for further run in combined mode. Once the initialization has finished successfully, the user has full control over the camera and calibration systems either from the CaCo GUI or via CeCo.

High Voltage ramping security procedure The setting of the pixel High Voltages has been programmed to offer a secure ramping up/down procedure. This prevents the pixels to be damaged by rapid variations of applied voltage. This HV ramping is done in both the HV power supplies and in the camera HV regulators. The HV power supply is ramped in steps of 50 V while the HV regulators are ramped in steps of 10 V. The HV is ramped until the requested settings have been reached. In case of ramping up the HV pixels settings, the HV provided by the power supply is always 100 V above the maximum pixel HV setting. In case of pixel variations less than 50 V around the final nominal value, we only ramp the HV regulators. If variations increase more than 50 V the HV power supply is ramped again in order to keep the 100 V margin.

The ramping can be stopped at any time. Moreover, if camera enters into *hot* state, i.e., the DC currents are larger than a preset upper limit, the ramping procedure is automatically stopped by the CaCo and, afterwards, if there are too many pixels in *hot* state ($\geq$40 pixels), an automatic ramp down and closing the camera lids is executed. This prevents damaging the camera in case of an operation mistake, like trying to ramp up the camera HVs if some light is present in the telescope.

Calibration system operation The calibration system can be operated using scripts or a special panel in the CaCo GUI. Each script contains a calibration light sequence. The CaCo executes all calibration tasks defined in the sequence by using appropriate commands in an optimized way. Usually the file name of a calibration script is sent from the CeCo, although

System ID	State 0	State 1	State 2	State 3	State 4	State 5	State 6	State 7	State 8
CamControl	ERROR	ALARM	BLOCKED!	WARM-UP	HOT	HV RAMPING	OK	INIT	SHUTD
Cam.HV.PS	error	HV mismatch	HV Trip	HV ramping	HV Off	HV nominal	Limit Current warning	-	-
Cam.LID	error	Safety Limit passed	-	T Point	closed	opened	moving	stopped	-
Cam.LV	error	LV Trip	LV Trip	-	LV Off	LV on	-	-	-
Cam.COOLING	error	Temperature Alarm	-	-	Cooling Off	Cooling Ok	Temp. warning	Cond. warning	-
Cam.HV	error	Cam HV mismatch	-	Cam HV ramping	Cam HV Off	Cam HV nominal	-	-	-
Cam.DC	error	DC Alarm	-	Test	-	DC Ok	warn	-	-
Cam.Act.Load	error	alarm	-	-	Off	On	-	-	-
Cam.Central Fix	error	alarm	disabled	-	Off	On	-	-	-
CamStrGuiderLEDs	error	-	-	-	StarGuider LEDs Off	StarGuider LED On	-	-	-
Cal. Control	ERROR	BLOCKED!	WAITING TO FIR	FIRING!	-	-	INIT	SHUTD	-
Cal. CanBus	error	-	-	Cal. CanBus Ok	-	-	-	-	-
Cal. IO	error	-	Waiting to fire	Firing!	-	-	-	-	-
Cal. LV	error	-	LV Off	LV On	-	-	-	-	-
Sentinel	error	All is OK!	Sun is present!	Bad Alm. Cond.	disabled	-	Only WARM-UP mode	-	-

Figure 3.11: Subsystem states and camera control and calibration global states.

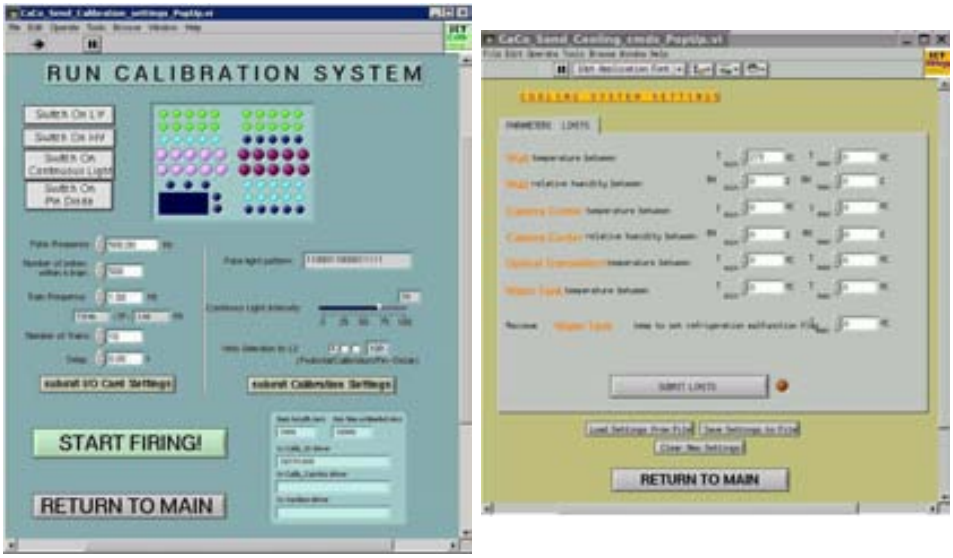

Figure 3.12: Calibration (left) and cooling (right) panels in CaCo.

calibration scripts can be launched from the CaCo directly by the operator. The scripts can be edited to use all the available functionalities of the calibration system.

All functionalities are also available from the special panel in the CaCo program (see Fig. 3.12, left panel). The operator can select the intensity and color of the pulsed or continuous light which is sent to the camera (all combinations are allowed), pulse frequency, train frequencies and delay time for the trigger lines to *LT2* trigger.

The 600 V power for the pulser box is switched ON when the CaCo is launched, i.e. typically two hours before data-taking. This voltage needs one hour to stabilize, in order to produce stable light pulses. The available pulse frequencies supported by the IO Card (up to 4 kHz) are: 160, 200, 250, 320, 400, 500, 625, 640, 800, 1000, 1250, 1600, 2000, 2500, 3125, 3200 and 4000 Hz.

The conversion factor from phe to ADC counts is obtained by means of the so-called F-Factor method that estimates the number of phe from the width of the charge distribution of calibration events (see Sec. 3.4).

Cooling system operation The goal of the cooling system is to regulate the temperature inside the camera. A stable temperature during data taking (within $\pm 1^{\circ}$C) is mandatory in order to minimize gain changes in several devices of the readout chain. Extremely high temperatures may also damage the camera electronics, whereas too low temperatures may result in water condensation inside the camera.

During data taking, 800 W of heat are dissipated inside the camera including both high and low voltage consumption[11]. The camera is cooled using a water-based system: a S-shaped copper tube runs along the external lateral wall of the camera and acts as a heat-cool exchanger. At the ground, a 200 liter tank filled with glycol's water (to avoid freezing) feeds the pipeline that goes up to the camera. The tank water can be cooled of heated with respectively a refrigeration unit (connected to the tank) or a 2400 W resistor inside the tank. Finally, a set of fans inside the camera homogenize the internal temperature and make the heat-cool exchange more efficient.

The CaCo sets the working conditions for the cooling system, but an autonomous PLC takes the decisions and actions to regulate the final temperature inside the camera. The initial and working conditions can be modified by using an expert panel from CaCo (see Fig. 3.12, right panel).The cooling system is monitored by the CaCo during data-taking time (which reports eventual emergency states to users) and during daytime (by means of special scripts).

Lids and instrumentation The camera side that faces the telescope mirror collector is protected from daylight with two light and water-tight lids. Since the PMTs can be damaged if they are exposed to too bright illumination, the lids are remotely closed in case of a sudden increase of the pixels DC current (e.g. due to an accidental car flash on the reflector). The CaCo can access remotely the PLC that controls the motors (which is the same PLC that manages the cooling system).

The lids open/close operation takes about 20 seconds. During this interval the movement can be aborted at any time from the CaCo. If access is needed to the camera front (e.g. during pixel replacement), the lids must be opened manually for safety reasons. When lids are opened manually (through a control panel located in the cooling cabinet of the telescope's lower drive), the CaCo is not able to operate the lids remotely.

The camera lids have been instrumented with two sets of LEDs: a first set is used to monitor the telescope pointing (*Star Guider LEDs*). A second set is used as reference for mirror alignment (*AMC LEDs*). Both sets of LEDs can be switched on/off from the CaCo. Figure 3.13 shows their location ah the camera front.

During September 2005 new camera lids were installed. They allow to take T-Points[12] in an easy way: the operator can select also the 'T-Point' button from CaCo main display to open only the upper lid.

The CaCo configuration file The CaCo provides a configuration file to set the most relevant parameters used in the decision manager, subsystem state reconstruction and other execution subroutines. It comprises: enable/disable sentinel, camera warm-up time, HV limits, sleep timers used for the program threads, cooling system initialization parameters, etc.

Communication to CeCo via TCP/IP The most common actions of the telescope are executed through the CeCo. The CaCo waits for CeCo commands in a dedicated TCP/IP socket. Responsible for the TCP/IP communication are the two daemon programs `tcp_server_read_socket` and `tcp_client_write_socket`. TCP/IP preserves the command/report channel philosophy. The communication with the CaCo is via *pipes*, like that with the camera subsystems. All available commands which can be executed from CeCo, and corresponding actions to be done by the CaCo are shown in Appendix B. Security checks are also implemented at this stage: not all functionalities are available via TCP/IP and checks to prevent any damage of the system.

[11]The medium voltages are produced at the control house, so do not dissipate heat inside the camera. Despite the HV is also produced in the control house, the HV regulators reduce the general HV by dissipating inside the camera the power as heat.

[12]The optical axis of the telescope (or pointing) is calibrated by taking pictures of stars at different azimuth and zenith angles. The system uses a CCD camera located in the middle of the dish and reference LEDs in the camera.

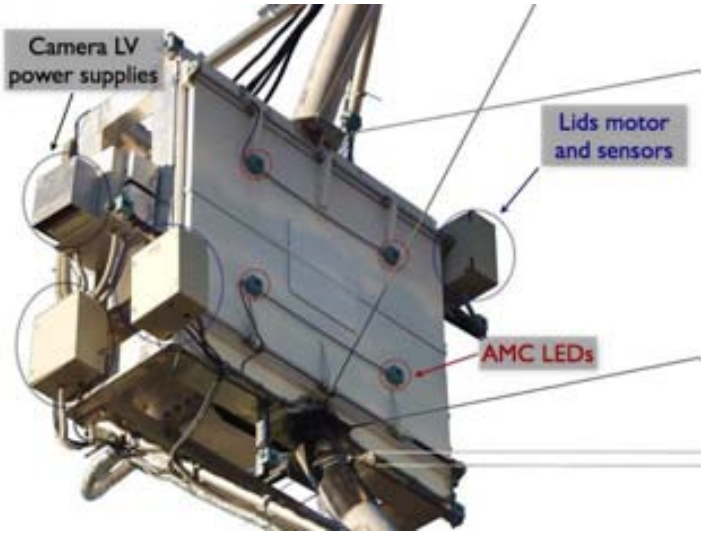

Figure 3.13: Camera instrumented lids.

The CaCo reports periodically (at 1 Hz rate) to CeCo about the global status of all systems through a special report TCP/IP socket. This information includes the global states, subsystem states, and all subsystem monitored values.

Logbooks and Data Storage During the regular operation mode, all camera and calibration subsystems keep track of all actions performed and an extensive monitor (debugging level is configurable) is stored into ASCII logbook files. The CaCo itself also produces a general ASCII logbook in which all actions and errors encountered during operation are stored (they are also displayed in the GUI). Logbooks have a size of $\sim$ 125 MBytes/night.

In an observation night, all 577-pixels anode DC currents are stored into disk at the maximum possible rate ($\sim$ 6 Hz, limited by the CANbus bandwidth) and used afterwards for source analysis (e.g. to find stars in the FOV and check for telescope mispointing). DC currents files have a size of $\sim$ 250 MBytes/night. All other subsystem data can be saved, although this is optional. During CaCo shutdown, all DC files and logbooks are transferred to a storage PC via NFS. Afterwards the DC current data are sent to tape together with all raw data files. Tapes (and data via network) are transferred to the MAGIC data center at PIC (Barcelona).

Chapter 4

Data analysis technique

In this chapter we introduce the steps performed in the analysis of the MAGIC data. The analysis methods developed for this thesis are presented in some detail, while the standard methods are briefly summarized.

The final aim of the data analysis method is the measurement of astronomical VHE γ-ray source's flux and its time evolution, energy spectrum, position and morphology. The main steps in the MAGIC telescope data analysis are the following:

Pixel signal extraction : The reconstruction of the size and arrival time of the pulses produced by the Čerenkov shower in each PMT in the MAGIC camera. The signal extraction algorithms and their performance are presented in detail in Sec. 4.1.

Event reconstruction : The event properties are reconstructed from the shower image in the camera in the following three steps:

- **Calibration** of the FADC information for each pixel into number of photoelectrons (phe).
- **Image cleaning** removing pixels containing noise.
- **Image parametrization**: calculation of the image parameters using survived pixels.

Signal/background separation : training of γ/hadron matrices and energy estimation matrices with a sub-sample of Monte-Carlo (MC) γ-ray events and a sub-sample of background (hadrons) events from the data. These matrices are afterwards applied to the data sample.

Signal evaluation : Determination of the effective on-time, the number of excess events and the effective area. Measurement of physical quantities which will finally yield the γ-ray estimated energy and incident direction, the significance of the γ-ray source detection, the lightcurve and the energy spectrum.

When observing a γ-ray source, the telescope not only records the images of γ-ray induced showers, but also the much more numerous background shower images of the cosmic ray flux (hadrons, electrons and photons) and LONS. In order to evaluate the residual background two independent samples (dubbed ON and OFF) are taken separately: for the ON data the telescope is tracking and pointing to the source, whereas for the OFF data the telescope is pointed to a position in the sky with no known source contained in the FOV but with similar observation conditions (similar background, zenith angle, sky brightness, etc.) of the ON runs.

But one may gain observation time as well as reduce the systematic differences between ON and OFF data by producing them simultaneously, as in the so-called *wobble mode*: the telescope tracks so that the source is always at a fixed angular distance off-axis (tipically 0.4°) from the camera center, so that the source position can be treated as ON and the symmetric

position respect to the camera center, as OFF. The data analyzed for this thesis were taken in both observational modes. The analysis of the data observed in this mode will be described in Sec. 4.4.1.

Observations with Čerenkov telescopes are generally conducted in moonless nights, due to the need for darkness to be able to detect the very faint flashes from Čerenkov light. With the MAGIC telescope, also observations with partial moon are possible. The analysis using moon light data will be presented in Sec. 4.4.2.

In addition to the statistical errors the determination of different physical magnitudes are affected by systematic uncertainties, summarized in Sec. 4.5.

4.1 Signal extraction: charge and arrival time

For each individual Čerenkov shower and pixel, the electric pulse produced by the incident photons is digitalized and recorded. The first step in analyzing the MAGIC raw data is the extraction of the charge and arrival time of the pulse recorded in each pixel. Four different extraction algorithms have been selected and their behaviour have been studied using MC simulations of the signal and noise pulses as well as pedestal and calibration signals. This study has allowed us to select the best of those algorithms for the signal extraction.

The signal extraction algorithms and their performance that are presented in detail in the following subsections have been published in [64] and [65].

4.1.1 Pulse shape reconstruction

The MAGIC telescope used , during the time of the observation presented in this work, a 300 MSamples/s FADC system to sample the PMT signals (see section 3.3). For the signal reconstruction, the following intrinsic characteristics of the read-out system are relevant:

- Inner and Outer pixels: The outer pixels have a factor 4 larger area than the inner ones, although their effective area (taking into account the light guides) is only a factor 2.6 higher. Since the high voltages of the different PMTs are adjusted (*flat-fielded*) to yield similar pulse amplitudes for the same photon flux, the inner pixels are operated at a three times higher gain than the outer ones. This results in a lower relative noise from the LONS for the outer pixels. Moreover, the signal of the outer pixels is delayed by about 1.5 ns with respect to the inner ones, due to the different PMT size and voltage settings.

- Asynchronous trigger: The FADC clock is not synchronized with the trigger. Therefore the time $t_{\rm rel}$ between the trigger decision and the first read-out sample is uniformly distributed in the range $[0, t_{\rm FADC}]$, where $t_{\rm FADC} = 3.3$ ns is the digitization period of the 300 Msamples/s FADCs.

- AC coupling: The PMT signals are AC-coupled at various places in the readout chain. Thus, the DC contribution to the PMT pulses from the LONS is zero on average. Only the signal fluctuations (RMS) depend on the intensity of the LONS. In moonless nights, observing an extra-galactic source, the average rate of LONS phe is ~ 0.13 per ns and inner pixel [64].

- Shaping: The optical receiver board shapes the pulse with a time constant of 6 ns FWHM, much larger than the typical intrinsic pulse width ($\sim$ 2 ns for a γ-ray shower). Since the shaping time is larger than the width of a single FADC slice, a strong correlation of the noise between neighbouring FADC slices is expected.

The fact that the signal pulses are sampled asynchronously by the FADCs allows the determination of the average pulse shape with high accuracy. To do that, the signal samples from the different recorded pulses are shifted to a common reconstructed arrival time, normalized to a common area/charge and averaged. Therefore, the precision of the determination of each point along the average pulse shape depends on the accuracy of the arrival time and charge

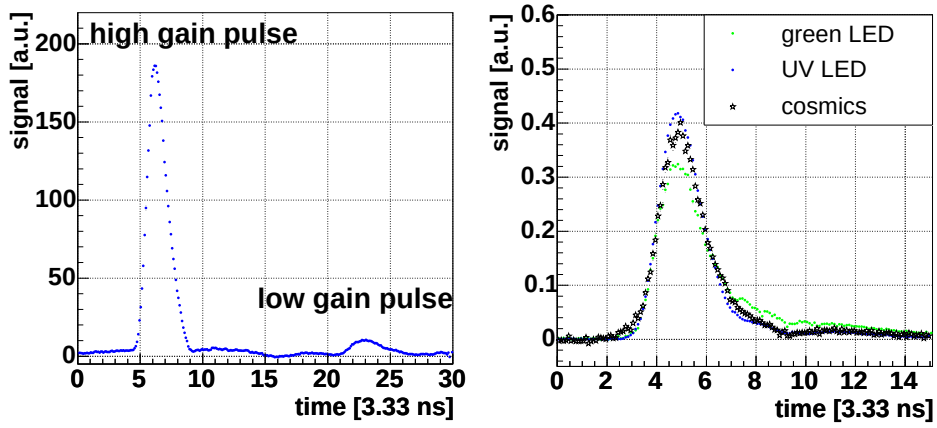

Figure 4.1: Left: Average reconstructed pulse shape from test 2.5 ns FWHM pulses. Right: Average normalized reconstructed shapes for high-gain calibration pulses with UV (in blue) and green (green) light, compared with air shower events (black). From [64].

reconstruction. Possible biases in the charge and arrival time reconstruction may introduce systematic errors, whose size are unknown at first hand. Figure 4.1 shows the reconstructed pulse shape of an electronic test pulse of about 2.5 ns FWHM, resembling the MAGIC PMT signals. The resulting average pulse shape yields a FWHM of 6.3 and 10 ns at the high and low gain branches, respectively.

Right panel in figure 4.1 shows the averaged reconstructed signal of a fast test pulser. The high and low gain pulses are clearly visible. The low gain is about 10 times smaller than the high gain and is delayed by about 55 ns. Left panel in figure 4.1 shows the normalized reconstructed pulse shapes, averaged over 1000 individual pulses, for green and ultra-violet calibration LEDs. The calibration pulse shape obtained from UV light resembles very well the one obtained from cosmics (both have FWHM about 6.5 ns) while the green light yields slightly broader pulses with a pronounced tail. Therefore UV pulses are used in MAGIC as standard for the calibration.

4.1.2 Criteria for optimal signal extraction

The goal of an optimal signal reconstruction algorithm is to compute an unbiased estimate of the charge and arrival time of the Čerenkov signal with the highest possible resolution and for all signal intensities.

Let us consider a large number of identical signals, corresponding to a fixed number of phe N_{phe}. By applying a signal extractor a distribution of estimated signals $\widehat{N}_{\mathrm{phe}}$ is obtained (for fixed N_{phe} and fixed background fluctuations). Criteria for an optimal signal reconstruction algorithm are developed according to [66]. The deviation between true and reconstructed value is defined as

$$X = \widehat{N}_{\mathrm{phe}} - N_{\mathrm{phe}} \ . \tag{4.1}$$

The distribution of X has a mean $B = \langle X \rangle = \langle \widehat{N}_{\mathrm{phe}} \rangle - N_{\mathrm{phe}}$, also called the **bias** of the estimator, and a variance $V = \langle (X - B)^2 \rangle$. The **root-mean-squared error** RMSE combines resolution and bias:

$$\mathrm{RMSE} = \sqrt{\langle X^2 \rangle} = \sqrt{V + B^2} \ . \tag{4.2}$$

Both B and RMSE depend generally on the size of N_{phe} and the background fluctuations.

The reconstructed charge should be directly proportional to the total number of phe in the PMT. This linearity is important for the reconstruction of the shower energy and hence for the measurement of energy spectra from the sources. Another important feature of the signal extractor is the robustness, i.e. the stability in reconstructing the charge and arrival

time for pulses with different intrinsic shapes and background levels. Finally, the extractor has to accurately reconstruct both high and low-gain channels.

4.1.3 Extraction algorithms

We have chosen the following four algorithms for the study of the reconstruction of the signal charge and arrival time:

Fixed Window : This extractor adds the pedestal-subtracted FADC slice contents of a fixed range of consecutive slices (window). The window has to be chosen large enough to cover the complete pulse, otherwise physical differences in the pulse position with respect to the FADC slice numbering would lead to integration of different parts of the pulse. Therefore, this algorithm adds up more noise than the others. Due to the AC-coupling of the read-out chain, the reconstructed signals have no bias. This extractor does not calculate the pulse arrival time. A slightly modified extractor is derived from the purely fixed window extractor, which is named **Fixed Window with Integrated Cubic Spline** (Fixed W Spline). It uses a cubic spline algorithm and integrates the spline interpolated FADC slice values from a fixed extraction range.

Sliding Window with Amplitude-weighted Time (Sliding Window): This extractor searches for the maximum integral content among those obtained from windows of fixed size contained in a defined range of FADC slices. The amplitude-weighted arrival time is calculated from the window with the highest integral as $t = \sum_{i=i_0}^{i_0+ws-1} s_i \cdot i / \sum_{i=i_0}^{i_0+ws-1} i$, where i denotes the FADC slice index, starting from slice i_0 and running over a window of size ws. The s_i are the pedestal-subtracted FADC slice contents at slice position i.

Cubic Spline with Integral or Amplitude Extraction : This extractor interpolates the pedestal-subtracted FADC slice contents of the full read-out window using a cubic spline algorithm, adapted from [67]. Afterwards, it searches for the position of the spline maximum. Then, two possibilities are offered for the charge reconstruction: either the *amplitude* of the spline maximum is taken as reconstructed signal (Spline Amplitude) or the spline is *integrated* in a fixed size window (Spline Int), with integration limits determined with respect to the maximum position[1]. Also, the pulse arrival time can be computed in two ways: it is determined by the position of the spline maximum or by the position of the half maximum at the rising edge of the pulse.

Digital Filter: In this method the extracted charge is calculated as the weighted sum of n consecutive FADC slices. The aim of using weights is to give more importance to the slices where most part of the signal is contained, hence where the signal to noise ratio is larger (reducing the noise contamination on the extracted signal). The weights are determined by taking into account the expected pulse shape, known by the pulse shaper and from MC simulation. The reader is also referred to [68] and [69] for a general description, and to [70] for a detailed study for the MAGIC telescope signals. Different configuration files containing the weights, the binning resolution and the window size have been created for cosmic, MC and calibration pulses.

4.1.4 Monte-Carlo studies of signal extraction

With the use of MC simulations (see section 4.2.5), the signal and noise pulses with a specific number of phe can be generated[2]. Moreover the same pulse can be studied with and without noise. Nevertheless, there are always systematic differences between the simulation and the real detector. In our case, e.g. no noise due to the low-gain switch has been simulated, the total dynamic range of the entire signal transmission chain was set to infinite, and the

[1] The charge integration is performed between the maximum position minus the rise time and the maximum position plus fall time.

[2] While under real conditions the number of phe is randomly distributed due to the PMT photoelectron statistics.

detector has been assumed to behave linearly. For the MC generation, the following settings have been used:

- The intrinsic arrival time spread of the photons was set to 1 ns, corresponding to the time spread of the Čerenkov photon produced by γ-ray showers.
- The conversion of charge in FADC counts to phe was set to be 7.8 FADC counts/phe, independently of the signal strength.
- Only one inner pixel has been simulated.
- The LONS was simulated approximately as for a typical extragalactic field of view.

In the subsequent studies, the MC simulation was used to determine, for each of the extractors, the **bias**, the **charge resolution** and the **time resolution** as a function of the input signal charge, as well as the effect of adding or removing noise to those quantities.

Once the signal is simulated, it is extracted using the algorithms previously described. Then the extracted signal charge (in FADC counts) is converted back to phe, using a **conversion factor**. Figures 4.2, 4.3 and 4.4 show the charge conversion factors (FADC counts per phe) for the tested extractor algorithms, with and without noise and for the high and low-gain channels, respectively. One can see that the conversion factors depend on the extraction window size and that all extractors using a sliding window show a bias at low signal intensities.

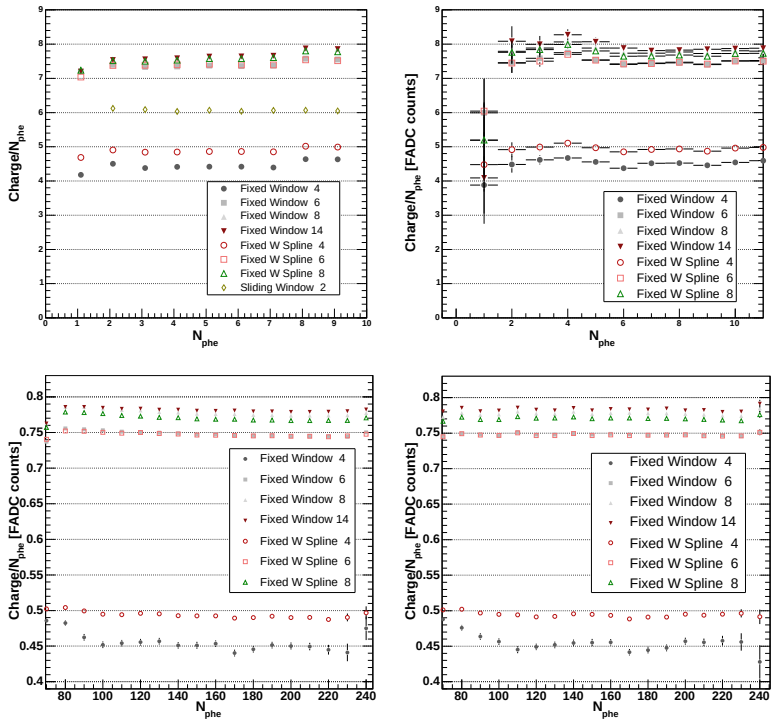

Figure 4.2: Charge conversion factor (FADC counts per phe) versus number of phes, for fixed window extractors in different window sizes. The upper plots show the high-gain and the lower ones low-gain regions. Left: without noise, right: with simulated noise.

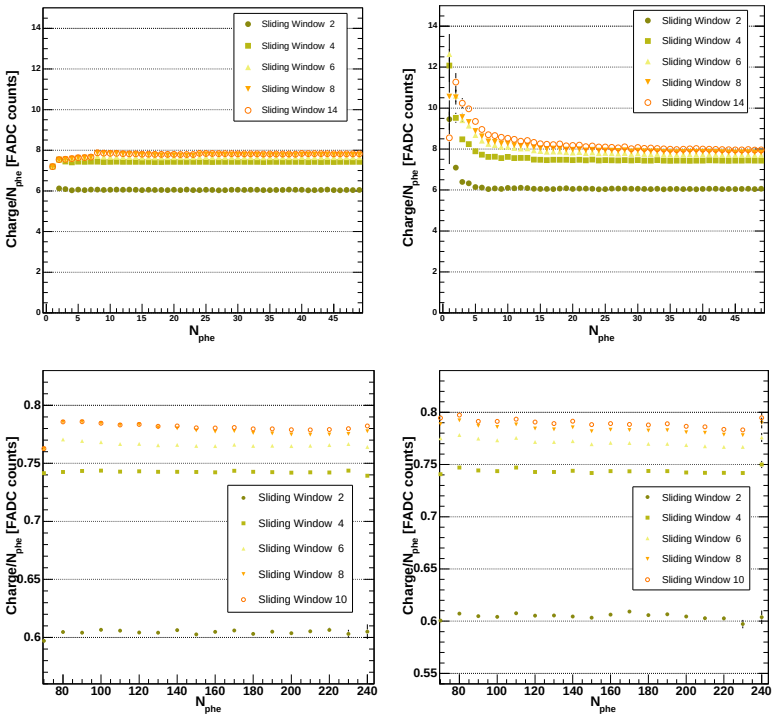

Figure 4.3: Charge conversion factor (FADC counts per phe) versus number of phes, for sliding window extractors in different window sizes. The upper plots show the high-gain and the lower ones low-gain regions. Left: without noise, right: with simulated noise.

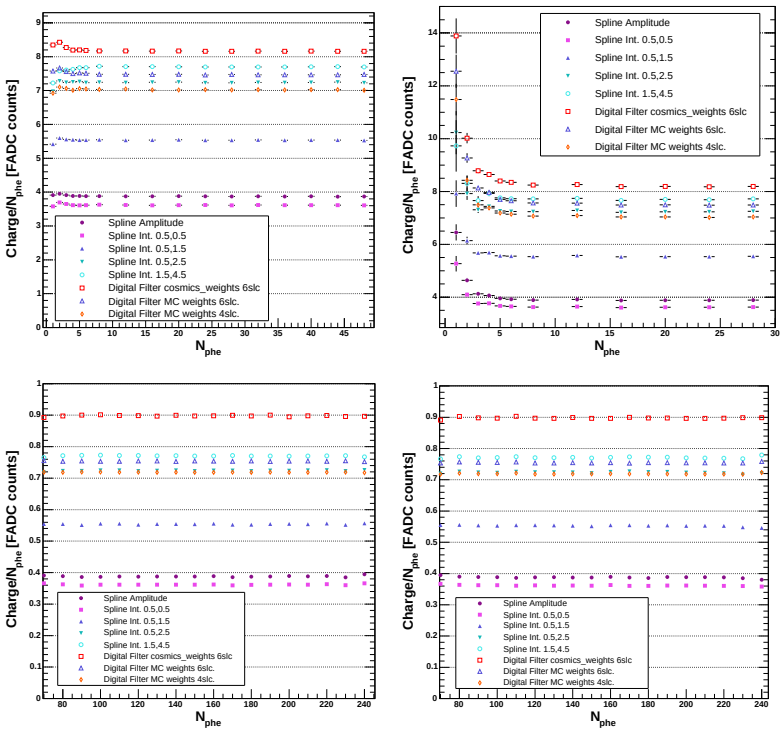

Figure 4.4: Charge conversion factor (FADC counts per phe) versus number of phes, for spline and digital filter extractors in different window sizes. The upper plots show the high-gain and the lower ones low-gain regions. Left: without noise, right: with simulated noise.

We fit the conversion factors above 10 phe (in a range where they become roughly constant) and use them to convert the extracted charge (in FADC counts) back to equivalent phe. We subtracted the simulated number of phe and obtained the **bias**:

$$B = \langle \widehat{N}_{\mathrm{phe}} - N_{\mathrm{phe}} \rangle \,. \tag{4.3}$$

Figure 4.5, 4.6 and 4.7 show the bias as a function of N_{phe} for the tested extractors (in units of phe), with and without noise and for the high and low-gain branches separately. The used conversion factors (c_{phe}) are given in the insets. As expected, the fixed window extractor does not show any bias up to statistical precision. All sliding window extractor, however, do show a bias. Usually the bias vanishes for signals above 5 phe, except for the sliding windows with window sizes above 8 FADC slices, for which the bias only vanishes above 12 phe. The size of the bias as well as the minimum signal strength above which the bias vanishes are clearly correlated with the extraction window size. Smaller window sizes yield smaller biases and extend the linear range to smaller charges. All integrating spline extractors and all sliding window extractors with extraction windows above or equal to 6 FADC slices yield the comparably smallest biases. The spline and digital filter biases fall down very steeply and have a bias only below 5 phe.

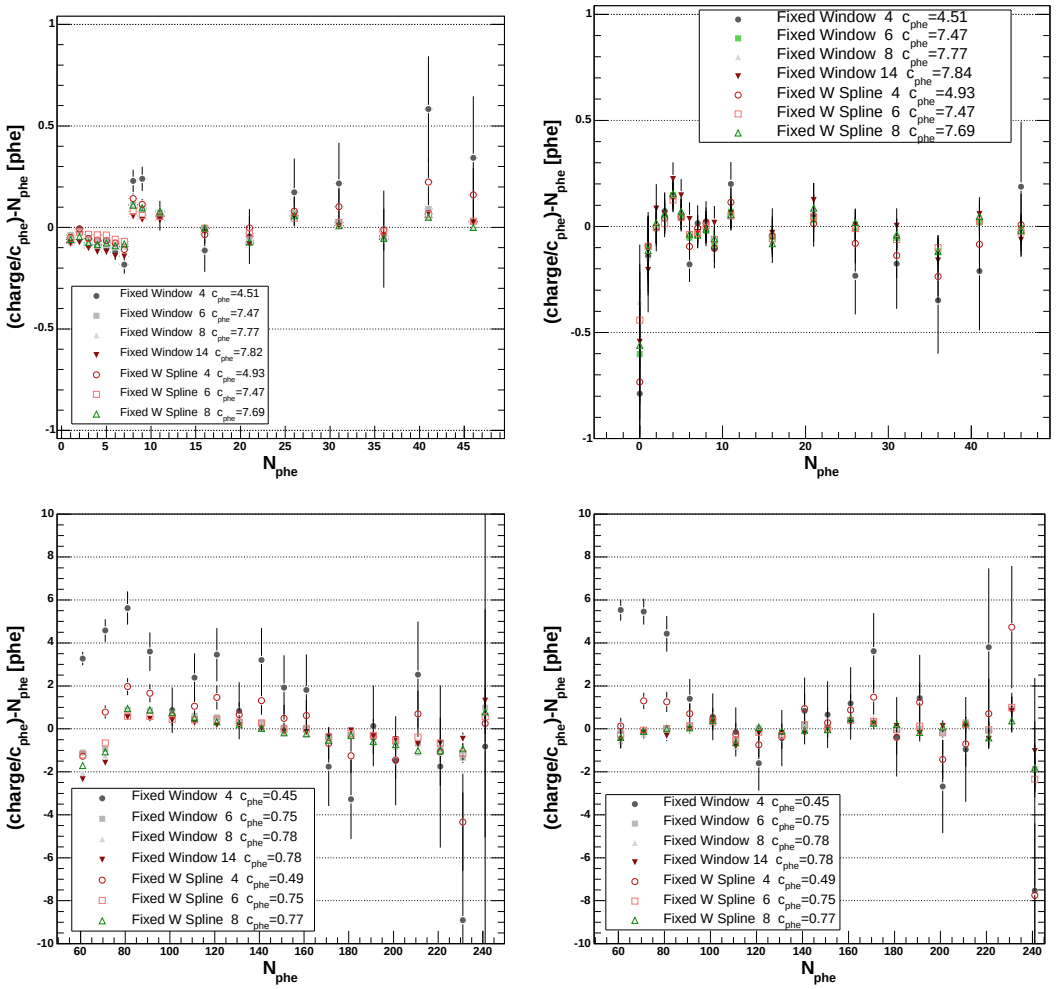

Figure 4.5: The measured bias (extracted charge divided by the conversion factor minus the number of phes) versus number of phe, for fixed window extractors. The upper plots show the high-gain and the lower ones low-gain regions with (right) and without (left) noise.

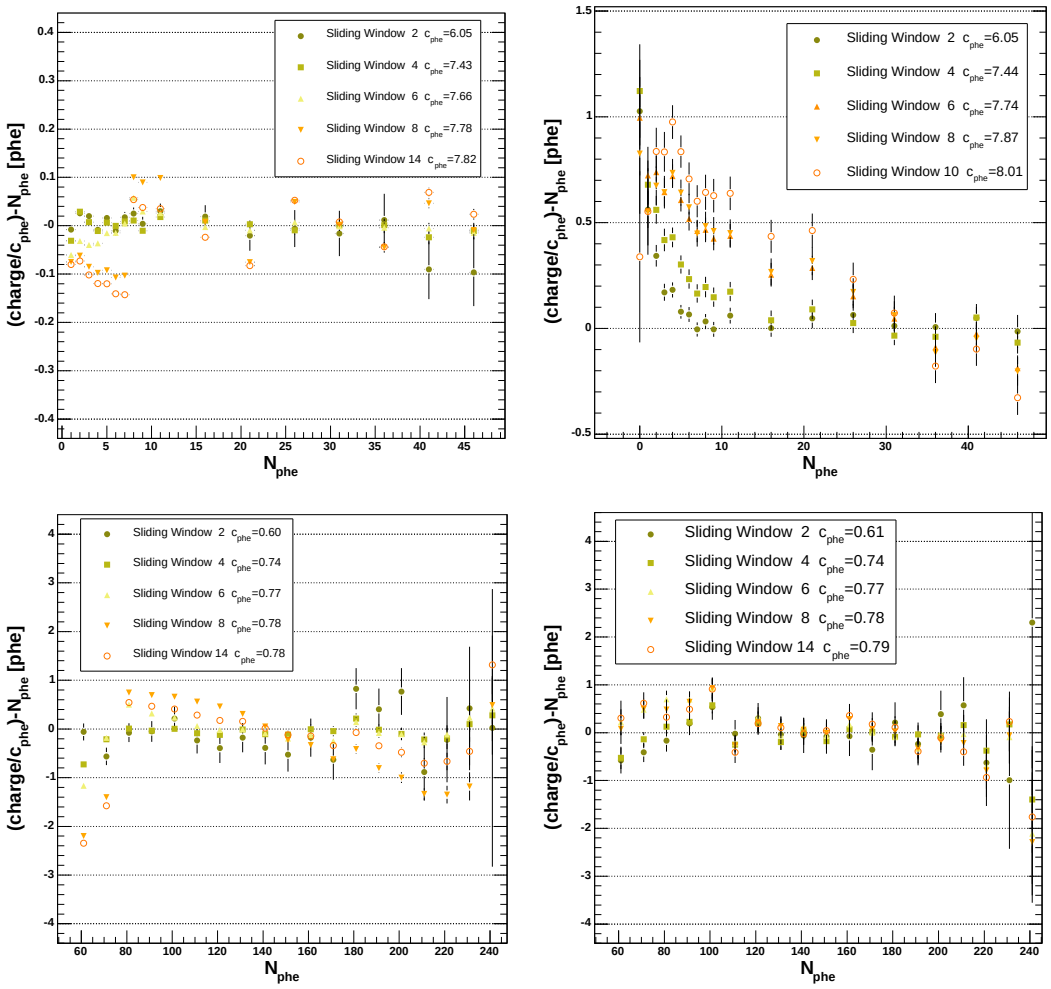

Figure 4.6: The measured bias (extracted charge divided by the conversion factor minus the number of phes) versus number of phe, for sliding window extractors. The upper plots show the high-gain and the lower ones low-gain regions with (right) and without (left) noise.

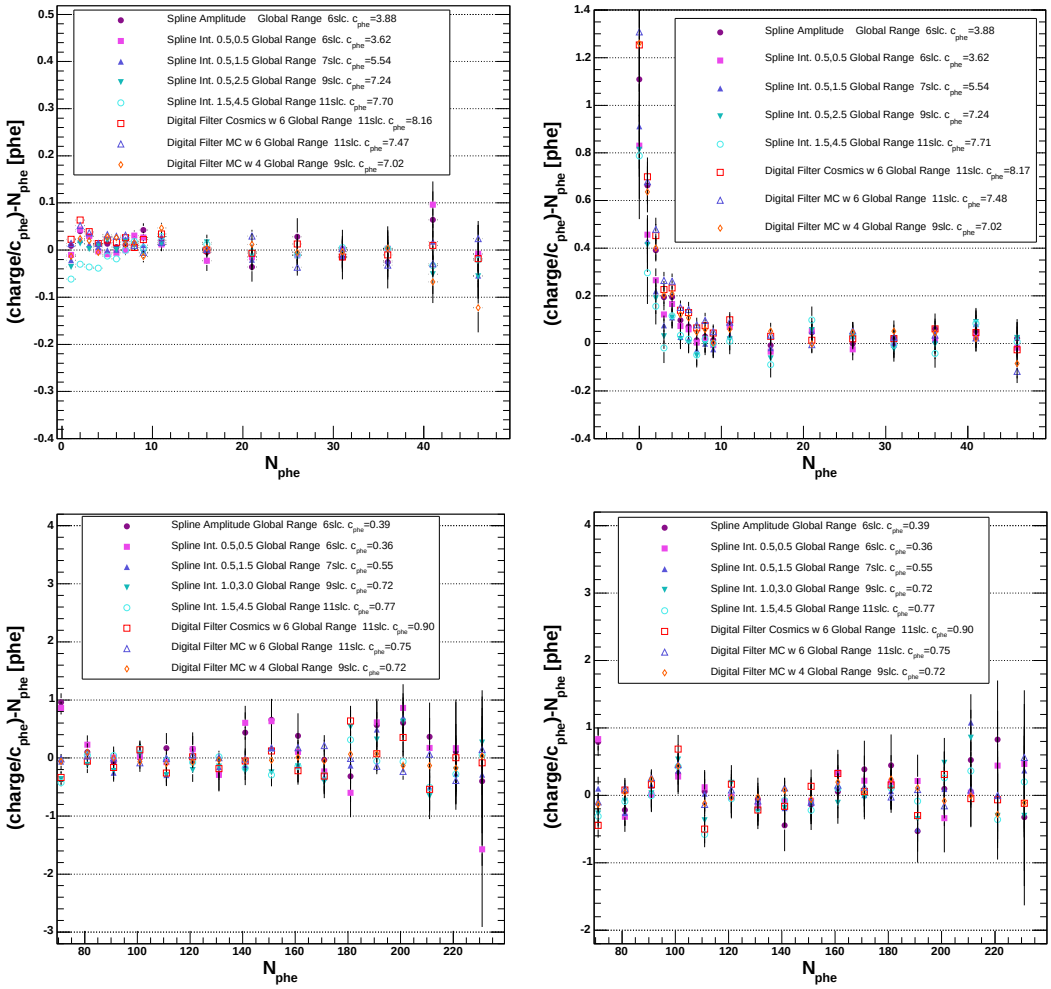

Figure 4.7: The measured bias (extracted charge divided by the conversion factor minus the number of phes) versus number of phe, for spline and digital filter extractors. The upper plots show the high-gain and the lower ones low-gain regions with (right) and without (left) noise.

In order to obtain the **charge resolution** of a given extractor, we calculated the RMS:

$$RMSE = RMS(\widehat{N}_{\rm phe} - N_{\rm phe}) \tag{4.4}$$

where the reconstructed charge $\widehat{N}_{\rm phe}$ is obtained by calibrating the extracted charge (in FADC counts) to phe, with the conversion factors $c_{\rm phe}$, obtained from Fig. 4.8 to 4.10. For signals with in the high-gain region with noise (e.g. upper right panel in Fig. 4.9) one can see that for small signals, small extraction windows yield better resolutions. However, the resolution from extractors which do not entirely cover the whole pulse show a dependency with the signal intensity. This dependency is seen for the sliding window extractor with 2 FADC slices, the fixed windows with 4 FADC slices for all spline extractors and the digital filter. Among them, the digital filter with 6 FADC slices extraction window shows the weakest dependency: it raises by about 80% between zero and 50 photo-electrons, but remains constant over the entire low-gain range (Fig. 4.10 right panels). The digital filter over 4 FADC slices shows also a good resolution in the high-gain region, but it is worse in the low-gain region.

Probably, the input light distribution of the simulated light pulse introduces an amplitude dependency. In fact, one can consider the RMSE as a linear superposition of the intrinsic precision of the extractor algorithm and the contribution due to background fluctuations. One can see (from Fig. 4.8 to 4.10, left panels) that the RMSE for signals without added noise depends linearly on the number of phe. While the charge reconstruction holds linear to statistical precision of the measurement of RMSE with noise for the digital filter and the spline extractors, and to a precision of less than 0.5 phe for all other extractors.

The last extractor feature under study is the **time resolution**. There are four main contributions to the time accuracy of the signal [71]:

1. The intrinsic arrival time spread of the photons on the PMT, given by $\Delta t \approx \frac{\delta t_{\rm IN}}{\sqrt{N_{\rm phe}}}$, where $\delta t_{\rm IN}$ is the intrinsic width of the input light pulse. $\delta t_{\rm IN}$ is about 1 ns for γ-ray pulses, few ns for hadron pulse, few hundreds of ns for muons and about 3 ns for the calibration pulses.

2. The transit PMT time spread between the release of an electron from the photocathode and the signal at the PMT output, given by $\Delta t \approx \frac{\delta t_{\rm TS}}{\sqrt{N_{\rm phe}}}$. It is about few hundreds of ps per single phe, depending on the incident light wavelength.

3. The reconstruction error due to the background noise and limited extractor resolution: $\Delta t \approx \frac{\delta t_{\rm rec} \cdot \sqrt{{\rm Var}[\widehat{N}_{\rm phe}]}}{N_{\rm phe}}$, where ${\rm Var}[\widehat{N}_{\rm phe}]$ is the extractor variance, which depends only very weakly on the signal charge.

4. And a constant offset due to the residual FADC clock jitter between different channels or the MC simulation time steps: $\Delta t = \delta t_0$.

In total, the time spread can be expressed as:

$$\Delta T = \sqrt{\frac{T_1^2}{N_{\rm phe}} + \frac{T_2^2}{N_{\rm phe}^2} + T_0^2}. \tag{4.5}$$

where T_1 contains the contributions of $\delta t_{\rm IN}$ and $\delta t_{\rm TS}$, T_2 contains the contribution of $\delta t_{\rm rec}$ and T_0 the offset δt_0.

Like in the case of the charge resolution, we calculated the RMS of the distribution of the deviation of the reconstructed arrival time with respect to the simulated time:

$$\Delta T_{\rm MC} \approx RMS(\widehat{T}_{rec} - T_{sim}) \tag{4.6}$$

where $\widehat{T}_{rec}$ is the reconstructed arrival time and T_{sim} the simulated one.

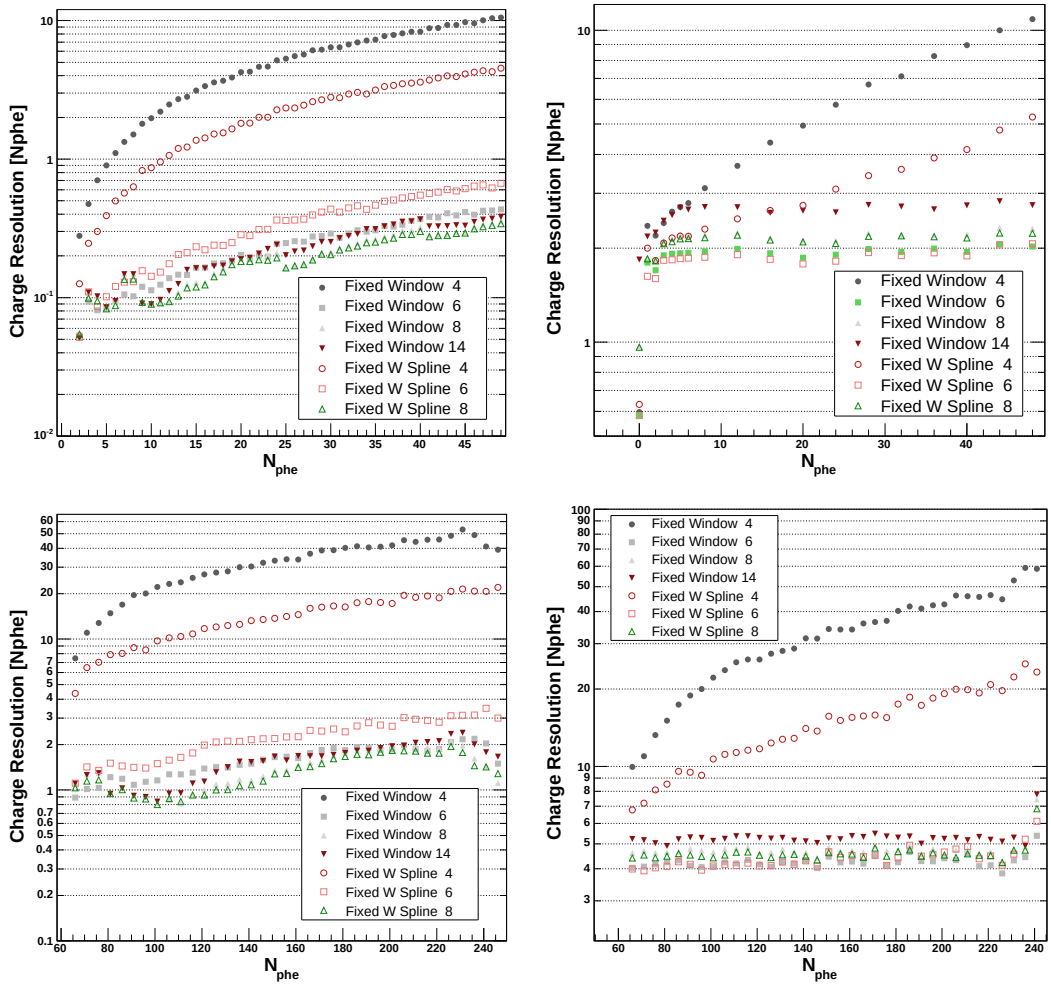

Figure 4.8: The measured charge resolution (RMS of extracted charge in FADC counts divided by the conversion factor minus the number of phe) versus number of phe, for fixed window extractors in different window sizes. The upper plots show the high-gain and the lower ones low-gain regions. Left: without noise, right: with simulated noise.

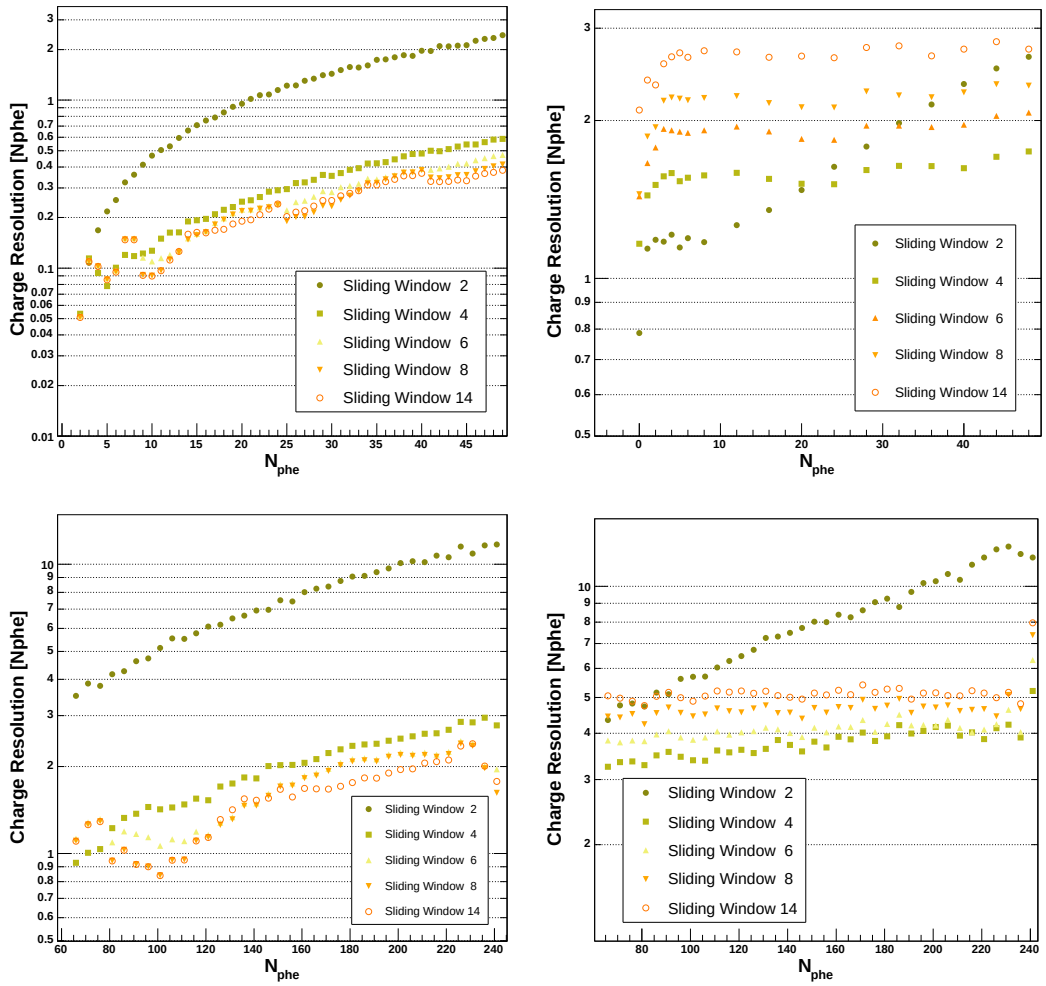

Figure 4.9: The measured charge resolution versus number of phe, for sliding window extractors in different window sizes. The upper plots show the high-gain and the lower ones low-gain regions. Left: without noise, right: with simulated noise.

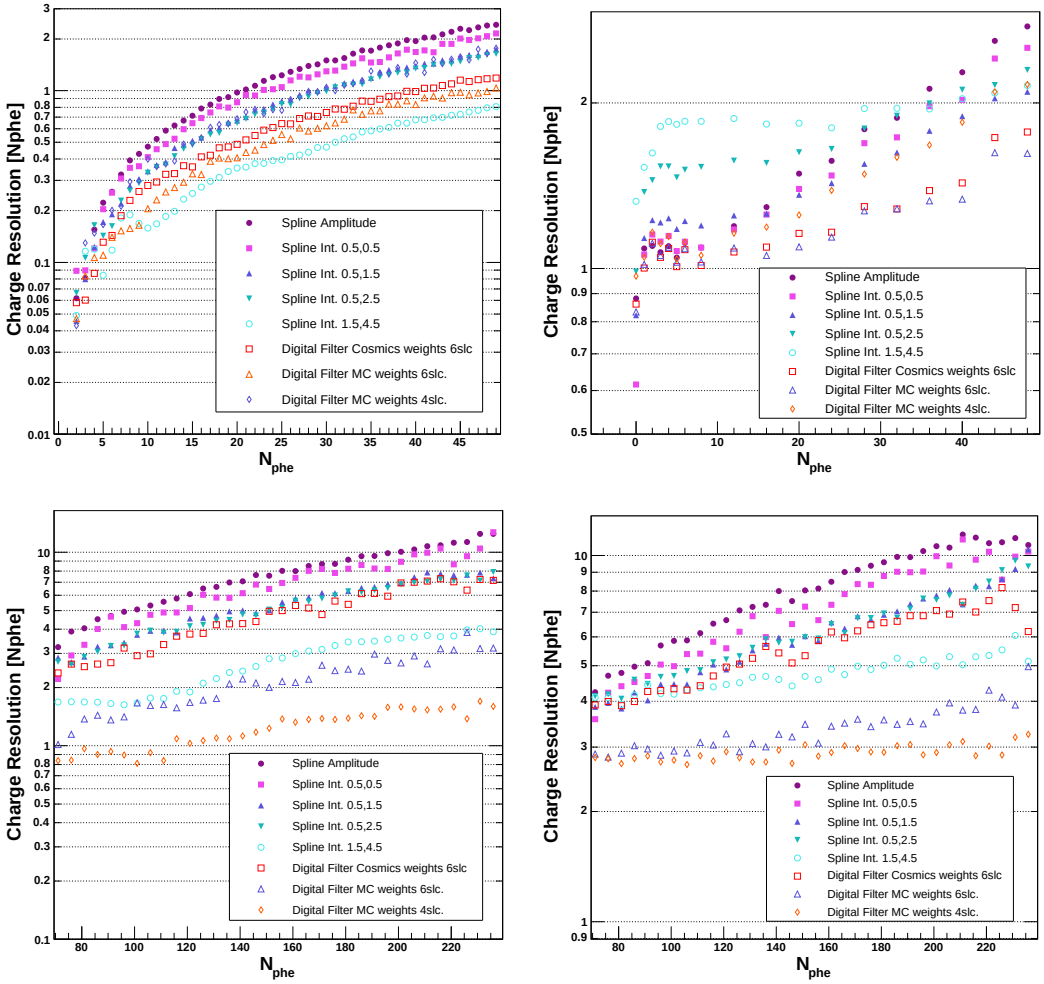

Figure 4.10: The measured charge resolution versus number of phe, for spline and digital filter extractors in different window sizes. The upper plots show the high-gain and the lower ones low-gain regions. Left: without noise, right: with simulated noise.

The time resolution for the studied extractors as a function of the simulated charge N_{phe} are shown in figures 4.11 and 4.12. The obtained results have been fit to equation 4.5. Generally, the time resolution parameter T_1 is about a factor 1.5 better than those obtained from the calibration (see section 4.1.6, figure 4.14). This is understandable since the MC pulses are smaller and the intrinsic time spread of the PMT has not been simulated.

In figure 4.11, one can see nicely the effect of noise in the time resolution. Whereas without noise all sliding window extractors with a window size of at least 4 FADC slices show similar time resolution, with noise the resolution degrades for larger extraction window sizes. This can be understood by the fact that an extractor covers the whole pulse if integrating at least 4 FADC slices and each additional slice can only be affected by the noise.

In the high-gain, only the small sliding windows below or equal 4 FADC slices yield a good time resolution, as well as the spline and the digital filters. In the low-gain, only sliding windows larger than 4 FADC slices, the half-maximum searching spline and the digital filter with 6 FADC slices improve the time resolutions with respect to the high-gain pulses. Note that the digital filter with 4 FADC slices yields a rather poor resolution in the low-gain, just as the poor charge resolution found before.

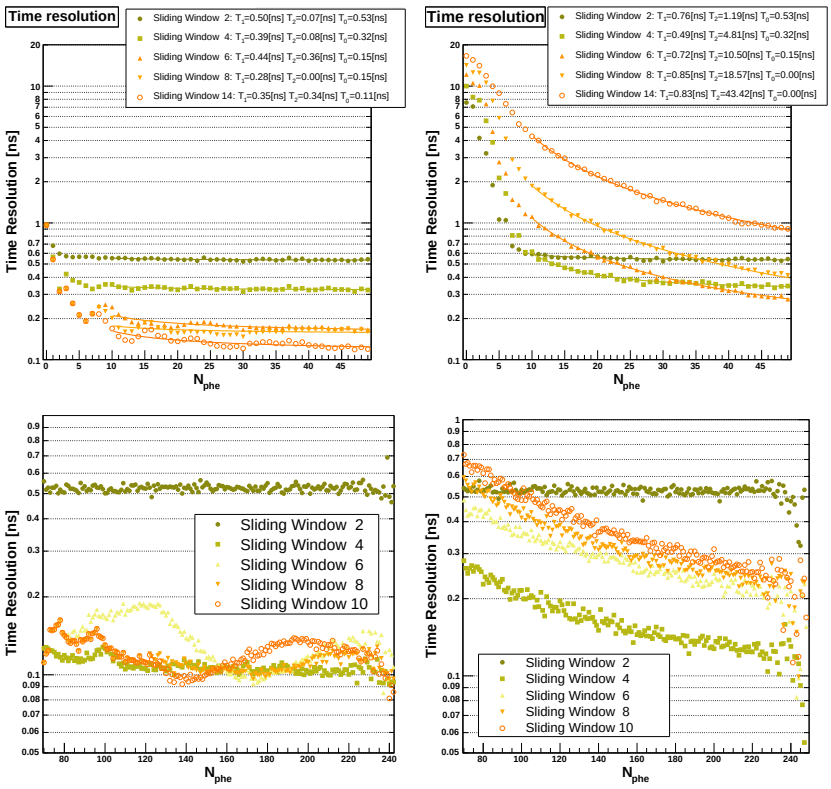

Figure 4.11: The measured time resolution (RMS of extracted time minus simulated time) versus number of phes, for sliding window extractors in different window sizes. The upper plots show the high-gain (fitter parameters to eq. 4.5 are given in the inset) and the lower ones low-gain regions. Left: without noise, right: with simulated noise.

4.1.5 Pedestal reconstruction

The pedestal is the average FADC count for the signal baseline (i.e. no input signal). To determine the pedestal setting off-line, dedicated pedestal runs are used, during which the MAGIC read-out is triggered randomly. The fluctuations of the pedestal are due to electronic noise and LONS fluctuations. Thus the pedestal RMS is a measure for the total integrated noise level.

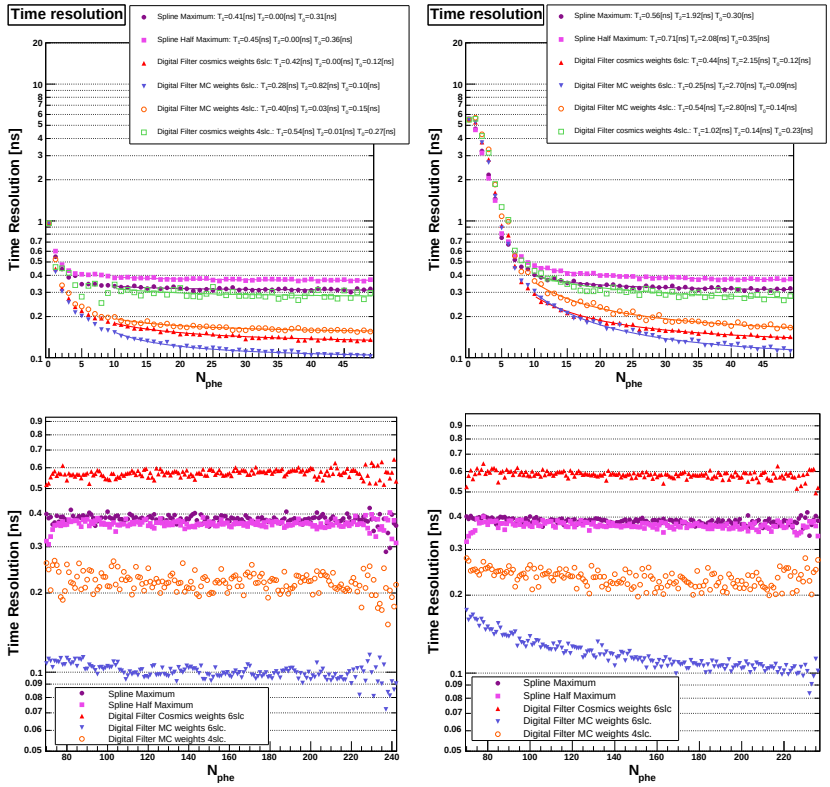

Figure 4.12: The measured time resolution (RMS of extracted time minus simulated time) versus number of phes, for spline and digital filter window extractors in different window sizes. The upper plots show the high-gain (fitter parameters to eq. 4.5 are given in the inset) and the lower ones low-gain regions. Left: without noise, right: with simulated noise.

The pedestal value is computed by applying the signal extractors to purely pedestal events. From the distribution of obtained values we can compute the bias and RMSE of the different extractors. Those parameters have been obtained in different conditions: for randomly triggered pedestal events with closed camera, for a sample observations in and outside the galactic plane and for a MC sample. Detailed comparison of the response of each extractor in all those cases can be found in [71]. These studies showed that the bias typically decreases and the RMSE increases with increasing sliding window size, except for the digital filter. In fact, the extractor with the smallest RMSE is the digital filter fitting 4 FADC slices with an RMSE of 1.7 phe for a typical galactic star field.

However, in the standard analysis, the pedestal is not extracted from dedicated pedestal runs but directly from the shower events. The DAQ system (see Sec. 3.3) reads in the low gain branch only if the signal is above a certain level; hence for signals below that level, all 30 FADC slices are high gain samples. This fact makes possible to use for small signals the last 15 FADC slices to measure the pedestal level, while regular data are being taken. This allows to measure the pedestal level with large statistics and almost synchronously with the data run which is calibrated.

4.1.6 Reconstruction of calibration pulses

The extractors introduced in section 4.1.3 have been applied to events where the camera is illuminated with the calibration pulses (see Sec. 3.4) of different colors and intensities. Figure 4.13 show the reconstructed mean number of phe $\langle \widehat{N}_{\mathrm{phe}} \rangle$ for the standard UV calibration pulse for different extractors. The results differ by less than 5%.

The measured time resolutions for different calibration pulses are shown in figure 4.14. The time resolutions over the inner pixels and for three representative extractors are shown to

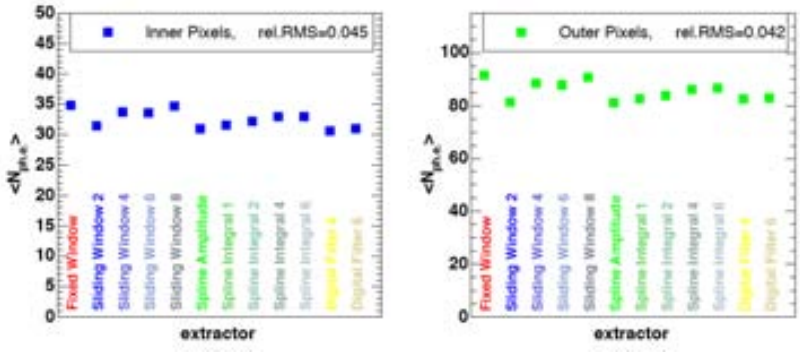

Figure 4.13: Mean number of phe $\langle \widehat{N}_{\mathrm{phe}} \rangle$ for the standard 10 LED UV calibration pulse for different extractors, reconstructed in the inner (left) and outer (right) pixels. From [64].

illustrate the calibration behaviour (for a detailed study of the calibration pulses the reader is referred to [71]). They are fitted by equation 4.5. The time resolutions for the UV pulses are better than those for other colors. This is due to the fact that the UV pulses have a smaller intrinsic pulse width and the UV LEDs are very stable from event to event [64]. Between the extractor methods, the sliding window yields poorer resolutions.

From the measured time resolutions for calibration pulses, one can estimate the expected time resolution for cosmic pulses [70]:

$$\Delta T \approx \sqrt{\frac{4.5\mathrm{ns}^2}{N_{\mathrm{phe}}} + \frac{20\mathrm{ns}^2}{N_{\mathrm{phe}}^2} + 0.04\mathrm{ns}^2}\,. \tag{4.7}$$

For signals above 10 phe, the time resolution is below 830 ps and improves up to 300 ps for the largest signals ($\sim$ 100 phe).

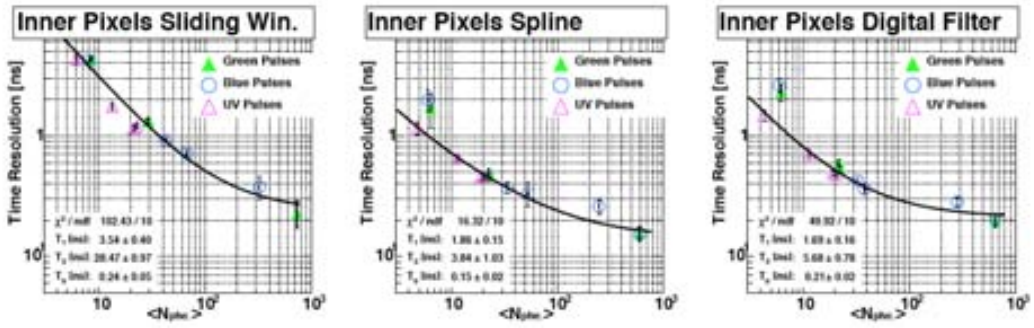

Figure 4.14: Mean arrival time resolution (for inner pixels) as a function of the extracted mean number of phe of three different extractors: sliding window for 6 FADC slices (left), spline amplitude (middle) and digital filter with 6 FADC slices (right). The fit parameters to eq. 4.5 are given in the inset. From [64].

4.1.7 Signal extraction conclusions

Based on the previous investigations using MC, pedestal and calibration events, the conclusions from the extractor performance are summarized in Table 4.1. The following criteria are used to compare the extractors:

- Robustness: The extractor should yield on average the true number of phe. And should not deviate more than 10% in case of small variations[3] of the pulse shape.

[3]Variations of the pulse form have a physical reason: average Čerenkov pulses from hadronic showers are

Extractor configuration (FADC slices)	robustness high gain	robustness low gain	RMSE	bias	time spread	speed
Fixed Window 8	OK	FAIL	FAIL	BEST	FAIL	BEST
Sliding Window 2	FAIL	FAIL	OK	OK	FAIL	OK
Sliding Window 4	OK	FAIL	FAIL	OK	FAIL	OK
Sliding Window 6	OK	OK	FAIL	OK	FAIL	OK
Sliding Window 8	OK	BEST	FAIL	OK	FAIL	OK
Spline Amplitude	FAIL	FAIL	OK	FAIL	OK	OK
Spline Integral 1	FAIL	FAIL	OK	OK	BEST	OK
Spline Integral 4	OK	FAIL	OK	OK	BEST	FAIL
Spline Integral 6	OK	OK	FAIL	OK	BEST	FAIL
Digital Filter 4	OK	FAIL	BEST	OK	OK	OK
Digital Filter 6	OK	OK	OK	OK	OK	OK

Table 4.1: The tested characteristics for different extractors (see text for description). OK means that the extractor has passed the test, FAIL means that the extractor has severely failed the test and should not be taken because of that reason, and BEST means that the extractor have come out as best of the particular test. Adapted from [71].

- The RMSE of the reconstructed charge for cosmic signals should not exceed the intrinsic Poissonian signal fluctuations above 5 phe. This condition allows to require a time coincidence of 3.3 ns between neighboring pixels to reject noise signals in the image cleaning and thus allow to measure differential energy spectra down to 60 GeV [72].

- Bias should be small or negligible and time resolution should not be worse than 2 ns at a signal strength of 10 phe.

- The speed of the extractor algorithms (number of reconstructed events per unit time) should not be too slow, so that this step does not limit the total event reconstruction speed.

In table 4.1 we present a summary for the most representative extractor algorithms, showing which of them fulfill the above criteria. One can see that there is no signal extractor without problems. However, the digital filter fitting 4 FADC slices can be used always for the high gain extraction, and the digital filter fitting 6 slices for the low gain extraction, whenever the mean pulse position is not critical. This combination has been chosen as the standard analysis for MAGIC data, and therefore is the one used in the data analysis of this thesis.

4.2 Event reconstruction

4.2.1 Calibration

The integrated charge of the extracted signal is stored in units of FADC counts. Integrated charge expressed in counts has no direct physical meaning and can not be straightforwardly used for the shower image description. It must be converted into photons which have a physical connection with the EAS produced by the primary particle.

As explained in section 3.4, after a relative calibration of the pixels to make their response uniform for a same input light, an absolute calibration is needed to compute the conversion factors from charge in FADC counts to number of phe. The so-called *F-Factor* method is applied to dedicated calibration runs. The number of phe arriving to the first dynode of each

usually broader than those from electromagnetic cascades. Additionally, there are differences between the pulse form of the calibration pulses and those of cosmic pulses. These variations affect mainly those extractors which integrate only small portion of the pulse form

PMT can be derived from equation 3.2:

$$N_{phe} = \frac{(\langle Q \rangle - \langle Q_{ped} \rangle)^2}{\sigma^2} F^2 \,, \tag{4.8}$$

where F represents the excess noise introduced by the PMT and readout chain ($F \sim 1.15$ for the MAGIC PMTs), $\langle Q \rangle$ is the mean charge in FADC counts of the pulse signal registered by the pixel and extracted from calibration pulses, $\langle Q_{ped} \rangle$ is the mean pedestal and σ^2 is the reduced variance of the charge distribution, corrected for the contribution of the pedestal variance ($\sigma^2 \equiv \sigma_Q^2 - \sigma_{ped}^2$). The conversion factor from FADC counts to phe C_{phe}^{FF} for each pixel is obtained from:

$$C_{phe}^{FF} = \frac{N_{phe}}{\langle Q \rangle - \langle Q_{ped} \rangle} = \frac{\langle Q \rangle - \langle Q_{ped} \rangle}{\sigma^2} F^2 \,. \tag{4.9}$$

4.2.2 Identification of bad pixels

In any observation with the telescope, it is very likely that among the 576 pixels of the camera, few of them present some kind of hardware malfunction, either in the pixel itself, in the analog transmission, or any other step in the read-out chain. Also pixels which are affected by a bright star in the field of view will show an increase of the pixel DC current, and subsequently a higher pedestal RMS.

The calibration is a perfect tool to recognize pixels which are unsuitable for the analysis. Once detected a diagnose of the hardware problem is performed to repair them. But also a specific treatment can be done to include them in the analysis.

Pixels with low mean $\langle Q \rangle$, too large fluctuations on the extracted charge for calibration runs, fluctuating arrival time of the pulses for the same pixel, too high or too low pedestal RMS, are labelled as *bad* pixels. Tagged pixels are treated in a special way in order not to bias the shower image calculation. They can be completely excluded from the calculation of the image parameters or the signal can be interpolated: signal, pedestal and pedestal RMS for the *bad* pixels are interpolated using the measured values of the neighbour (not *bad*) pixels. Then these pixels with their new contents are once again included in the standard analysis data chain.

4.2.3 Image cleaning

After the calibration of the signal, the next step in the analysis is to determine which pixels should be considered part of the recorded image. The goal is to keep pixels which contain information about the EAS and reject those whose signal is more likely due to NSB fluctuations. This procedure is called image cleaning.

The image cleaning algorithm used consists of two loops over the pixels comparing their signal with two cleaning levels. In a first loop those pixels with a signal larger than the highest cleaning level are kept and labelled as *core* pixels of the event. In a second loop pixels that are adjacent to the core image are rescued if they pass the lowest cleaning level, and are named *boundary* pixels.

Depending on the way the cleaning levels are determined, two cleaning algorithms can be performed:

Relative The cleaning levels are determined by the mean pedestal RMS, σ_{ped}, of the pixel. Those pixels with a signal above r_1 times the noise level are selected as the core of the image, their neighbors with a signal above r_2 times the pedestal RMS are also kept. Typically r_1=3 and r_2=2.5.

Absolute A fixed threshold in number of phe is defined for a pixel considered as a core pixel, and a lower threshold for the surrounding pixels to be accepted. 10 phe for the core and 5 phe for the boundary pixels are the standard values currently used in the MAGIC data analysis.

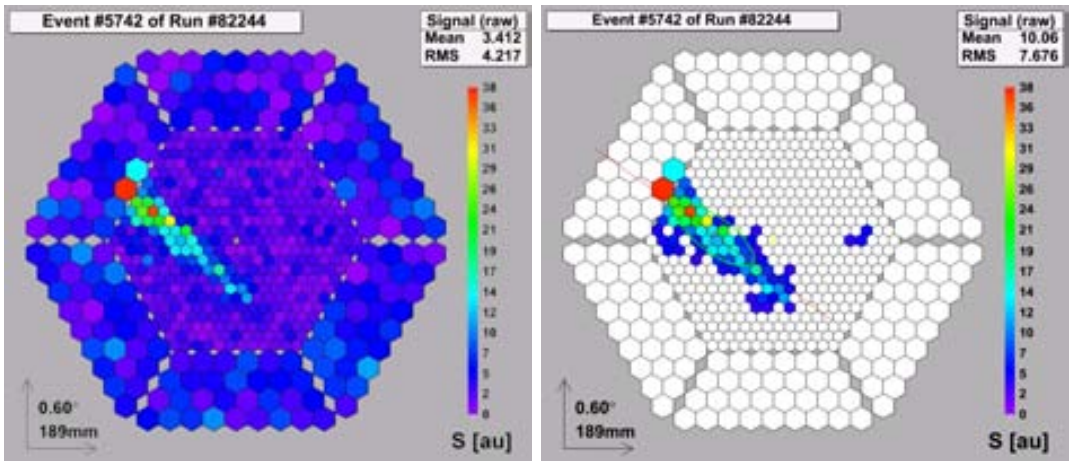

Figure 4.15: An event before (left) and after (right) the image cleaning procedure (absolute cleaning with 10 and 5 phe boundary levels). An ellipse resulting after the calculation of the image parameters is also shown.

The main advantage of the relative cleaning is that it retains as much as possible of the image in order to have the largest amount of information about the shower compared with the absolute cleaning. Nevertheless, relative cleaning depends on the pedestal RMS, which noticeably depends on the NSB conditions. For example, it is different for galactic and extragalactic sources. Therefore the image parameters depend on the night sky and weather conditions, which make the combination of data more difficult. Moreover, when using the relative cleaning, the noise level in the MC simulation should be set carefully equal to the one in the data analysed samples. That also makes the MC vs. data comparison much more complex than for the absolute cleaning.

In the data analysed for this Thesis, an absolute cleaning is used, with core and boundary levels of 10 and 5 phe respectively. An image before and after cleaning can be seen in Figure 4.15.

The arrival time of the signal in each pixel can also be used to clean the image. Presently several timing based cleanings are under study and are already giving promising results specially for the smaller images [73]. The analysis of the islands of pixels of the resulting image to discriminate if they are from noise origin or not is also another possible tool to improve the image definition [74] (see e.g. the isolated group of three pixels in Fig. 4.15). Neither time cleaning nor island methods are used in this analysis.

4.2.4 Image parameters

The telescope images atmospheric shower on the camera. γ-ray and hadron-induced showers develop in a different way, so their images allow to discriminate the primaries.

In 1985 Hillas proposed a parametrization [75] based on the first, second and third momenta of the two-dimensional distribution of the signal along the image. The shower image is parametrized as an ellipse and the n^{th} order momenta are estimated with respect to a system of coordinates, with center at the center of gravity of the image, x-axis along the major axis of the ellipse, and y-axis along the short axis.

Many image parameters have been defined in the literature. They can be grouped in two classes: those describing the shape of the shower and therefore independent of any reference point, and those depending on a reference point (depending on the source position on the camera). The image parameters most commonly used for IACTs data analysis and the information they contain about properties of the primary particle that initiated the shower are presented below. Figure 4.16 schematically shows some of them. In all cases, the parameters are extracted using the pixels selected during the image cleaning. In the momentum calculation, the pixel position in the camera is weighted by the number of phe in

this pixel.

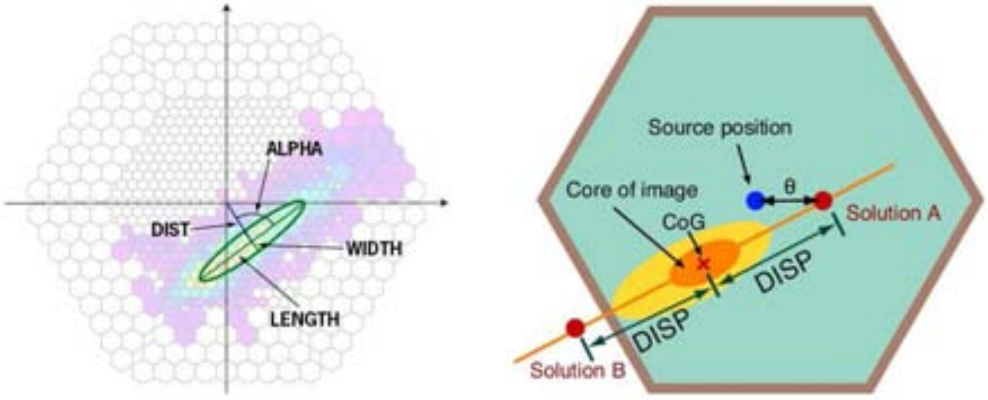

Figure 4.16: Left: Scheme of the parametrization of shower image with ellipse. Right: Sketch of the Disp and θ parameters (from [40]).

Source-position independent parameters:

Size is the total charge collected on the image, in number of phe. This parameter is related to the number of Čerenkov photons (and secondary particles) in the EAS, and therefore to the energy of the primary particle, as illustrated for MC γ-rays in Figure 4.17.

Width and Length are the half width and half length of the major axis of the shower ellipse. They provide information about the lateral and longitudinal development of the shower in the atmosphere. As we have seen in section 2.4.2, the lateral spread of a γ-induced EAS is substantially lower than that corresponding to a hadron.

Mean x and mean y are the center of gravity (CoG) coordinates of the image.

Conc is the fraction of the total charge with is contained in the two brightest pixels. In general, γ-ray induced showers are more compact than hadron induced ones, so they exhibit a higher concentration.

Asym is the vector connecting the image center of gravity and the brightest pixel. It informs about the asymmetry of the phe distribution along the major axis. It helps to discriminate between the shower's head and tail.

Leakage is the fraction of the total charge which is contained in the pixels of the outermost ring of the camera. High Leakage values indicate that the image is truncated, so information from some parts of the shower is not contained in the camera. Fully contained images have zero or very small Leakage. In this work Leakage2 parameter is used, which is the fraction of signal contained in the 2 outermost rings of pixels.

Source-position dependent parameters:

M3Long is the third moment of the image along the ellipse major axis. It keeps information about the head/tail of the shower image. It is positive when the head of the image points to the source position. γ-rays are expected to point to the source position while hadrons are isotropically distributed.

Dist is the angular distance between the image CoG and the source position. It is related with the shower impact parameter.

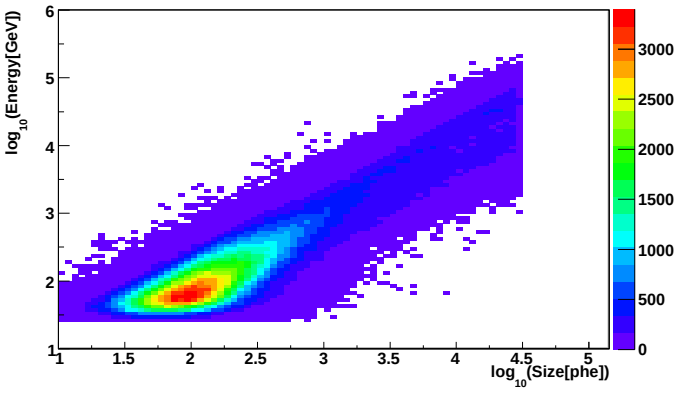

Figure 4.17: Correlation between energy of the primary γ-ray particle and the Size parameter of the image. An upper limit of 120 m on the impact point of the showers is applied.

Alpha is the angle between the major shower axis and the line connecting the image CoG and the source position. It is expected to be small for γ-ray showers and extenly distributed between 0° and 90° for hadron showers. It is the parameter with the largest γ/hadron separation power.

θ is the angular distance between the source position and the estimated source position of an event. The source position is estimated using the so-called Disp method, that will be described in Sec. 4.2.9. For convenience, θ^2 is used, because its distribution is flat for background events and has an exponential shape (for Gaussian PSF) for γ-ray signals peaking at zero.

4.2.5 MAGIC Monte-Carlo simulation

In IACTs the γ/hadron separation cut efficiency and the energy estimation cannot be evaluated by means of test beams of VHE γ-rays of known energy. Therefore the analysis of IACT data requires a detailed Monte-Carlo simulation of γ-ray and hadron-initiated air showers and the detector response.

The MC simulation for the MAGIC telescope (see [76] for a detailed description) is divided into three main stages, summarized in the following steps:

1. **Primary particle simulation**: The development of the γ and hadron-initiated air showers are simulated with CORSIKA (COsmic Ray SImulations for KAskade) version 6.019 [77] with some custom modifications [78]. This program simulates the interaction of the primary particle (γ-ray or hadron) with atmospherical nuclei and all secondary particles interactions produced in the EAS. The Čerenkov light emitted by the charged particles in the EAS is also simulated. For each Čerenkov photon arriving in a radius of 20 m around the telescope the wavelength, arrival location and direction are stored in a binary file.

2. **Reflector**: The reflector program [79] accounts for the Čerenkov light attenuation in the atmosphere and the reflection of the surviving photons on the mirror dish to obtain their location and arrival time on the camera plane.

3. **Camera**: The camera program [80] simulates the behaviour of the MAGIC PMT camera, trigger system and DAQ electronics. It takes into account some special characteristics, which may differ for each data sample, such as: the diffuse NSB or the size of the reflector area. A particularly important parameter to be tuned in the simulation is the width of the point spread function distribution of the light collected by the mirror dish and focused onto the camera.

	campaign I	campaign II
Primary particle	γ-ray	
Energy range	10 GeV - 30 TeV	
Spectrum slope	$E^{-2.6}$	
Impact parameter range	0 - 300 m	
σ of the PSF[a]	14 mm	
Mode	On/Off	Wobble
Zenith angle range	31 - 60°	30 - 55°
Num. simulated showers	$\sim$ 34 M	$\sim$ 46 M
Num. triggered showers	$\sim$ 430 k	$\sim$ 630 k
diffuse NSB level	0.178 phe/ns for 0.1×0.1 deg^2	0.183 phe/ns for 0.1×0.1 deg^2

Table 4.2: Input parameters of the two MC samples used in the analysis presented in this Thesis.

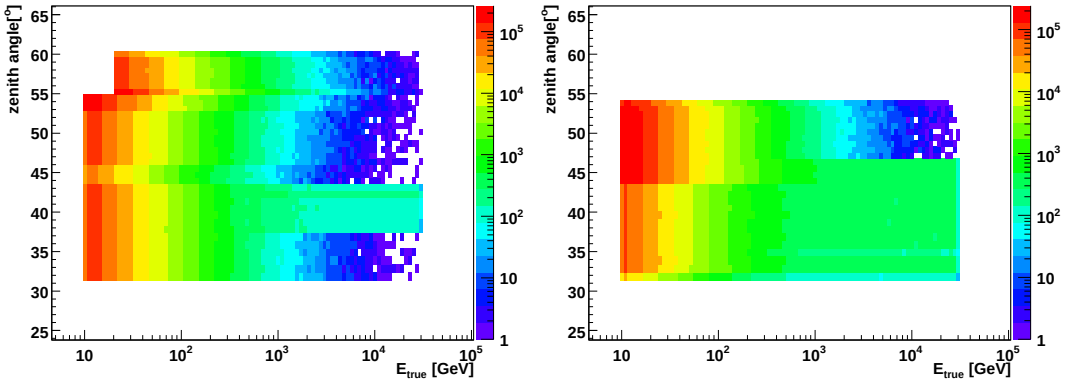

Figure 4.18: Distribution of Monte-Carlo γ-ray events for different energies and zenith angles for the two MC samples used (left for cycle I and right for cycle II). Note that for lower zenith angles (from 36-44° in cycle I and below 42° in II) the statistics is higher for higher energies. The generated zenith angles have been selected to cover the LSI +61°303 observation ranges.

Table 4.2 summarizes the parameters of the MC sample used in this work. Figure 4.18 shows the distribution of number of MC events generated for zenith angles between 32-55° and energies from 10 GeV to 30 TeV.

The PSF depends critically on the accuracy of the active mirror control and the bending model of the telescope. To estimate the telescope focusing, we used the muon analysis. Muons travelling through the atmosphere may also emit Čerenkov radiation. As they travel with almost negligible energy losses and deflection, the profile of Čerenkov photons at ground will follow a ring distribution, easily recognized in the camera images. Comparing the relative ring broadening of muon ring images with those from MC muons simulated with different PSF widths, the PSF of the MAGIC reflector can be characterized. The simulated optical PSF in this analysis has a Gaussian shape with the sigma of 14 mm.

4.2.6 Data quality checks

Before applying the γ/hadron separation methods the data are scanned for runs with technical problems or poor atmospheric conditions. The **rate** of events surviving the image cleaning is checked and compared with the rate before image treatment. Runs with problems in the signal extraction, calibration or image cleaning will show a lower rate after cleaning than normal data runs. The rate after cleaning is also checked for high values, as well as departure from the usual linear dependency of the rate with the cosine of the zenith angle (see Fig. 4.20).

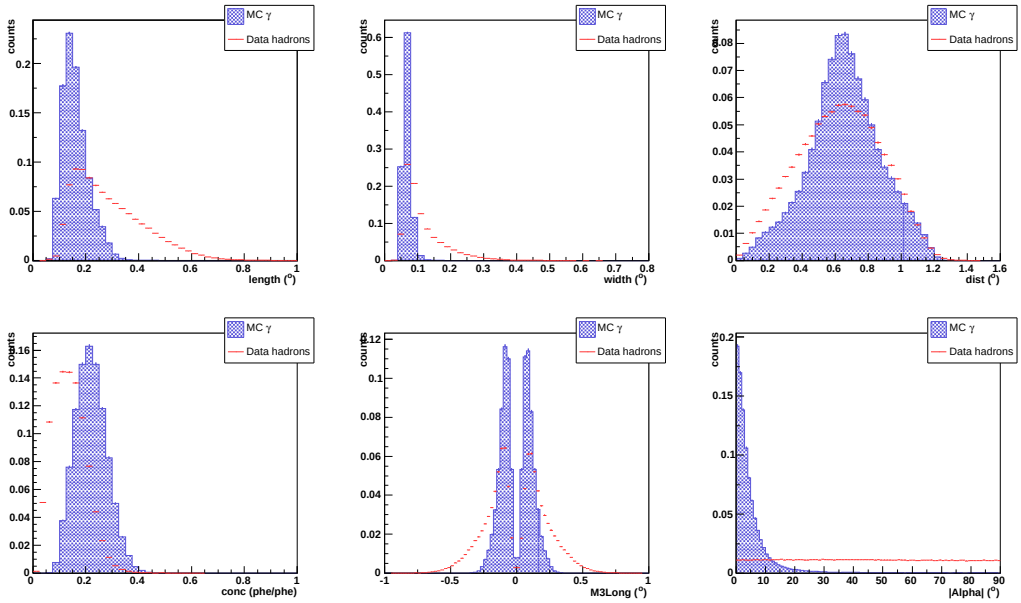

Figure 4.19: Comparison of the distribution of Hillas parameters between MC simulated γ-rays (blue histograms) and OFF data (in red) samples, for size above 200 phe. Substantial differences can be observed, which points to a non negligible γ/hadron separation power of the chosen image parameters.

The distribution of events in the trigger region on the camera plane is expected to be uniform. However, it has been observed that some regions of the camera show a lower number of events than others. These inefficiencies can be related to trigger macro-cells misbehaviour, pixels with a wrong response, etc. and produce **inhomogeneities** in the camera response. These inhomogeneities could produce distortions in the image parameters distributions because images near inefficient regions could be truncated. The center of gravity of the shower image is used to detect this effect. Fig. 4.21 illustrates how CoG distribution looks for a night of LSI +61°303 data; no significant inhomogeneities are visible.

Not only the CoG but also the other **image parameters** are compared for data of different sources (ON, OFF and Crab Nebula as a reference) and data from different observation periods for the same source. Since hadronic showers largely dominate the data sample before event selection, all distributions should be compatible. This check allows to determine if a data sample selected as OFF for a concrete ON sample is really suitable. If they are not compatible, subsequent γ/hadron separation methods will have different efficiencies for each sample.

Finally, noise events produced by light **sparks** are removed. They display roundish images with small Width and Length but large Size and Concentration that trigger the camera. They are probably produced by discharges between the PMTs shielding and some other metallic element. A fast flash of light may be partially reflected towards the PMTs by the plexiglas window and illuminate the pixels around the sparky one. These events can be recognized using a logarithmic Size vs. Concentration graph, as shown in Fig. 4.21. This cut is used for all data samples under consideration.

4.2.7 Gamma/Hadron separation

The MAGIC telescope does not only record γ-ray showers, but also cosmic ray showers, single isolated muons and fluctuations triggered by the light of the NSB. These background images are by a factor up to several thousand more numerous than events generated by γ-ray showers. It is essential to discriminate between γ-ray candidates (signal) and background events.

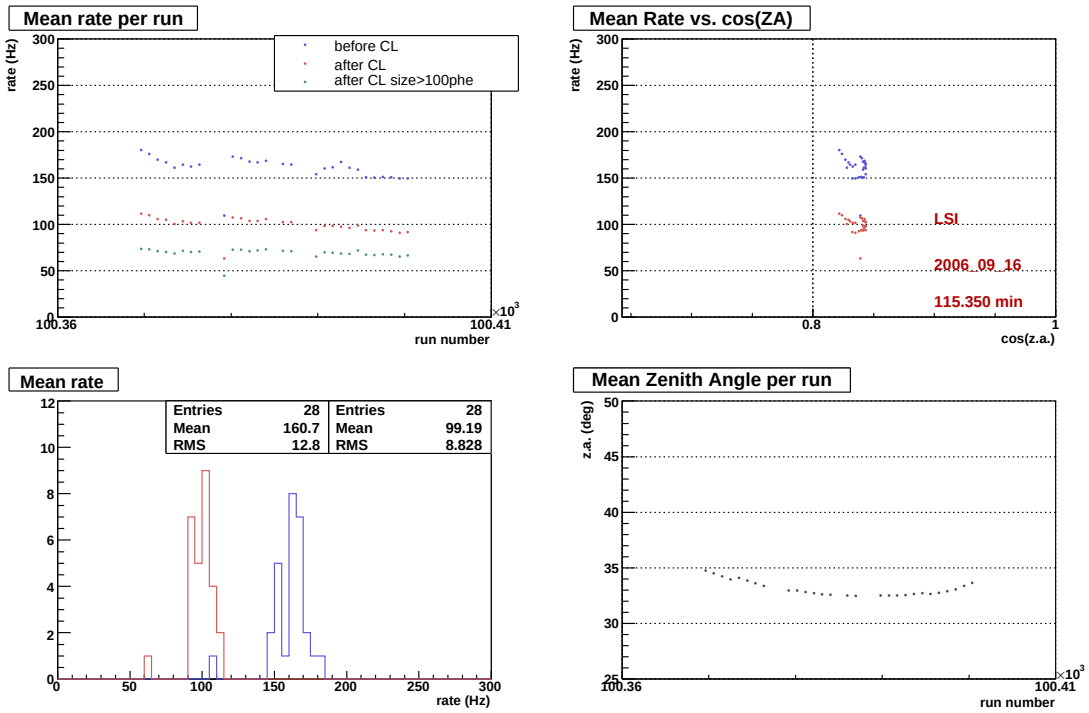

Figure 4.20: Upper left panel: Rate of events per run as observed (in blue), after image cleaning (in pink) and with a Size cut of 100 phe (in green). The distribution of the rate mean values per run before and after cleaning are shown in lower left panel. The evolution of the zenith angle during observation is also sown (lower right panel), as well as the dependency of the rate with the cosine of the zenith angle (upper right panel). Those panels correspond to an observation night of LSI +61°303 on September 16th 2006 (with an observation time of 115.5 min), which present normal rates before and after cleaning. This checks makes evident that, e.g. run number 100382 present a deficient trigger rate (and thus rates after cleaning are also lower) and is therefore excluded for the rest of the analysis.

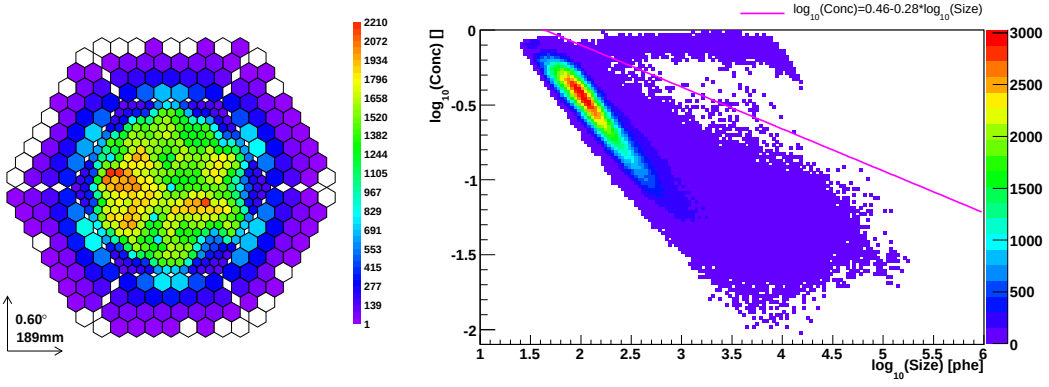

Figure 4.21: Left: Distribution of the center of gravity of the shower images in the camera for an LSI +61°303 data night on 11th October 2005. Right: The so-called *spark* events are practically removed from the data sample with the cut in log(Size) and log(Conc) shown in the figure.

The γ/hadron separation tool used is a statistical method which exploit the differences in shape and position of the images in the camera. In order to determine the features that distinguish γ and hadron induced events, a sample of pure γ-ray showers is necessary. This sample is obtained from MC simulations. OFF data runs from real observations are employed to characterize the background.

A separation method widely used in high energy physics is the **Random Forest** (RF) (see [81] for a review) which, with a custom implementation [82], is standard in the MAGIC analysis. In the RF method to each event several not completely independent decision trees (series of cuts) are applied. By combining the results of the individual decision trees, the parameter **Hadronness** is calculated, which is a measure of the probability that the event is not γ-ray like. The separation method is trained with two samples of data, each of them belonging to one of the two categories that need to be classified: pure γ showers from MC and a sample of hadron showers from OFF real data.

The source-position independent image parameters Size, Width, Length and Conc are selected to parametrize the shower images. The parameter Alpha is not included in the RF, but rather spared for the final evaluation of the signal.

In order to choose an optimal Hadronness cut, two different approaches are considered:

- Based on the maximum acceptance of γ events together with the best quality of the γ/hadron discrimination. Test samples of MC γ-rays and OFF data events (independent of the samples used for the RF training) are used to evaluate the distributions of the Hadronness parameter. The higher the Size, the better the separation of both populations, being the Hadronness of the MC γ-rays closer to 0 and that of the OFF data closer to 1. For each Hadronness cut value $h_{\rm cut}$, the efficiency of the cut or acceptance of γ-rays is evaluated as follows:

$$\epsilon_\gamma = \frac{N_\gamma(h < h_{\rm cut})}{N_\gamma^{total}}. \tag{4.10}$$

  The acceptance of hadrons $\epsilon_{\rm had}$ is correspondingly computed. Then, the so-called **Q-factor** is defined as

$$Q = \frac{\epsilon_\gamma}{\sqrt{\epsilon_{\rm had}}}\,. \tag{4.11}$$

  The Q-factor quantifies the γ/hadron separation power of a given Hadronness cut. Figure 4.22 shows the acceptances and Q-factors corresponding to the RF tree which is used in part of this Thesis. For the optimal Hadronness cut, an ϵ_γ above 80% is also required, to guarantee that enough γ-rays survive the selection. In addition, by requiring this minimum efficiency, the Hadronness cut is set in a region of the efficiency curve (see Fig. 4.22) where the slope is not too steep, which avoids systematic errors produced by very small discripancies between data and MC.

- Based on the maximum significance or the best achievable sensitivity. The events of the ON data sample of a reference source such as the Crab Nebula and a OFF data sample are subject to the RF decision trees. The signal is evaluated comparing the Alpha distributions for different Hadronness cuts. The cuts providing a maximum significance are selected. In Fig. 4.23 we show the signal of the Crab Nebula (from a data sample from Oct/Nov 2005[4]) evaluated for different Hadronness and Alpha cuts.

In both cases, if the analysis is performed for different Size bins or different integral Size cuts, the selected optimal cuts may be different in each sample.

4.2.8 Energy reconstruction

The energy associated to the γ-like events after the γ/hadron separation will be an important quantity, as it will be used to determine the shape of the differential energy spectrum of the primary γ-ray candidates associated to the source emission.

[4]The Crab Nebula was observed during the same period and in similar conditions as LSI $+61^\circ303$ during the first campaign, and therefore, used to optimize the Hadronness and Alpha cuts.

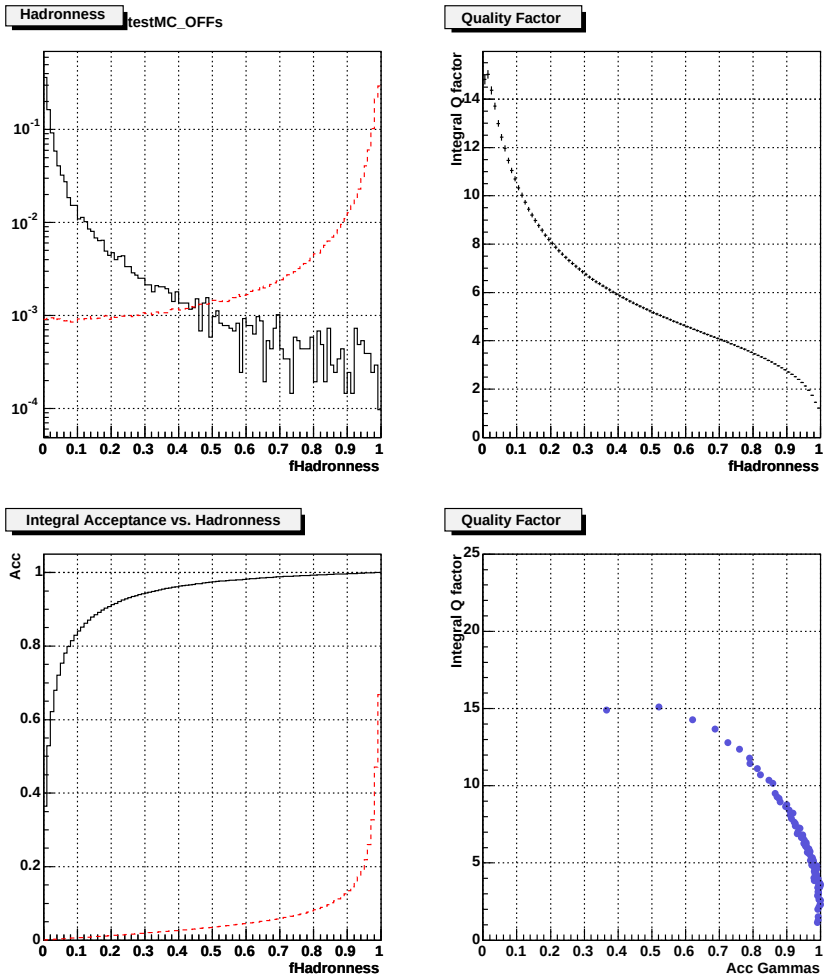

Figure 4.22: Diagnosis of the quality of the γ/hadron separation achieved when applying a certain Hadronness cut. Left upper panel: Distribution of Hadronness for a test sample of MC γ-rays (black histogram) and OFF data (red dashed histogram) for a Size cut above 100 phe. Right upper panel: Q factor value achieved for each Hadronness cut. Left lower panel: acceptance of MC γ-ray and background events as a function of the Hadronness cut applied. Right lower panel: Q factor value achieved for different values of γ-ray acceptance.

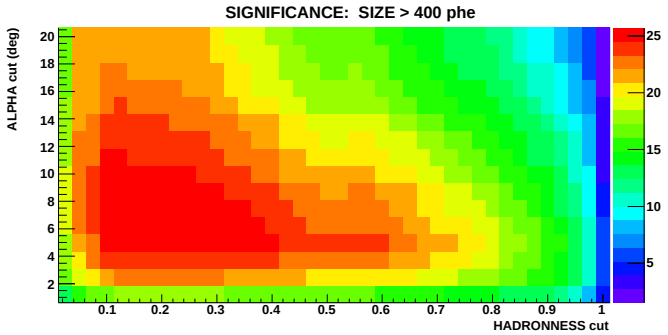

Figure 4.23: Significance of the Crab Nebula source (data sample from Oct/Nov 2005 with around 200 min observation time) with an Size cut above 400 phe, evaluated for different Hadronness and Alpha cuts.

The energy of the primary γ-rays is derived from the shower image parameters. The number of phe in the shower image, expressed in the variable Size, is correlated with the shower energy and can by itself serve as an energy estimate. But the Čerenkov light density on the ground depends on the distance to the EAS maximum, changes in zenith angle, changes on the atmospheric conditions, etc. Or it can be that part of the signal may be lost due to leakage effects in the camera. All these factors might be taken into account in order to accurately determine the primary γ-ray candidate energy.

A more precise approach uses a slightly modified version of the RF algorithm. Instead of separating signal from background distributions, RF is trained to separate the population of events matching the simulated energy from those with a reconstructed energy outside a corresponding energy bin. The combination of image parameters determines the 'probability' of an event to belong to a given energy bin. The one with the highest 'probability' is selected. This approach yields an energy resolution in the order of $\sim$25% at the higher energies and $\sim$30% around the energy threshold.

4.2.9 Source position reconstruction

After the γ/hadron separation and energy reconstruction, for each original shower we associate a probability that it would be a γ event and an energy estimate. A further task is the determination of the source position in the sky. This is especially important in case the position of the source under study is uncertain (as e.g. in EGRET unidentified sources or in serendipitous searches) or in the study of the morphology of extended sources. In order to produce a non-correlated map of the sky in VHE γ-rays, a unique source position in the sky (also called *arrival direction*) has to be assigned to each event.

For each event the arrival direction of the primary in the sky is estimated by using the **Disp-method** [83]. The Disp method reconstructs the arrival direction of the primary γ-ray on an event-by-event basis. The arrival direction is assumed to lie on the major axis of the Hillas ellipse that fits the shower image in the camera at a certain distance (named Disp) from the image center of gravity (see Fig. 4.16). Shower images which are closer to the source position in the camera are more roundish, whereas showers which are further away are more elliptical. Thus the 'ellipticity' (defined as the ratio Width/Length) can be used to infer the position of the source of individual showers using a single IACT. Thus Disp can be parametrized as a function of the ellipticity [84]:

$$\mathrm{Disp} = \xi \cdot \left(1 - \frac{\mathrm{Width}}{\mathrm{Length}}\right), \tag{4.12}$$

where the parameter ξ has to be determined from a pure sample of γ events, i.e. from MC simulations.

For the MAGIC telescope data analysis, a more general parametrization has been adopted [85], which better describes the correlation between the shower elongation and the distance shower-CoG/source-position:

$$\mathrm{Disp} = A(\mathrm{Size}) + B(\mathrm{Size}) \cdot \frac{\mathrm{Width}}{\mathrm{Length} + \eta(\mathrm{Size}) \cdot \mathrm{Leakage2}}, \tag{4.13}$$

where A, B and η are second order polynomials on the logarithm of the image Size. Optimal values for these parameters are determined by minimizing the squared angular distance θ^2 between reconstructed and true direction of MC γ-rays from a point-like source (also known as γ-ray point-spread function PSF). Finally a correction to the Leakage parameter in the Length term is introduced to account for images truncated at the edge of the camera (similarly to the correction performed in CT1 HEGRA telescope [86]).

The reconstruction of the source position by means of the Disp parametrization is not univoque: it provides two possible primary origins along the major shower axis (named solution A and B in sketch Fig. 4.16). Images in the telescope camera carry some information about the longitudinal development of the shower in the atmosphere. The Asymmetry parameter

(which accounts for the charge asymmetry distribution in the image) or the M3Long (the third moment of the photoelectrons distribution along the major image axis, multiplied by the sign that defines the orientation with respect to the camera center) allows in most cases to determine the head-tail of a shower image.

The Disp method yields the arrival direction of the primary γ-ray in camera coordinates. By knowing the telescope pointing direction and the time, the camera coordinates can be converted to celestial coordinates [87]. A point-like source of γ-rays yields a reconstructed sky distribution of γ-candidates with can be fitted by a two-dimensional Gaussian.

The angular resolution is defined as the sigma of a two-dimensional Gaussian fitted to the brightness distribution (photons per solid angle) of a γ-ray point source in the center of the MAGIC camera. The reconstructed γ-ray PSF using the Disp method for the Crab Nebula source is about $\sigma_{2D} \sim 0.1^\circ$. This contains the contribution of the instrument pointing accuracy and the reconstruction accuracy of the Disp method itself.

In order not to bias the arrival direction calculation to any position, only source position independent image parameters are used in the RF training of the γ/hadron separation (e.g. Dist parameter cannot be used).

4.3 Signal evaluation and spectral reconstruction

4.3.1 Evaluation of the significance of a positive detection

The number of γ-rays is estimated as the number of events remaining after subtracting the Alpha distributions of the ON and OFF samples. γ-rays are expected to peak at low values of Alpha while the distribution of the background is flat. Hence, both distributions should agree for large Alpha values and may differ for low Alphas, if a signal is present.

The number of γ-rays is calculated from the number of ON events in the signal region N_{ON} minus an estimate of the number of background in the same region N_{bg},

$$N_{ex} = N_{ON} - N_{bg}\,. \tag{4.14}$$

N_{bg} is proportional to the number of OFF events in the same region, but has been normalized to the ON sample $N_{bg} = F_{norm} \cdot N_{OFF}$. For the analysis performed in this thesis the signal region is defined for Alpha below 6°. In case the analysis is performed with wobble data, the θ^2 variable is used instead of Alpha, and the signal region is considered below 0.03.

The normalization can be obtained from the ratio of the effective observation times $F_{norm} = \frac{T_{ON}}{T_{OFF}}$. But if during the ON and OFF observations the weather conditions and/or telescope performance vary slightly, this will lead to small differences in the distribution of their image parameters, and hence the efficiency of the cuts might be slightly different. In this case the normalization factor can be estimated by the ratio between the number of events located in the background region of the Alpha plot, i.e. from 30° to 80°: $F_{norm} = \frac{N_{ON}^{30^\circ<\alpha<80^\circ}}{N_{OFF}^{30^\circ<\alpha<80^\circ}}$. This only applies for ON/OFF data, but not for wobble data, where the relation between ON and OFF is fixed selecting how many OFF regions we consider (three in our case).

The significance gives the probability that a given excess may be due to a statistical fluctuation of the background. It is usually expressed as a number of standard deviations σ assuming that the distribution of the number of excess is Gaussian.

For the estimation of this significance, one can consider that ON and OFF data are two independent measurements, thus the variance of the excess will be

$$\sigma^2(N_{ex}) = \sigma^2(N_{ON}) + \sigma^2(N_{bg}) = \sigma^2(N_{ON}) + F_{norm}^2\sigma^2(N_{OFF}), \tag{4.15}$$

where fluctuations of ON and OFF samples are given from Poissonian statistics as $\sigma^2(N_{ON}) = \sqrt{N_{ON}}$ and $\sigma^2(N_{OFF}) = \sqrt{N_{OFF}}$. Then the standard deviation of the excess signal can be estimated as:

$$\sigma(N_{ex}) = \sqrt{N_{ON} + F_{norm}^2 N_{OFF}}. \tag{4.16}$$

And the significance will be the number of excess over its standard deviation:

$$N_\sigma = \frac{N_{ex}}{\sigma(N_{ex})} = \frac{N_{ON} + F^2_{norm} N_{OFF}}{\sqrt{N_{ON} + F^2_{norm} N_{OFF}}}. \tag{4.17}$$

However Li and Ma [88] made a critical examination of the methods that were used in the analysis of the γ-ray experiments to estimate the statistical significance of observations. They proved using MC studies that formula (eq. 4.17) overestimates the significance of a positive signal and proposed a new formula to correctly evaluate the significance:

$$N_\sigma = \sqrt{2}\left(N_{ON} \ln\left[\frac{1+F_{norm}}{F_{norm}} \frac{N_{ON}}{N_{ON}+N_{OFF}} \right] + N_{OFF} \ln\left[(1+F_{norm}) \frac{N_{OFF}}{N_{ON}+N_{OFF}} \right] \right)^{1/2} \tag{4.18}$$

In what follows equation 4.18 is used.

The analysis can also be quantified in terms of sensitivity. A common sensitivity unit for the different IACTs is the flux which is measured with 5σ significance in 50 hours of observation. This number is generally used to compare experiments. It is, however, not common to use eq. 4.18 to compute the sensitivity but instead a Gaussian approximation of it. The resulting number of standard deviations for a given observation time t is

$$\mathrm{Sens}(t) = \frac{N_{\mathrm{ex}}}{N_{\mathrm{bg}}} \cdot \sqrt{\frac{t}{T}}\,, \tag{4.19}$$

where T is the observation time and t is the normalization time[5].

4.3.2 Upper Limit calculation

If we analyze a source and no signal is observed for the devoted observation time, an upper limit to the flux emitted by the source with a certain confidence level CL $= 100(1-\alpha)\%$ can be established. In that case, the number of events measured in the telescope N^{obs} is zero on average, but the actual measured N^{obs} can be negative or positive.

The upper limit is obtained in two steps. First, given the hypothesis on the mean value of excess events μ_{ex} and background events μ_{bg}, the probability density function for observing N_{ex} is built. A second probability density function is constructed from this one to predict μ_{ex}, given the measured N_{ex} and N_{bg}. The latter is a non-trivial problem and various approaches have been proposed. One is the Bayesian approach of Helene [89], which assumes a uniform probability for the entire signal range.

Other is the frequentist approach, as developed by Feldman and Cousins [90] who proposed a prescription to construct a central confidence interval $[\mu^{\mathrm{low}}_{\mathrm{ex}}, \mu^{\mathrm{up}}_{\mathrm{ex}}]$. This method yields a correct *coverage*, as by construction, in a series of experiments the true mean value μ_{ex} is found in between the limits in $100(1-\alpha)\%$ of the cases (while the bayesian construction does in general not yield the correct coverage). An other advantage of this approach is the so-called *flip-flop* problem: in the Bayesian approach there is no guidance to obtain two-sided intervals instead of upper limits[6] while in the second approach the confidence intervals automatically become upper limits[7].

Rolke et al. [91, 92] generalized the method for extraction of unified confidence intervals in the presence of background and efficiency, with Binomial or Gaussian distribution (including a probability model for the background and the efficiencies). In the following we will use the Rolke method to extract the upper limits.

[5]Note that this definition does not take into account fluctuations of the uncertainty of the mean number of the background events and thus underestimates the sensitivity

[6]In practice it means that one has to decide a priori a significance level (e.g. 2σ) below which the upper limit will be calculated.

[7]If the lower value in the confidence interval $[\mu^{\mathrm{low}}_{\mathrm{ex}}, \mu^{\mathrm{up}}_{\mathrm{ex}}]$ is above zero, one sets the mean value as the measurement; if it is zero, the upper value in the interval becomes the upper limit

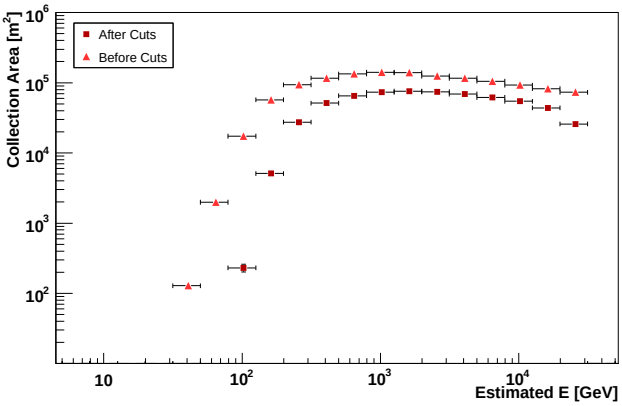

Figure 4.24: Effective area distributions as a function of the reconstructed energy before (orange triangles) and after (red squares) γ/hadron separation cuts. A Hadronness cut lowers the effective area since a fraction of the incident γ-rays are always lost.

4.3.3 Reconstruction of the energy spectrum

The energy differential spectrum is the number of γ-rays per unit energy, time and arriving at the Earth:

$$\frac{\mathrm{d}F}{\mathrm{d}E} = \frac{\mathrm{d}N_\gamma}{\mathrm{d}t\,\mathrm{d}A\,\mathrm{d}E}\,. \tag{4.20}$$

We will describe in this section the calculation of the effective detection area A from MC simulations, whereas the effective observation time t is calculated from the data. Afterwards, the effect of the instrumental energy resolution will corrected by an unfolding algorithm and finally source energy spectrum will be determined.

- The **effective collection area** is the area within which the MAGIC telescope observes a γ-ray event. It depends on the energy E of the incident particle and telescope's zenith angle ϕ. It varies with the trigger conditions and the analysis cuts. The effective collection area is computed from MC simulations as

$$A(E,\phi) = \frac{N_\gamma^{\mathrm{reco}}}{N_\gamma^{\mathrm{sim}}} \cdot A_{\mathrm{sim}}\,, \tag{4.21}$$

  where N_γ^{sim} is the total number of γ-ray events simulated in an area A_{sim}, and N_γ^{reco} are the number of γ-rays that trigger the telescope and pass all the analysis cuts. Figure 4.24 shows the effective collection area as a function of the estimated γ-ray energy for zenith angles between 32 and 45° (with a Size cut above 200 phe).

- The **effective observation time** is defined as the time within which the telescope was effectively recording events. Real detectors have a finite dead time during which they are not available for data acquisition and results in a loss of a fraction of events. The dead time is due to the fact that the readout chain of a detector may be busy with processing the data of an event while another event has occurred.

  The time differences of successive cosmic ray events follow a Poissonian distribution, and the probability distribution for the time differences should therefore exhibit an exponential behaviour. But as the dead time is not constant, the effective time is determined by a fit to the distribution of observed time differences between consecutive recorded air showers [93]

$$\frac{\mathrm{d}N}{\mathrm{d}t} \propto e^{-\delta t}\,, \tag{4.22}$$

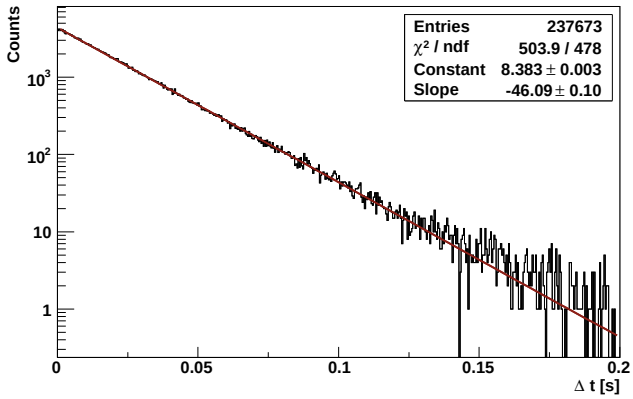

Figure 4.25: Distribution of time differences between consecutive air shower events (for size above 200 phe) for a sample of LSI +61°303 data on 26th December 2006. The effective observation time is determined by a fit to the exponential distribution.

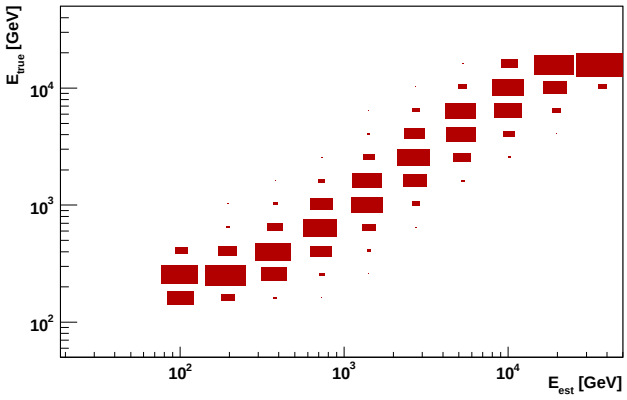

Figure 4.26: Simulated vs. reconstructed energy for MC γ-rays (migration matrix) after all data analysis cuts. This migration matrix corresponds to the LSI +61°303 data sample in campaign II for phase bin 0.6 to 0.7, with a Size cut of 200 phe.

where dN is the number of recorded shower arrival time differences in the time interval $[t, t + \Delta t]$ and δ is the average shower rate assuming a vanishing dead time (ideal detector). In order to yield the true shower rate, the fit has to be performed only for time differences much larger than the maximum dead time. The effective observation time is thus given by

$$t_{\mathrm{eff}} = \frac{N}{\delta}\,. \tag{4.23}$$

Figure 4.25 shows a distribution of the time differences of consecutive events above 200 phe for a sample of LSI +61°303 data. In total about 2.4×10^5 events are recorded. For larger time differences the rate is determined to be 46.17 ± 0.16 Hz, leading to an effective observation time of 5126 ± 20 s. This has to be compared to the time differences between run starts and stops of 5232 s, which yields a dead-time in the order of 2% of the total observation time.

- The number of γ-ray excess events is evaluated in bins of estimated energy of the primary γ-ray. The distribution of estimated energies E_{EST} is a convolution of the distribution true energies E_{TRUE} with the energy resolution function describing the detector response. The aim of the **unfolding** procedure [94] is to recover the original true

energy distribution from the measured one, by means of a resolution function which is determined from MC simulations. MC events have both the true and estimated energy. One classifies the events in nb and na bins of true and estimated energy respectively, and calculate the so-called *migration matrix*. The elements M_{ij} of the migration matrix can be interpreted as the probability that an event from the bin j of E_{TRUE} migrates to the i bin of E_{EST}:

$$M_{ij} = \frac{N_{ij}}{\sum_{k=1}^{na} N_{kj}} \quad i = 1, \ldots, na; j = 1, \ldots, nb\,, \tag{4.24}$$

where N_{ij} is the number of events in bin (i, j). An example of a migration matrix is given in Figure 4.26.

Different methods are used in the MAGIC experiment, to unfold the experimental energy distributions. They are described in detail in [94]. Used in this thesis are the Tikhonov, Bertero, Schmelling and Forward methods. We accept the unfolding results when the parameters obtained from the different approaches are consistent with each other.

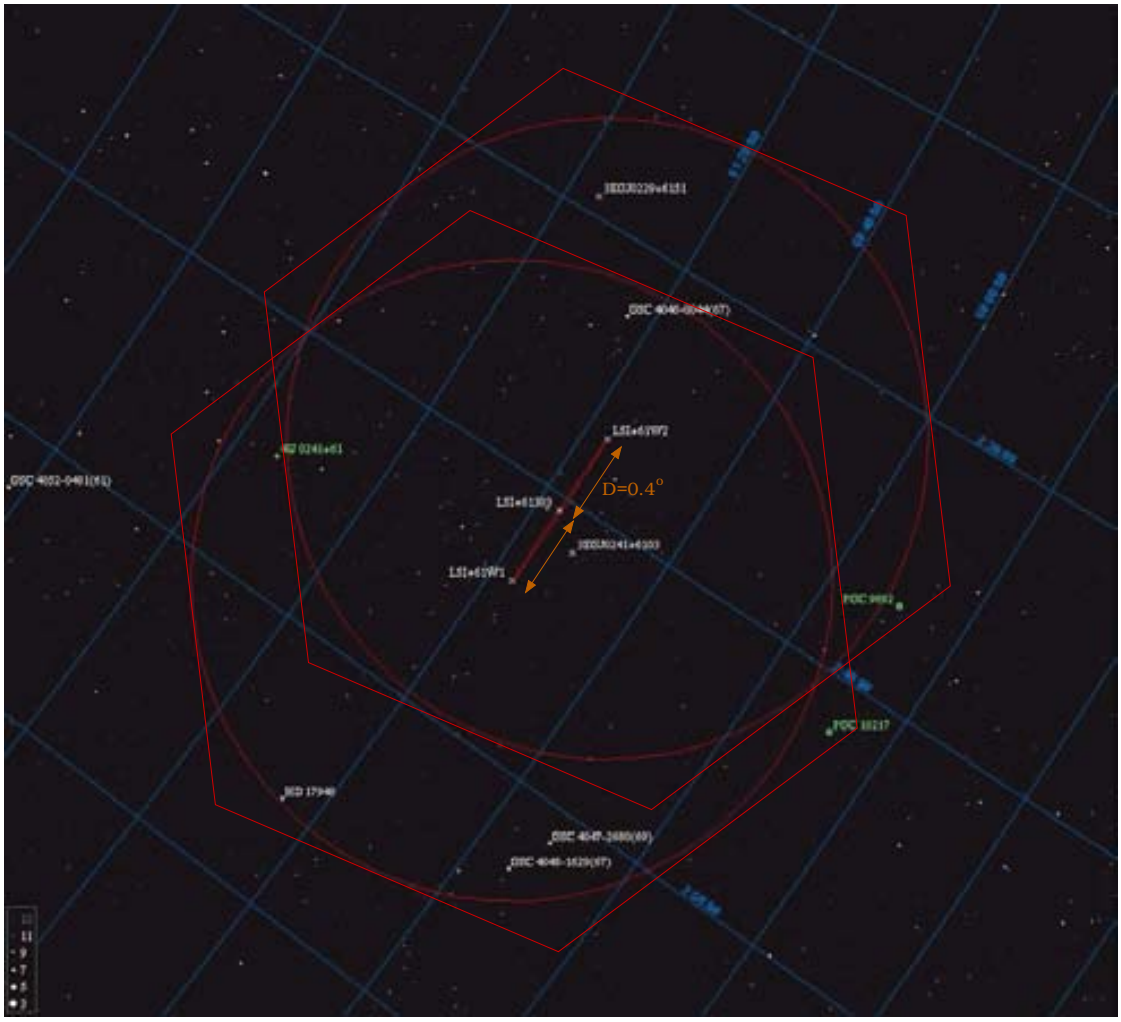

Figure 4.27: Field of view centered on LSI +61°303. Coordinate greed in blue correspond to RA and Dec. Both wobble positions located 0.4° away are labelled as LSI+61W1 and LSI+61W2. Sketches of the camera (with a FOV about 3°) pointing to the wobble positions are drawn in red.

4.4 Observation modes

4.4.1 On/Off and Wobble

One of the standard observation modes with Čerenkov telescopes is the so-called **ON/OFF mode** (as defined in the beginning of this Chapter). In this mode, dedicated observation time is needed for OFF observations. If the sample of OFF events is not large enough to correctly estimate the background, one can also use some ON data taken in similar conditions and where no significant γ-ray signal is detected. The ON/OFF mode was used for the first season of LSI +61°303 observations.

This mode of observations allows the maximum sensitivity (as the source is in the camera center) and helps to compensate the possible inhomogeneity effects on the camera (as ON and OFF samples are expected to show same inhomogeneities shapes). However, this mode requires additional observation time for OFF data, which will be close in time but not simultaneous with the ON; so the analysis is prove to systematic differences between the ON/OFF samples.

The other standard mode of observation used is the **wobble mode**, where the telescope does not track the source but two symmetric positions at a certain angular distance (W1 and W2), typically 0.4°. The telescope moves from W1 to W2 and back at regular time intervals, typically 20 minutes. The second LSI +61°303 data sample analysed in this Thesis was observed in this mode. Figure 4.27 show in a sky map the selected wobbles positions that were tracked.

In this method, the OFF events are extracted along with the ON events, from different regions in the camera that are geometrically equivalent to the source region in the camera plane. In the LSI +61°303 analysis, three background regions are used: the mirrored source position with respect to the camera center (named anti-source position) and positions perpendicular to the joining line source and anti-source (see scheme in Figure 4.28).

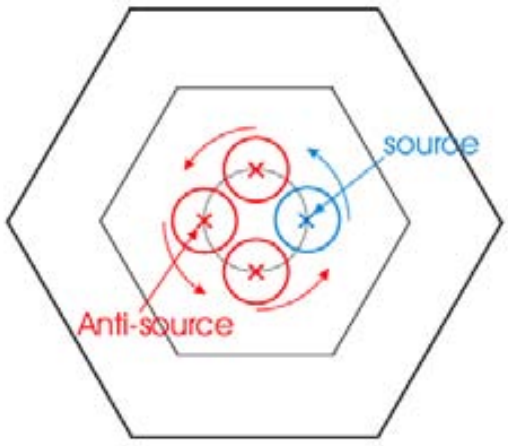

Figure 4.28: Wobble mode observation: The source and anti-source position are located opposite with respect to the camera center. The camera rotates due to the altitude-azimuth mount of the telescope. The blue region around the source defines the ON-region, whereas all three red regions are used for the background estimation. From [95]

Therefore the total observation time is shorter, and since the ON and OFF observations are strictly simultaneous, this allows a reliable background estimation independent of possible changes in observation conditions (as weather). However, an off-center observation is affected by the finite trigger region (about 0.9° radius) which results in a loss in γ-ray efficiency. This leads to a reduction of the sensitivity.

In wobble observations, a statistically independent definition of the ON and OFF data sample is necessary. The γ-ray signal in this case is usually evaluated using the θ^2 **analysis**.

For every event which survives the γ/hadron separation and cuts, the source position angular distance to the shower CoG θ (as defined in Sec. 4.2.4) are calculated using the Disp method (see Sec 4.2.9). An ON θ^2 plot is produced with respect to the source position. In addition, one can produce three θ^2 plots, one with respect to each of the three OFF-source positions. Note that the ratio between ON and OFF regions is 1 to 3, improving the estimation of the expected number of background events. The individual OFF θ^2 distributions are added together and scaled by 1/3 to be compared with the ON source θ^2 plot. To compute the significance of the signal, a cut in θ^2 is applied (instead of an Alpha cut, as for ON/OFF data).

4.4.2 Observations in presence of moonlight

IACTs normally carry out observations during clear, moonless night. But MAGIC telescope has been designed to operate also during moderate moonlight. This feature increases the duty cycle per year from $\sim$ 1000 to $\sim$ 1500 hours and allows a more uniform coverage of variable sources, such as LSI +61°303.

The PMTs in the MAGIC are operated with amplification gain around 3×10^4, which avoids high anode currents. The maximum moonlight illumination allowed in MAGIC corresponds to an anode current of 8 μA (in order to do not damage the last PMT dynode resulting in rapid ageing of the PMT). This permits observations in the presence of the Moon until (since) 3-4 days before (after) full Moon, for an angular distance to the Moon greater than 50° [96].

The increase in the LONS produced by the moon enhances the probability of accidental triggers. Therefore the trigger discriminator threshold (DT) is increased, ensuring a low rate of accidentals and keeping the total rate below the DAQ technical maximum rate ($\sim$ 500 Hz). But an increase of the DTs can affect the image parameters. In order to study this effect on the gamma-ray efficiency and the source detection sensitivity, we study a sample of Crab Nebula observations under different moonlight conditions.

Under moonlight conditions and high DT, the showers with low light content (low Size) have a lower probability to trigger the telescope, and the distribution of Size is depleted at lower values (see Fig. 4.29). However, showers with high Size values, up to 10^4phe, are also suppressed.

All other distributions of the Hillas variables (Length, Width, Conc) have similar shapes for events recorded either during dark or moonlight nights. This implies that, as these parameters have high discriminator power between gamma and hadron events, the γ/hadron separation will not degrade in moonlight data.

Below 200 phe the distributions are distorted by the different trigger threshold. A study of this effect can be found in [97] and [98]. For the LSI +61°303 analysis, we perform a Size cut of 400 phe, an thus the moonlight causes no effect on the threshold.

The moonlight effect is visible in the Dist parameter distribution of figure 4.29. For a Size cut of 400 phe and above, the showers get lost for large Dist ($> 0.8°$). But the difference disappear when only showers fully contained in the inner camera are displayed. This indicates that showers that are not fully contained in the trigger area are more sensitive to the increase in DT. Although a large shower is in principle above the trigger level, then Dist is large, an important fraction of the shower lies in the outer pixels, and the fraction of the ellipse included in the trigger area may not be large enough to fulfill the trigger condition.

Therefore the shower images are not distorted by the moonlight. But the performance of the telescope is modified for moonlight observations with respect to dark conditions, due to the increase of the DTs. Thus we can parametrize the dependence of the telescope response on the level of Moon illumination as a function of DT. For each of the Crab Nebula observation

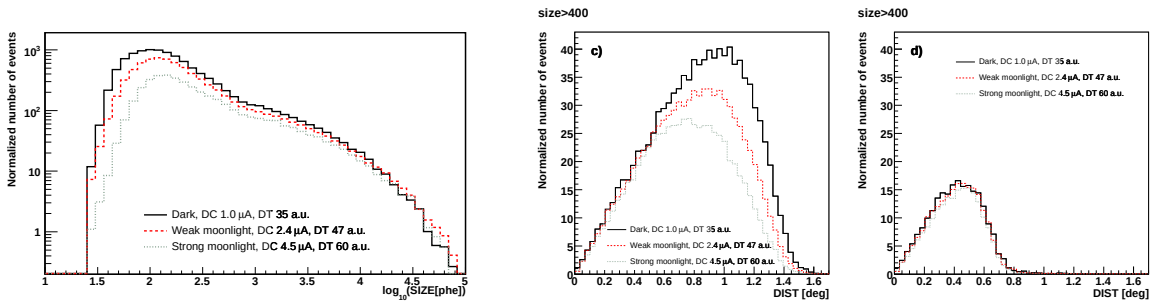

Figure 4.29: Distribution of Size (left) and Dist (middle) before analysis cuts for three Crab Nebula samples acquired under different moonlight conditions. Right panel shows the Dist distribution of the events fully contained in the camera. The histograms are normalized to the observation time and have a Size cut at 400 phe. From [98].

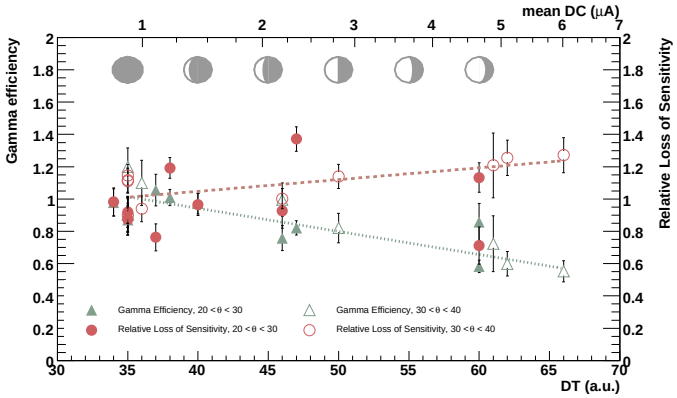

Figure 4.30: Effect of the moon observation for γ-ray efficiency (green dotted line) and sensitivity (red dashed line) for increasing DT and Size above 400 *phe*. The top axis shows the mean DC values and a schematic view of the moon light. From [98].

samples under different moonlight conditions we extract the γ-ray rate R, that are the number of excess events per unit time. The γ-ray detection efficiency with respect to dark observations is $\epsilon = R/R_0$, which depends linearly with the DT:

$$\epsilon = 1 - S_\epsilon(\mathrm{DT} - \mathrm{DT}_0)\,, \tag{4.25}$$

where S_ϵ is the efficiency loss rate and $\mathrm{DT}_0 = 35$ is the reference DT in dark observations. The results for Size above 400 phe are shown in Fig. 4.30. The fit parameters yield $S_\epsilon = (1.4 \pm 0.3) \times 10^{-2}$. This implies that the γ-ray detection efficiency is reduced with the moonlight brightness with a rate of 1.4% per DT count.

The MAGIC sensitivity in dark conditions s_0 above 400 phe is 2.5% of the Crab Nebula flux [99]. The relative sensitivity is given by

$$\frac{s}{s_0} = \frac{N^0_{\mathrm{ex}}\sqrt{tN_{\mathrm{bg}}}}{N_{\mathrm{ex}}\sqrt{t^0 N^0_{\mathrm{bg}}}}\,, \tag{4.26}$$

for a number of excess N_{ex} and background N_{bg} events in an observation time t (the upper index 0 refers to values for DT= 35). And depends also linearly with the DT

$$\frac{s}{s_0} = 1 - S_s(\mathrm{DT} - \mathrm{DT}_0)\,, \tag{4.27}$$

with a sensitivity loss rate $S_s = (6.3 \pm 1.6) \times 10^{-3}$ per DT unit. This gives for a high moonlight conditions e.g. DT= 60 a γ-ray detection efficiency of 65%, but the sensitivity decreases only 15% (from 2.5% to 2.9% of the Crab Nebula flux). This is due to the fact that signal and background rates both are equally reduced by an increase of the trigger threshold.

The efficiency loss rate and sensitivity also depend on Size and hence on the energy: the loss is larger for intenser camera illuminations mainly at low energy values. In order to understand this dependence, we perform the same study in different Size bins. We find that the efficiency and sensitivity can be parametrized as

$$S_\epsilon = (2.24 \pm 0.13) \times 10^{-2} - (7.2 \pm 1.2) \times 10^{-6} \cdot \mathrm{Size}\,[\mathrm{phe}] \tag{4.28}$$

$$S_s = (1.63 \pm 0.14) \times 10^{-2} - (7.4 \pm 1.8) \times 10^{-6} \cdot \mathrm{Size}\,[\mathrm{phe}]\,. \tag{4.29}$$

S_ϵ decreases as Size increases, since the probability of showers passing a higher trigger level is higher for larger images. And for lower Size, the sensitivity degrades with increasing DT.

For the LSI +61°303 analysis, we calculate the efficiency ϵ for the first and second campaign, since 17% and 22% of the data are taken under moonlight conditions, respectively. We

perform this correction in the integral flux in a day-by-day bases. There is no need to correct the spectra, since it will be dominated by the more significant flux levels measured in dark nihgts (see Sec. 6.5).

In February 2007, the MAGIC telescope DAQ was upgraded from a 300 MSamples/s FADCs to a fiber-optic multiplexing, using a 2 GSamples/s FADC. Although the analyzed LSI +61°303 data in the second campaign were recorded with the old system, during few months, both systems were operating together. The analog signals coming from the camera through the optical fibers were duplicated using optical splitters, to fed both setups. This caused a shift in the value of the discriminator threshold of 2.5 factor. Therefore the efficiency rate is written as

$$\epsilon = 1 - (3.5 \pm 0.8) \times 10^{-2}(\mathrm{DT} - 15.5)\,, \tag{4.30}$$

for a Size cut above 400 phe.

4.5 Systematic errors

In addition to statistical errors the γ-ray flux (and thus the spectrum) and source position are affected by systematic uncertainties. The most important systematic effects are the following [40]:

- **Atmospheric conditions and atmospheric model**: In the MC simulations a standard model for the atmosphere and the Elterman model [100] for the distribution of aerosols and ozone have been used. Microclimate conditions at La Palma and weather seasonal or daily variations (as humidity, temperature, high clouds, haze, calima[8]) may produce atmosphere transmission changes but are not taken into account in the simulation and may lead to an underestimation of the shower energy. The systematic effect on the energy scale is therefore estimated to be 15% [101].

- **Systematics from the hardware**, mainly due to the following items:

  - Reflectivity of the mirrors. The assumed mirror reflectivity is 85%, although worsens when dust accumulates and due to aging. The estimated uncertainty is 5% in the γ-ray energy estimation.
  - Quality of the optical PSF. The simulated optical PSF has a Gaussian shape with $\sigma = 15$ mm. The estimated uncertainty is 5% in the γ-ray energy estimation.
  - Photon losses on the camera entrance. Both camera plexiglas and Winston cones may also suffer from dust. The estimated uncertainty is 3-5% in the γ-ray energy estimation.
  - Light-to-photoelectron conversion has been estimated to have a systematic error of 5-10% in the energy estimation; this uncertainty is mainly due to the uncertain in light collection efficiency of the first PMT dynode.
  - Trigger inefficiencies, which affects flux and energy estimation up to 20% for energies below 150 GeV; it is lower at higher energies and reaches 5% at about 1 TeV.

- **Analysis chain**:

  - The calibration chain using the F-Factor method introduces a systematic error of 8% [71] in the energy estimation.
  - Errors in the estimation of the effective observation time, due to dead times of the system which are not considered in the analysis. It yields a systematic error of 2% in the γ-flux estimation (independent of energy).
  - Differences in the analysis details (signal extraction, cleaning, γ/hadron separation, unfolding) lead to a systematic error of 3% [102]. And possible software bugs are assumed to be about 3% in a conservative approach.

[8] Calima is fine dust or sand blown from the Sahara Desert.

- **Agreement between Monte-Carlo and Data**: Possible differences between simulated and real showers may lead to an error in the effective areas, affecting both the energy and flux level. It is estimated to be 10%.

The overall systematic error on the energy scale is 16%. Depending on the spectral slope of the γ-ray source, the error on the flux differs. Assuming a slope of 2.5, the error on the flux is about $-30 + 50\%$ (for a steeper slope, the effect is larger, up to $-50 + 100\%$ for a 4.0 slope). The influence of the systematic errors on the spectral slope is conservatively estimated to be 0.2.

The systematic error of the position (and therefore morphology) determination is dominated by the 2' telescope pointing accuracy.

Chapter 5

LSI +61°303: physical and phenomenological description

In this chapter we review the properties of the galactic binary LSI +61°303, as deduced from observations in different wavelengths, from radio to X-ray. Two different scenarios have been proposed to account for the broadband emission: the microquasar model, where relativistic jets are powered by a compact object via mass accretion from the companion star, and the colliding wind model, where the pulsar wind, powered by the rotation of a neutron star, interacts with the companion star wind. In both cases, very high energy γ-rays are expected.

5.1 X-ray binaries

An X-ray binary is a binary system which is very bright in X-rays. It contains a compact object, neutron star (NS) of stellar-mass black hole (BH).

X-ray binaries are divided in two main classes depending on the mass of the companion star:

High Mass X-ray Binary, HMXB If the companion has a mass above $5M_{\odot}$, it is assumed that large scale mass transfer has occurred in the system before the supernova (SN) explosion: the initially more massive star evolves faster and reaches the end of its life first, becoming a red giant, filling the Roche lobe and allowing the smaller companion to accrete from it. Then the red giant explodes in a SN leaving behind either a NS or a BH. This can disrupt the binary system, but if the SN progenitor star was less massive than its companion at the moment of the explosion, the systems will remain linked, though the orbits may be more eccentric. In most HMXB systems the companion results in a rapidly rotating star, of spectral type O or B which transfers mass to the compact object. This transfers occurs via decretion disk (Be stars) or via strong wind or Roche lobe overflow. The accreted material heats up because of friction producing the X-ray emission.

Low Mass X-ray Binary, LMXB In this scenario the compact object is a NS or BH, and the companion is a low mass , $5M_{\odot}$ star. The optical companion is usually a late spectral type (K, M) and the mass transfer on to the compact object occurs only through Roche lobe overflow. This mass transfer can spin up a NS so that it becomes a millisecond pulsar, spinning hundreds of times a second [103]. LMXBs tend to emit X-rays in bursts and transients, and usually have softer X-ray spectra than HMXBs.

Binaries containing a white dwarf and a low-mass companion are not referred to as LMXBs even though they are X-ray sources. Instead, they are classified as cataclysmic binaries, because they show very large variations in their brightness, such as nova events, and are weaker X-ray sources than binaries containing neutron stars or black hole candidates.

Figure 5.1: Examples of typical HMXB and LMXB. From [106].

There are different theories to account for the origin of LMXBs. One of the scenarios assumes first the formation of a NS or BH, which afterwards couples with its companion in a capturing process. The LMXB formation may also take place through helium star SNe in binary systems that have each emerged from a common-envelope phase. The reader is referred to [104] and [105] for a detailed revision of LMXBs evolution.

A schema illustrating a typical HMXB and LMXB is shown in figure 5.1.

Up to now, 299 accreting X-ray binaries have been catalogued in the Galaxy are 114 HMXBs and 185 LMXBs [107, 108], but only 65 of them are radio emitting sources (9 HMXBs and 56 LMXBs) [109]. Some (∼20) of these radio emitting sources show a relativistic jet and are called microquasars.

Microquasars [110] are stellar-mass compact objects in our Galaxy that mimic, on a smaller scale, many of the phenomena seen in quasars. They combine two relevant aspects of relativistic astrophysics: an accreting compact object which is identified by the production of hard X-rays and γ-rays from surrounding accretion disks, and relativistic jets of particles that are observed by means of their synchrotron emission (in radio wavelengths).

Some of these sources were widely observed in all wavelengths, such as the LMXBs Circinus X-1 or GRS 1915+105 and the HMXBs Cyg-X3, Cyg-X1, LS 5039 or SS 433. Although all of them are classified as microquasars, there are some physical properties that make them individually interesting, depending on the nature of the compact object, the display of superluminal velocities, the periodicity of the radio emission, etc. A compilation of the properties of the microquasars in our Galaxy can be found in [111].

On this thesis we will focus on the radio emitting HMXB LSI +61°303. Although it has been classified as a microquasar, the presence of relativistic jets is still unclear; we will discuss on the proposed emission scenarios for this source in Sec. 5.5. In section 5.6 we will review binary objects similar to LSI +61°303, that have been classified as γ-ray binaries.

The properties of LSI +61°303 in the optical, infrared, radio and X-ray spectra will be reviewed in the following section.

5.2 Optical observations and the nature of the objects in the system

Already back in 1981, Hutchings & Crampton [112] performed ultraviolet (UV) spectroscopy of LSI +61°303 and showed that the companion is a rapidly rotating B0-B0.5 main-sequence star, with a stable shell. For a Be star of B0 V spectral type the typical effective temperature is $T_{\rm eff} \sim 26000$K and the radius $R \sim 4.7 \times 10^{11}$ cm. At a distance of 2.0 ± 0.2 kpc [113, 114, 115], this yields a bolometric luminosity of $L = 4\pi\sigma T_{\rm eff}^4 \sim 10^{38}$ erg sec^{-1}, where σ is the Stefan-Boltzmann constant. The optical spectrum is that of a rapidly rotating star, with an equatorial disk and mass loss.

Casares et al. performed in 2005 [116] a spectroscopical study of LSI +61°303 and measured the projected rotational (or Doppler) velocity $V \cdot \sin i \sim 113$ km s^{-1}, where i is the inclination of the orbital phase. Although this value is about 3 times smaller than what reported by

Parameter	Hutchings & Crampton 1981	Casares et al. 2005	Grunsdtrom et al. 2007
orbital eccentricity e	0.60±0.13	0.72±0.15	0.55±0.05
periastron phase $\phi_{\rm peri}$	0.25±0.04	0.23±0.02	0.301±0.011
mass function $f(M)$	0.019±0.015 $M_\odot$	$0.0107^{+0.0163}_{-0.0077}$ $M_\odot$	0.011±0.003 $M_\odot$
radial velocity $V \cdot \sin i$	360 km s^{-1}	113 km s^{-1}	104±5 km s^{-1}
companion star radius R_s	6.7±0.9 $R_\odot$		
inclination i	10-60^o		
companion star mass M_s	10-15 $M_\odot$		
compact object mass M_X	0.01-3.2 $M_\odot$		

Table 5.1: Summary of LSI +61°303 orbital parameters. Left column values are from 1981 [112], middle column are from 2005 [116] and right column are from 2007 [117] measurements. Fifth row is the star radius from the spectral classification [118]. Last three rows give the allowed inclination and mass ranges.

Hutchings & Crampton in 1981 [112] ($V \cdot \sin i = 360 \pm 25$ km s^{-1}), the instrumental resolution in the 2005 measurement is higher (83 versus 130 km s^{-1}), which would favour the latest determination. Recently in 2007 Grunsdtrom et al. [117] presented a new Hα study and measured a rotational velocity of 104 ± 5 km s^{-1}. These authors argue that the measurements for the rotational velocity are affected by weak emission in the line wings that make the absorption cores appear narrower. This then can reconcile these results with those performed in 1981.

Table 5.1 summarizes the most important orbital parameters of LSI +61°303 as reported in the three publications.

As the stars in the binary system rotate around their common center of gravity, they approach and recede in the line of sight. This motion shows up in their combined spectra as a regular oscillation of the spectral lines. If only spectral lines from one component can be seen, one can only measure the orbital period P and the projected semi-major axis $a \sin i$. By combining Newton's laws of gravitation and motion one can derive the relation between the the masses of the two components through the *mass function*

$$f(M) = \frac{4\pi^2 (a \sin i)^3}{GP^2} = \frac{(M_X \sin i)^3}{(M_X + M_s)^2} \tag{5.1}$$

where M_X and M_s are the masses of the compact object and the companion star respectively and G is the Newton's gravitational constant. For LSI +61°303 the mass function is $f(M) = 0.0107^{+0.0163}_{-0.0077}$ $M_\odot$ [116].

The mass function provides a lower limit to M_X, corresponding to a zero-mass companion $M_s = 0$ viewed at the maximum inclination angle $i = 90°$: $M_X > f(M)$. The upper limit to the NS mass is 3.2 $M_\odot$, obtained from the most extreme equation of state that produces a NS [119]. This means that the determination of the inclination and companion mass is mandatory to determine the type of the compact object.

The mass of the optical companion can be inferred from its atmospheric properties (see e.g. [112, 120]) yielding a mass range $M_s = 10 - 15$ $M_\odot$. With this constraint, the compact object would be a NS for inclinations $i > 25°$ and a BH otherwise [116].

An independent method to constrain the inclination is by means of the rotational velocity. The critical rotation velocity of the companion star of LSI +61°303 would be about 500-550 km s^{-1} and the Be stars usually rotate at a velocity that do not exceed 0.9 of the critical one [121], yielding an inclination angle $i \gtrsim 10 - 15°$. Recent observations indicate that Be stars rotate at $\simeq 0.7 - 0.8$ of the critical velocity [122], which would give an inclination of the orbit about $15 - 20°$. This inclination would imply that the compact object is a BH. If we use the previous rotational velocity measured by [112] of 360 ± 25 km s^{-1}, the inclination constraint is $i > 50°$, in agreement with an NS nature of the compact object.

On the other hand, the lack of clear shell lines in the UV spectra points to an upper limit of $i \leq 60°$ [116].

Finally, as pointed out by Zdziarski et al. (2008) [123], all other Be binaries known to date have NS companions. The reason may lie in the evolution of such systems. The fast rotation, which is characteristic of Be stars may be achieved during a period of Roche-lobe overflow mass transfer from its (initially) more massive companion onto a B star (see Sec. 5.1). However, the companion loses most of its mass in the process and becomes a He star with a mass of only a few $M_\odot$. When it later explodes as a SN it usually gives rise to a NS (see [124] and references therein).

And as considered by Zhang and colleges (2004) [125], Be/BH binaries have also been predicted to form when the progenitor star has a mass higher than 20 $M_\odot$. However it is not yet clear how Be stars eject the circumstellar envelope and which effect on the production of the dense disk have the physical properties of the donor star (as metallicity, instabilities in the photosphere). However, Be/BH systems should exist in our Galaxy, according to population synthesis studies [126]. They are expected to be highly eccentric narrow systems, with orbital periods of a few days. The Be/BH binaries may haven not been observed due to a selection effect. The interaction of the two stars leads to a very effective truncation of the decretion disk around the Be star, and the system would have a very low X-ray luminosity.

Ultraviolet and infrared observations of Be stars show that their stellar wind has two components: a fast, polar outflow with properties typical of radiatively-driven winds and approximately isotropic; and a slow equatorial outflow forming a thin decretion disk [127]. The disk appears to be viscous and nearly Keplerian[1], with a radial velocity much smaller than the rotational one. The optical and Hα emission of the disk is modulated. The optical modulation in the V-band was discovered in 1989 [128]. There is a well established record of variations in the emission line over the past decade [129, 130, 131]. A 26.5 day period is found in the Hα emission line, in connection with the orbital motion of the compact object (see Sec. 5.3). Paredes et al. (1994) [129] also found evidence for a $\sim$4 yr modulation in the Hα line (later confirmed by e.g. [130, 132]), that could be a result of

- variations in the mass loss rate of the Be star, and/or
- density variability in the circumstellar disk, or
- precession of the Be star (this requires some constrains in the inclination angle $i > 60°$ and the precession angle $\chi > 6°$ [133]), or
- quasi-cyclic star Be envelope variations, or
- precessing relativistic jet (see Sec. 5.3.2), or
- variability in the size of the circumstellar disk.

Those measurements also indicated that the circumstellar disk in LSI +61°303 is among the densest of Be stars. The orbital and superorbital periods are also detected in radio wavelengths, and will be discussed in the next Sec. 5.3.

A modulation with the orbital period is also observed [130]. This has been interpreted an effect of the propagation of global density waves in the circumstellar disk [134], which makes the disk not axially symmetric.

The size of the decretion disk can be measured by the Hα equivalent width. Recent measurements [117, 132] yield an Hα equivalent width $EW_{H\alpha}$ that varies from -6 to -18Å. In Keplerian disks, the $EW_{H\alpha}$ correlates with the velocity difference between the blue and

[1] A Keplerian accretion disk does not have sufficient mass to be self-gravitating and spins in a gravitational field that is set by the object at its center. Its rotation is given from Kepler's law of orbital motion. The gas in the disk orbits in a circle. The time to complete one orbit is proportional to the radius to the 3/2 power. The structure of the disk is determined by the temperature, which can be related to the accretion luminosity, which is the maximum power that can be generated from material falling onto the central object.

red peaks of the Hα line ΔV which is related to the disk outer radius $R_{\rm out}$ and the stellar radius R_s by the following relation [135]

$$\frac{\Delta V}{2v\sin i} = \left(\frac{R_{\rm out}}{R_s}\right)^{-1/2} . \tag{5.2}$$

The disk size is then found to vary about $(4-7)$ R$_s$. The circumstellar disk of the Be X-ray binaries have outer radii limited by the closest approach of the companion in the high eccentric systems and by resonances between the orbital period and the disk gas rotational periods in the low eccentric systems [136]. LSI +61°303 has an orbit eccentricity that falls between these two cases. The expected disk truncation radius due to resonances with the orbital motion for LSI +61°303 is estimated to $(5.1-5.5)$ R$_s$ [117], where the radius of the companion star from spectral classification [118] is $R_s = (6.7\pm0.9)R_\odot \simeq 0.47\times10^{12}$ cm.

Some parameters of the circumstellar disk can be derived from the observed infrared excess [137]. The model used to interpret the IR curves assumes an isothermal equatorial disk envelope emitting both IR free-free and free-bound radiation [127]. Assuming temperature disk of $T_D \sim 17500$ K and a half opening angle of $\theta = 15°$, the disk density distribution can be described as a power law

$$\rho_D(r) = \rho_0(r/R_s)^{-n} , \tag{5.3}$$

where r is the distance from the primary Be star center, $\rho_0 \sim 10^{-11}$ g cm^{-3} the estimated stellar surface envelope density and $n = 3.2$ the power law index. The corresponding stellar mass loss rate $\dot{M}_D$ is given by

$$\dot{M}_D = 4\pi R_s^2 \rho_0 v_0 \sin\theta , \tag{5.4}$$

where v_0 is the velocity of the envelope flow at the star surface, which is a rather uncertain parameter. Martí & Paredes (1995) [137] assumed values between 2-20 km s^{-1}, although others authors favored lower values $v_0 << 1$ km s^{-1} [138]. Despite this and the uncertainties in θ, the estimated equatorial mass-loss rate is about $\dot{M}_D \sim 10^{-8}$ M$_\odot$ yr^{-1}. The velocity of the circumstellar disk outflow, within $\sim 10R_s$ is less than few km s^{-1}.

The polar outflow is a radial, lower density and fast wind, whose parameters have not been measured for LSI +61°303. A general estimates from Waters et al. (1988) [127] are $\dot{M}_\odot \sim 10^{-8}$ M$_\odot$ yr^{-1} and rapid wind velocity $v_D \sim 10^3$ km s^{-1}.

The orbit is inferred to be quite eccentric, with eccentricity estimates from $e = 0.72 \pm 0.15$ [116] to $e = 0.55 \pm 0.05$ [117] With this high eccentricity, an important parameter is the orbital phase of the periastron passage[2]. For a given observation time the orbital phase is determined as

$$\phi = \left(\frac{t-T_0}{P}\right) - \text{integer part}\left(\frac{t-T_0}{P}\right) , \tag{5.5}$$

where P is the orbital period (accurately measured from radio observation, see below Sec. 5.3) and $T_0 =$ JD2443366.775 is the time which corresponds to $\phi = 0$. To dates back to the first radio detection of the system [139]. The periastron phases are found to be $\phi = 0.23 \pm 0.02$ and 0.301 ± 0.011, from the radio measurements in [116] and [117], respectively.

To estimate the distance between the two stars, it is necessary to make some assumptions. The third Kepler law yields the semi-major axis a for a known period P:

$$P^2 = \frac{4\pi^2 a^3}{G(M_s + M_X)} \tag{5.6}$$

If we consider a mass for the Be star of 12.5 M$_\odot$ and a NS compact object of 1.5 M$_\odot$ and period of 26.5 days, the semi-major axis is $a \simeq 6.3\times10^{12}$cm $\simeq 0.5$ AU. The maximum and minimum distances between the stars, named the apoapsis and periapsis, are given by

$$r_p = a(1-e) \quad \text{and} \quad r_a = a(1+e) . \tag{5.7}$$

[2]the points in the orbital motion of a binary star when the two stars are closest or furthest to one another are called periastron and apastron.

Then, the separation at periastron and apastron will be $r_p \simeq 2.8 \times 10^{12}\text{cm} \simeq 6R_s$ and $r_p \simeq 9.7 \times 10^{12}\text{cm} \simeq 21R_s$, respectively. Thus the radius of the truncation disk is comparable in size to the distance between the two stars at periastron, and the compact object could directly interact with the disk around periastron (if the circumstellar disk reached its maximum size at the same time).

5.3 Radio and X-ray observations

Numerous radio and X-ray observations have been performed on LSI +61°303 over the last three decades. In this section we review the time, spectral and morphological features of the radio and X-ray emissions.

5.3.1 Time and spectral features

The most peculiar characteristic of LSI +61°303 are its periodic radio outbursts with a period $P_1 = 26.496 \pm 0.0028$ days [140] which is generally attributed to the orbital period. This radio activity was first noticed by Gregory & Taylor in 1978 [139] and since then, it has been extremely monitored.

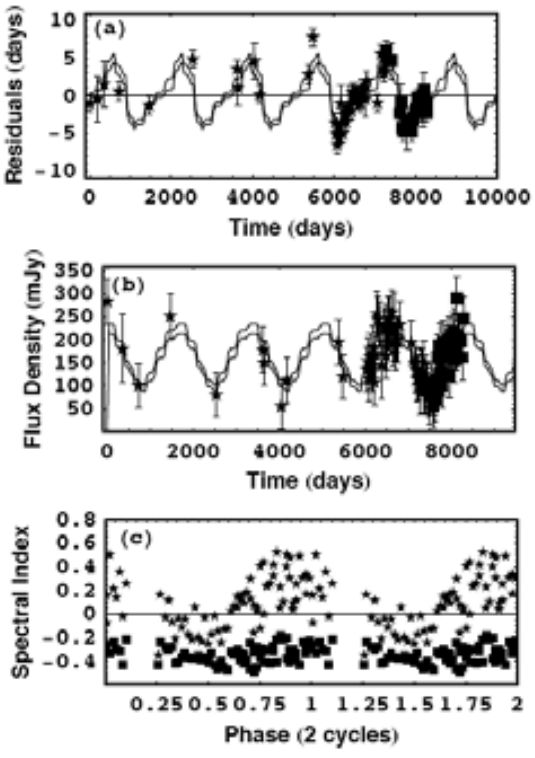

Figure 5.2: Top and Middle: modulation of the timing residual (i.e. difference between the observed and predicted outburst time) and peak flux vs. time (in JD measured from T_0). Bottom: tow spectral index statistics vs. P_2 phase. From [140].

The amplitude of each outburst is also modulated with a periodicity of ~ 4.5 years [141]. Phase, peak flux and spectral index modulations with the radio period P_2 are shown in Fig. 5.2.

An analysis over 20 years of radio observations (5-10 GHz) confirmed the existence of a periodic or quasi-periodic modulation of the radio outburst peak flux with a mean period $P_2 = 1667 \pm 8$ days [142, 140]. In what follows we will use Φ to refer to the phase of the superorbital P_2 period and ϕ to the phase of the orbital period P_1. The peak flux density reaches its minimum at $\Phi \sim 0.45$ and its maximum at $\Phi \sim 0.05$.

The orbital phase at which the radio outbursts occur also modulated [143] with P_2. The peak of the radio emission in each orbit occurs somewhere in the orbital phase range $\phi = 0.4 - 0.9$: for $\Phi \sim 0.6$ the radio outburst occurs at orbital phase $\phi \sim 0.4$, and as the cycle continues, the outburst are progressively delayed, reaching $\phi \sim 0.9$ for $\Phi \sim 0.4$. According to this superorbital period, LSI +61°303 displays the so-called *active* and *quiet* radio variability states, as shown by Paredes et al. (1990) [144] radio measurements (at 8.4 GHz) shown in Fig. 5.3. We also show, in the same figure, two samples of the 8.4 GHz historical data archive from the Green Bank Interferometer (GBI), which illustrate the weak and strong variability phases of the orbital period.

The radio spectral index also exhibits a marked evolution with the Φ phase. The maximum positive spectral index (between 2-8 GHz) exhibits a rise at $\Phi \sim 0.6$. For most of the outbursts the spectrum is consistent with $\Gamma = -0.45$.

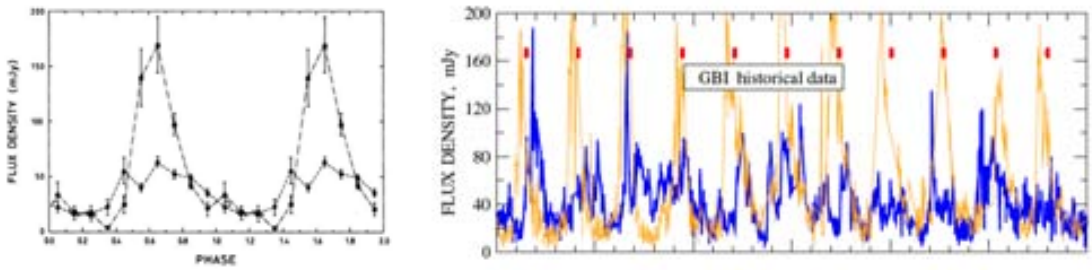

Figure 5.3: Left: Average radio lightcurves for the active (dot-dashed) and quiet phases (dashed), corresponding to epochs near the maxima and minima of the P_2 modulation, respectively (from [144]). Right: Two separate pieces from historical GBI data at 8.3 GHz, demonstrating both the weak (in blue) and strong (in yellow) variability of the LSI +61°303 orbital cycle (from [115]) The short vertical red bars show the phase of 0.7, where the radio peaks on average.

Short radio term variability has been also observed in the Very Large Array (VLA) radio monitoring (at 5 GHz) data [145]. Small amplitude (~ 4 mJy) radio flares have been detected with a possible recurrence period of 1.4 hours. The microflares were observed when the source was decaying from a bright flux level, possibly the peak of the radio outburst.

A faint X-ray counterpart to LSI +61°303 was identified by Bignami et al. (1981) [146] with the Einstein satellite, with a flux constant within 30% of 2×10^{-12} erg cm^{-2}s^{-1} in the $0.2 - 5$ keV energy range. However, the detection was based only in two observations (at phases 0.4 and 0.6) taken several cycles apart. A number of X-ray observations have followed:

- Early ROSAT observations [147] reported the detection of X-ray variations by a factor of 3 within 5 observed days, with an average X-ray flux of 4×10^{-12} erg cm^{-2}s^{-1} in the 0.1-2.4 keV range. The fitted power law spectrum gave a photon index $\Gamma = 1.1 \pm 0.3$ and absorption $N_H = 4.7 \pm 0.8 \times 10^{21}$ cm^{-2}.

- Subsequent ROSAT observations [148] were performed over a total orbital cycle in the energy range 0.07-2.48 keV. The spectral energy distribution was fitted to a power law with $N_H = 0.84 \times 10^{21}$ cm^{-2} and index $\Gamma = 2.00 \pm 0.14$. Simultaneous radio observations at 4.9 GHz were performed with the VLA. Both the radio and X-ray emission exhibit changes in flux by a factor 10 within one orbital period. Moreover, the time of the emission peak differs by ~ 0.5 in phase (Fig. 5.4). The maximum flux in X-ray was found for phase 0.48. There is a suggestion of hardening of the X-ray emission at the peak X-ray flux.

- The ASCA satellite reported two pointed X-ray observations [150]: one for orbital phase 0.23, which showed a photon index in the range $\Gamma = 1.63 - 1.78$ and a second one for 0.47, with $\Gamma = 1.75 - 1.90$, in the 2-10 keV band. Radio simultaneous observations driven by the GBI interferometer at 2.5 and 8.3 GHz [151] reported a radio maximum at phases $\phi \sim 0.5 - 0.6$. These authors performed a short-term periodicity analysis of the two ASCA observations: the first pointing at lower phases is consistent with no variability on any time scale, whereas during the second pointing the source varies by $\sim$50% on time scales of 30 minutes.

- Two different analyses have been applied to 11 pointed RXTE observations in the 2-25 keV band. Harrison et al. (2000) [151] confirmed the modulation of the X-ray emission with the orbital period. They found a significant offset between the peak of the X-ray and radio flux, by comparing simultaneous observations with GBI (at 2.23 and 8.3 GHz) and Ryle Telescope (at 15 GHz) over an entire orbital cycle. As seen in Fig. 5.4 the X-ray emission peaks almost half an orbit before the radio. In the RXTE data no high frequency signals (range 0.01-500 Hz) were found, failing to

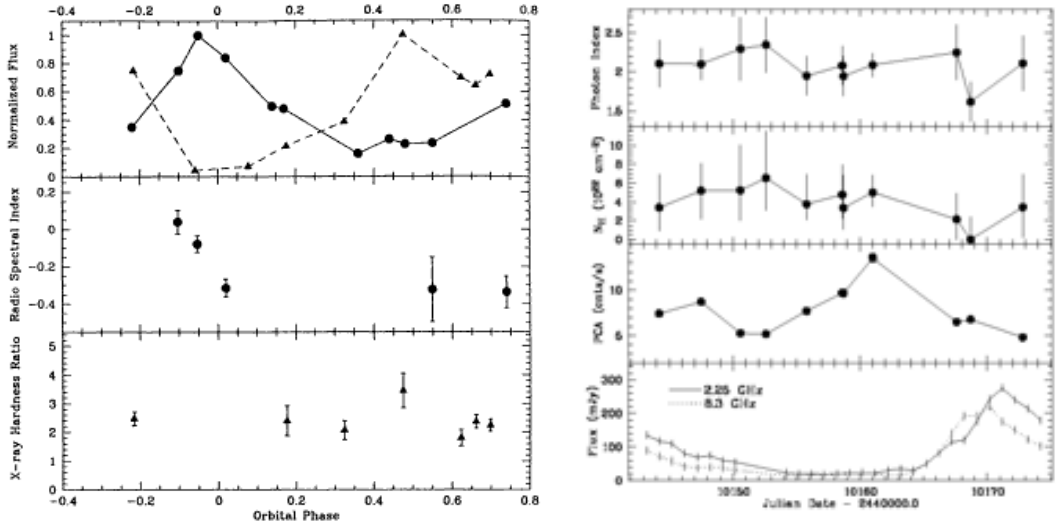

Figure 5.4: Left panel from top to bottom: the VLA radio flux density (solid line) and X-ray ROSAT flux (dashed line) as measured by [148], normalized to the peak flux; the radio spectral index (between 4.9 and 1.5 GHz) and the X-ray hardness ratio (between 0.1-2.48 and 0.07-1.0 keV). Right panel from top to bottom: the X-ray spectral index and absorbing column, the count rate in the RXTE instrument (from 2-25 keV) and the radio flux as measured by the GBI. From [149].

detect X-ray pulsations that would point to the presence of a young NS. Greiner & Rau (2001) [149] calculated the photon index around the orbit, as seen in Fig. 5.4. For 10 of the 11 pointings around the orbit, the spectra above 20 keV are consistent with being constant over a time interval of 30 days, with no spectral break, and with power law mean fit values of $\Gamma \sim 2.1$ and $N_H \sim 4.3 \times 10^{22}$ cm^{-2}. Only one point, at phase 0 and simultaneous with the onset of a radio outburst, showed a flat power law photon index of 1.6.

- Paredes and collaborators (1997) [152] carried out a periodicity analysis using the data in the 2-10 keV band provided by ASM on board RXTE [152]. The X-ray emission level appears to vary by a factor ~ 5. The X-ray outbursts in LSI +61°303 are very likely to be modulated by the orbital motion. A period 26.7 ± 0.2 d was derived from these data. The X-ray peak, which is wider and spans longer than the radio peak, is shifted with respect the radio outburst by a few days. Recently, and by folding INTEGRAL (IBIS/ISGRI) and ASM data, the soft and hard X-ray peak were found to be simultaneous, allowing the estimation of the X-ray maximum at phase ~ 0.55 (in the 1-100 keV band) [153].

- A study of LSI +61°303 in the 0.5-100 keV energy band with XMM-Newton and INTEGRAL [154] showed that the spectrum of the source is well fitted by a simple power-law, without any signature of a high-energy cut-off. In agreement with previous observations, the 2-10 keV flux during XMM-Newton observations was variable with phase: rather low near phase $\phi \sim 0.2$ and about 3 times higher at phases larger than 0.5. Figure 5.5 shows the dependence of the INTEGRAL (20-60 keV) and XMM-Newton (2-10 ad 0.5-2 keV) fluxes on the orbital phase. Comparing data from different years, X-ray lightcurves seem to vary in a more regular way than radio lightcurves. The X-ray spectrum is hard (photon index $\Gamma \sim 1.5$) in the orbital phases corresponding to high and low X-ray states and soft ($\Gamma = 1.78 \pm 0.04$) during the transition from high to low state (at phase $\phi = 0.01$).

- Deep XMM-Newton observations in the 0.3-12 keV band (January 2005) [156] showed

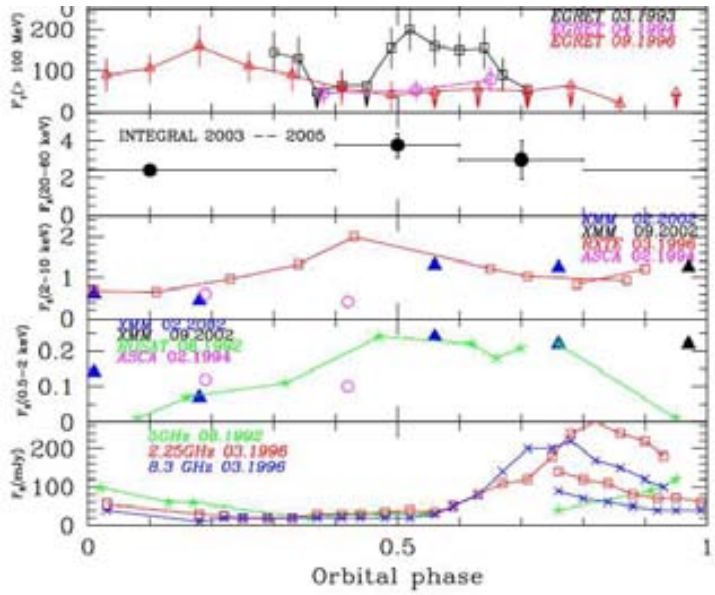

Figure 5.5: From top to bottom: EGRET GeV data [155], INTEGRAL at 20-60 keV, XMM-Newton at 2-10 ad 0.5-2 keV and RXTE and ROSAT radio data [151] (from [154]).

an X-ray flux decreased from $\sim 13 \times 10^{-12}$ cm^{-2}s^{-1} to $\sim 4 \times 10^{-12}$ cm^{-2}s^{-1} within 2-3 hours, at the time when the system was in orbital and superorbital phases $\phi = 0.61$ and $\Phi = 0.02$, respectively. The decrease in flux was accompanied by a significant softening of the spectrum (Γ changed from 1.62 to 1.83). The hardness ratio $HR = f(2/12 \text{ keV})/f(0.3-2 \text{ keV})$ suffered a drop from ~ 1 to ~ 0.8 in about 1 ks. Moreover, a correlation between hardness and intensity is also found when comparing observations spanning almost 10 years and covering various orbital phases. Evidence of variability was also found in the hard X-ray range from a study of archival BeppoSAX (15-70 keV) observations.

- Soft X-ray observations with Swift/XRT (0.3-10 keV) [157] showed a clear orbital modulation (at 26.5 d period) and a broad peak with maximum flux around $\phi = 0.65$. The emission appears to be variable (up to a factor 3) on time scales of ~ 1 ks. The photon index spectrum is found to be $\Gamma = 1.78 \pm 0.05$. No accretion disk signatures (such as an iron line) are found in the spectrum.

- Paredes et al. (2007) [158] performed X-ray observations with the *Chandra* satellite, in the 0.3-10 keV band. The source was observed at orbital phase $\phi \sim 0.04$. The flux, hydrogen column density and photon index were found to be $F_{0.2-10 \text{ keV}} = (7.1^{+1.8}_{-1.4}) \times 10^{-12}$ erg cm^{-2}s^{-1}, $N_H = (0.70 \pm 0.06) \times 10^{22}$ cm^{-2} and $\Gamma = 1.26 \pm 0.09$, respectively. This photon index is harder than previously measured values in the range $1.6 - 1.9$.

To sum up, we see that the X-ray emission is weak ($L_X \sim 10^{33}$ erg s^{-1} in average and up to 10^{34} erg s^{-1} at maximum) and variable (by a factor 10 over one orbit). The hard power-law spectrum extends up to 10 keV without breaks, with photon index $\Gamma \sim 1.7$ and absorbing column density $N_H \sim 5 \times 10^{21}$cm^{-2}. This hard index is inconsistent with low temperature plasma emission, so the Be star can be excluded as a main contribution to the X-ray emission. The spectrum softens at the moment of transition from high to low X-ray state. Soft and hard X-rays are correlated, with a maximum at orbital phase $\phi \sim 0.55$. But the emission is uncorrelated with radio, which shows maxima from 0.4 to 0.9, few days after the X-ray outburst. No spectral lines or extended X-ray emission have ever been reported. The absence of thermal features in the X-ray spectrum is used to argue against the existence of accretion in the system.

5.3.2 Morphological features

The first high-resolution radio images on LSI +61°303 were produced in 1983 [159] using the Very Long Baseline Interferometer (VLBI). Data were taken at 8.4, 5 and 1.66 GHz, when the system was in phase $\phi \sim 0.1-0.2$ and in a quiescent state. Only marginal detections were reported at 8.4 GHz yielding an upper limit to the source size and intensity of **less than 5 milliarcsecond (mas)** and 18 mJy, respectively. The 1.66 GHz observations resolved the source yielding an angular size of 4.1 mas with 40 mJy. No detection was reported on the 5 GHz frequency.

LSI +61°303 has been mapped again with VLBI, VLA and European VLBI Network (EVN), giving angular sizes from 0.5 to 7 mas (see table 2 in [160] for a summary on historic measurements). In 1993 Massi and collaborators [161] used VLBI (Fig. 5.6, bottom panel) to find a structure with an angular **size of milliarcseconds**, corresponding to a physical size of few AU for a distance of 2 kpc. The observation of such a structure included LSI +61°303 in the small subclass of X-ray binaries with relativistic radio jets (we will discuss on this model in Sec. 5.5). Despite this observation, the complex morphology in that and successive VLBI observations made an interpretation in terms of a collimated ejection with a constant position angle difficult [120].

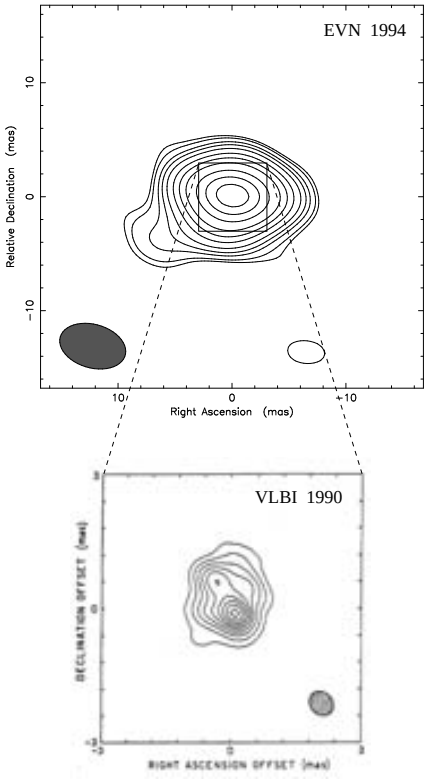

Figure 5.6: Top: EVN radio map of LSI +61°303 at 5 GHz frequency, from [160]. The filled ellipse in the bottom-left corner corresponds to the FWHM of the beam 6.9×3.8 mas. Bottom: VLBI radio map at 5 GHz, from [161], with beam resolution 0.6×0.5 mas (grey ellipse in the bottom-right corner).

Later EVN observations at 5 GHz by Massi et al. (2001) [160] revealed an extended structure of **∼20 mas** (tens of AU), elongated to the southeast, as seen in the upper panel of Fig. 5.6. The position angle of this extended feature was $PA \sim 120°$ and the flux density ~ 35 mJy. This was interpreted as a collimated radio jet (as found in several other X-ray binaries). The apparent expansion velocity, corresponds to an intrinsic velocity of at least $\beta \sim 0.4c$ for a jet close to the line of sight.

Massi and coworkers (2004) [120] explored LSI +61°303 at larger distances from the core, using the **∼50 mas** resolution Multi-Element Radio-Linked Interferometer Network (MERLIN) at 5 GHz frequency. The first two consecutive images (one day apart) in the upper panels of Fig. 5.7 show a double S-shaped jet extending for about 200 mas (~ 400 AU) and located at both sides of the central core. The corresponding orbital phase during this observation is $\phi \sim 0.7$. The similarity between the MERLIN image and a simulated radio emission from SS 433 (also shown in the figure inset) suggested a precession of the jet in LSI +61°303. The position angle of the South-East feature in the first image is $PA = 116°$ and the North-East feature in the second is $PA = 67°$. If both features are real and form part of a precessing jet, they correspond to a large rotation angle in only 24 hours. The feature at 3σ to the East in the first image is compatible with a velocity of $\beta \sim 0.6c \times 24$ hours.

The same images have been split into blocks of a few hours, as seen in Fig. 5.7 bottom panels. Based on these images the authors conclude that the radio jet strongly changes its morphology at a scale of hundreds of AU, evolving from an initial double-sided jet into a one-sided jet.

However, VLA imaging at 2.3 and 8.3 GHz obtained by Dhawan et al. (2006) [115] over a full orbit of LSI +61°303 has rather shown a rotating elongated morphology. The radio measurements

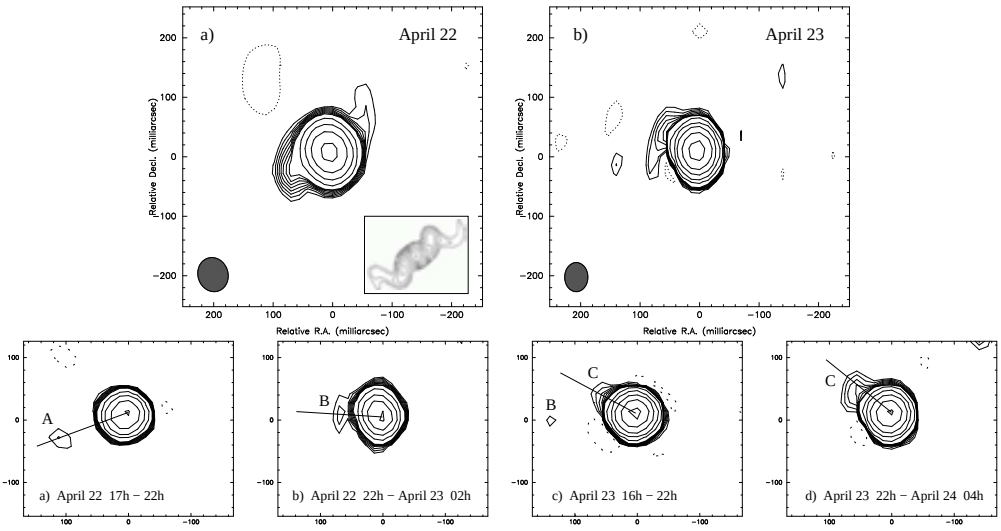

Figure 5.7: Top: MERLIN radio maps at at 5 GHz, from [120], on 2001 April 22nd (orbital phase $\phi = 0.68$) with beam resolution 51×58 mas (left) and 2001 April 23th ($\phi = 0.71$) with beam 39×49 mas (right). In the left inset a simulated radio emission of a precessing jet in SS 433 is shown for comparison. Bottom: Same data sample as upper panels but split into four blocks of a few hours each. The first contour represent the 3σ level in all images except C, where it starts from 2σ to display the faint B component.

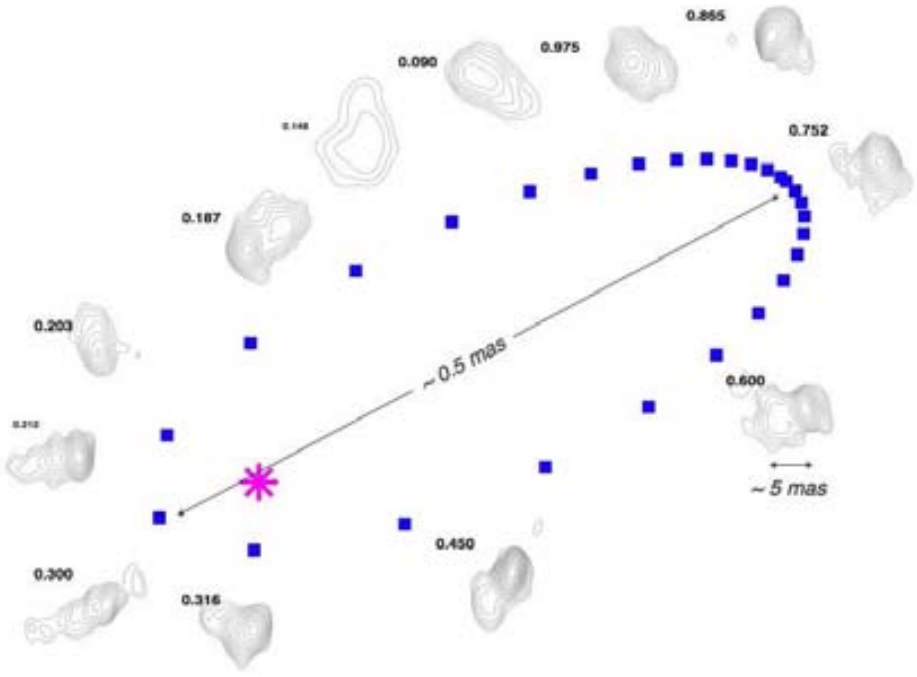

Figure 5.8: VLBA radio maps of LSI +61°303 at 8.3 GHz frequency, from [115]. Beam resolution is 1.5×1.1 mas. The figure is not to scale, with the orbit exaggerated (ellipse parameters from [116]) to illustrate the radio morphology in each orbital phase. No evidence of jets is found at these scales.

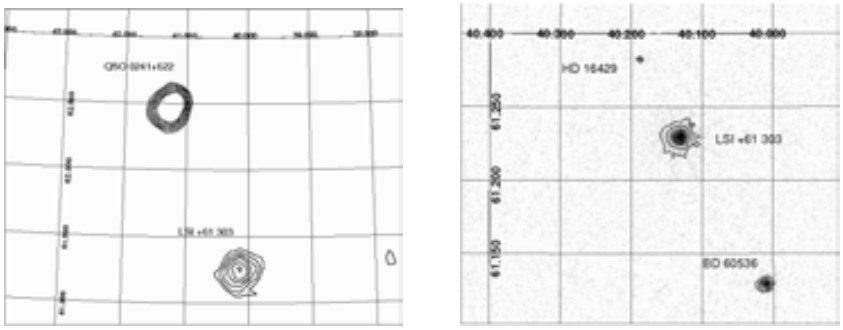

Figure 5.9: Contour plots of LSI +61°303 field of view for the XMM-Newton (left) and INTEGRAL (right) data, from [154].

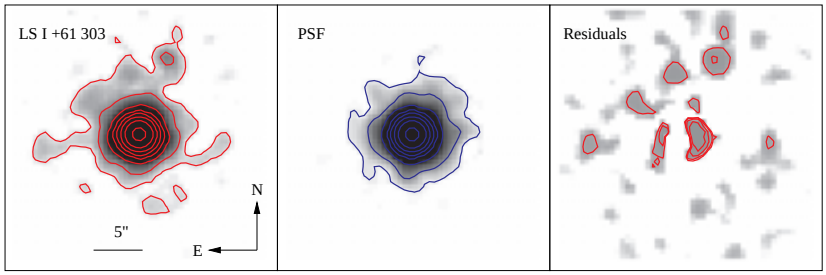

Figure 5.10: *Chandra* X-ray maps of LSI +61°303 in the 0.3-10 keV energy band from [158]. The LSI +61°303 image (left), its PSF (middle) and the residuals (right) after fitting the PSF are shown. The image size is $24.5'' \times 24.5''$. The residuals may indicate some structure at distances greater than $5''$.

at 8.3 GHz reported fluxes from $\sim 20 - 100$ mJy, typical values for the source in its weaker state (see Fig. 5.3). The maximum of the radio emission was detected at phase $\phi \sim 0.5$. As seen in Fig. 5.8 a significant structure shows up at **5-10 mas** angular scales (which at 2 kpc correspond to 10-20 AU). The radio emission appeared cometary-like, with rapid changes in the orientation of the tail (of size about 6.5 mas) near periastron passage. At other phases the tail is amorphous. The changes within a 3 hours observation were found to be negligible, so the velocity can not be much greater than $0.05c$. The estimated outflow velocity is at least ~ 7500 km s^{-1} near periastron, and reduces gradually to ~ 1000 km s^{-1} near apastron. The cometary-like emission has been interpreted to be pointing away from the high mass companion star. No relativistic motion, halos, larger-scale structures or high-velocity flows were detected at any orbital phase. The position of the maximum radio flux peak intensity is always outside the binary orbit (whose semi-major-axis size is about 0.5 AU).

Based on these findings, the authors concluded that the radio emissions of LSI +61°303 stems from the interaction of the wind of a young pulsar with that of the stellar companion. We will discuss this scenario in Sec. 5.5.

Imaging analysis has also been performed in X-rays. Contour maps of LSI +61°303 were produced by XMM-Newton with 2002 data [154] and are shown in Fig. 5.9 (left panel). In the same figure (right panel) these authors also presented an INTEGRAL map in the 22.1-63.2 keV band, with data from 2003-2005. As the INTEGRAL angular resolution is of several arcminutes, the source QSO 0241+622 lying some 1.4° away from LSI +61°303 is clearly separated.

The highest angular resolution X-ray observations to date were performed by Paredes et al. (2007) [158] using the ACIS-I array aboard the *Chandra* satellite, in the 0.3-10 keV band. Possible evidence of an extended asymmetric structure, at a distance between 5-12 sec towards the North have been reported, as shown in the map of Fig. 5.10. Measurements were performed for an orbital phase $\phi \sim 0.04$.

5.4 Previous γ-ray observations

Interest on LSI +61°303 at γ-rays began in 1978, when Gregory & Taylor [139] proposed the association of this system with the COS B γ-ray source 2CG 135+01 [162]. This association however remained controversial because of the presence of an alternative counterpart, the quasar QSO 0241+622, within the relatively large COS B error box.

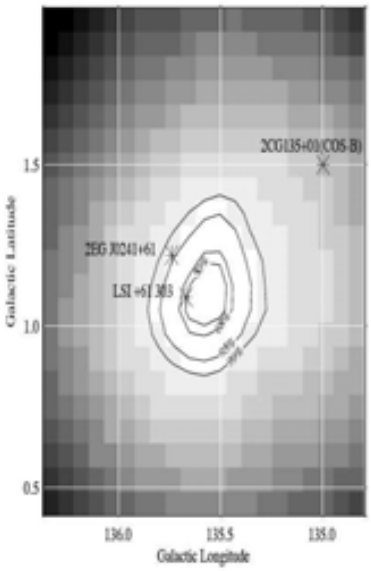

Figure 5.11: Probability contour of a fit to the EGRET photon distribution [163] to a putative γ-ray point source in the direction of 3EG J0241+6103.

2CG 135+01 was later confirmed by EGRET onboard the Compton Gamma Ray Observatory (CGRO) satellite mission, named as 2EG J024+61 in the first catalogue and 3EG J0241+6103 in the second one [34]. EGRET observations from 1991 April through 1995 September showed that 3EG J0241+6103 is a relatively persistent and strong source of high energy γ-rays. The measured flux and position values reported by Kniffen et al. (1997) [163] are slightly different from those quoted in the EGRET catalogs because of the addition of data after the 1993 September cutoff data for the catalog. Their reported flux above 100 MeV is $9.2 \pm 0.6 \times 10^{-7}$ cm^{-2} s^{-1}with a photon spectral index of 2.05 ± 0.06 [163]. The position of the γ-ray source is given at $l = 135.^\circ68$, $b = 1.^\circ13$, which as seen in Fig. 5.11 is only $8'$ distant from LSI +61°303.

Although there is some suggestion of time variability, no compelling evidence for time variations in the γ-ray flux associated with the periodical radio outburst or spectral variations were reported in [163].

Despite the fact that there are only a few EGRET pointings, Tavani et al. (1998) [155] reported with 98.8% confidence that the γ-ray flux from 2CG 135+01 is variable in 1-day time scales. Figure 5.12 show the γ-ray flux for three selected high-quality EGRET samples, with averaged gamma flux above 100 MeV of $7.9 \pm 0.5 \times 10^{-7}$ cm^{-2} s^{-1}. The variablity was later confirmed by Wallace et al. (2000) [164].

Massi (2004) [166] examined the same EGRET data set as a function of the orbital phase, as shown in Fig. 5.12, and pointed out the existence of a modulation with time scales similar to the orbital period of LSI +61°303. The maximum of the emission is likely near the periastron passage, with a second peak at phase 0.5. This EGRET data is compared with (non-simultaneous) data at other wavelengths in Fig. 5.5 as a function of the orbital phase.

An object compatible with 2CG 135+01 was also detected with the COMPTEL detector

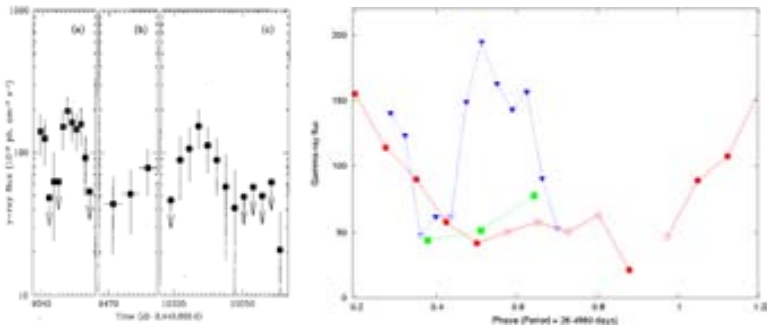

Figure 5.12: EGRET light curve of 3EG J0241+6103 above 100 MeV for three selected observations (from [155]) (left) and same data folded in phase (from [165]) (right). The data correspond to *(a)* 1993 February-March (blue), *(b)* 1994 April-May (green) and *(c)* 1996 September (red). The empty symbols in the right panel are upper limits.

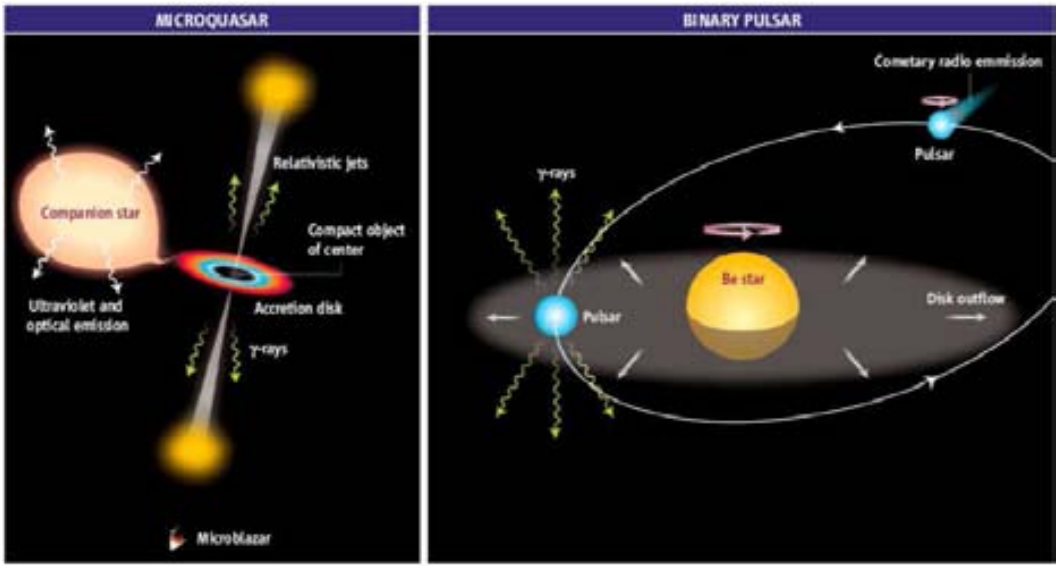

Figure 5.13: Diagrams for the two alternative models which account for the γ-ray emission of LSI +61°303: microquasar (left) and a stellar wind/pulsar wind system (right). See text for description. From [170].

onboard CGRO, between November 1991 and May 1994, in the energy range 1-30 MeV, with photon index $1.95^{+0.2}_{-0.3}$ [167]. No significant temporal correlation between the radio and γ-ray emission was found.

The Whipple group [168, 169] set an upper limit on the TeV flux from this source at two different energies: $F(E > 500 \text{ GeV}) = 0.88 \times 10^{-11}$ cm^{-2} s^{-1} and $F(E > 350 \text{ GeV}) = 1.7 \times 10^{-11}$ cm^{-2} s^{-1}. Both upper limits fall below an extrapolation of the EGRET spectrum.

5.5 Accretion vs colliding wind models

On this section we review the main scenarios proposed to explain the phenomenology of LSI +61°303 from radio to γ-rays. As the main object of this thesis is the study of this binary at very high energies with MAGIC, we will focus on the possible mechanisms that could explain the γ-ray emission.

As summarized by Mirabel (2006) [170] in the diagram of figure 5.13, there are two main scenarios to account for the LSI +61°303 emission: a microquasar or a binary system of a massive star and a pulsar wind nebula. We will describe them in the following subsections.

5.5.1 The microquasar scenario

Due to the apparently presence of relativistic radio emiting jets reported by Massi et al. (2004) [120] LSI +61°303 was proposed to be a **microquasar**. As we introduced in Sec. 5.1, microquasars are X-ray binaries composed by a main sequence star with an equatorial wind forming a circumstellar decretion disk, and a compact object that accretes matter from the decretion disk.

The word *microquasar* was proposed for the first time in 1992 by Mirabel et al. [110] to refer to this new class of Galactic sources, not only because of the observed morphological similarities with the more distant quasars, but also because of the physical similarities: the system itself behaves as a scaled-down version of quasars and active galactic nuclei (AGN). If the compact object is a BH some parameters scale with its mass. BHs in quasars have about $10^6 - 10^9$ solar masses. They may result when huge quantities of gas collapse into the central region of a new born galaxy. On the contrary, BHs in microquasars have just a few times the mass of the sun ($\sim 10 M_\odot$), and are probably the remains of a supernova. The microquasar

surrounds itself with a smaller accretion disk and displays smaller jets, i.e., is a scaled-down version of a quasar.

Since the two components of the binary are orbiting one around the other, gas falling onto the BH inevitably has some angular momentum that forces it into orbit around the object. Once in the disk, the angular momentum is redistributed via viscosity: some gas spreads outwards and (to conserve the momentum) some gas slowly spirals inwards to the disk's center until it reaches the last stable orbit, creating a disk. This last orbit or inner radius R_{in} is, for a non rotating BH, approximately three times the Schwarzschild radius[3] ($R_{\rm Sch}$):

$$R_{in} \sim 3R_{\rm Sch} \sim 3\left(\frac{2GM_X}{c^2}\right) \sim 9\left(\frac{M_X}{M_\odot}\right) {\rm km}\,. \tag{5.8}$$

Besides the transport of angular momentum, viscosity helps to dissipate heat: the accreted gas in the disk get warmer as its gravitational potential energy is converted into thermal energy. The temperature reaches its maximum at the inner disk T_{in}, where it raises up to [171]

$$T_{in} \sim \left(\frac{M_X}{M_\odot}\right)^{\frac{-1}{4}} 2\times 10^7{\rm K}\,. \tag{5.9}$$

Therefore, for a microquasar of one $M_\odot$, the gas in the disk is heated up to 10^7K, radiating predominantly in the X-ray band, while for a quasar, the achieved temperature is about 10^5K, so the emission takes place in the optical and UV domains. The characteristic jet size and time scales also scale with the mass of the BH. This means that those phenomena taking place in time scales of years in quasars can be studied in minutes in microquasars.

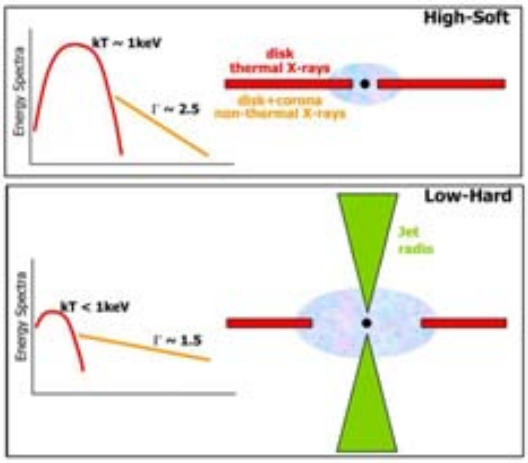

Figure 5.14: Microquasar high-soft and low-hard state diagrams. Adapted from [172].

Microquasars present two different characteristic spectral states (see diagram in Fig. 5.14):

• A **High-Soft state** characterized by two spectral component contributions. First, a peak in the spectral energy distribution at about 1 keV, which is interpreted as originated in the accretion disk and can be approximated by a black body distribution with a temperature corresponding to $kT \sim 1$ keV ($k = 8\times 10^{-5}$ eV K^{-1}). A second spectral component can be fitted to a power-law with soft spectral index $\Gamma \sim 2.5$. It is interpreted as the result of inverse Compton up-scattering of low energy disk photons with thermal and non-thermal electrons located in a corona above the disk. In this state, no jets are visible. The energy output is dominated by thermal emission from the accretion disk, which extends until the last stable orbit ($R_{in} \sim 3R_{\rm Sch}$).

• A **Low-Hard state** characterized by three spectral components: A spectral energy distribution in which a weaker thermal component peaks at lower temperature $kT \sim 0.1$ keV and a strong contribution of a non-thermal power law with hard spectral index $\Gamma \sim 1.5$. The accretion disk is truncated at a larger inner radius $R_{in} > 50R_{\rm Sch}$: either the disk was removed or it shifted to a cooler state, becoming invisible in X-rays. In this state a jet emitting synchrotron radiation is observed.

[3] An object becomes a black hole when it is compressed in a sphere whose radius is smaller than the *Schwarzschild radius*.

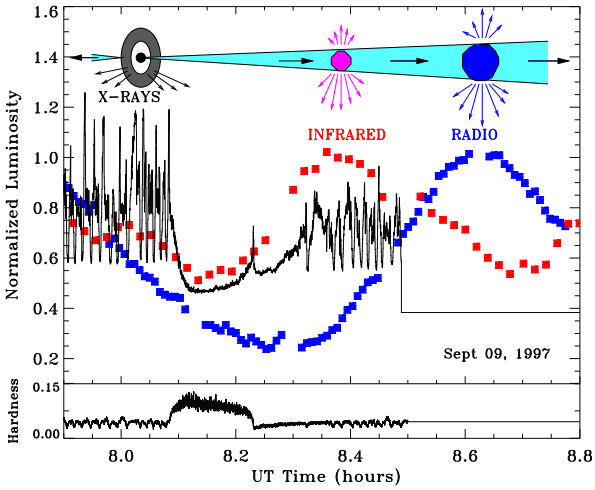

Figure 5.15: Radio, infrared and X-ray light curves for GRS 1915+105 [173]. A scheme of the relative positions where the emissions originate is shown in the upper panel. The hardness ratio $f(13-60\ \mathrm{keV})/f(2-13\ \mathrm{keV})$ is shown at the lower panel.

A transition from a thermal dominated high-soft state to the non-thermally dominated low-hard state therefore corresponds to a change in the disk structure. Such a transition was illustrated in the observations of the microquasar GRS 1915+105 [173] in 1998. These observations showed the connection between the rapid disappearance and replenishment of the inner accretion disk, evidenced by the evolution in X-rays, and the ejection of relativistic plasma clouds, observed as synchrotron emission at infrared and radio wavelengths. The flare is visible first at infrared and then at radio wavelengths (Fig. 5.15), a behaviour which is consistent with a delay from synchrotron radiation from expanding magnetized clouds of relativistic particles.

In the low-hard state, the total power of the jet (L_j) depends on the accretion rate on the compact object as

$$L_j = q_j \dot{M} c^2 \,, \tag{5.10}$$

where q_j is the efficiency of energy conversion ($q_j \sim 0.1$ for NS). Part of this power is in the form of relativistic particles. If leptons are accelerated, the jet can produce γ-rays via inverse Compton scattering. The low energy photons which the leptons interact with may come from their own synchrotron field, or the photon field from the accretion disk, the corona or the companion star. If hadrons are accelerated, *pp* interactions with protons from the stellar wind can also produce γ-rays. Since microquasars have usually eccentric orbits, present state transitions and possible jet precession, their possible γ-ray emission is expected to be variable.

Within this general context, many authors developed specific models to interpret the LSI +61°303 broad band emission. Some of the most recent theories are the following:

- Bosch-Ramon and coworkers (2006) [174] developed a leptonic model. It was based on accretion of matter from the slow inhomogeneous equatorial wind of the companion star. Part of the accreted matter is ejected as a jet. The particle injection is assumed to be proportional to the accretion rate. And the jet interact with the circumstellar disk and triggers electron acceleration via shocks. Accelerated electrons radiate mainly by synchrotron and interact with soft photons by IC process. γ-ray produced by the latter are significantly absorbed (for certain orbital phases) via photon-photon annihilation with the stellar and the circumstellar disk photon fields. Convection of particles, including adiabatic losses, as well as the angle dependence of the photon-photon and IC cross sections have been considered in the calculations. The radio to VHE orbital variability is explained because the radiation along the orbit is strongly affected by the variable accretion rate, the magnetic field strength, and by the ambient photon field

via IC losses and photon-photon absorption.

- Gupta & Böttcher (2006) [175] proposed a time-dependent leptonic jet model. Dermer & Böttcher (2006) [176] already presented a similar model, but with steady-state leptonic jets. In this new dynamic approach a γ-ray modulation is produced not by the accretion rate but rather by geometrical effects. VHE emission originates near the base of the jet. Soft photons from the companion star, the accretion disk as well as from jet synchrotron radiation are Compton up-scattered by the ultrarelativistic electrons in the jet. This time-dependent approach takes into consideration the angle dependence of the stellar radiation field, the time dependent electron injection and acceleration, and the adiabatic and radiative cooling of non-thermal electrons. The VHE modulation can be explained by the geometrical effect of changes in the relative orientation of the stellar companion with respect to the compact object and jet as it impacts the position and depth of the photon-photon absorption trough.

- Bednarek (2006) [177, 178] applied an IC $e^{\pm}$ pair cascade model to predict the high energy spectra (TeV) of LSI +61°303, assuming that electrons are accelerated in the inner part of the jet. In this context, γ-rays, if injected relatively close to the massive companion, may escape in the direction of the star. Since the massive star is very luminous, the γ-ray should be strongly absorbed, initiating cascades in the stellar photosphere. And some γ-rays could, in principle, be redirected toward the observer. The γ-ray spectrum produced in such a way is different than the one produced by electrons in a jet pointing directly to the observer. The cascade processes occurring inside the binary significantly reduce the γ-ray opacity obtained in other works by simple calculations of the escape of γ-rays from the radiation fields of the massive star. This model predicts an anticorrelation between the GeV (1-10 GeV) and TeV ($>$ 200 GeV) γ-ray fluxes.

- Alternative models based on hadronic processes in the jet, or in the interaction between the jet and the interstellar medium have also been proposed by Romero et al. (2005) [179] (revisited by Orellana & Romero in 2007 [180]). The γ-rays are produced via hadronic interactions of relativistic protons from the jet (launched close to the compact object) and cold protons from the equatorial wind of the Be star. The *pp* interactions can occur either because there is some mixing of the stellar wind with the jet or because some protons escape from the jet into the wind. The jet is assumed to be steady in this model. The opacity effects introduced by the photon fields of the primary star and the stellar decretion disk are shown to be essential in shaping the γ-ray light curve at energies about 200 GeV.

- Torres & Halzen (2007) [181] presented a phenomenological study on the neutrino flux from LSI +61°303 if the γ-ray emission have an hadronic origin. Upper limits imposed by AMANDA-II and further measurements by IceCub may constrain the γ-ray to neutrino flux, and thus the possibility of a hadronic origin of the VHE emission.

5.5.2 The colliding winds scenario

A scenario where the γ-ray emission is due to a collision of two winds was first proposed for LSI +61°303 by Maraschi & Treves (1981) [182]. Those authors proposed that the compact object in the binary is a relatively young pulsar (of age $10^4 - 10^5$yr) losing energy via a relativistic wind. The pulsar, with a spin-down power of about 10^{36}erg s^{-1} generates a strong radial and isotropic wind of relativistic electrons and positrons. A substantial fraction of the spin down power is in the form of the wind and the rest in form of low-frequency electromagnetic radiation (i.e. part of the power goes to the pulsar magnetic field). The ratio of the electromagnetic energy flux to the kinetic energy flux of particles in the wind is called *magnetization*.

A shock forms at the boundary between the pulsar wind and the stellar wind of the companion, beyond which the leptons from the pulsar wind are accelerated and isotropized. The

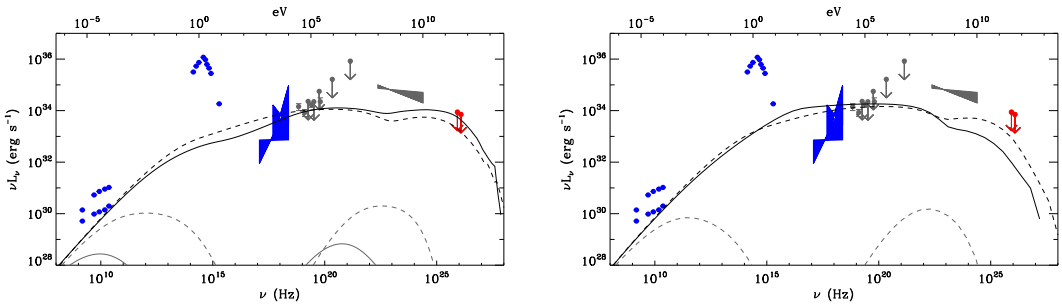

Figure 5.16: Spectral energy distribution for LSI +61°303 at periastron (black lines) and apastron (dashed lines), for a polar (top) or an equatorial (bottom) stellar wind, as modelled by Dubus 2006 [185].

relativistic electrons interact via IC with the optical photons of the luminous and hot Be star. The existence of such a dense photon field (which varies along the orbit) result in conversion of a significant fraction of the electron-positron wind power into X and high-energy γ-rays. Synchrotron radiation from the same electrons would explain the radio emission.

Later on, Protheroe & Stanev in 1987 [183] discussed the importance of the absorption of the HE γ-rays on the thermal radiation of the companion star (optical and infrared photons) to explain the orbital modulation in the X-ray and IR emissions (using Cyg X-3 as an example). Mooskalenko, in 1995 [184], reviewed the TeV emission mechanism from close binaries. He proposed that, once produced, VHE γ-rays pass through regions with various physical conditions, which have a strong influence on the observed γ-rays. These regions can be separated in:

- near the NS environment filled with accreting matter, X-ray photons and a strong magnetic field;
- space in the binary system filled with IR, visible and UV radiations of the companion star and gas shell around the system;
- interstellar space contains 2.7 K background photons.

And in those environments pair production $\gamma+\gamma \rightarrow e^+e^-$ is likely to absorb a part of the VHE photons. Besides, γ-absorption is possible in a strong magnetic field near the NS, together with Compton scattering and pair production in accreting gas or the companion star matter in the system. However, the γ-rays attenuation due to the 2.7 K background photons via pair production is only important for γ-rays above 10^{14} eV and negligible for the 0.1-10 TeV region (the minimum path length is 7 kpc at 10^{15} eV) [184].

Dubus, in 2006 [185], investigated this scenario for LSI +61°303, modelling the two components of the Be stellar wind separately: a fast polar outflow and a slow equatorial wind. The resulting spectral energy distributions at periastron and apastron for both winds are shown in Fig. 5.16. The major difference between the two types of stellar winds is at periastron. However the emission at GeV (EGRET spectrum) is not properly reproduced.

Sierpowska-Bartosik & Torres (2008) [186] emphasized the importance of the geometry of the system. They presented a model (for the particular case of LS 5039) including the angular dependence of the process such as Klein-Nishina IC and $\gamma\gamma$ absorption, and a detailed Monte-Carlo simulation of the cascading process.

Zdziarski et al. (2008) [123] argue that the detailed structure of the stellar wind is crucial for explaining the LSI +61°303 properties. They presented a clumpy polar wind, that causes the two winds to mix rather than form a bow shock. They have also proposed two models for the superorbital variability of the radio emission: one involving precession of the circumstellar disc, which is misaligned with respect to the orbital plane, an the other a cyclic disk activity.

In this interpretation the stellar wind confines the pulsar wind producing a jet-like radio morphology that points opposite to the star. This is in fact what is observed in the VLBA

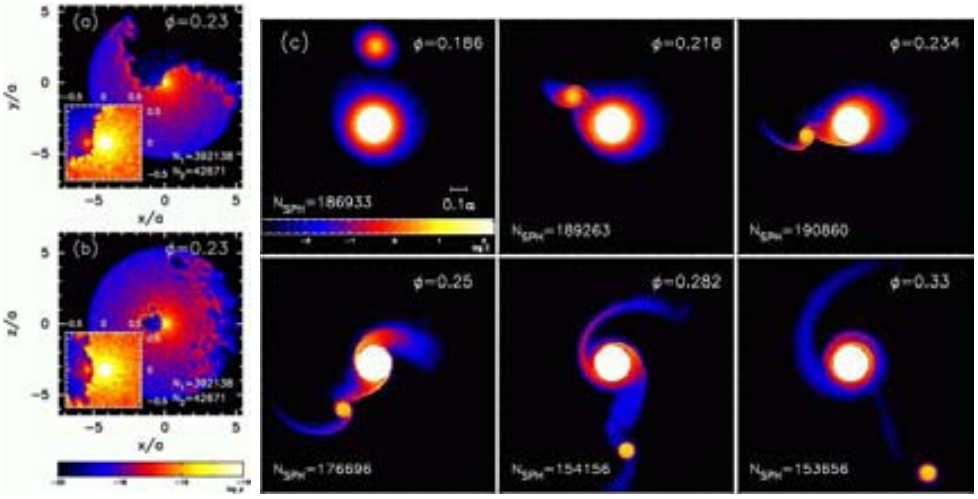

Figure 5.17: Left: Colliding wind snapshots at periastron passage from 3D simulations of LSI +61°303. The bright spot is the Be star and the small point is the pulsar. The orbit is in the xy-plane. Lengths are in units of the semi-major axis a. Right: 3D simulation of the interaction between the accretion disk of the compact object (BH with mass $2.5M_{\odot}$) and the circumstellar disk, around periastron passage. From [187].

images shown by Dhawan et al. (2006) [115], where a rotating elongated morphology is visible. These radio tails are predicted by [185], where the radio fluxes are explained by the emission from cooled PWN particles.

However, 3D time-dependent simulations have been performed under the assumptions of the Be/pulsar hypothesis by Romero et al. (2006) [187], although no evidence of cometary tail was seen. Figure 5.17 (left panel) shows snapshots of these 3D simulations. Nevertheless, the hydrodynamical simulations present, in general, a very complex and assumption-dependent problem. Be wind inhomogeneities may for instance play an important role in the system [123]. Thus, a failure of some specific simulation should not be used to rule out the model. On the other hand, relativistic hydrodynamical simulations of the wind interactions have been developed by Bogovalov et al. (2007) [188]. They applied the simulations to the PSR B1259-63 binary system and showed that the shocked pulsar wind is collimated.

Romero et al. [187] also produced simulations of an accretion model, where the mass transfers from the Be star and its circumstellar disk to the compact object (assuming a BH of mass 2.5 $M_{\odot}$). Near periastron, the BH deforms the circumstellar disk and particles are captured and accreted. As seen in Fig. 5.17 (right panel) an accretion disk appears around the compact object, in which a strong density wave is excited. When the wave arrives near the compact object (around phase 0.5) there is an increase in the accretion rate, which is correlated with the maximum of the expected γ-ray emission.

5.6 Other γ-ray binaries

Three other high mass X-ray binaries have been recently identified as variable VHE γ-ray sources. They are PSR B1259-63 [189], LS 5039 [19] and Cyg X1 [18]. With the VHE observations in the work of this thesis, we will prove that LSI +61°303 belongs also to this new class of objects, dubbed **γ-ray binaries**. The spectral and temporal similarities between the three binaries hint at a common scenario. Figure 5.18 illustrates the key parameters of the four binary systems in a sketch.

The nature of the compact objects is only known for two of the binaries: for PSR B1259-63 it is a pulsar whereas for Cyg X1 it is a black hole.

The VHE phenomenology of Cyg X1 is very different from that of the others. It has been

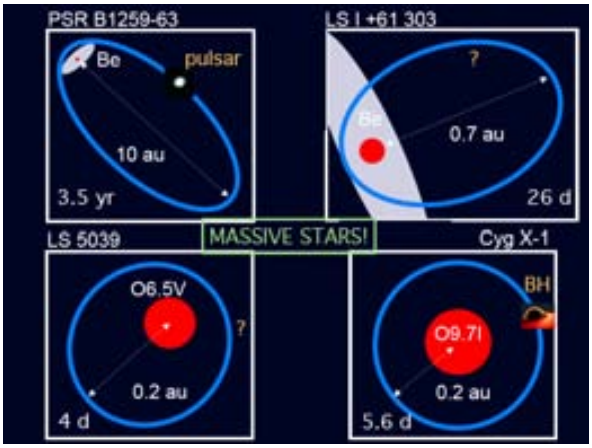

Figure 5.18: Orbital sketch of the four γ-ray binaries known so far. All are composed of a massive star and a compact object, neutron star or black hole. From [185].

detected just once in a flare state of duration between 1 hour and 1 day, for which a duty cycle is yet unknown.

The other sources, instead, show variability which is correlated with the orbital period. The orbital period is ~ 1237 days for PSR B1259-63, ~ 4 days for LS 5039 and ~ 26.5 days for LSI $+61°303$. In all three cases, with quite eccentric orbits, the presence of a luminous early-type star (with masses of 10-23 $M_\odot$) provides a copious source of seed photons for inverse Compton scattering, which is probably instrumental to VHE γ-ray emission. And they have all been also detected in X-ray and radio wavelengths. PSR B1259-63 contains a young pulsating neutron star, and is understood in the pulsar wind scenario. The question that remains open is whether the relativistic particles in LS 5039 and LSI $+61°303$ come from accretion powered jets or from the rotational energy of pulsars that are spinning down, as in PSR B1259-63.

LS 5039 shows steady, two sided jets, with components with velocities of about $0.2 - 0.3c$. Moreover, no radio outburst, similar to those in PSR B1259-63, are observed in LS 5039.

The detection of pulsations and radio images with high sensitivity and angular resolution would be the direct way to distinguish between the two scenarios for LS 5039 and LSI $+61°303$.

Chapter 6

VHE spectral and temporal properties of LSI +61°303

In this chapter we report on the discovery of VHE γ-rays with the MAGIC telescope in the direction of LSI +61°303. The results of the analysis of $\sim$ 170 hours of observations of LSI +61°303 during 2005 and 2006 are summarized. We perform a detailed study of the temporal properties of the VHE emission and derive the energy spectrum.
The results presented in this chapter are partially published in [190] and [191].

6.1 Introduction

LSI +61°303 was initially proposed as a possible counterpart of the high-energy COS B γ-ray source 2CG 135+01 [162], which was also detected by EGRET (3EG J0241+6103) [34]. LSI +61°303 fell within the 99% C.L. error box of the EGRET detection. However, the association was unclear due to the low angular resolution of EGRET, although no radio loud active galactic nucleus or strong radio pulsar is known within this zone. This, together with the fact that jet flows were claimed from radio interferometric observations, made LSI +61°303 a promising microquasar candidate [120].

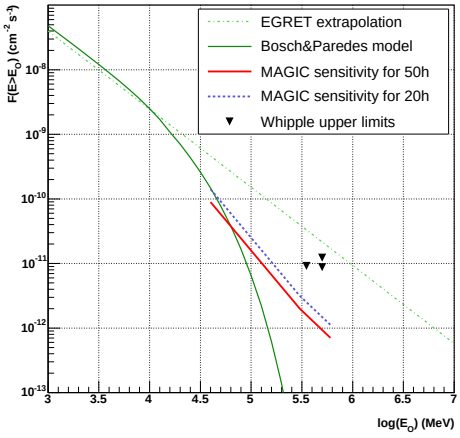

Figure 6.1: Extrapolation of the EGRET flux for LSI +61°303 (dot-dashed green line) and a leptonic cut-off model (continuous green line). We also marked Whipple upper limits (black triangles) and 5σ MAGIC sensitivity for 20 hours (in blue) and 50 h (in red).

The observation of LSI +61°303 at very high-energy γ-rays with MAGIC was proposed in an attempt to better understand the nature and physical properties of this system. The angular resolution of MAGIC allows to improve the determination of the high energy source position by a factor 10, and check the spatial coincidence with the radio source with better precision.

Hall et al. [168] gave upper limits to the emission associated to LSI +61°303 at higher energies (above 350 and 500 GeV), from observations performed with the Whipple Čerenkov telescope. Extrapolating the spectrum measured by EGRET (photon index about 2.1 for energies above 100 MeV) to the threshold of Whipple ($\sim$ 350 GeV), suggested that a detection with this telescope could be possible. The really upper limits imply a steepening of the spectrum above EGRET energies.

As we discussed in Chapter 5, several models predict that LSI +61°303 emits VHE γ-

rays. As an example we show, in figure 6.1, the energy spectrum predicted by a model from Bosch-Ramon & Paredes (2004) [192] based on a microquasar leptonic jet. With a reasonable set of parameter values, they reproduced the spectrum observed by EGRET and extrapolated it up to a few hundreds of GeVs. In the same figure we plot the extrapolated EGRET data flux, the Whipple upper limits as well as the sensitivity limits of MAGIC for 20 and 50 hours [193]. Therefore, for an energy threshold estimation of 50 GeV, the required time for a 5σ detection would be about 20 hours.

6.2 Observations and data selection

LSI +61°303 exhibits a periodic modulation of the optical, X and radio emission, attributed to the orbital motion. Hence, we may expect a dependence of the VHE emission with the orbital phase.

At the latitude of the MAGIC telescope, LSI +61°303 culminates at a zenith angle of 32^o but is circumpolar and therefore is visible for 5 full months every year, roughly from September to January. However, the Moon and LSI +61°303 orbital period are very similar (about 28 and 26.5 days), which makes difficult to cover all LSI +61°303 orbital phases within one observation season. In appendix A, we present the possible observations time slots of LSI +61°303 from the MAGIC site up to March 2009.

The observations on LSI +61°303 were performed in two campaigns, at the end of 2005 and the end of 2006. The physics objectives and data taking conditions of the two campaigns are reviewed in the following subsections.

6.2.1 Campaign I

The aim of the first observational campaign was to establish whether LSI +61°303 emits VHE γ-rays. LSI +61°303 was observed for 54 h (after standard quality selection, see below) between October 2005 and March 2006, covering six orbital periods of the binary system. About 22 % of the data were recorded under moonlight conditions. The zenith angles between 32-55° were covered.

For this campaign, there was no devoted OFF observations, thus data samples corresponding to other sources were used to evaluate the residual background. The data were selected according to the following criteria:

- OFF data must have been acquired not long before or after the LSI +61°303 observation, in order to ensure that the telescope conditions are similar (mirror reflectivity, PSF, camera inhomogeneities ...).

- Similar zenith angles: Fig. 6.2 (lower right panel) shows the range of zenith angles of the LSI +61°303 observations and the OFF data sample. Only data above 31° are considered for the analysis (because LSI +61°303 culminates at 32° from MAGIC site). The selected OFF sample reaches only 40°, but there were no suitable data to increase the sample above this zenith distance.

- Stable mean trigger rate (above 150 Hz) and good weather conditions.

- Stable rate after cleaning. For each day, the rate of events per run is evaluated (see e.g. Fig. 4.20). Only a few runs have been discarded due to abnormal values of the rate, caused by technical problems, car flashes illuminating the telescope camera, etc. These problems were usually pointed out by operators in the data taking run-book. The same criteria is applied to select LSI +61°303 ON data where, e.g. night 2006/02/01, with an observation time of $\sim$ 40 min, was discarded completely due to cloudy weather conditions. We also take into account that data taken under moonlight conditions have higher discriminator thresholds, and therefore the rate will be affected.

- Compatible Hillas parameter distributions: the shape of the distributions of the Hillas parameters are compared. Figure 6.2 shows the good consistency of the Length, Width,

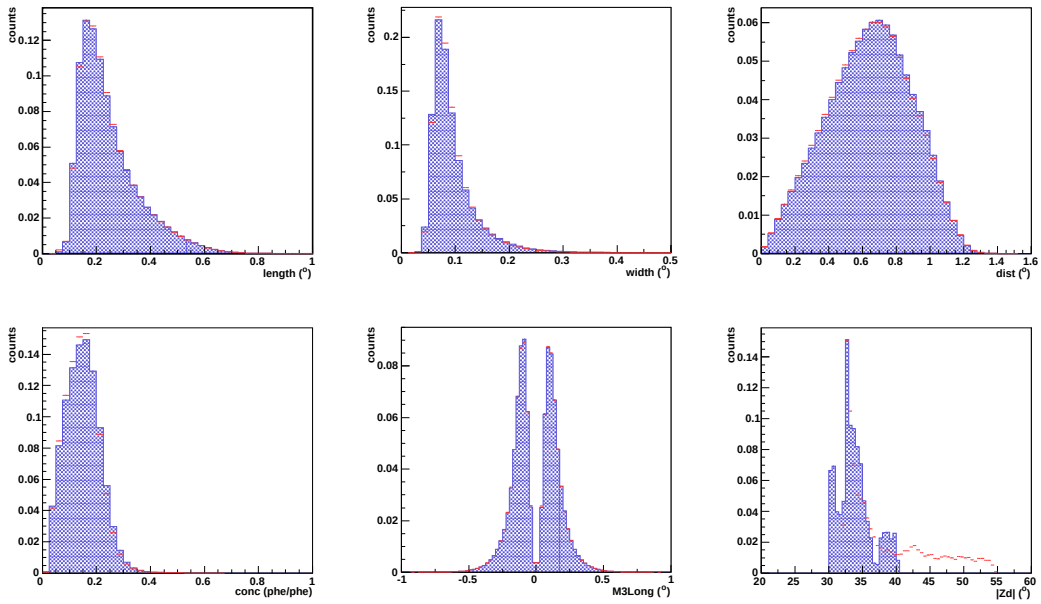

Figure 6.2: Comparison of the distribution of some Hillas parameters between OFF data (blue histograms) and LSI +61°303 campaign I (red dots) samples, for Size above 200 phe. An overall good agreement is observed. Bottom right plot shows the zenith angle distribution of the ON and OFF selected samples.

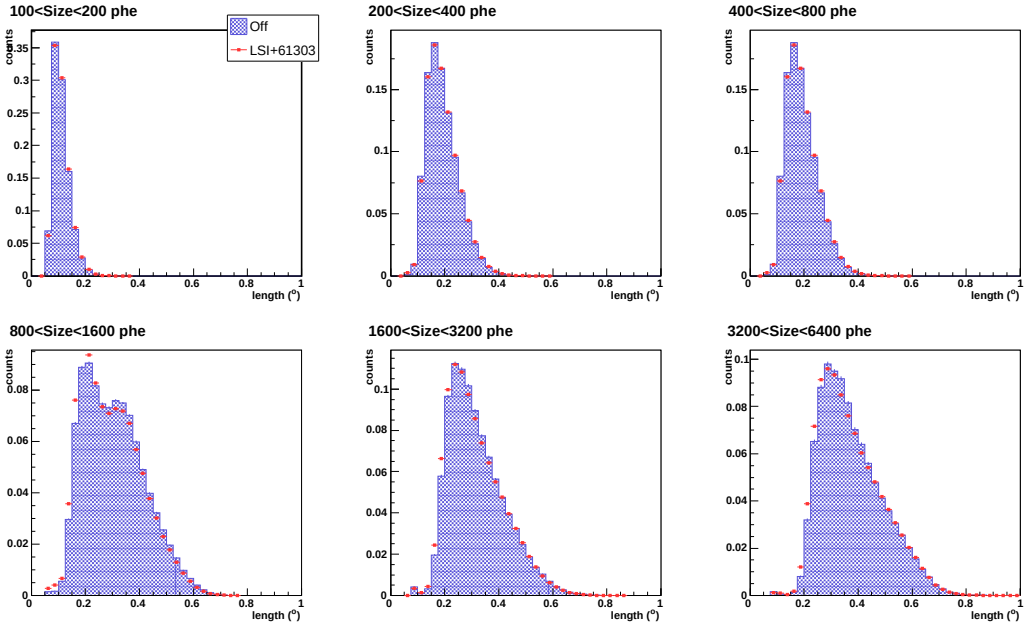

Figure 6.3: Comparison of the distribution of the Length Hillas parameter between OFF data (blue histograms) and LSI +61°303 campaign I (red dots) samples, for different bins of Size. An overall good agreement is observed.

Dist, Conc and M3Long distributions of LSI +61°303 and the OFF data samples, before applying event selection cuts. Good agreement is observed also for the remaining image parameters used to train the Random Forest. The consistency is also checked for different bins of Size, as shown e.g. in figure 6.3 for the Length parameter.

- No γ-ray signal must be present in the OFF data sample: Data from PSR J0205+6449, PSR J2229+6114, 1ES 0414+009 and 1ES 0806+524 (ON observations) have been previously analyzed and no γ-ray signal was found; only upper limits have been derived. PSR J0205+6449 is an X-ray pulsar embedded in the 3C58 nebula, while PSR J2229+6114 is a pulsar in the Boomerang nebula; the analysis of the MAGIC data on both sources can be found in [74]. The sources 1ES 0414+009 and 1ES 0806+524 are X-ray blazars, whose analysis is published in [194].
- Data taken under dark (no moonlight) conditions.

A summary of the characteristics of the OFF and LSI +61°303 data samples in campaign I are presented in Tables 6.1 and 6.2, respectively, where we review the individual sample date, data-taking periods[1], observed time, zenith angle, mean rate after cleaning and Moon efficiency. We use the following convention for the dates: e.g. date *2005/11/02* corresponds to the night from 1st to 2nd November (or, in the usual internal MAGIC data storage convention 2005_11_02).

Source	Dates	Period	T_{eff} (min)	Zd (°)	Rate (Hz)
OffTeV2032-1	Nov 2005	35	37	31-38	135.6
Off0736-1	Dec 2005	36	82	31-37	168.5
PSR J2229+6114	Sept-Dec 2005	34-36	499	32-37	125.4
PSR J0205+6449	Nov-Dec 2005	36	149	37-41	125.6
1ES 0414+009	Nov 2005-Jan 2006	36-38	199	31-37	164.5
1ES 0806+524	Dec 2005	36	7	31-32	168.4
Total	16.2 (h)				

Table 6.1: OFF data samples used for background evaluation in LSI +61°303 campaign I analysis. The data taking time and conditions are reviewed: source, approximated observational dates, MAGIC period, observation time, zenith angle range and mean rate after cleaning. The final effective observation time is given in the last row.

6.2.2 Campaign II

We followed the source for several orbital periods, with the maximum possible orbital phase coverage with the aim of determining the orbital emission profile, checking the stability of the γ-ray profile from period to period and searching for possible periodicities in the γ-ray flux. We requested to observe the source about 120 hours, from September to November 2006, to collect enough data to perform spectral studies for different phases. This much longer sample would also allow us to systematically look for possible intranight variabilities.

The second campaign lasted from September to December 2006. This observation covered 4 orbital periods, and a total amount of 116 h (after quality selection) were recorded, 17% of which were taken under moonlight conditions. While in campaign I the observations were carried out in ON/OFF mode, in campaign II the data were taken in wobble mode (see Sec. 4.4.1), i.e. by alternatingly tracking two symmetric positions at 0.4° offset from the source position. Thus, the normalization factor $F_{\rm norm} = \frac{N_{\rm Bkg}}{N_{\rm OFF}}$ is 1/3 (as we used three wobble regions for background estimation). The zenith angle range of campaign II is 32-55°. Table 6.3 reviews the characteristics of the data sample.

[1] A MAGIC observation period extends between two full Moons, so it corresponds to roughly one month. They are useful to plan the observation schedules since Čerenkov telescopes stop their data taking when the Moon is up and therefore no observations are carried out during the 3-4 nights of full Moon night.

Period	Dates	T_{obs} (min)	ϵ_{Moon}	Zd (°)	Rate (Hz)
34	2005/10/07*	133	1.000	32-36	30-120
	2005/10/11	79	0.991	32-36	134.2
	2005/10/12	151	0.986	32-36	136.5
35	2005/11/03	153	0.999	32-40	110.1
	2005/11/04	150	0.990	32-36	128.4
	2005/11/05	134	0.998	32-38	120.0
	2005/11/06	155	0.991	32-42	118.5
	2005/11/07	157	0.997	32-36	105.7
	2005/11/08*	180	1.000	32-37	103.1
36	2005/12/02	88	1.019	32-37	120.9
	2005/12/03	145	1.009	32-36	125.6
	2005/12/04	74	1.019	32-34	109.7
	2005/12/05	148	1.009	32-37	126.0
	2005/12/07	68	0.998	32-37	122.3
37	2006/01/02	16	1.006	32-35	112.1
	2006/01/03	86	0.998	32-35	113.4
	2006/01/04	14	1.001	34	97.4
	2006/01/06*	98	0.874	35-45	99.3
38	2006/01/29	117	0.991	33-42	98.4
	2006/01/30	117	0.998	34-44	90.8
	2006/01/31	106	0.997	34-43	93.2
	2006/02/01*	40	1.001	34-39	70-110
	2006/02/02	98	0.950	34-44	88.29
	2006/02/03	105	0.877	34-44	81.52
	2006/02/04	101	0.707	35-45	59.19
	2006/02/05	48	0.474	35-45	43.47
39	2006/02/17	107	0.960	40-52	122.7
	2006/02/18	119	0.988	40-55	117.3
	2006/02/19	97	0.997	41-55	115.3
	2006/02/20	115	0.985	41-54	139.9
	2006/02/23	106	0.994	41-54	135.6
	2006/02/24	99	0.979	42-54	85.8
	2006/02/25	97	0.976	43-55	79.4
	2006/02/27	79	0.979	44-54	129.0
	2006/03/03	55	0.942	47-55	110.8
	2006/03/04	80	0.869	44-54	93.0
	2006/03/05	31	0.758	54-58	73.3
	2006/03/06	85	0.498	48-58	57.6
Total		63.8 (h)			

Table 6.2: LSI +61°303 data samples in campaign I. The data taking time and conditions are reviewed: MAGIC period, date, observation time, Moon efficiency, zenith angle range and mean rate after cleaning. Days marked with * are completely excluded due to bad weather conditions. The total observation time is given in the last row.

Period	Dates	T_{obs} (min)	ϵ_{Moon}	Zd (°)	Rate (Hz)
46	2006/09/15	141	0.786	32-35	76.3
	2006/09/16	115	0.897	32-35	99.2
	2006/09/17	160	0.965	32-36	125.1
	2006/09/19	233	1.000	32-41	134.3
	2006/09/20	220	1.000	32-40	129.1
	2006/09/21	136	1.000	32-42	122.5
	2006/09/23	96	1.000	32-37	137.7
	2006/09/24	201	1.000	32-45	155.1
	2006/09/25	159	1.000	33-45	143.5
	2006/09/26	173	1.000	32-45	141.9
	2006/09/27	177	1.000	32-47	146.5
	2006/09/28	178	1.000	32-45	135.4
	2006/09/29	142	1.000	32-43	121.1
	2006/09/30	174	1.000	32-46	146.2
	2006/10/01	150	1.000	32-41	118.4
	2006/10/05	7	1.000	42	121.6
47	2006/10/14	201	0.795	32-45	90.9
	2006/10/15	282	0.936	33-44	119.4
	2006/10/16	20	0.959	33	166.5
	2006/10/21	137	1.000	32-41	149.8
	2006/10/22	170	1.000	32-45	135.2
	2006/10/23	176	1.000	32-45	146.9
	2006/10/24	142	1.000	32-43	149.0
	2006/10/27	152	1.000	32-44	141.8
	2006/10/31	96	1.000	32-38	124.4
48	2006/11/17	192	1.000	32-42	156.8
	2006/11/18	233	1.000	32-45	153.2
	2006/11/19	75	1.000	37-44	143.3
	2006/11/20	58	1.000	38-43	132.4
	2006/11/21	17	1.000	33	105.3
	2006/11/23	230	1.000	32-43	136.9
	2006/11/24	233	1.000	32-42	140.8
	2006/11/25	77	0.998	32-37	134.9
	2006/11/26	77	0.984	35-42	156.8
	2006/11/27	188	0.958	32-41	158.0
	2006/11/28	221	0.959	32-48	146.2
	2006/11/29	182	1.000	34-49	140.0
49	2006/12/13	19	1.000	110.0	35
	2006/12/14	83	1.000	153.6	34-42
	2006/12/15	38	1.000	119.9	33-37
	2006/12/16	65	1.000	158.9	35-40
	2006/12/17	134	1.000	114.5	35-47
	2006/12/18	326	1.000	115.7	32-40
	2006/12/19	153	1.000	110.1	37-42
	2006/12/20	97	1.000	112.2	37-50
	2006/12/21	30	1.000	77.7	32-34
	2006/12/22	179	1.000	133.6	32-38
	2006/12/23	142	1.000	159.6	32-36
	2006/12/24	94	1.000	154.6	32-35
	2006/12/25	94	1.000	150.8	34-40
	2006/12/26	87	1.000	95.4	37-46
	2006/12/27	75	0.944	119.7	39-48
	2006/12/28	69	0.879	77.9	44-55
Total		121.8 (h)			

Table 6.3: LSI +61°303 data samples in campaign II. The data taking time and conditions are reviewed: MAGIC period, date, observation time, Moon efficiency, zenith angle range and mean rate after cleaning. The total observation time is given in the last row.

6.3 Source Detection

The data were analyzed using the standard analysis and calibration programs as described in Chapter 4. For each data taking campaign a separate Monte-Carlo set of γ ray events was generated, taking into account the zenith angle of the observation, the observational mode (ON/OFF or wobble) and the hardware configuration of the telescope (as the width of the point spread function which is tuned in the simulation to be 1.4 cm; see Sec. 4.2.5).

The Random Forest algorithm (Sec. 4.2.7) is then trained using the following image parameters: Width, Length, Conc, Dist, M3Long and Size. The Alpha parameter in campaign I and Theta square in campaign II are used to extract the signal. The Hadronness and Alpha or θ^2 cuts are optimized with a Crab Nebula data sample, as shown in Sec. 4.2.7. We apply a Hadronness cut of $h < 0.1$ and, to determine the excess events, a cut $\alpha < 6^\circ$ and $\theta^2 < 0.03\text{deg}^2$ in each campaign respectively.

A clear signal was obtained in both data campaigns. Figure 6.4 shows the Alpha distribution of the γ-ray candidates of the campaign I. Above 400 GeV and for an integrated observation time of 54 hours an excess of 493 ± 69 events was found, which for the residual background, has a statistical significance of 8.8 standard deviations (σ). We normalize the ON/OFF histograms in the region $30 < \alpha < 80^\circ$

The θ^2 distribution for the second campaign data sample is shown in figure 6.4. A signal of 445 ± 53 excess events over 1807 ± 24 normalized background events were found, corresponding to a significance of 8.7 σ. We normalize ON and OFF distributions by a factor 1/3, since we evaluate the background using three OFF regions.

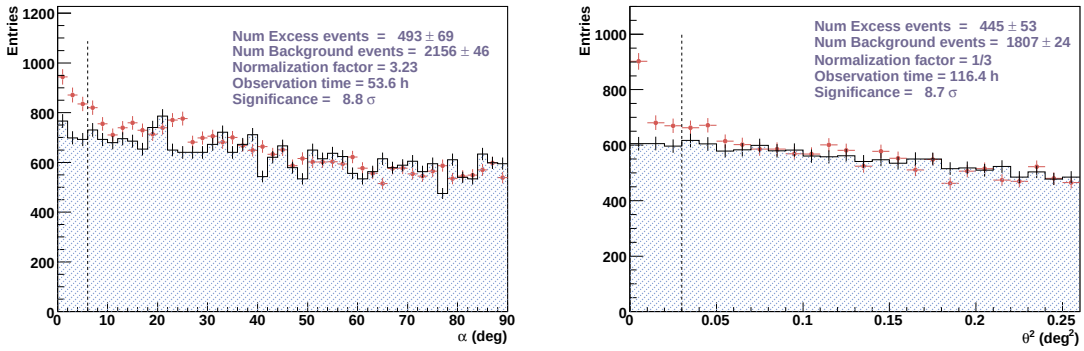

Figure 6.4: Alpha (left) and θ^2 (right) distributions with energy threshold of 400 GeV for LSI +61°303 campaigns I and II, respectively. ON data are shown in red dots and the normalized OFF data as blue histogram. The vertical dashed lines indicates the cuts ($\alpha < 6^\circ$ and $\theta^2 < 0.03$ deg^2) used to define the signal region.

The difference between ON and OFF, for the Alpha and Theta square plots, gives the distribution of excess events and are shown in figure 6.5 (red points). In the left panel, we plot the distribution of excess events in campaign I around phases 0.4-0.7 ($\sim$ 10 hours of observation). The excess distribution is overlaid with the Monte-Carlo γ-ray prediction for a point source (black points) and agree well with them. The agreement is better in the second campaign (right panel), where the statistic is much larger.

The number of excess events, significance and integral flux above 400 GeV measured in each individual night are shown in tables 6.4 and 6.5. The maximum observed flux reaches almost 20% of the Crab Nebula flux at the same energy.

Figure 6.6 shows the sky maps produced with the Disp method (see Chapter 4) using the first campaign data in two different orbital phase bins: around periastron passage (phase between 0.2-0.3), over 15.5 hours. and at higher (0.4-0.7) orbital phases, using 10.7 hours of observation. In the maps, the number of events is normalized in both cases to 10.7 hours. No significant excess in the number of γ-ray events is detected around periastron passage, whereas there is a clear detection (9.4σ statistical significance) at later orbital phases. This

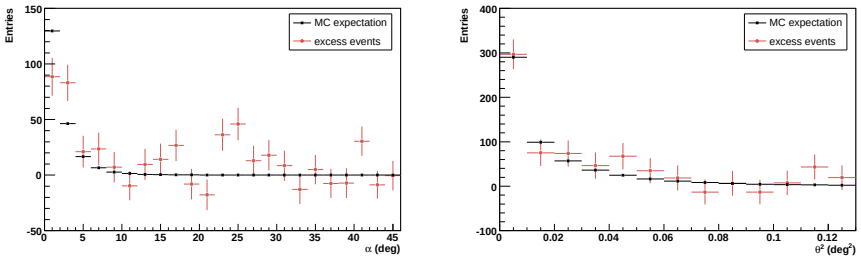

Figure 6.5: Alpha distribution of excess events, using data from campaign I at phases $0.4-0.7$ (left) and θ^2 distributions from the whole campaign II sample (right) are shown (in red). Overlaid, we plot the Monte-Carlo expectation for a point source (in black).

result shows that the γ-ray emission from LSI $+61°303$ is variable.

The excess seen in the later phases is consistent with a point-like source located at (J2000): $\alpha = 2^{\rm h}40^{\rm m}34^{\rm s}$, $\delta = 61°15'25''$, with statistical and systematic uncertainties of $\pm 0.4'$ and $\pm 2'$, respectively. This position is in agreement with the position of LSI $+61°303$. In the natural case in which the VHE emission is produced by the same object detected at EGRET energies, this result identifies a γ-ray source that resisted classification for the last three decades.

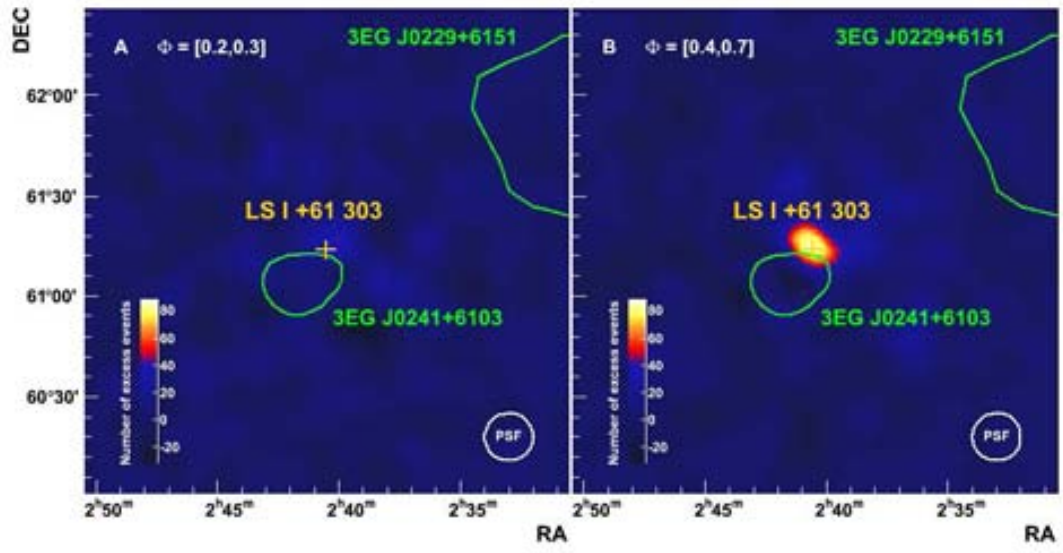

Figure 6.6: Smoothed maps of γ-ray events (background subtracted) 400 GeV around LSI $+61°303$ using data from campaign I. *(A)* Observations around periastron. *(B)* Observations at phase $0.4 < \phi < 0.7$. The position of the optical source LSI $+61°303$ (yellow cross) and the 95% confidence level contours for 3EG J0241+6103 and 3EG J0229+6151 (green contours) are also shown. The bottom right circle shows the size of the point spread function of MAGIC (1σ radius).

6.4 Light Curve

The integral γ-ray flux above 400 GeV versus the orbital phase obtained for each night of observation, are shown in Fig. 6.7 and 6.8 (upper panels). The measurements from both campaigns show that the VHE γ-ray emission from LSI $+61°303$ is variable. The probability for the distribution of measured fluxes to be a statistical fluctuation of a constant flux

Day (MJD)	N_{ON}	N_{Bkg}	F_{norm}	σ	T_{eff} (min)	Phase	Flux ($E > 400$ GeV) (10^{-12}cm^{-2}s^{-1})	Flux Upper Limit (10^{-12}cm^{-2}s^{-1})
53654.119	26	21	0.07	0.9	57	0.28	2.34 ± 2.80	11.24
53655.114	50	49	0.15	0.1	151	0.32	0.19 ± 1.55	4.54
53677.069	72	66	0.20	0.6	143	0.15	1.10 ± 1.85	6.92
53678.032	60	41	0.13	2.4	111	0.18	4.93 ± 2.20	-
53679.031	59	49	0.15	1.1	124	0.22	2.19 ± 1.96	8.54
53680.055	82	70	0.22	1.2	155	0.26	2.08 ± 1.77	8.38
53681.035	77	66	0.20	1.1	152	0.30	2.05 ± 1.88	8.01
53706.011	32	25	0.08	1.2	87	0.24	2.16 ± 1.95	8.56
53706.971	37	37	0.12	-0.1	140	0.27	-0.09 ± 1.38	3.74
53707.946	23	12	0.04	2.5	73	0.31	4.40 ± 2.01	-
53708.970	57	41	0.13	2.1	148	0.35	3.11 ± 1.58	-
53710.979	26	23	0.07	0.6	67	0.43	1.39 ± 2.34	8.68
53736.830	11	6	0.02	1.7	16	0.40	8.91 ± 5.99	31.40
53737.856	20	21	0.07	-0.2	85	0.44	-0.36 ± 1.68	4.36
53738.840	1	2	0.01	-0.6	10	0.48	-2.29 ± 3.40	11.25
53763.883	62	50	0.15	1.4	117	0.42	2.64 ± 1.90	10.05
53764.883	60	43	0.13	2.1	116	0.46	3.61 ± 1.85	-
53765.883	67	47	0.15	2.3	106	0.50	4.70 ± 2.15	-
53767.882	71	37	0.12	4.2	97	0.57	9.05 ± 2.41	-
53768.880	89	39	0.12	5.9	104	0.61	13.37 ± 2.65	-
53769.879	39	27	0.08	1.9	101	0.65	3.95 ± 2.30	14.44
53770.884	10	7	0.02	1.1	48	0.69	3.40 ± 3.48	20.54
53782.896	64	58	0.18	0.7	100	0.14	1.47 ± 2.29	9.88
53783.901	67	73	0.23	-0.6	105	0.18	-1.48 ± 2.35	5.46
53784.898	75	53	0.16	2.5	93	0.22	5.94 ± 2.56	-
53785.894	92	67	0.21	2.4	115	0.25	5.49 ± 2.37	-
53788.887	91	64	0.20	2.7	91	0.37	7.36 ± 2.92	-
53789.888	84	68	0.21	1.6	99	0.40	4.06 ± 2.70	14.70
53790.889	81	68	0.21	1.3	93	0.44	3.61 ± 2.86	14.45
53792.884	70	57	0.18	1.4	83	0.52	4.06 ± 2.91	15.39
53796.884	60	33	0.10	3.6	52	0.67	15.29 ± 4.74	-
53797.872	62	45	0.14	2.1	80	0.71	6.37 ± 3.19	-
53798.908	19	17	0.05	0.3	31	0.74	2.45 ± 7.35	19.85
53799.887	39	30	0.09	1.3	82	0.78	6.53 ± 5.12	24.19
Total					53.9 (h)			

Table 6.4: Number of ON and background events, normalization factor $F_{norm} = \frac{N_{Bkg}}{N_{OFF}}$ and the corresponding significance obtained from LSI +61°303 for each day in campaign I. The central time of the observation window (in MJD), the effective time duration of the observation, orbital phase and integral flux values above 400 GeV are quoted for each night. Flux upper limits at 95% CL following Rolke prescription [92] are given in the last column for those nights where the significance of the detection is lower than 2σ. The total effective time is given in the last row.

Day (MJD)	N_{ON}	N_{Bkg}	σ	T_{eff} (min)	Phase	Flux ($E > 400$ GeV) (10^{-12}cm^{-2}s^{-1})	Flux Upper Limit (10^{-12}cm^{-2}s^{-1})
53993.178	32	21	1.9	137	0.08	4.19 ± 2.34	8.70
53994.167	26	22	0.9	112	0.11	1.90 ± 2.15	6.33
53995.173	36	36	0.1	157	0.15	0.18 ± 1.75	3.71
53997.149	59	61	-0.2	229	0.23	-0.33 ± 1.41	2.61
53998.152	57	51	0.8	211	0.26	1.14 ± 1.50	4.29
53999.104	36	26	1.5	133	0.30	2.80 ± 1.93	6.69
54001.118	21	24	-0.6	91	0.38	-1.48 ± 2.45	3.39
54002.093	68	67	0.1	196	0.41	0.18 ± 1.79	3.97
54003.075	59	53	0.7	151	0.45	1.43 ± 2.06	5.86
54004.076	51	56	-0.6	170	0.49	-0.99 ± 1.77	2.92
54005.074	77	57	2.3	173	0.52	4.15 ± 1.93	-
54006.072	73	56	1.9	175	0.56	3.62 ± 1.99	8.11
54007.079	63	38	3.0	139	0.60	6.44 ± 2.34	-
54008.065	91	63	2.9	170	0.64	6.04 ± 2.23	-
54009.083	48	31	2.3	146	0.68	4.48 ± 2.06	-
54013.239	2	3	-1.1	7	0.83	-8.18 ± 6.74	14.59
54022.104	54	45	1.2	193	0.17	2.12 ± 1.88	6.42
54023.097	32	56	-2.8	276	0.20	-3.31 ± 1.08	0.74
54024.083	7	6	0.7	20	0.24	3.27 ± 5.43	16.6
54029.024	48	44	0.6	134	0.43	1.22 ± 2.25	5.88
54030.011	40	42	-0.2	167	0.47	-0.43 ± 1.78	3.08
54031.007	74	49	2.7	173	0.50	5.29 ± 2.07	-
54032.011	60	50	1.2	139	0.54	2.46 ± 2.17	7.31
54035.111	93	56	3.7	150	0.66	8.98 ± 2.65	-
54039.088	1	5	-1.2	93	0.81	-1.42 ± 1.08	0.99
54055.973	77	59	2.0	181	0.45	3.55 ± 1.83	7.78
54056.957	76	68	0.8	229	0.48	1.21 ± 1.58	4.53
54057.903	26	19	1.4	70	0.52	3.63 ± 2.81	10.64
54058.896	12	10	0.4	57	0.56	0.80 ± 2.26	6.09
54059.996	5	1	2.6	17	0.60	10.21 ± 5.65	-
54061.960	71	47	2.5	221	0.67	3.85 ± 1.61	-
54062.959	91	58	3.2	228	0.71	5.30 ± 1.75	-
54063.947	16	13	0.5	56	0.75	1.69 ± 3.29	7.73
54065.000	24	20	0.7	71	0.79	2.22 ± 3.07	8.84
54066.018	45	52	-0.9	185	0.82	-1.47 ± 1.66	2.25
54067.042	68	65	0.3	217	0.86	0.51 ± 1.71	4.11
54068.081	50	48	0.2	120	0.90	0.39 ± 2.24	5.51
54081.888	2	4	-1.0	17	0.42	-4.49 ± 4.09	5.52
54082.852	31	29	0.2	77	0.46	0.62 ± 2.77	6.85
54083.876	8	7	0.3	31	0.50	1.27 ± 4.34	9.91
54084.848	27	23	0.8	63	0.54	2.31 ± 3.12	9.42
54085.949	13	8	1.6	130	0.58	1.34 ± 0.92	3.78
54086.950	119	74	4.2	322	0.61	5.03 ± 1.30	-
54088.011	30	20	1.4	81	0.65	3.96 ± 2.88	10.7
54088.946	40	25	2.3	120	0.69	4.55 ± 2.12	-
54089.889	1	2	-0.5	31	0.73	-1.43 ± 2.48	1.84
54090.883	41	32	1.3	177	0.76	2.03 ± 1.64	5.13
54091.896	61	41	2.8	140	0.80	5.83 ± 2.26	-
54092.924	49	19	4.9	92	0.84	13.37 ± 3.23	-
54093.970	36	23	2.3	92	0.88	5.48 ± 2.60	-
54095.010	4	4	0.2	85	0.92	0.27 ± 1.13	2.63
54096.017	28	25	0.5	73	0.96	1.31 ± 2.85	8.06
54097.054	1	0	0.3	57	1.00	0.28 ± 0.94	1.76
Total				116.4 (h)			

Table 6.5: For each night in campaign II we quote the number of ON and background events, significance, central time of the observation window, effective time duration of the observation, orbital phase and integral flux of LSI +61°303 above 400 GeV.

(obtained from a χ^2 fit of a constant function to the entire data sample) is about 10^{-11}, with $\chi^2/NDF = 195.4/86$ (which corresponds to 3×10^{-5} and 4×10^{-6} for the individual campaigns I and II, respectively). The flux measurements for each orbital period can be compared in the phaseogram of Fig. 6.9 (upper panel), where each cycle is indicated in a different color.

The γ-ray flux is detected systematically around phase $\phi \sim 0.6$ every orbital cycle, with a maximum integrated flux above 400 GeV of $15\pm5\times10^{-12}$cm^{-2}s^{-1} on MJD 53796.9. A second maximum, reaching a similar flux level is measured in the last observed orbital cycle at phase 0.84 (on MJD 54092.9).

Around the periastron passage, the flux level is always below the MAGIC sensitivity. Following the ephemeris from Casares et al. (2005) [116] the periastron passage takes place at $\phi = 0.23$. At this phase, we have an individual measurement (MJD 53997.149) with a 95% CL upper limit on the flux above 400 GeV of 2.6×10^{-12}cm^{-2}s^{-1}. However, recent measurements from Grundstrom et al. (2007) [117] locates the periastron passage at a phase $\phi = 0.30$, for which we derive an upper limit of 6.7×10^{-12}cm^{-2}s^{-1} (night MJD 53999.1).

We have computed the average flux versus orbital phase for each individual campaign (figures. 6.7 and 6.8) and for the whole data sample (Fig. 6.9). The maximum flux level is observed in the phase bin 0.6-0.7 yielding an average integral flux of $F(E > 400\text{GeV}) = 5.7 \pm 0.6_{\text{stat}} \pm 2.4_{\text{syst}} \times 10^{-12}\text{cm}^{-2}\text{s}^{-1}$. This corresponds to ∼8% of the Crab Nebula flux at the same energy.

The fact that the detections always occur at similar orbital phases hints at a periodic nature of the VHE γ-ray emission, which will be studied in detail in Sec. 6.6.

Phase bin	Campaign I		Campaign II		Campaign I+II	
	T_{obs} (min)	Flux (10^{-12}cm^{-2}s^{-1})	T_{obs} (min)	Flux (10^{-12}cm^{-2}s^{-1})	T_{obs} (h)	Flux (10^{-12}cm^{-2}s^{-1})
0.0-0.1			137	4.2 ± 2.3	2.3	0.6 ± 0.9
0.1-0.2	459	1.6 ± 1.1	462	1.3 ± 1.1	15.3	1.4 ± 0.8
0.2-0.3	923	2.1 ± 0.7	869	-0.8 ± 0.7	29.9	0.7 ± 0.5
0.3-0.4	462	2.8 ± 0.9	91	-1.5 ± 2.4	9.2	2.2 ± 0.9
0.4-0.5	710	2.3 ± 0.8	1353	0.7 ± 0.7	34.4	1.4 ± 0.5
0.5-0.6	181	7.9 ± 1.9	997	2.5 ± 0.6	19.6	3.0 ± 0.6
0.6-0.7	305	7.9 ± 1.5	1341	5.2 ± 0.7	27.4	5.7 ± 0.6
0.7-0.8	193	5.9 ± 2.5	558	2.5 ± 1.0	12.5	2.9 ± 0.9
0.8-0.9			822	0.7 ± 0.7	13.7	0.5 ± 0.6
0.9-1.0			335	0.3 ± 0.7	5.6	0.2 ± 0.6

Table 6.6: Average flux above 400 GeV of LSI +61°303 and observation time T_{obs} at each orbital phase bin for campaigns I, II and both together.

6.4.1 Intranight variability

LSI +61°303 was found to be variable on timescales of days in the previous section. A still open question is whether it also shows variability on shorter time scales.

We investigated the data set for intranight variability. We subdivided those nights with significant flux level $F(E > 400\text{GeV}) > 4 \times 10^{-12}\text{cm}^{-2}\text{s}^{-1}$ on time scales ranging from 30 to 75 minutes, in steps of 15 minutes. This flux level threshold will prevent us from counting non significant changes of flux fluctuations below zero.

For campaign I, this cut yields 11 suitable nights. Among those, the longest one was 30th January 2006, MJD 53768.88, which corresponds to the orbital phase 0.46. Its intranight light curve is show in Fig. 6.10, where each bin has ∼29 min width. The light curve is fitted to a constant flux level with a probability of 88% ($\chi^2 = 0.66/3$), which corresponds to a post-trial chance probability of 99%. From all the inspected nights, the one showing the maximum intranight variation is 4th March 2006, MJD 53797.87 ($\phi = 0.71$). The intranight

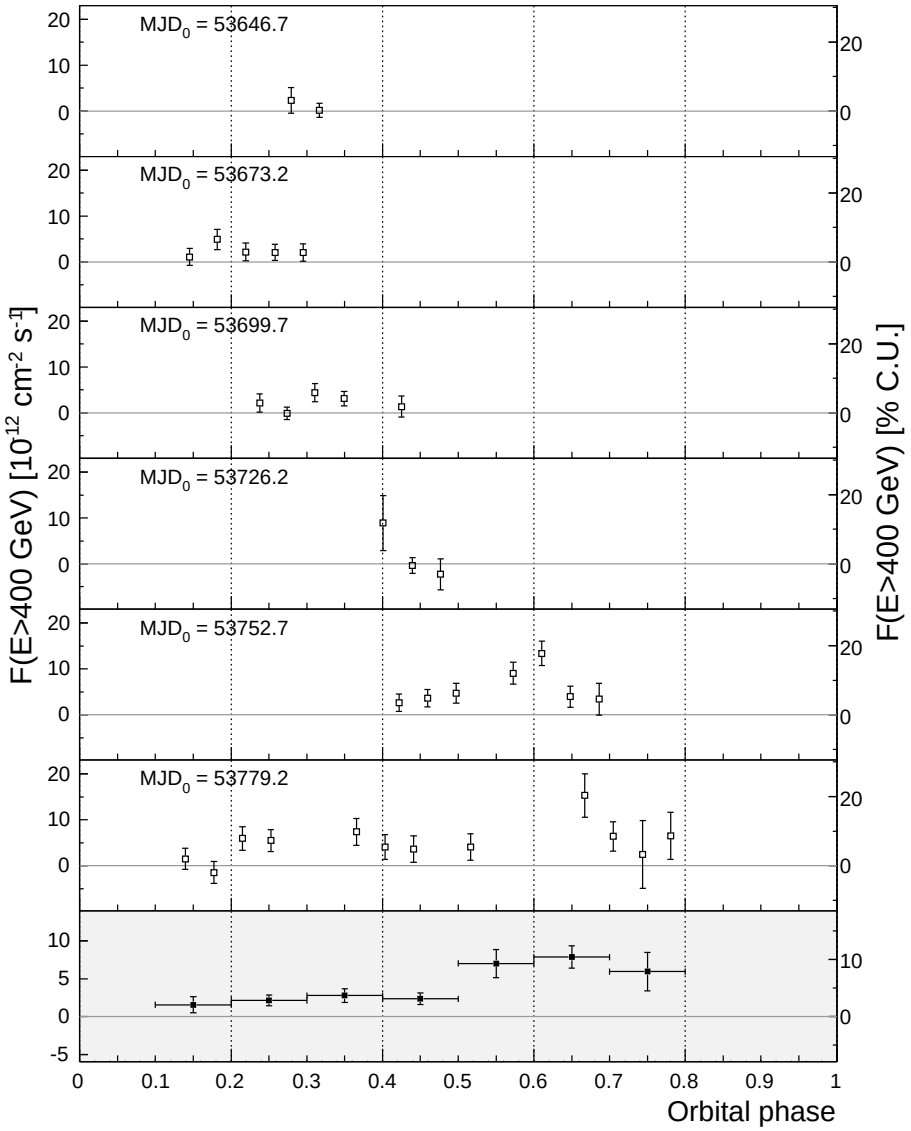

Figure 6.7: VHE γ-ray flux of LSI +61°303 as a function of the orbital phase, for campaign I. In the six upper panels, the individual orbital cycles are shown (from October 2005 to March 2006), with one point per observation night. The bottom panel shows the averaged flux over those periods. Vertical error bars include 1σ statistical error and 10% systematic uncertainty on day-to-day relative fluxes. The modified Julian date (MJD) corresponding to orbital phase 0 is indicated for every orbital period. Right axis indicates the flux level in Crab Units, as measured by MAGIC $\frac{\mathrm{d}F}{\mathrm{d}E} = 5.7 \times 10^{-10} \left(\frac{E}{300\mathrm{GeV}}\right)^{-2.48}$ $\mathrm{cm}^{-2}\mathrm{s}^{-1}\mathrm{TeV}^{-1}$ [72].

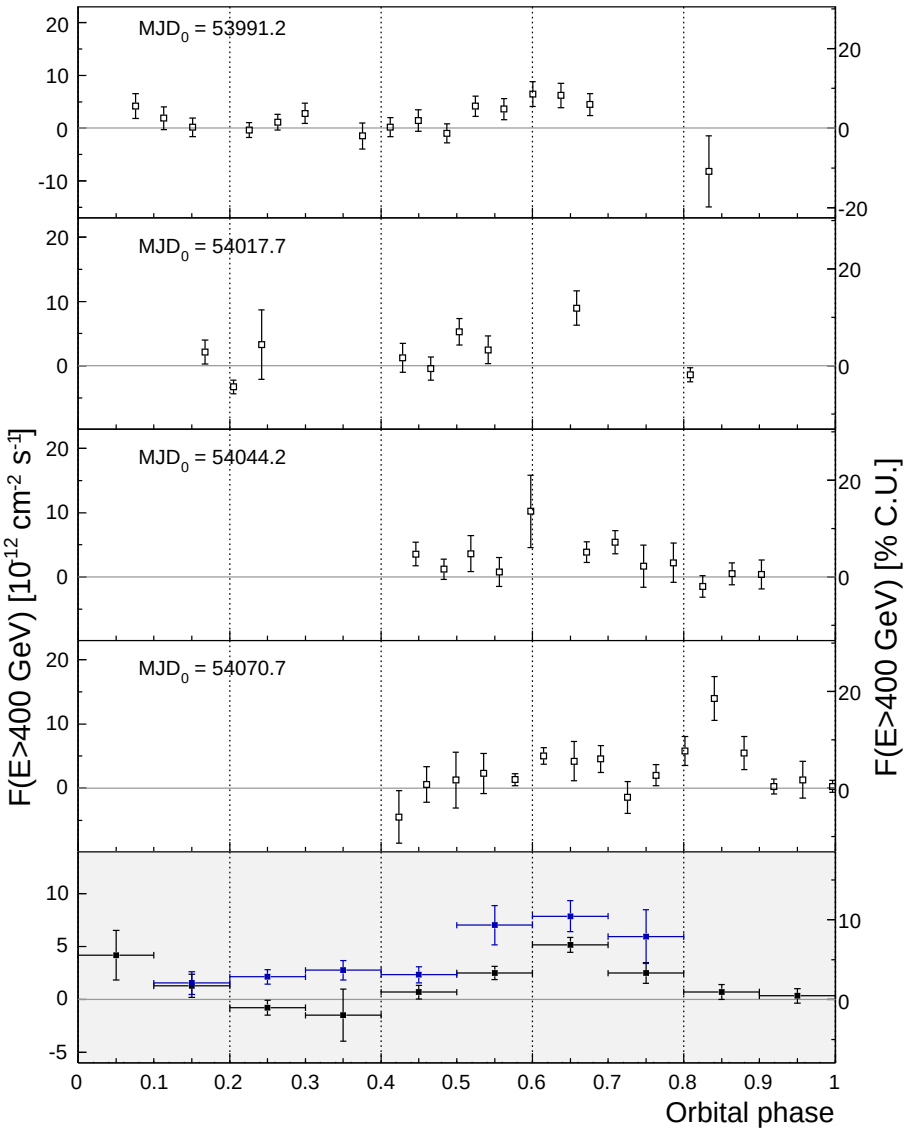

Figure 6.8: VHE γ-ray flux of LSI +61°303 as a function of the orbital phase, for campaign II. In the four upper panels, the individual orbital cycles are shown (from September to December 2006), with one point per observation night. The bottom panel shows the averaged flux for campaign II (in black) and I (in blue). Vertical error bars include 1σ statistical error and 10% systematic uncertainty on day-to-day relative fluxes. The MJD corresponding to orbital phase 0 is indicated for every orbital period. Right axis indicates the flux level in Crab Units, as measured by MAGIC [72].

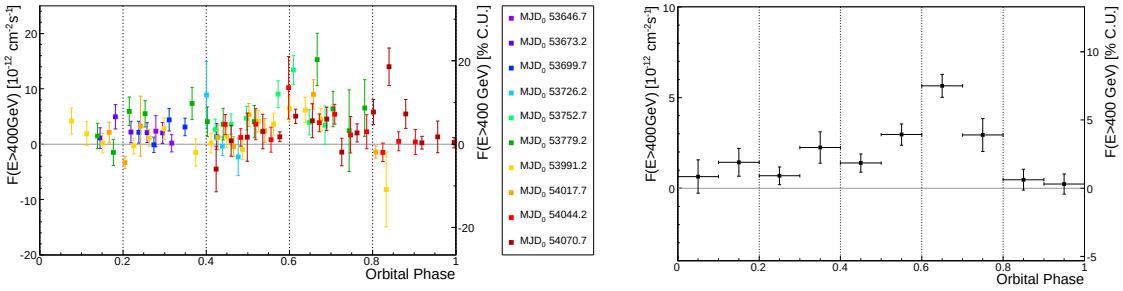

Figure 6.9: Left panel: Integral γ-ray flux of LSI +61°303 above 400 GeV as a function of the orbital phase [116] (10 orbital cycles) on a day-by-day basis ,folded with the orbital period of 26.496 days. Each colour represent a different orbital period: the MJD corresponding to the orbital phase 0 is indicated in the legend. Right panel: Average integral γ-ray flux of LSI +61°303 above 400 GeV phaseogram for both data taking campaigns. Right axes indicate the flux level in Crab Units [72].

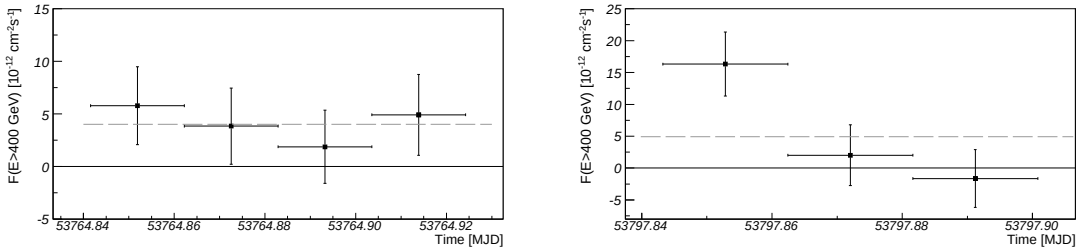

Figure 6.10: Integral flux above 400 GeV for two nights in campaign I: the longest observed one 30th January 2006 (MJD 53768.9) (left) and the one which show maximum intranight variation 4th March 2006 (MJD 53797.9) (right). The post-trial chance probability of the flux being a statistical fluctuation of a constant flux are 99% and 20%, respectively.

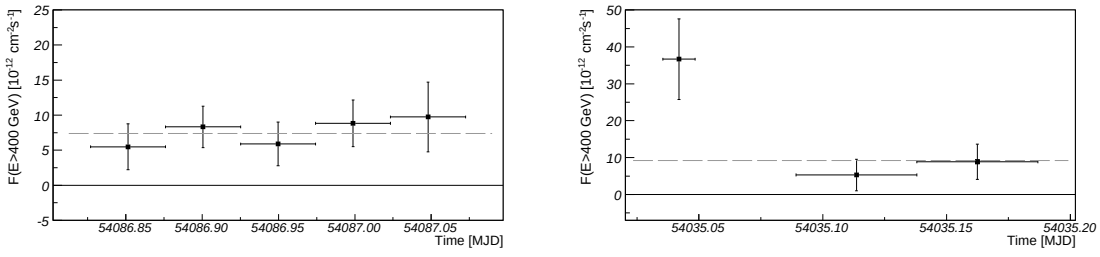

Figure 6.11: Intranight integral flux curve above 400 GeV two nights in campaign II: the longest observed one 18th December 2006 (MJD 54086.95) (left) and the one which show maximum intranight variation 27th October 2006 (MJD 54035.11) (right). The post-trial chance probability of the flux being a statistical fluctuation of a constant flux are 99% and 30%, respectively.

light curve is shown in Fig. 6.10, were each bin has ∼26 min width. The pre and post-trial chance probability for this night are 2% ($\chi^2 = 7.61/2$) and 20%, respectively.

We also investigated the data from campaign II. We selected the 13 longest nights with a mean flux above 400 GeV higher than 4×10^{-12}cm^{-2}s^{-1}. Among them, the light curve for the longest night (MJD 54086.95, phase 0.61) shows a constant flux with probability of 90% ($\chi^2 = 1.08/4$), which corresponds to a post-trial chance probability of 99%. The light curve for that night is shown in Fig. 6.11, were each bin has ∼1 hour width. In the same figure we show the light curve for the night showing the maximum intranight variation in cycle II (MJD 54035.11). For that night, the post-trial probability of being random fluctuation of a constant flux is about 31%.

We conclude that any putative variation of the VHE emission of LSI +61°303 on timescales of $30 - 75$ minutes is below the sensitivity of MAGIC, since the post-trial chance probability are not significant.

6.5 Spectral Variability

The VHE spectrum derived for campaign I between ∼200 GeV and ∼4 TeV at orbital phases between 0.4 and 0.7 is shown in Figure 6.12. For the spectrum calculation we combined the 4 nights in period 38 with individual significances above 2σ (MJD 53764.9, 53765.9, 53767.9 and 53768.9) which summed up to 7 hours of data. The resulting average differential energy spectrum can be fitted ($\chi^2/NDF = 6.6/5$) to a power law function:

$$\mathrm{d}N_\gamma/(\mathrm{d}A/\mathrm{d}t/\mathrm{d}E) = (2.7 \pm 0.4 \pm 0.8) \times 10^{-12} \times E^{(-2.6\pm0.2\pm0.2)} \quad \mathrm{cm}^{-2}\mathrm{s}^{-1}\mathrm{TeV}^{-1}$$

where N_γ is the number of gamma rays reaching the Earth per unit area A, time t and energy E (expressed in TeV). Errors quoted are statistical and systematic, respectively. This spectrum is consistent with that measured by EGRET only if we assume a spectral break between 10 and 100 GeV.

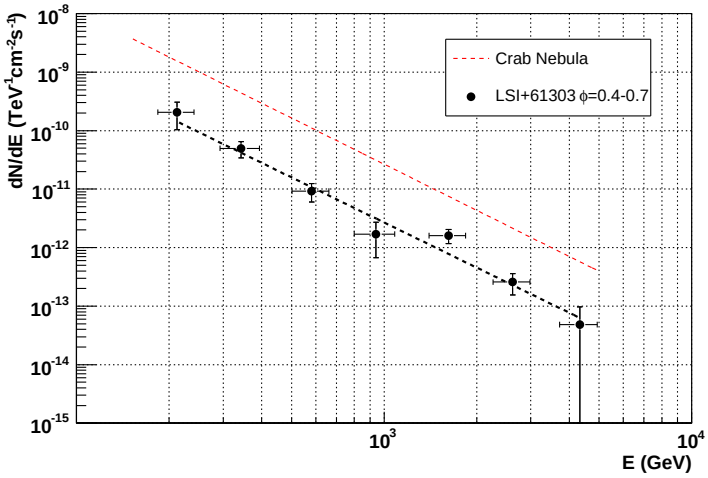

Figure 6.12: Differential energy spectrum for LSI +61°303 campaign I for energies between 200 GeV and 4 TeV and averaged for orbital phases between 0.4 and 0.7. The error bars show the 1σ statistical uncertainty. The solid, black line is a fit of a power law to the measured points, whose parameters are given in the text. The dashed, red line corresponds to the Crab Nebula differential spectrum also measured by MAGIC [72].

For campaign II, we measured significant flux levels for the phases $0.5 < \phi < 0.6$ and $0.6 < \phi < 0.7$. For these two phase bins, we were able to determine the differential energy spectra, as shown in Fig. 6.13. They are both compatible with a power law. The fit parameters are summarized in Table 6.7.

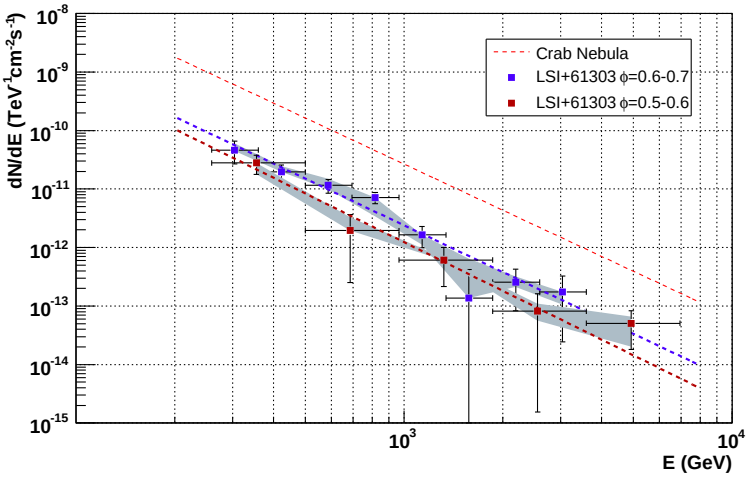

Figure 6.13: Differential energy spectra for LSI +61°303 campaign II and orbital phases between 0.5-0.6 (red points) and 0.6-0.7 (blue points). Both energy spectra are obtained using the *Bertero* unfolding method. The systematic uncertainty from using different unfolding methods is shown by the grey area. The x-axis error bars indicate the width of the energy bins. The dotted, color lines are fits of a power law to the measured points. The fit parameters are tabulated in table 6.7. For comparison, the Crab Nebula energy spectrum as measured by MAGIC is shown [72] (red dashed line).

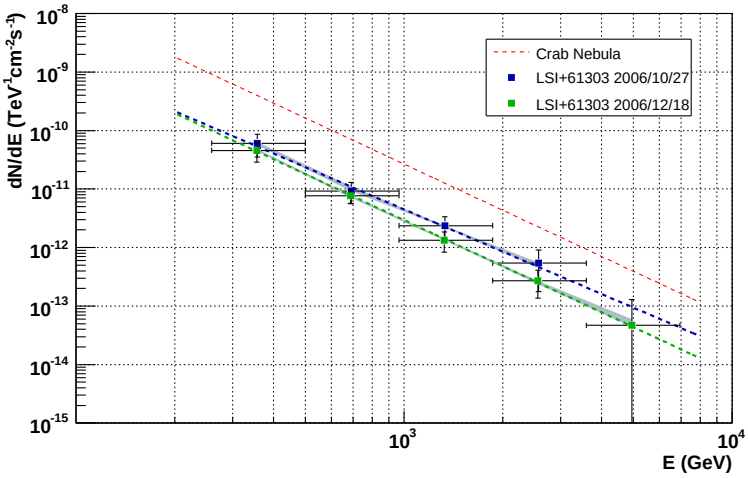

Figure 6.14: Differential energy spectrum for two individual nights of campaign II: 2006/12/18 (in green) and 2006/10/27 (in blue), both with orbital phases between 0.6-0.7. Both energy spectra are obtained using the *Bertero* unfolding method. The systematic uncertainty from using different unfolding methods is shown by the grey area. The x-axis error bars indicate the width of the energy bins. The dotted, color lines are fits of a power law to the measured points. The fit parameters are tabulated in table 6.7. For comparison, the Crab Nebula energy spectrum as measured by MAGIC is shown [72] (red dashed line).

Campaign	Phase/Date	f_0 (10^{-12}cm^{-2}s^{-1})	α	χ^2/NDF
I	0.4-0.7	2.69± 0.45	2.56 ± 0.21	6.60/5
II	0.5-0.6	1.23± 0.33	2.77 ± 0.47	2.59/3
	0.6-0.7	2.40± 0.34	2.65 ± 0.20	5.07/5
	2006/10/27	4.49± 1.22	2.40 ± 0.47	0.50/2
	2006/12/18	2.94± 0.60	2.62 ± 0.33	0.06/3

Table 6.7: Parameters from a power law fit to the different LSI +61°303 spectra. The power law fit has the form $\mathrm{d}N/\mathrm{d}E = f_0(E/1\mathrm{TeV})^{-\alpha}$. The quality of the fit is given in terms of χ^2 divided by the number of degrees of freedom (NDF).

In addition we derived differential energy spectra for two nights with high signal significance $\gtrsim 4\sigma$ (2006/10/27 and 2006/12/18) in the phase bin $0.6 < \phi < 0.7$. Both spectra are shown in Fig. 6.14 and are well fitted with power laws, whose parameters are given in Table 6.7. No evidence for spectral variations has been found.

The obtained spectral indices are compatible within errors with a constant value, indicating that any spectral change happening between the different phase bins and between the different explored orbital cycles is below the sensitivity of the instrument. The spectral index is rather stable during the phases where LSI +61°303 is detected at TeV energies. In the phase bins $0.0 < \phi < 0.5$ and $0.7 < \phi < 1.0$ the γ-ray flux is too low to obtain meaningful differential energy distributions. Thus we can not draw conclusions for these phase bins.

The spectra for individual nights could only be obtained for the two samples with the highest significance. However, for the days with lower flux significance, we can still investigate the spectral hardness, which is given by the hardness ratio HR, defined as the ratio of the fluxes in two energy bands, namely $E > 900$ GeV and $300 < E < 900$ GeV. Figure 6.15 show the HR as a function of the integral flux above 300 GeV. Only data samples with significance flux are considered (significance above 1.5σ for the flux above 300 GeV). We do not find any clear correlation between the HR and the flux level. The evolution of the HR with the orbital phase and time is shown in Fig. 6.16. The hardness ratio is constant within errors.

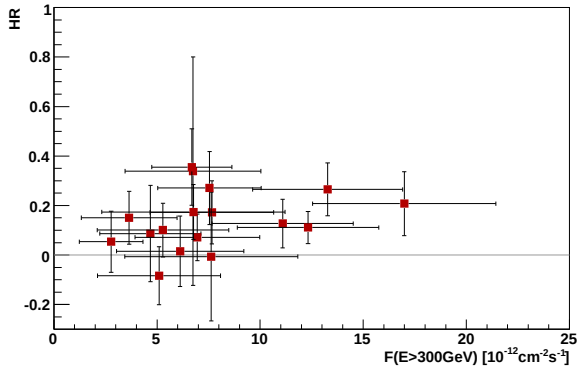

Figure 6.15: Hardness ratio $F(E > 900\ \mathrm{GeV})/F(900 > E > 300\ \mathrm{GeV})$ as a function of the integral flux above 300 GeV. Only nights with significance above 1.5σ are considered. No clear correlation is found.

In figure 6.17 we present a broad band spectrum of LSI +61°303. The radio data points are taken from [195]. CGRO data points are from [196, 155], and MAGIC points correspond to cycle I presented in this work. As an eye guide, the solid (dashed) line shows a model with synchrotron-inverse Compton model for the high (low) flux state, as proposed by [154] assuming a young pulsar powered source.

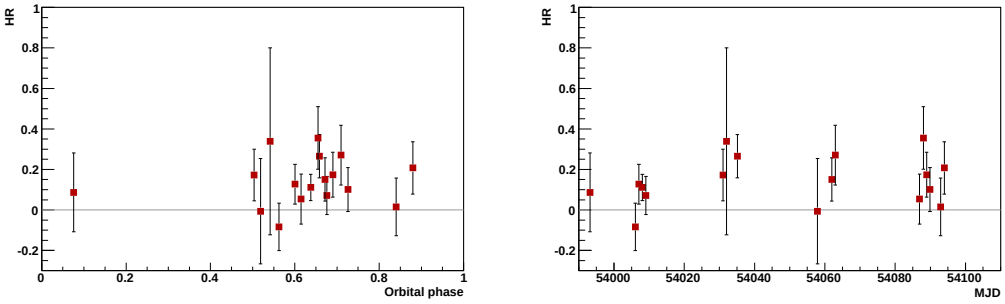

Figure 6.16: Hardness ratio $F(E > 900\ \mathrm{GeV})/F(900 > E > 300\ \mathrm{GeV})$ as a function of the orbital phase (left) and MJD (right). Only nights with significance above 1.5σ are considered. No clear correlation is found.

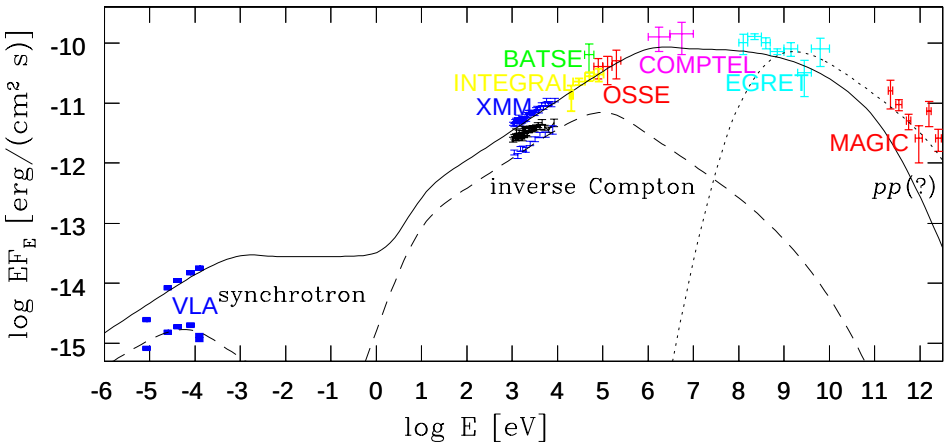

Figure 6.17: Broad band spectral energy distribution from [154]. In red, MAGIC data points from this work.

6.6 Periodicity Analysis

The emission of the LSI +61°303 binary system is not only variable but periodic in radio, optical and X-rays (see chapter 5). In all of these wavebands the period of the modulation in the signal corresponds to the orbital period within the errors of the measurements. Because of this it is assumed that the variability could be linked to the geometrical properties of the system. No periodicity was found in the EGRET measured HE emission, but the lack of statistics prevent us from drawing a valid conclusion out of this fact. One of the major aims of the extension of the observation to the second campaign on LSI +61°303 was to search for periodicity in the VHE emission.

In the next sections we describe the methods used for analysing the temporal characteristics of LSI +61°303 MAGIC data. The aim of this study is to find whether within the LSI +61°303 TeV observations exists a periodic behaviour. The data consists of a series of γ-ray candidates arrival times which may be folded at a given frequency to produce a phase distribution of the total data set.

The TeV data sample under study comprises campaign I and II, with 54 and 116 hours respectively. In total 10 orbital periods were covered. The measurements from both campaigns show that the VHE γ-ray emission from LSI +61°303 is variable (see Sec. 6.4). The fact that the detections occur at similar orbital phases $\phi \sim 0.6$ already hints at a periodic nature of the VHE γ-ray emission.

In order to test for possible periodic structures in the TeV light-curve, we use two methods: the formalism developed by Lomb and Scargle [197, 198] and the Rayleigh statistic test [199]. We first review the statistical tests with its characteristics and describe the methods used for obtaining the chance probability. Then after some technical considerations, we apply them to the LSI +61°303 TeV data.

6.6.1 Statistical tests

When a periodic signal with a certain frequency and/or shape is expected, a specific test can be applied; otherwise a more general test of uniformity must be used. Two of the general tests are the Rayleigh [199] and the Lomb-Scargle tests [198]. Both are based on the Fourier transform, which we introduce here.

A physical variable x_j (the integral γ-ray flux above 400 GeV in our case) is measured a set of times t_j where $j = 1, ...n$. The discrete Fourier transform is defined as

$$FT_X(\omega) = \sum_{j=1}^{n} x_j e^{-i\omega t_j} \tag{6.1}$$

where ω is the angular frequency, defined as $\omega = 2\pi\nu$. The so-called classical periodogram (spectral power as a function of frequency) is defined as:

$$\begin{aligned} P_{\text{class}}(\omega) &= \frac{1}{n}|FT_X(\omega)|^2 \\ &= \frac{1}{n}\left[\left(\sum_{i=1}^{n} x_i \cos(\omega t_i)\right)^2 + \left(\sum_{i=1}^{n} x_i \sin(\omega t_i)\right)^2\right] \end{aligned} \tag{6.2}$$

([198] and references therein). If the measured signal is dominated by a sinusoidal component with angular frequency ω_0, the factors x_j and $e^{-i\omega_0 t_j}$ are in phase. As a result, the sums in eq. 6.2 and therefore the periodogram $P_{\text{class}}(\omega)$ reaches a local maximum for ω equal or close to ω_0. At frequencies significantly different from ω_0 the factors x_j and the exponential are out of phase, the individual factors of the sum cancel with each other in average and the periodogram has a small value. Thus, prominent frequency components in the data are visible as peaks in the periodogram [200].

In the case of *even data spacing*, the significance of a certain frequency power is estimated by means of hypothesis testing: Given the null hypothesis that the data sample only consists

of Gaussian white noise[2], the values in the periodogram follow an exponential probability density function (PDF):

$$\mathcal{P}(z < P_{\text{class}}(\omega) < z + \mathrm{d}z) = e^{-z}\mathrm{d}z \tag{6.3}$$

We treat in detail the problem of the significance estimation in section 6.6.1.4.

6.6.1.1 Rayleigh test

The Rayleigh power at a particular frequency is a measure of the probability that the data contain a sinusoidal component with a frequency. The Rayleigh test is a special case of the classical periodogram, where t_i for $i = 1, \cdots n$ are the set of arrival times where γ-ray event candidates are detected (also called *sampling*).

The power of the Rayleigh test $R(\omega)$ as a function of the angular frequency ω (the periodogram) is defined as:

$$R(\omega) = 2n \left[\left(\frac{1}{n} \sum_{i=1}^{n} \cos(\omega t_i) \right)^2 + \left(\frac{1}{n} \sum_{i=1}^{n} \sin(\omega t_i) \right)^2 \right] \tag{6.4}$$

In absence of a periodic signal, $R(\omega)$ follows a χ^2 distribution with two degrees of freedom as n tends to infinity. This is so because $\cos \omega t_i$ and $\sin \omega t_i$ are Gaussian distributed, the square of a Gaussian variable is χ^2 distributed and the sum of χ^2 variables is also a χ^2 variable for which the number of degrees of freedom is given by the sum of the degrees of freedom from the individual variables. In general, the χ^2 PDF with k degrees of freedom is

$$PDF(\chi^2) = \frac{(1/2)^{k/2}}{\Gamma(k/2)} x^{k/2-1} e^{-x/2} \tag{6.5}$$

Then the χ^2 for $k = 2$ degrees of freedom is an exponential function (recovering the result of eq. 6.3).

But this exponential behaviour is only achieved for uniform random distributions, where the arrival times t_i are homogeneously sampled over time or *evenly sampled*. If the set of arrival times is *unevenly sampled* (arbitrary t_i's) or has gaps with uncovered phases, eq. 6.5 does not hold and a dedicated Monte-Carlo must be developed to determine the PDF of the Rayleigh power. We develop further on this issue in section 6.6.1.4.

In the case of LSI $+61°303$ TeV data, we perform the test using as physical quantities t_i, the arrival times of the events passing all signal selection cuts (including θ^2 or α cut). These events are referred to as the ON sample. Note from eq. 6.4 that the t_i are the only observables entering the Rayleigh test. For the sake of computing the chance probability (see Sec. 6.6.1.4) we merge the events into 15 minute bins, and assign all of them a common, average arrival time. This has no practical effect on the accuracy of the periodogram since the scanned frequencies are much smaller than $\frac{1}{15\text{min}} = 96\ \text{day}^{-1}$. We discuss about the effect of selecting different binnings in section 6.6.3.

6.6.1.2 Lomb-Scargle test

In the case of *unevenly sampled* data, one can recover a relatively simple behaviour of the power PDF with a slightly modified definition of the classical periodogram. The Lomb-Scargle periodogram as a function of the angular frequency ω is defined as [198, 200]:

$$P(\omega) = \frac{1}{2\sigma_X^2} \left[\frac{[\sum_{i=1}^{n}(x_i - \bar{X}) \cos(\omega(t_i - \tau))]^2}{\sum_{i=1}^{n} \cos^2(\omega(t_i - \tau))} + \frac{[\sum_{i=1}^{n}(x_i - \bar{X}) \sin(\omega(t_i - \tau))]^2}{\sum_{i=1}^{n} \sin^2(\omega(t_i - \tau))} \right] \tag{6.6}$$

where the phase factor τ is defined as:

$$\tau = \frac{1}{2\omega} \arctan \left(\frac{\sum_{i=1}^{n} \sin(2\omega t_i)}{\sum_{i=1}^{n} \cos(2\omega t_i)} \right) \tag{6.7}$$

[2]A time series of independent Gaussian random numbers is denoted as Gaussian white noise

and $\bar{X}$ and σ_X^2 are the mean and variance of the variable x_i. τ is an offset that makes $P(\omega)$ completely independent of shifting all the t_i's by a constant.

The Lomb-Scargle periodogram has the same theoretical exponential PDF as the classical periodogram (in case of evenly spaced data, expression 6.6 tends to 6.2). This statement, however, relies on the fact that the periodogram is offset by the mean $\bar{X}$ and normalised onto the variance σ_X^2. When the mean and variance are not known a priori, they have to be estimated from the data themselves. As a result the PDF (eq. 6.3) changes into [201]:

$$\mathcal{P}(z < P(\omega) < z + \mathrm{d}z) = \left(1 - \frac{2z}{n}\right)^{\frac{n}{2}} \mathrm{d}z \tag{6.8}$$

For small Fourier power values z and a large number of data points n, this distribution converges to the exponential distribution.

We perform the practical application of the Lomb-Scargle method to the LSI +61°303 TeV data as following. We calculate the periodogram using as input x_i the integral flux above 400 GeV, measured in a time interval $[t_i - \frac{\Delta t}{2}, t_i + \frac{\Delta t}{2}]$ (where Δt is the width of the time bin). As in the Rayleigh test we calculate the fluxes in $\Delta t = 15$ minute bins.

However, there is an other possibility to apply the Lomb-Scargle test, without relying on the MC. In that case, x_i, is the number of arrival γ-ray candidates in a time interval $[t_i - \frac{\Delta t}{2}, t_i + \frac{\Delta t}{2}]$ passing all signal selection cuts and background subtracted (so called N_{ex}), which can be positive (excess) or negative (defect). As in the Rayleigh test, and for the sake of computing the chance probability (see Sec. 6.6.1.4) we merge the events into 15 minute bins, and assign all of them a common, average arrival time. In this case we will see in Sec. 6.6.1.5 that we have to compensate or equalize the number of excess by the number of γ-ray candidates arrived in the same window interval in the background region. With this method, we do not need to rely in MC simulations, since we use only the number of γ-ray candidates in the ON and background regions. Therefore, using the equalization we can correct for any periodic change in the telescope sensitivity that is not reproduced by MC. We will perform the Lomb-Scargle test over the TeV LSI +61°303 data using also this second approach to cross-check of the results.

6.6.1.3 Natural frequencies

Given n data points there is a discrete finite set of $n/2$ independent frequencies in the periodogram. For the case of *evenly spaced* data there is a natural set of frequencies

$$\omega_k = 2\pi k/T;\ k = 1, \cdots, n/2 \tag{6.9}$$

where $T = t_{last} - t_{first}$ is the total time interval spanned by the data set. These frequencies are selected so that their discrete Fourier transform (eq. 6.1) contains just enough information to recover the original data. The Fourier power values $FT(\omega_k)$ are independent of each other.

The fundamental frequency (or Independent Fourier Spacing, IFS) $\omega_1 = 2\pi/T$, corresponds to a sine wave of period equal to the whole interval T and is the lowest frequency for which the data contain relevant information.

The so-called Nyquist frequency is $\omega_{Ny} = \omega_{n/2} = n\pi/T = \pi\Delta t$ where $\Delta t = T/n$ is the sampling interval. This characterises the largest frequency component which can be resolved by the given data spacing Δt. In table 6.8 we show the value of the fundamental and Nyquist frequencies for our data samples.

Campaign	n points	T (days)	ν_1 or IFS (d^{-1})	ν_{Ny} (d^{-1})
I	226	145	0.00686	0.779
II	491	103	0.00972	2.386
I+II	717	441	0.00226	0.813

Table 6.8: For each observational campaign we show the number of points (using 15 minute bins), the total elapsed time T and the fundamental (or IFS) and Nyquist frequencies.

In case the sampling is *uneven*, the situation becomes more complex, since the natural frequencies are no longer independent. But if the grid of frequencies is carefully selected, the degree of dependence between the powers at the different frequencies is usually small.

The fundamental frequency ω_1 is unchanged for even or uneven sampling, since the interval T is still well defined. But the Nyquist frequency might change with the data sampling (especially when the data points are closely clumped together, like in our case). The Nyquist frequency can be estimated by means of the *spectral* or *periodogram window* [198, 200]:

$$W(\omega) = \frac{1}{N} \left| \sum_{j=1}^{n} e^{-i\omega t_j} \right|^2 \tag{6.10}$$

This function, evaluated at $W(\omega - \omega')$, gives the correlation coefficient between $P(\omega)$ and $P(\omega')$ for arbitrary ω and ω'. Thus this quantity contains all relevant information about dependencies and correlations. For $P(\omega)$ and $P(\omega')$ to be independent, it is necessary (but not sufficient) that $W(\omega - \omega') = 0$. Furthermore, for mutual independence of a set $P(\omega_k)$ of spectral powers, it would be also necessary (but not sufficient) to have the ω_k evenly spaced. These are very difficult conditions to realise in practice.

The power of the final periodogram is actually given by the convolution of the true physical process with the spectral window. The pathology of the data distribution is all contained in the spectral window, which can be calculated from the data spacing alone, and does not depend directly on the data themselves. The interference of the spectral window can be described as one of two types: due to the finite length of the data and due to the data spacing, which is called *aliasing*. For continuously recorded data, aliasing does not exit, while for equally spaced data, it exists in its most extreme form. In astronomical observations, such aliasing often arises due to one day, one month, or one year gaps in the data.

The straightforward generalisation of the spectral window to the Lomb-Scargle periodogram (replacing the term $x_i - \bar{X}$ in eq. 6.6 by unity) is not completely correct window function (see [198], Appendix D). But nevertheless, as suggested by Kranich (2001) [200], the windowing function gives some hints on the independent frequency components. The periodogram window for the LSI +61°303 observations in the second campaign is shown in Fig. 6.18. The maximum shows up at $\nu = 1\mathrm{d}^{-1}$ (day-night interruptions). In campaign II the step between the natural frequencies is $\nu_1 = \frac{1}{103\mathrm{days}} \simeq 0.01\mathrm{d}^{-1}$ for which the windowing function is $W(0.01) \simeq 10$. This means that there is correlation between the scanned frequencies.

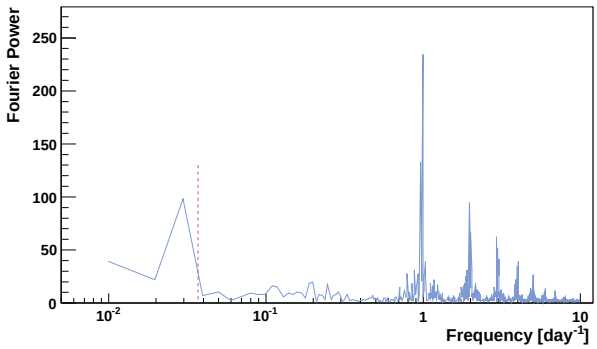

Figure 6.18: Windowing function as derived for the LSI +61°303 data in campaign II. The red dotted line marks the LSI +61°303 orbital period of 26.496 days.

But in spite of the loss of independence of the random variables $P(\omega)$ at the natural frequencies, the *chance probability* (see below Sec. 6.6.1.4) still provides a reliable significance test [202]. We will evaluate the modified periodogram at the natural frequencies defined by the data span, and use the chance probability calculated or estimated from the Monte-Carlo simulation (see Sec. 6.6.1.4) for unevenly spaced data to evaluate the significance of the periodogram peaks.

In this study, we scan frequencies up to 0.25 d^{-1}, which covers the frequency of interest ($1/26.496 = 0.038 d^{-1}$) while keeping relatively low the number of trials.

6.6.1.4 Estimation of the chance probability

Given the probability distribution for the spectral power, we can write down an expression for the so called *post-trial chance* or *false alarm* probability. If the probability that a spectral power z is above some value z_0 is $\mathcal{P}(z > z_0)$ (also called *pre-trial* probability), then the post-trial probability F is given by

$$F = 1 - (1 - \mathcal{P}(z > z_0))^M \tag{6.11}$$

where M is the number of independent frequencies that were examined. Thus F is the probability that *at least one* of the computed powers z is above the threshold z_0. A small value for the chance probability indicates a highly significant periodic signal.

However the principal difficulty encountered when searching for a false alarm function in the case on unevenly spaced data is the loss of the independence of the natural frequencies (see section 6.6.1.3). The only alternative to a theoretical chance probability function is an empirically generated one.

The practical method for determining the chance probabilities is, as suggested by [202], the following:

1. Using the sampling times of the actual data set to be analysed, we construct a large number of random data series.

2. Select a convenient grid of frequencies that cover the frequency range in the periodogram that is to be inspected (see section 6.6.1.3 for how to choose them).

3. For each random series, we construct a periodogram sampling it for the selected frequencies.

4. For each frequency, we compare the power of the real data set with the PDF obtained from the random series, in order to determine empirically the (pre-trial) probability of this power to happen by chance.

5. The overall (post-trial) chance probability is computed by the following generalisation: for each simulated data series we inspect the corresponding periodogram, identify the highest power that occurs at any of the pre-selected frequencies, and use its highest values to construct the post-trial PDF.

By integrating the PDF from a given power value z_0, we obtain an empirical cumulative probability function (CPF). The CPF is used to determine the probability that pure noise alone could produce a power higher than or equal to a given threshold power value z_0 for one (pre-trial) or any (post-trial) of the selected frequencies. The influence of the uneven sampling in the observation time has been taken into account.

The maximum power in the CPF constructed in this way depends on the number of generated random data series. If a power of the actual time series is below the maximum power in the CPF, we can empirically determine its probability. If on the contrary, the power for the actual time series is above the maximum power of the random generated series, we can only resort to fitting the CPF with the false alarm function of choice. If fit succeeds, we can calculate the significance for the given data set.

If the fit is not good however, the significance levels predicted by these fitted functions are likely to lead to erroneous rejection or acceptance of periodogram peaks. In such a case, we can only use the empirical CPF to give a limit on the probability for a given data set, up to the level of the maximum obtained power in the CPF.

We apply this method to the LSI +61°303 data sample in order to obtain the pre and post-trial probabilities in the next subsections.

Pre-trial probability Following the procedure described above, we evaluate the pre-trial probability via Monte-Carlo simulation of random data series. Let us illustrate the method with an example. We use the sampling times of LSI +61°303 data in campaign II and the values of x_i randomly selected from a Poisson distribution of mean equal to the average number of events observed in 15 minutes in the real data. Using these data we calculate the power for the selected frequencies. Figure 6.19 shows the Rayleigh and Lomb-Scargle periodograms for such a data sample.

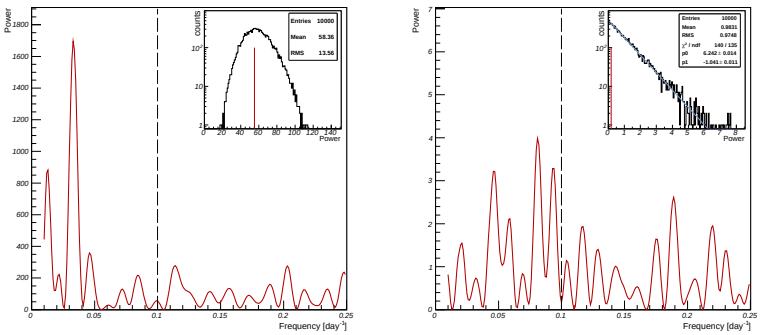

Figure 6.19: Rayleigh (left panel) and Lomb-Scargle (right panel) periodograms for a Monte-Carlo simulation of LSI +61°303 campaign II sampling. For every scanned frequency, the power of each test is determined. As an example, for frequency $\nu = 0.1\mathrm{d}^{-1}$ (dashed line) we plot in the inset the distribution of the powers (PDF) of 10^4 resampled flux series. The red line in the inset marks the value of the power for the original data set (see text for details).

To estimate the probability of each power, we produce random data series by shuffling the original fluxes, i.e., we keep constant the arrival times and assign a random flux taken (without repetition) from the original sample of measured fluxes. In this way, we obtain quasi-independent random data series. We produce 10^4 shuffled series and calculate the periodogram for each of them. For a given frequency, the probability to obtain a power value between z_0 and $z_0 + \mathrm{d}z$ is then given by the number of simulated light curves resulting in such a power value, divided by the overall number of simulations:

$$\mathcal{P}(z_0 < P(\omega_i) < z_0 + \mathrm{d}z) = \frac{N_{sim}(z_0 < P(\omega_i) < z_0 + \mathrm{d}z)}{N_{sim}} \tag{6.12}$$

In our example, for the frequency $\nu = 0.1\mathrm{d}^{-1}$ a power of Rayleigh test of $R(0.1\mathrm{d}^{-1}) = 55$ is obtained. To estimate the probability of this or higher power to occur, it is compared to the distribution of the Rayleigh power (PDF) for 10^4 randomly resampled fluxes (Fig. 6.19 left panel, inset). The probability is then given by

$$\mathcal{P}(R(0.1\mathrm{d}^{-1}) \geq 55) = \frac{N_{sim}(R(0.1\mathrm{d}^{-1}) \geq 55)}{10^4} = 0.59 \tag{6.13}$$

The same procedure is applied to the Lomb-Scargle test, where a power of $P(0.1\mathrm{d}^{-1}) = 0.17$ is obtained, which corresponds to a probability of $\mathcal{P}(P(0.1\mathrm{d}^{-1}) \geq 0.17) = 0.83$.

In case the power obtained for the original data series is larger than the highest simulated power, an estimation of the probability has to be done. For the Lomb-Scargle method, as the PDF has by construction an exponential shape, an exponential fit (see e.g. inset in Fig. 6.19) is extrapolated up to the desired power. In figure 6.20 (upper panels) we present the pre-trial PDF and its CPF of the Lomb-Scargle power, determined by Monte-Carlo simulations for campaign II and a frequency of $\nu = 1/26.496$ day^{-1}. To obtain this MC simulation, we used the sampling times of the LSI +61°303 data and the values of the flux randomly selected from a Gaussian distribution of mean equal to the average flux measured in 15 minutes of

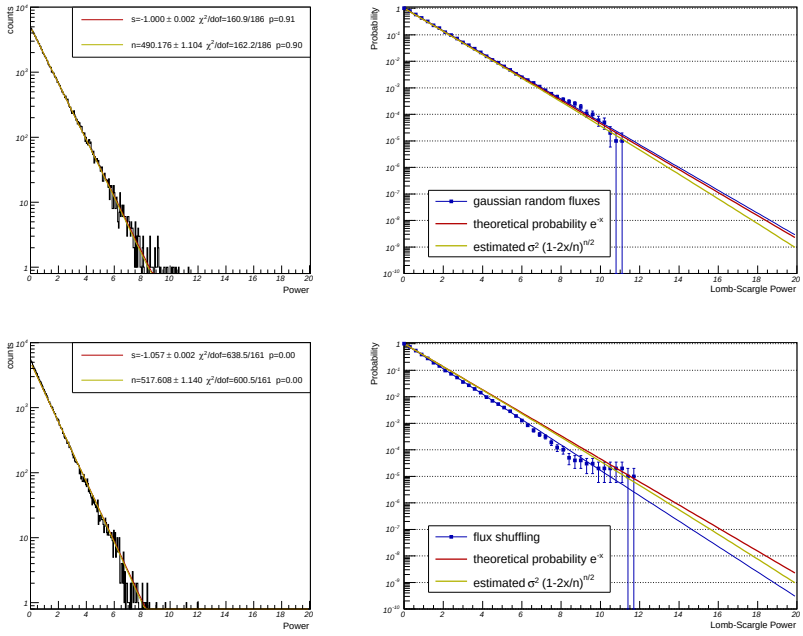

Figure 6.20: Pre-trial PDF (left) and CPF (right) of the Lomb-Scargle power determined by Monte-Carlo simulations (upper panels) or flux shuffling (lower panels) for LSI +61°303 campaign II and frequency $\nu = 1/26.496$ day^{-1}. We fit an exponential function (in red) to the PDFs (and draw it in the CPF panels). We also fit the expected PDF from the normalisation of the Lomb-Scargle periodogram on the measured variance (in yellow). Fitted slope s and number of points n are given in the inset.

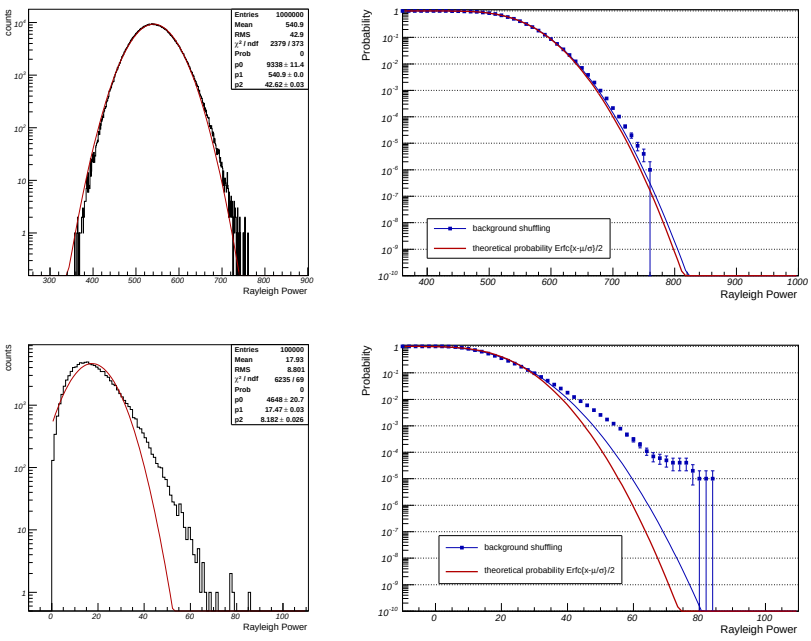

Figure 6.21: Example of two Rayleigh power distributions (left) and CPFs of the pre-trial probability (right) computed using MC simulations with campaign II sampling, for frequencies $\nu = 0.038\text{d}^{-1}$ (upper panels) and $\nu = 0.060\text{d}^{-1}$ (lower panels). The power distributions do not fit well to Gaussian functions. The red line in left panels corresponds to the complementary error function (from the integral of the Gaussian distribution) while the blue line is a fit to the data using the error function form.

the real data, and width of 1σ (that is a Gaussian white nose or null hypothesis). Due to the fact that the periodogram is normalised to the variance σ^2 estimated from the data, the PDF does not follow perfelcty an exponential shape with index -1 (classical periodogram, red line) with fitted χ^2/dof= 160.9/186. Expression 6.8 also reproduces well the distribution, as seen in Fig. 6.20, upper left panel (yellow line). We obtain a fitted parameter $n = 490.2 \pm 1.1$ (and the number of used data points is 491) with χ^2/dof= 162.2/186. Thus both functions reproduce well (fit probabilities about 90%) the PDF distribution. Note that we fit the PDF and not the CPF, because error bars in the CPF are correlated.

We also estimated the PDF and CPF producing random data series by shuffling the fluxes, as seen in Fig. 6.20 (bottom panels). In this case, the PDF do not follows the exponential distribution, since a modulation is embedded in the data sample. For the same Lomb-Scargle power, this random resampling of fluxes PDF yields lower probability than the MC one.

For the Rayleigh test we do not have a suitable function to describe the probability distribution, since the Rayleigh power is distributed as χ^2 with 2 degrees of freedom only if the data set is uniformly distributed. In figure 6.21 we see as an example the power distribution of Monte-Carlo simulations corresponding to campaign II, for two frequencies $\nu = 0.038\mathrm{d}^{-1}$ (upper panel) and $\nu = 0.060\mathrm{d}^{-1}$ (lower panel). A Gaussian function does not fit well. The pre-trial CPF for those two example frequencies are also shown (right panels). The distributions do not follow the integral of a Gaussian distribution (*erfc* or complementary error function). We conclude that the value and distribution of the Rayleigh power changes with the frequency we study. Then if the obtained power for a given frequency is higher than the maximum simulated power, we use the RMS of the distribution to estimate the pre-trial probability. This method will work in the identification of the peaks in the periodogram, but the probability will be more and more over-estimated as the power grows. Nevertheless we apply the Rayleigh test only to crosscheck the Lomb-Scargle method, and draw the conclusions exclusively using the Lomb-Scargle test.

Post-trial probability To obtain an appropriate post-trial probability we first construct an empirical CPF as described above, and fit this distribution with the false alarm function of choice.

We calculate the CPF for LSI +61°303 campaigns I, II and I+II as follows. For each Monte-Carlo data series we construct the Lomb-Scargle periodogram and use the maximum obtained power at any of the scanned frequencies to build the corresponding PDF and CPF. All three distributions are shown in Fig. 6.22. For campaign I+II and by producing 10^5 time series, we reach a highest Lomb-Scargle power just above 17.

In this case of null hypothesis, where the series are sampled by a pure Gaussian noise process (without any modulation embedded), the Lomb-Scargle periodogram originate at each frequency follows a simple exponential distribution e^{-z}. Thus the cumulative probability function of the largest spectral peak z_0 is

$$F(z > z_0) = 1 - (1 - e^{-z_0})^M \,. \tag{6.14}$$

The PDF of the largest value is obviously

$$\mathrm{d}F/\mathrm{d}z = Me^{-z}(1 - e^{-z})^{M-1} \tag{6.15}$$

from which the integration above a threshold z_0 gives eq. 6.14. Using this equation, we fit the PDF distributions in figure 6.22 (left panel) for each LSI +61°303 campaigns (fit parameters are given in the inset). For campaign I+II we obtain a probability of 95% (χ^2/dof= 74.8/96) and a number of independent frequencies of $M = 480.7 \pm 1.0$. This result is used to estimate the chance probability of the Lomb-Scargle powers.

We have also produced the CPF by shuffling of the original LSI +61°303 data series as shown in figure 6.23. As in the case of the pre-trial probability, the PDF do not follows the distribution of null hypothesis (equation 6.15). The obtained CPFs give a lower probability than the MC ones. We fit an exponential function to extrapolate the CPFs (parameters are given in Fig. 6.23 inset). For campaign I+II we obtain a probability of 99% (χ^2/dof= 36.8/60), and a slope of -1.050 ± 0.016.

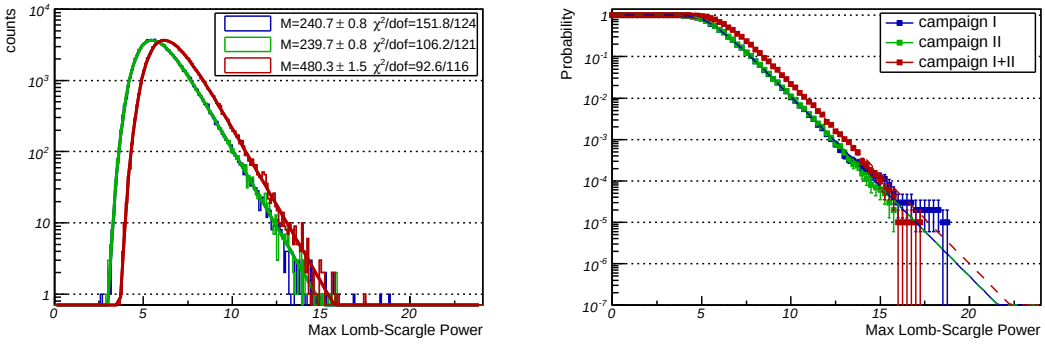

Figure 6.22: Unnormalized probability density functions of the highest Lomb-Scargle power (left) and corresponding cumulative probability functions (right) computed using MC simulations of LSI +61°303 campaign I (in blue), II (in green) and I+II (in red) samplings. The CPFs are fitted with equation 6.11 and obtained parameters M are given in the legend.

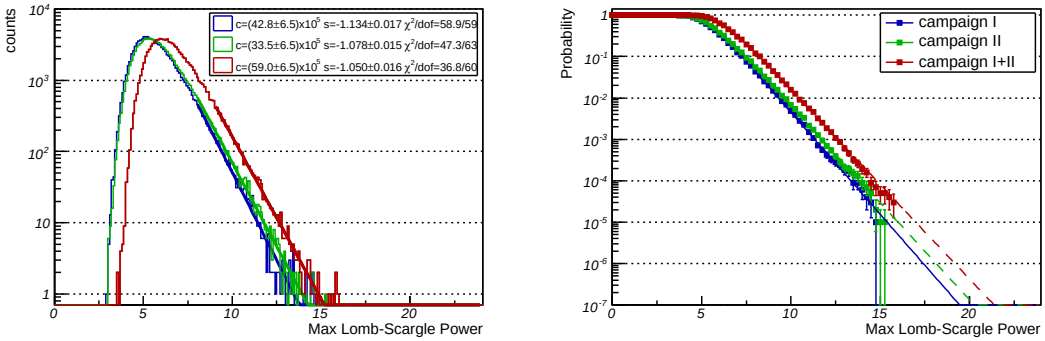

Figure 6.23: Unnormalized probability density functions of the highest Lomb-Scargle power (left) and corresponding cumulative probability functions (right) computed using random shuffling of LSI +61°303 data in campaign I (in blue), II (in green) and I+II (in red). The parameters of the exponential fit extrapolations in the PDFs (in the right part of the distribution) are given in the inset.

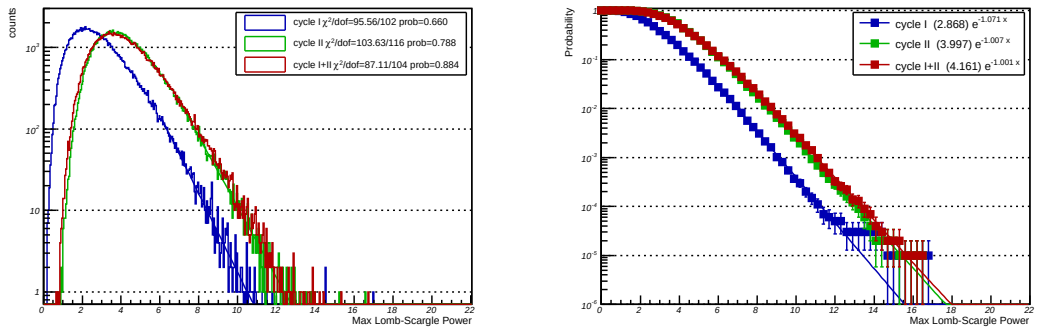

Figure 6.24: Unnormalized PDFs of the highest Lomb-Scargle power (left) and corresponding CPFs (right) determined by random resampling of LSI +61°303 γ-ray candidates in campaign I (in blue), II (in green) and I+II (in red). The parameters of the exponential fits performed (in the right part of the distributions) are given in the inset.

To cross-check, we calculated the post-trial PDF and CPF for the Lomb-Scargle test using the equalized number of excess for the LSI +61°303 campaigns I, II and I+II samplings. The distributions are shown in Fig. 6.24. Exponential fits to the CPFs are used to compute the post-trial probability from the data periodograms (see Sec. 6.6.2). However, this method of calculating the chance probability is not feasible for the Rayleigh test in unevenly sampled data. This is due to the fact that the pre-trial probability density function strongly depends on the sampling, so the tested frequency and it makes no sense to tabulate the higher Rayleigh power, since it is not the most probable. Nevertheless we calculate the Rayleigh (pre-trial) periodograms and use them for comparison and cross-check of the Lomb-Scargle method.

6.6.1.5 Background periodograms

To show that the peaks that may appear in the Lomb-Scargle tests over the LSI +61°303 data are genuinely associated with the source, we perform the same statistical test over the background. We construct the periodogram using an OFF sample obtained simultaneously with the LSI +61°303 data. This is treated in different ways for campaigns I and II:

For campaign I the data are taken in ON/OFF mode, i.e. ON and OFF data are taken at different times. To obtain a simultaneous OFF data sample we use an anti-cut in Alpha. As for ON data the alpha cut is $\alpha < 6°$, we consider the events with $20 < \alpha < 30°$. With these number of γ-ray candidates and the collection area (given by MC simulations) and observation time, we estimate the corresponding flux.

For campaign II , since the data are taken in wobble mode, we use the signal candidates recorded by the anti-source position, and estimate the background with the other two wobble regions to evaluate the flux.

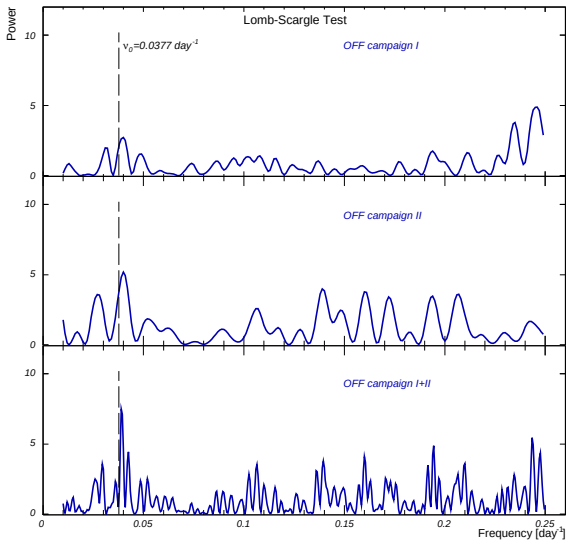

Figure 6.25: From top to bottom: periodogram obtained with the Lomb-Scargle test for a background region simultaneously with LSI +61°303 campaign I, II and I+II. The vertical dashed line marks the LSI +61°303 orbital frequency (1/26.496 day^{-1}).

In both cases we obtain a simultaneous fluxes of a background region and construct the Lomb-Scargle periodogram with them as shown in figure 6.25. In campaign I and II, the obtained powers are below 5, what corresponds (using the CPF in Fig. 6.22) to a post-trial chance probability of 0.80. In campaign I+II the highest power is 7.5 that yields a probability of 0.23. Thus none of the obtained peaks in the background periodograms is significant.

We also perform the statistical tests over the background using the number of arrival γ-ray candidates to cross-check of the results. But in the case of the Rayleigh and Lomb-Scargle tests applied over the number of excess, there are some technical considerations that have to be taken into account and we will discuss next. Nevertheless, these considerations do not apply to the Lomb-Scargle test using the flux as physical magnitude. For calculating this flux from the number of excess, we use (apart from the observation time) the effective area, which is obtained from Monte-Carlo. And Monte-Carlo already takes into account the known variations (such as zenith angle). But in the case of the number of excess we have to perform an equaliza-

tion procedure, which considers these variations (and any other unknown variations, such as weather conditions).

The fact that the telescope detection efficiency might show periodicities (e.g. periodic changes of zenith angle), could cause non-physical peaks in the periodogram. In order to evaluate and correct for this effect, we construct the periodogram using a background sample obtained. For campaign I we use a higher hadronness cut to select a simultaneous background. As for ON data the hadronness cut is $h < 0.1$, for OFF we use $0.3 < h < 0.5$. We tested with Crab of the same period that this cut does not contain any significant signal. For campaign II, as the data are taken in wobble mode, we use the signal candidates recorded by the anti-source positions for constructing the Lomb-Scargle periodogram.

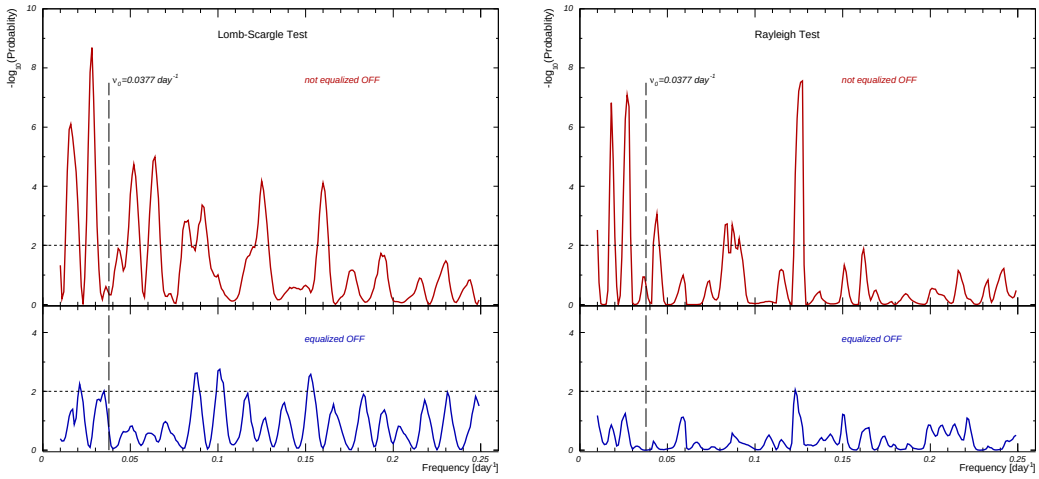

Figure 6.26: Periodogram obtained with the Lomb-Scargle (left) and Rayleigh (right) tests for the OFF region in campaign I. The upper (lower) panel shows the probabilities without (with) equalisation. The vertical dashed line marks the LSI +61°303 orbital frequency. The horizontal dotted line marks the level of probability $< 10^{-2}$.

The periodograms for campaigns I, II and I+II using the OFF samples are shown in Figs. 6.26, 6.27 and 6.28 (upper panels) respectively. Significant peaks (probability $< 10^{-4}$) appear for some frequencies such as: 0.016 and 0.028 day^{-1} for the first campaign and $\nu = 0.03, 0.04$ and 0.63 day^{-1} for the second. To remove these unphysical peaks from the periodogram, we perform the statistical tests using the *weighted* or *equalised* quantity $\hat{x}_i = k_i * x_i$, where x_i are the number of γ-candidates: N_{ON} (for the Rayleigh test) or excess events N_{ex} (for the Lomb-Scargle test) reaching the telescope at time t_i; and the equalisation weights k_i are defined as

$$k_i =< N_{bg} > /N_{bg\,i} \tag{6.16}$$

for $i = 1, \cdots n$. $N_{bg\,i}$ is the number of events detected at time t_i in the background region and $< N_{bg} >$ their mean value.

To reduce the statistical error on k_i, we relax the selection cut for N_{bg} with respect to that used in the signal selection. Therefore, for the evaluation of the weights in *campaign II*, we use the mean background from the 3 OFF regions and apply a softer hadronness cut, so that the γ-ray efficiency is 0.95. For the signal extraction, we use a hadronness cut with γ-ray efficiency 0.8.

Figure 6.29 shows that the background events obtained with efficiencies 0.8 and 0.95 are well correlated. So one may use the second, softer cut to have more statistics for the background estimation in the equalisation. For *campaign I*, we use a different hadronness cut $0.5 < h < 0.6$ of simultaneous data, where the signal contribution is not expected (tested with a Crab data sample), and use it for the equalisation.

In order to check if the equalisation method eliminates the spurious frequencies due to any periodic behaviour in the collection area, we build the periodogram for a set of inde-

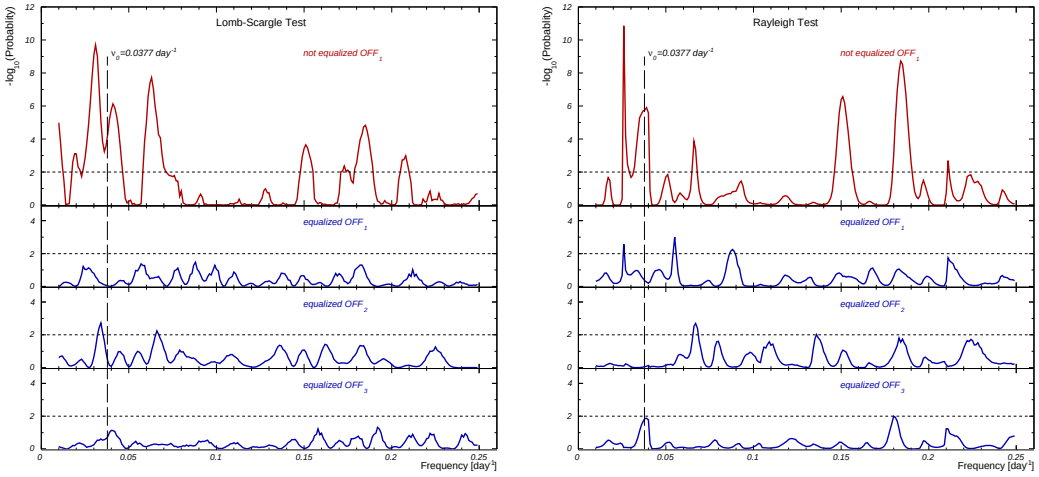

Figure 6.27: Periodogram obtained with the Lomb-Scargle (left) and Rayleigh (right) tests for the OFF data in campaign II: Upper panels show the probabilities for one anti-source region without equalisation applied; second, third and last panels show the probabilities for each one of the three independent OFF regions, equalised using the data from the remaining two. The vertical dashed line marks the LSI +61°303 orbital frequency. The horizontal dotted line marks the level of probability $< 10^{-2}$.

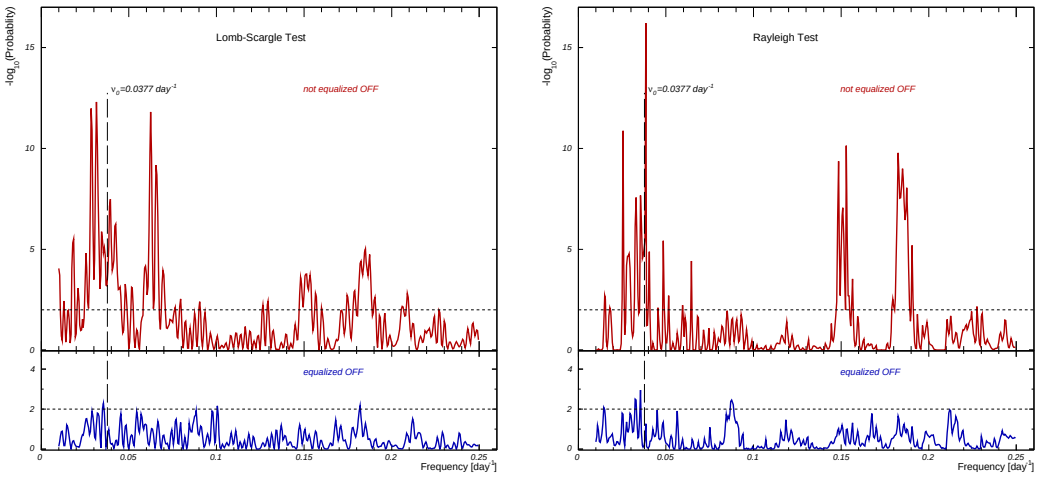

Figure 6.28: Lomb-Scargle (left) and Rayleigh (right) periodograms for the OFF region in campaign I+II: The upper (lower) panels show the probabilities for the OFF region without (with) equalisation. The vertical dashed line marks the LSI +61°303 orbital frequency. The horizontal dotted line marks the level of probability $< 10^{-2}$.

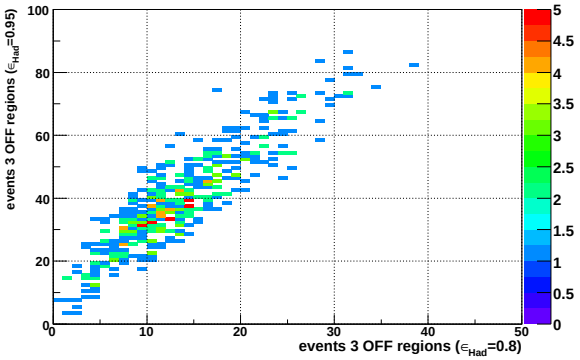

Figure 6.29: Distribution of OFF events in the 3 OFF regions of campaign II, for hadronness cut with γ-ray efficiency 0.8 versus distribution with efficiency cut 0.95.

pendent OFF samples, using the equalized quantities $\hat{x}_i$. The results for the Lomb-Scargle and Rayleigh tests for the different campaigns are shown in Fig. 6.26, 6.27 and 6.28 (lower panels).

For campaign II we perform this test over three different samples corresponding to the three independent OFF wobble regions. In each case, the weights k_i are computed using the remaining two OFF samples. We obtain no significant probability peaks (above 10^{-3}) in any of the samples for any of the tested frequencies and those obtained from the non-equalised data (top panels) are removed.

6.6.1.6 Merging data from different observational campaigns

Due to differences in telescope performance in the two observational campaigns and the change of observation mode, we expect the telescope sensitivity to be different. This is evident in Crab observations: The γ-ray rate recorded from Crab Nebula samples contemporaneous to each campaign is different. Hence, we need to define a new quantity, comparable between both campaigns, over which we perform the statistical tests.

The phaseograms of the number of excess event N_{ex} for campaigns I and II are shown in Fig. 6.30 (left panel). We scale N_{ex} to the same level by using the relation between the values of the γ-ray rate obtained from two Crab data analyses, contemporaneous with each of the campaigns. For campaign I we used 212 minutes of Crab data taken in October and November 2005. With an analysis completely analogue to the one performed over LSI +61°303 data in campaign I, we obtain a γ-ray rate of $R_{CI} \simeq 287 \pm 10$ excess events/h. For campaign II, 116 minutes of Crab data in September 2006 were analysed obtaining an excess rate of $R_{CII} \simeq 156 \pm 9$ excess events/h. Thus, the scale factor between LSI +61°303 data campaigns is $S_{ex} = R_{CII}/R_{CI} = 0.55$. The phaseogram with the scaled number of excess is shown in Fig. 6.30 (right panel).

To scale the OFF data (used for crosscheck, as seen in Sec. 6.6.1.5) we proceed in the same way: by comparing the Crab analyses. As the normalization factors in each campaign are different, we use the relation between the background rate in the Crab campaigns which are 1.29 and 0.39 excess events/min, respectively. This yields a scale factor of $S_{OFF} = 0.30$. The phaseogram for N_{OFF} with and without applying the scale factor are presented in Fig. 6.31.

For the Rayleigh test, we use the N_{ON} as physical variable and the direct comparison with Crab is not feasible. As an approximation, we use the same scale factor as in the OFF data set S_{OFF}. The phaseograms with and without applying the scale factors are shown in Fig. 6.32.

Of course, in case we perform the Lomb-Scargle test using the integral fluxes as input parameters, this discussion is of no need, as all the required scale factors are included in the computation of the effective areas for each case, and we can directly merge both data campaigns.

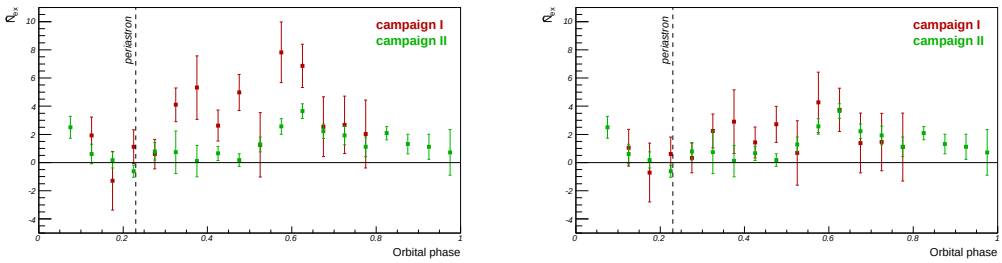

Figure 6.30: Number of equalized γ-excess for first (red) and second (green) campaigns versus phase (folded with the LSI +61°303 orbital period). Each analysis campaign has a different N_{ex} level (left panel), which is scaled by a factor 0.55 obtained from the analysis of Crab Nebula samples, to obtain a comparable base-line (right panel).

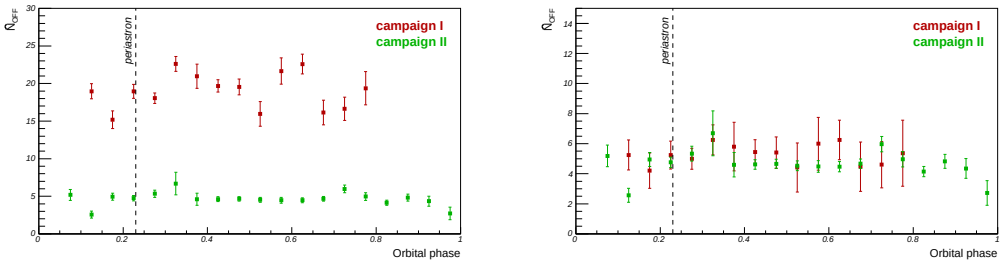

Figure 6.31: Number of equalized N_{OFF} for first (red) and second (green) campaigns versus phase (folded with the LSI +61°303 orbital period). Each analysis campaign has a different level (left panel), which is scaled by a factor to obtain a comparable base-line (right panel). See text for details.

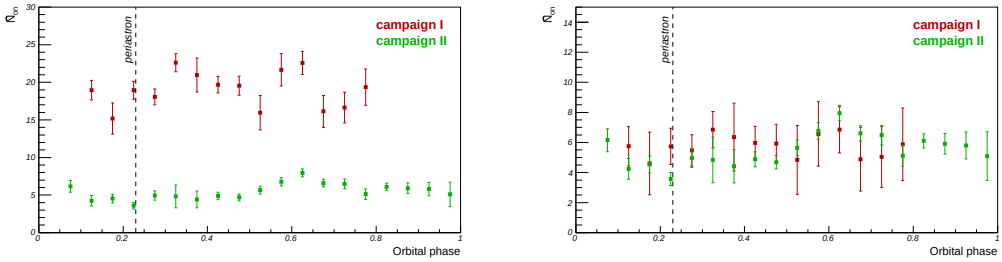

Figure 6.32: Number of equalized N_{ON} for first (red) and second (green) campaigns versus phase (folded with the LSI +61°303 orbital period). Each analysis campaign has a different level (left panel), which is scaled by a factor to obtain a comparable base-line (right panel). See text for details.

6.6.2 Periodic analysis of the LSI +61°303 data

For each LSI +61°303 campaign (I, II and I+II) we present the periodic analysis performed with the Lomb-Scargle test, using the fluxes as physical quantities to compute the periodogram. We compare the results with a periodogram performed over background region, observed simultaneously to the LSI +61°303 data. We also compute a periodogram subtracting a sinusoidal component with the maximum probably frequency obtained. To cross-check the results we perform also the Lomb-Scargle and Rayleigh tests using the number of γ-candidates.

Lomb-Scargle periodograms using LSI +61°303 integral fluxes. We apply this method to the LSI +61°303 TeV integral flux (above 400 GeV) from campaign I and II separately. The obtain the periodograms presented in Fig. 6.33. A maximum peak in the periodogram is seen for frequency $\nu = 0.04\text{d}^{-1}$ (power of 8.01) and $\nu = 0.038\text{d}^{-1}$ (power 18.19) for first and second campaign, respectively. Using the CPF shown in Fig. 6.22, we compute the corresponding post-trial probability, which results to be 7.0×10^{-2} and 3.0×10^{-6} in each campaign.

The fact that the power obtained in campaign I is lower than the one obtained in campaign II is due to the lower observation time (54 hours compared to the 116h in campaign II) and because the orbital coverage is lower: in the 6 observed periods there are no data taken below phase 0.1 neither above phase 0.8. In campaign II we observed 4 periods but we achieved a better coverage.

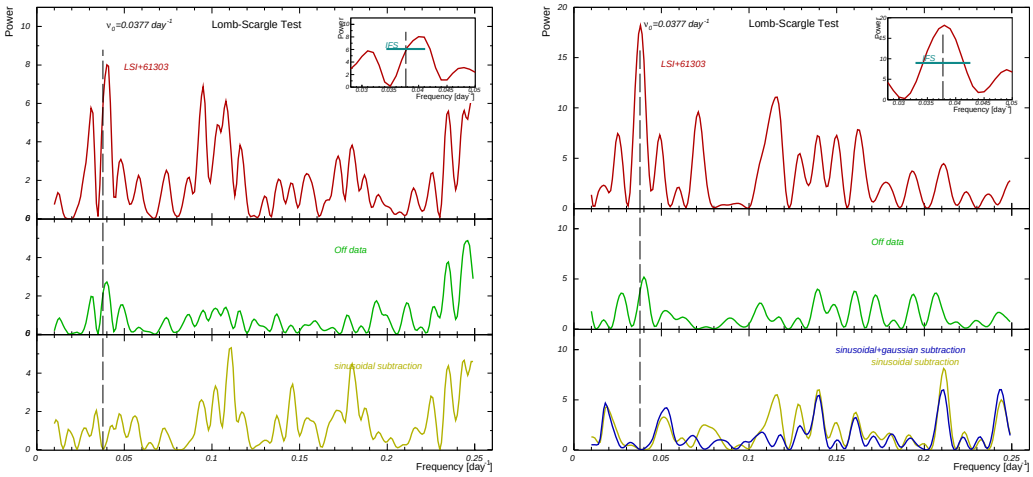

Figure 6.33: Periodograms for Lomb-Scargle test over the LSI +61°303 campaign I (left) and II (right) data (upper panel) and OFF data (middle panel). In the lower panel we present the powers for the data after subtraction of a purely sinusoidal signal at the orbital period (yellow line) and a sinusoidal plus a Gaussian wave form (blue line). The dotted vertical line corresponds to a frequency of 0.037 day^{-1} (period of 26.496 days).

We combine campaigns I and II data, which allows us to scan more frequencies, because the elapsed time between the first and the last measurements is 442 days. The results are shown in Fig. 6.34. A peak at frequency $\nu = 0.0375\text{d}^{-1}$ is clearly seen, with a Lomb-Scargle power of 22.05, which gives a post-trial probability of 1.3×10^{-7} (see Fig. 6.22).

Less prominent, significant peaks are detected for other frequencies. For instance in campaign I+II, frequencies 0.040 and 0.115 d^{-1} have probabilities of about 2.0×10^{-4} and 7.7×10^{-3}, respectively. All those peaks are related to the signal, since they do not show up in the OFF periodogram (Fig. 6.34, middle panel). They correspond to beat periods of the orbital period with various gaps present in the LSI +61°303 data-set, that is, rational fractions of beat periods added to the orbital period.

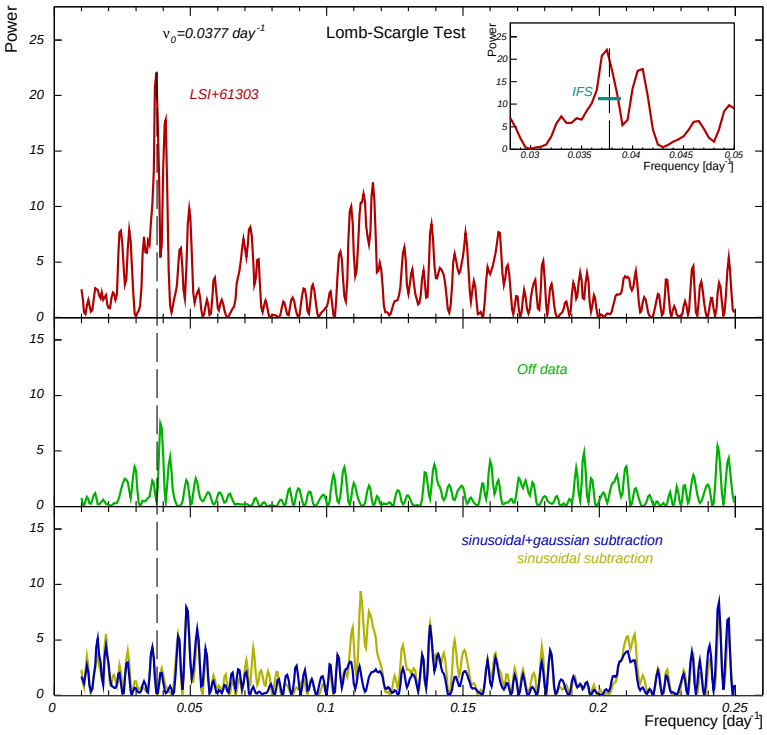

Figure 6.34: Periodogram for Lomb-Scargle test over the LSI +61°303 campaigns I+II (right) data (upper panel) and OFF data (middle panel). In the lower panel we present the probabilities for the data after subtraction of a purely sinusoidal signal at the orbital period (yellow line) and a sinusoidal plus a Gaussian wave form (blue line). The dotted vertical line corresponds to a frequency of 0.037 day^{-1} (period of 26.496 days).

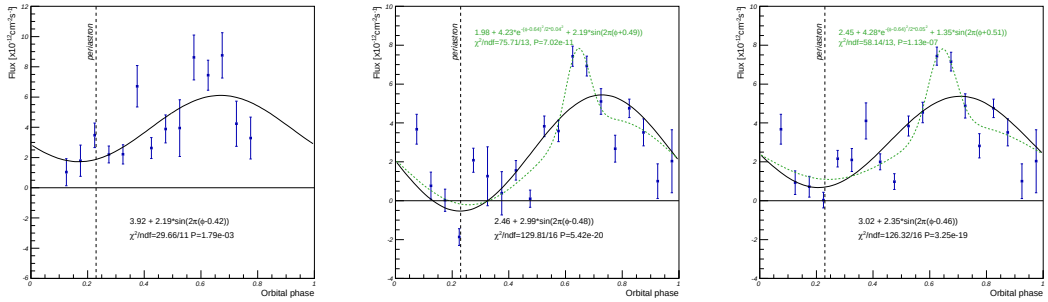

Figure 6.35: LSI +61°303 integral flux folded with period $P = 26.496\text{day}^{-1}$. From left to right we present data for campaigns I, II and I+II. Black curves are fits of a sinusoidal signal (fit parameters are given in the insets). For campaign II and I+II, there is also the possibility to investigate other wave forms, and we fitted a sinusoidal signal plus a Gaussian component (green dashed lines). Vertical dotted line indicates the periastron passage according to [116].

We fold the data with the orbital period ($P = 26.496$, $\nu = 0.037\mathrm{d}^{-1}$) for campaign I, II and I+II. The results are presented in figure 6.35. A sinusoidal fit is performed in each case, and the obtained parameters are given in the inset.

If we subtract the sinusoidal signal from the fit to the data and perform the statistical tests, we obtain the periodogram probabilities shown in Figs. 6.33 and 6.34 (lower panels, yellow line) for campaigns I, II and I+II respectively. The peak corresponding to the orbital frequency has been removed in all cases as expected. With subtracting the orbital period we also remove or reduce some satellite peaks. But the fact that these other peaks do not achieve a level consistent with the background test indicates that the signal in LSI +61°303 data is not purely sinusoidal.

We also subtract a sinusoidal plus a Gaussian signal contribution, fitted to campaign II and campaign I+II data[3] (Fig. 6.35, green dotted lines). The corresponding periodograms are presented in Fig. 6.33 (right panel) and Fig. 6.34 (lower panels, blue lines). The orbital frequency peak has been removed and the rest of the periodogram peaks are much more reduced than in the purely sinusoidal subtraction, being compatible with the background periodogram.

Cross-check with Rayleigh and Lomb-Scargle periodograms using the number of γ-candidates. As noticed in Sec. 6.6.1.2, the Rayleigh and Lomb-Scargle tests can be applied to the number of γ-ray candidates, measured in a time interval $[t_i - \frac{\Delta t}{2}, t_i + \frac{\Delta t}{2}]$. We apply the Rayleigh and Lomb-Scargle statistical tests to the LSI +61°303 data campaign I and II separately. The results are presented in figures 6.36 and 6.37. For campaign I, a maximum peak in the periodogram probability is seen for frequency $\nu = 0.038\mathrm{d}^{-1}$ and $\nu = 0.035\mathrm{d}^{-1}$ with the Lomb-Scargle and Rayleigh tests, respectively. The pre-trial chance probability is about 10^{-5}. Using the CPF shown in Fig. 6.24, we compute the corresponding post-trial probability, which results to be 2.0×10^{-4}. For campaign II the maximum peak in the Lomb-Scargle periodogram is clearly seen for frequency $\nu = 0.038\mathrm{d}^{-1}$, for which we obtain a Lomb-Scargle power of ~ 17. It is highly significant with a pre-trial chance probability of about 10^{-8}, and a post-trial chance probability of 0.8×10^{-7}. For the Rayleigh statistical test, the maximum peak is seen at $\nu = 0.040\mathrm{d}^{-1}$, (with a power of 223) which corresponds to a pre-trial probability of $\sim 10^{-10}$.

The periodograms combining campaigns I and II data, are shown in Fig. 6.38. A peak at frequency $\nu = 0.038\mathrm{d}^{-1}$ is seen with a Lomb-Scargle power of ~ 22, which gives a pre-trial chance probability about 10^{-12}. The corresponding post-trial probability is 1.3×10^{-9}. Similar behaviour is observed for the Rayleigh test with a maximum in $\nu = 0.038$ which has a probability of $\sim 10^{-12}$.

This results are in agreement with the frequencies and probabilities obtained using the Lomb-Scargle test with integral fluxes. As in that case, less prominent but significant peaks are detected for other frequencies, which are not seen in the OFF periodograms.

We fold the data with the LSI +61°303 orbital frequency (see Fig. 6.39). We fit a sinusoidal and a sinusoidal plus a Gaussian signal contribution. If we subtract these functions to the data and perform the statistical tests, we obtain the periodograms shown in figures 6.34, bottom panels.

We conclude that all three methods tested for the periodicity analysis (the Lomb-Scargle test using integral fluxes and the Rayleigh and Lomb-Scargle tests with number of γ-ray excess) are in good agreement in terms of frequencies and probabilities.

To cross-check these results, we apply the Rayleigh and Lomb-Scargle methods to a simulated sample containing a purely sinusoidal signal with the parameters taken from the fit to the data. For each arrival time t_i, taken from the real data, we simulate a signal as a random Gaussian with mean $B + A \cdot \sin(2\pi(\phi_i + \phi_0))$ where A, B and ϕ_0 are taken from the sinusoidal fits to the data folded with the orbital period; the width σ of the Gaussian function is taken from the data spread in the phaseogram. We obtain the periodograms shown in Figure 6.40. We detect a signal of about 10^{-18} chance probability for $\nu = 0.037\mathrm{d}^{-1}$ for Lomb-Scargle

[3]For campaign I alone, this function is difficult to fit (see folded phaseogram in Fig. 6.35) due to the uncovered phases and so we do not try this test on these data.

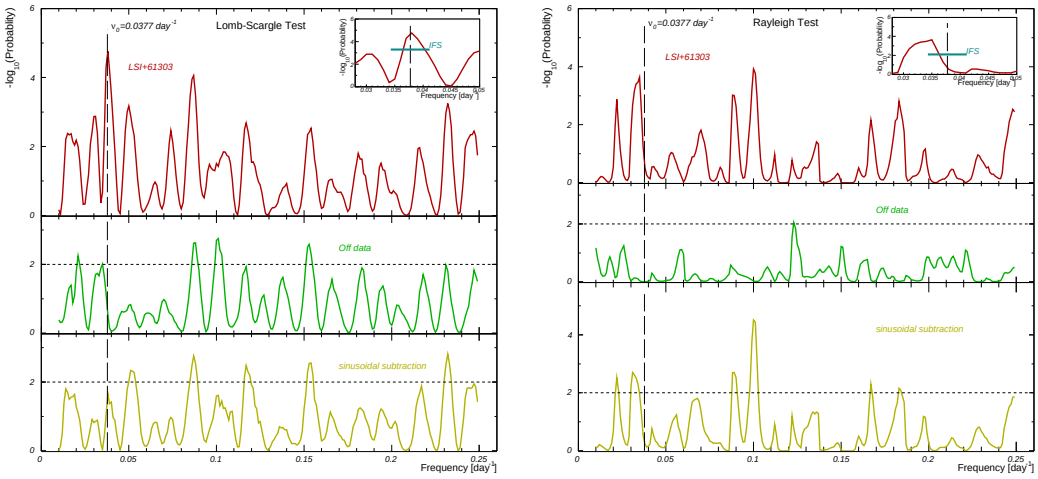

Figure 6.36: Pre-trial periodograms for Lomb-Scargle (left) and Rayleigh (right) tests over the LSI +61°303 data in campaign I (upper panel) and OFF data (middle panel). In the lower panel we present the probabilities for the LSI +61°303 data after subtraction of a purely sinusoidal signal at the orbital period. The vertical dotted line corresponds to the orbital frequency.

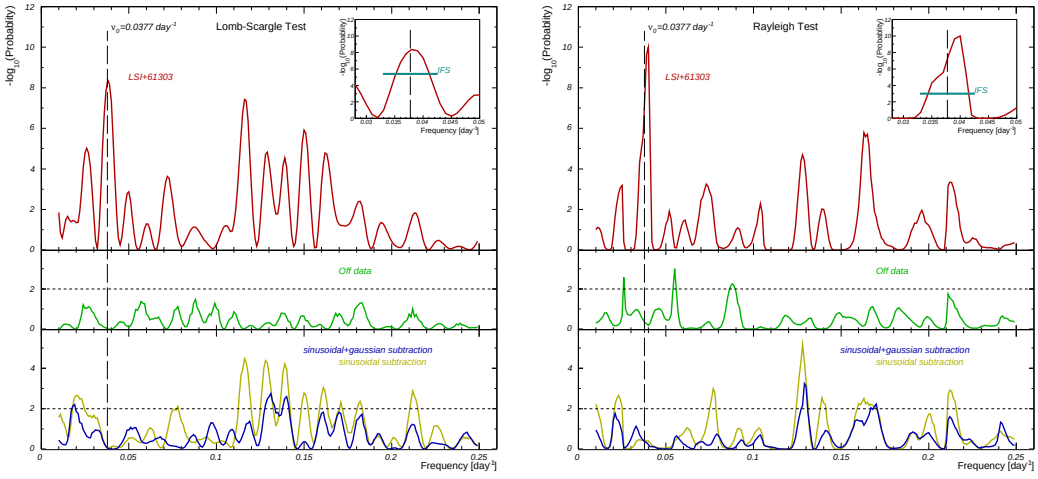

Figure 6.37: Pre-trial periodograms for Lomb-Scargle (left) and Rayleigh (right) tests over the LSI +61°303 data campaign II (upper panel) and OFF data (middle panel). In the lower panel we present the probabilities for the data after subtraction of a purely sinusoidal signal at the orbital period of the system (yellow line) and after subtraction of a sinusoidal plus a Gaussian peak (blue line). Vertical dotted line corresponds to the orbital frequency.

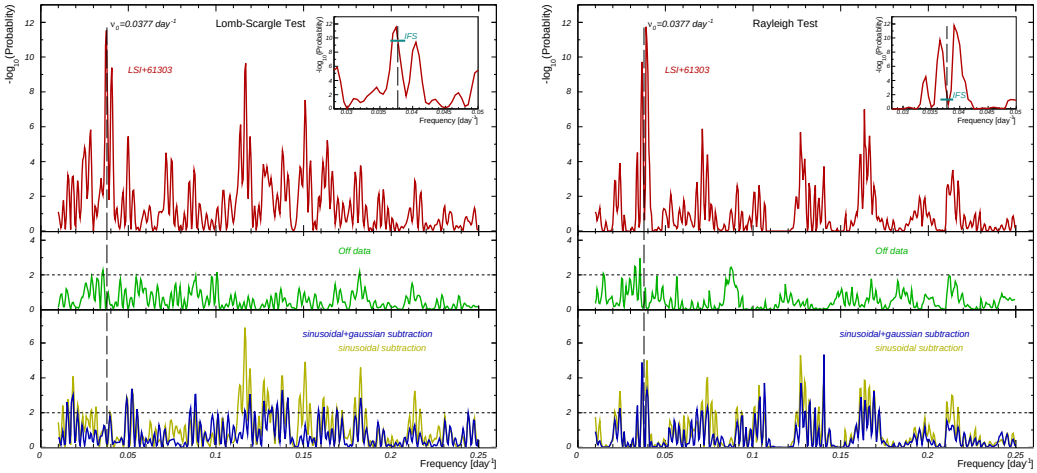

Figure 6.38: Pre-trial periodograms for Lomb-Scargle (left) and Rayleigh (right) tests over the LSI +61°303 combined campaign I+II data (upper panel) and OFF data (middle panel). In the lower panel we present the probabilities for the data after subtraction of a purely sinusoidal signal at the orbital period (yellow line) and a sinusoidal plus a Gaussian wave form (blue line). The dotted vertical line corresponds to the orbital frequency.

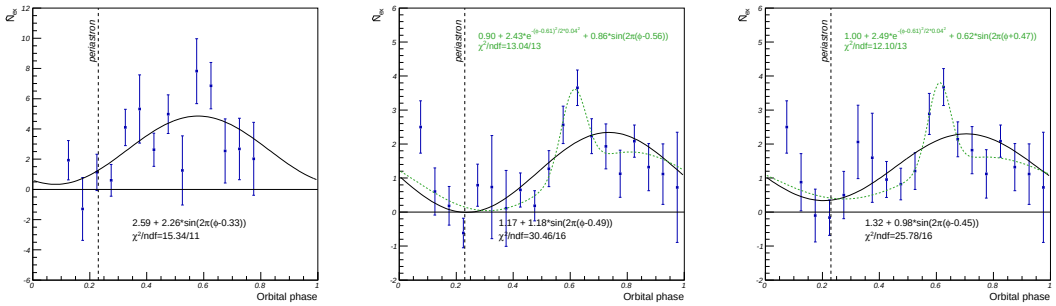

Figure 6.39: LSI +61°303 (equalized) number of γ-ray candidates folded with period $P = 26.496\text{day}^{-1}$. From left to right we present data for campaigns I, II and I+II. Black curves are fits of a sinusoidal signal (fit parameters are given in the insets). For campaign II and I+II, there is also the possibility to investigate other wave forms, and we fitted a sinusoidal signal plus a Gaussian component (green dashed lines), which adjusts better to the data (χ^2/dof= 11.53/13 for campaign I+II). The vertical dotted lines indicate the periastron passage according to [116].

test and campaign I data. The same procedure is applied to campaign II and we obtain a probability of 10^{-39} for the same frequency. For campaign I+II a peak with probability 10^{-45} is detected for frequency $\nu = 0.0375\mathrm{d}^{-1}$.

So far, we have scanned the periodograms up to frequency 0.25 d^{-1}, which includes the orbital period of interest, but due to the long elapsed observation time, we are able to search for higher frequencies (see Sec. 6.6.1.3). To search for possible features in the high frequency region, we perform an extended Lomb-Scargle test for LSI +61°303 campaign II data as shown in Fig. 6.41. Apart from the peaks around the orbital period, already discussed, we see significant signals (chance probability lower than 10^{-4}) for frequencies 1.04 (period about 23 h), 2.04, 3.08, 4.8 and 5.08 d^{-1}. From the OFF periodogram (Fig. 6.41 middle panel) we see that those peaks are related intrinsically to the LSI +61°303 data, since they do not appear in the simultaneous background. However, if we subtract a sinusoidal or a Gaussian plus a sinusoidal function to the data, the peaks (together with the orbital peak) disappear or reduce up to the level of the background probabilities. We conclude that those peaks are due to aliasing effects. In fact, the highest peak at about one day we already expected from the windowing function (see Sec. 6.6.1.3) because the measurements were done with time gaps of about 24 hours.

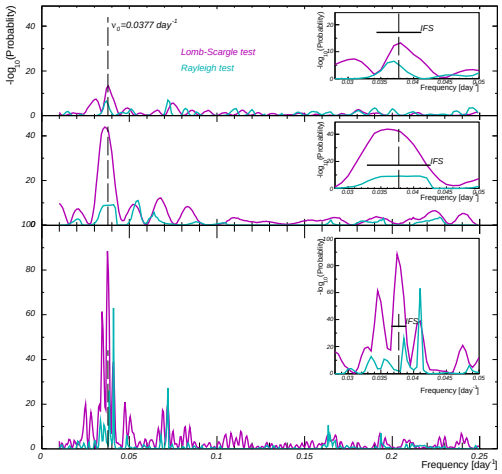

Figure 6.40: Pre-trial periodogram for a simulated sinusoidal signal using the Rayleigh (blue) and Lomb-Scargle (pink) tests for samplings campaigns I (upper panel), II (middle panel) and I+II (lower panel).

6.6.3 Effect of the time binning

All previous results are obtained using bins of 15 minutes. In this section we study the effect of the bin size (Δt) on our results. From inspection of eq. 6.6 it becomes evident that:

- the Lomb-Scargle power increases with the number of points: for a sinusoidal signal in a data set, $(x_i - \bar{x}) \propto \sigma \cos \omega t$ or $(x_i - \bar{x}) \propto \sigma \sin \omega t$ and then

$$P(\omega) \propto \frac{1}{2\sigma_X^2} \left[\frac{[\sum_{i=1}^{n} \sigma \cos^2 \omega t_i]^2}{\sum_{i=1}^{n} \cos^2 \omega t_i} + \frac{[\sum_{i=1}^{n} \sigma \sin^2 \omega t_i]^2}{\sum_{i=1}^{n} \sin^2 \omega t_i} \right], \tag{6.17}$$

  therefore $P(\omega) \propto n$. Therefore, the chance probability increases with the increasing number of data points, for the same number of scanned frequencies (same number of trials). Averaging the data increases the effective sampling interval Δt, thus decreasing the Nyquist frequency. If we scan the averaged data set at a lower number of frequencies, the post-trial probability will also decrease. The fact that the post-trial probability

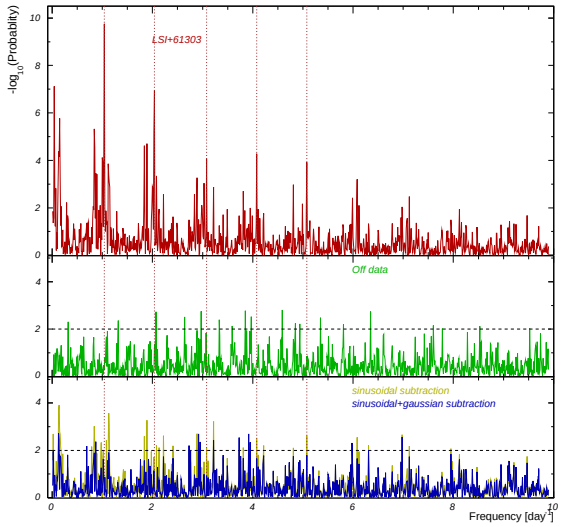

Figure 6.41: Extended (scanned up to frequency 10 d^{-1}) periodogram for Lomb-Scargle test over the LSI +61°303 data campaign II (upper panel) and OFF data (middle panel). In the lower panel we present the periodogram for the data after subtraction of a purely sinusoidal signal at the orbital period of the system (yellow line) and after subtraction of a sinusoidal plus a Gaussian peak (blue line). The vertical dotted lines mark significant peaks in the LSI +61°303 periodogram which disappear or reduce in the all other periodograms.

increases with the number of scanned frequencies is the *statistical penalty* that we pay for inspecting a large number of frequencies[198].

- Successive sub-divisions of a data sample produce progressively less effect on the CPF, until it eventually converges to a limiting CPF beyond which no further division of the sample changes the result. The original time domain data contain a finite amount of information. There is therefore a limit to how much information the data sample can yield.

- A variable binning of (e.g. each bin corresponds to an observation night, of different duration) is not appropriate because in such a case the data points have different relative errors. Since the statistical tests used here do not take errors into account, all points are weighted the same in the calculation of the periodogram. This effect becomes even worse since the LSI +61°303 orbit is not uniformly covered: we observed more days and for longer times in phases with expected higher flux, about $\phi \sim 0.6$, and hence their relative weight in the periodogram is very much reduced by taking a fixed number of data points per night.

The periodograms obtained in campaign II using bins of 7.5, 15, 30 and 60 minutes, half nights and night-by-night bins are shown in Fig. 6.42. We see that the significance of the peak around frequency 0.0377 decreases for longer bins, except between 7.5 and 15 minute bins, where the saturation limit is reached. The amplitude of the sinusoidal function obtained folding the data with the orbital frequency (see inset in Fig. 6.42) scales approximately proportionally with the size binning. The main effect when combining data for widening bins is the loss of statistics. The number of data points decreases from 419 points in 15 minutes bins to 51 points in night-by-night bins.

The second peak seen in Fig. 6.42 at frequency $\sim 0.12 d^{-1}$ (about 8 days) is a beat period of the $0.037 d^{-1}$ peak. We saw that it decreases when subtracting a sinusoidal signal and vanishes for a sinusoidal plus Gaussian signal (Fig. 6.37 lower panel).

To confirm these results we have generated Monte-Carlo data series with the sampling and sinusoidal signals corresponding to the different time binnings. The Lomb-Scargle probability

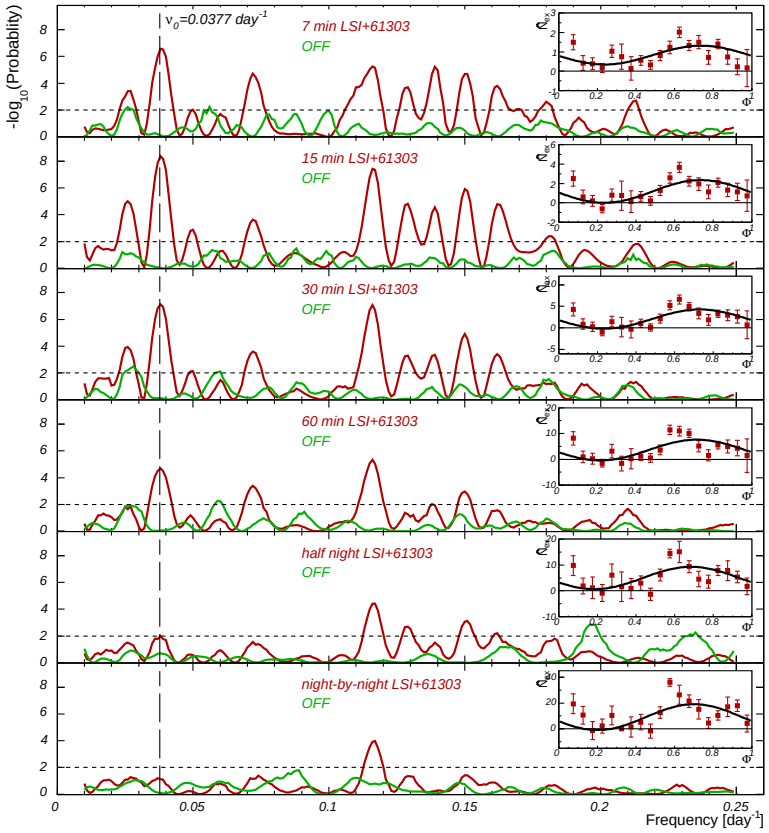

Figure 6.42: From top to bottom: Periodogram for Lomb-Scargle test over the LSI +61°303 campaign II data using 7.5, 15, 30 and 60 min, half-night and night-by-night bins. Red curves are for LSI +61°303 data while green curves are for OFF data. In the inset, the phase folded data for the orbital frequency is fitted with a sinusoidal function.

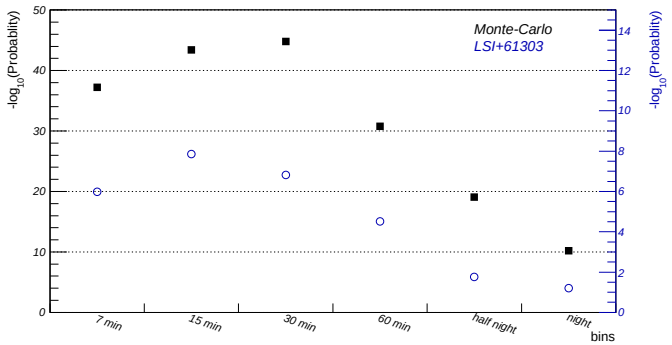

Figure 6.43: Pre-trial probability for LSI +61°303 campaign II and frequency 0.037d^{-1} obtained using Lomb-Scargle test with different time-bins for a simulated sinusoidal signal (in black) and real data (in blue, right axis).

for frequency 0.037d^{-1} is reduced as the bin width increases as seen in Fig. 6.43. The power obtained for the same frequency with LSI +61°303 data is also shown for comparison (Fig. 6.43, blue points), showing that the same trend is reproduced.

6.6.4 Peak frequency and its error

In case of evenly sampled data, the distance between independent frequencies (see Sec. 6.6.1.3) is the Independent Fourier Spacing: for instance in campaign II the elapsed time is $T \simeq 100$ days, and the number of points $n \simeq 500$ points, for 15 minutes time bins. In this case we may scan the natural frequencies (eq. 6.9) from $\nu_1 = 1/100 = 0.01\text{d}^{-1}$ to $\nu_{250} = 250/100 = 2.5\text{d}^{-1}$. The step between these natural frequencies is the IFS: $1/T \simeq 1/100 = 0.01\text{d}^{-1}$. However, the position of the peak in a periodogram can be estimated with better accuracy than this value.

An accurate determination of the peak frequency is done by the fine scanning of frequencies (increasing the oversampling factor) around the periodogram peak. The power values around the most probable frequency for each campaign are shown in Fig. 6.44 and the frequency values are summarised in table 6.9.

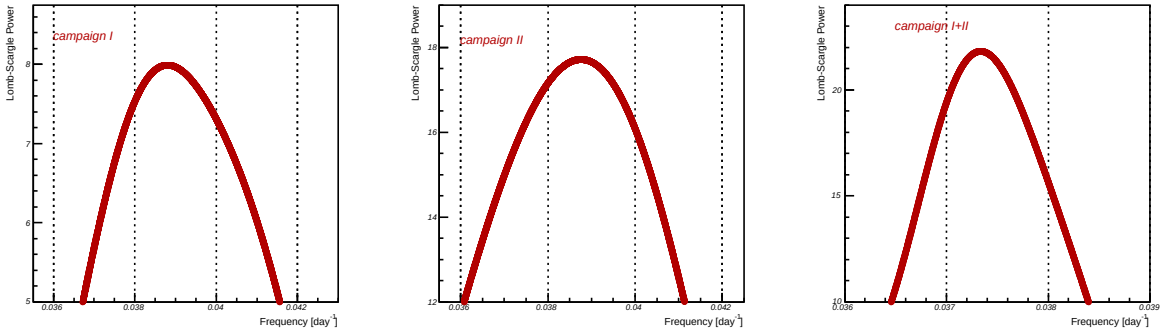

Figure 6.44: Lomb-Scargle power around the most probable frequencies in the periodograms for LSI +61°303 campaigns I, II and I+II (from left to right).

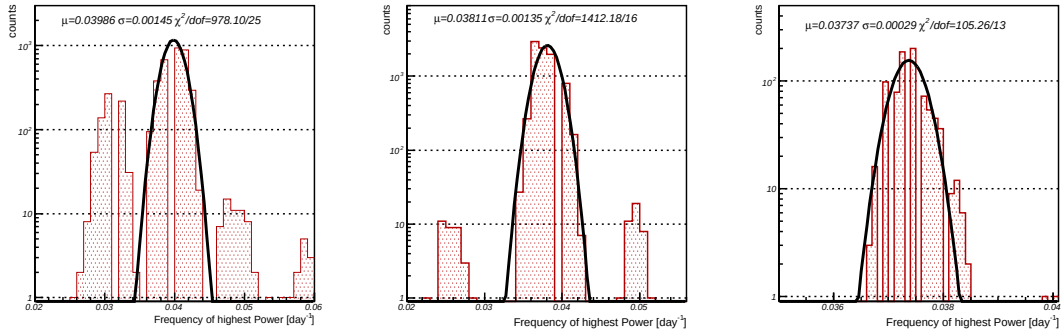

Figure 6.45: Distribution of frequencies with the highest Lomb-Scargle power determined by letting the data points in the LSI +61°303 light curve vary according to Poissonian distributions. From left to right: campaigns I, II and I+II.

In case the sample is unevenly spaced, while the statistical properties of the periodograms have received much attention, the frequency error estimation is rarely discussed in the literature [203]. We will discuss below a possible approach.

Sometimes, an astrophysical quantity is not an obvious function of the measurements, thus, the regular error propagation formula cannot be applied. This is the case of the signal

frequency derived from the power spectrum. We therefore applied a Monte-Carlo simulation to evaluate the error in the frequency estimation, as we did for the false alarm probability (see Sec. 6.6.1.4).

One possible approach to the error estimation is to propagate the Poissonian error of the ON and OFF measurements. For every arrival time, the ON and OFF events are selected randomly from two Poissonian distributions of mean equal to the actually measured number of events. The number of excess is transformed into flux using the MC effective area and the effective time, and the simulated lightcurve is obtained.

The periodogram is calculated for 10^4 of those randomly generated series, and the distribution of the resulting peak power frequencies are shown in Fig. 6.45. The region around the orbital frequency is fitted with a Gaussian function. The other peaks can be attributed to the aliasing effect and are of no interest for this study.

For campaign I+II we obtain an error of 0.0003 d^{-1} which corresponds to an error in the period of 0.2 days. The frequency value is calculated with enough accuracy by increasing the oversampling in the LSI +61°303 Lomb-Scargle periodogram. The frequency and period with their errors are given in table 6.9 for the different campaigns.

Campaign	Frequency ν (d^{-1})	Period (d)	Chance prob (post-trial)	IFS (d^{-1})
I	0.0405 ± 0.0015	24.7 ± 0.9	7.0×10^{-2}	0.0069
II	0.0380 ± 0.0014	26.3 ± 0.9	3.0×10^{-6}	0.0097
I+II	0.0373 ± 0.0003	26.8 ± 0.2	1.3×10^{-7}	0.0023

Table 6.9: For each observational campaign we present the frequency ν and period P (obtained with the Lomb-Scargle test) and their errors. The post-trial chance probability of the frequency peak is quoted for each campaign. The IFS is also given.

6.6.5 Periodicity conclusions

A search for periodicity over LSI +61°303 TeV data in campaigns I, II and I+II has been carried out using the Lomb-Scargle test over the number of excess and over the integral fluxes and also using the Rayleigh test. All three inspected methods give consistent and compatible results. The associated (post-trial) chance probability has been calculated by Monte-Carlo simulations using the data unevenly sampling and the Lomb-Scargle method.

The periodograms for each campaign display peaks around the orbital frequency $\nu = 1/26.496$ d^{-1}. The peak is purely associated with the LSI +61°303 data, since it does not appear for the simultaneous OFF data periodogram (see Fig. 6.34). Other peaks appearing in the periodogram are beat periods of the orbital period with various gaps present in the dataset. This is confirmed by subtracting a purely sinusoidal signal to the data, and performing the same statistical test. In this case, the orbital frequency peak is removed as expected, but also those satellite peaks are removed or reduced. If, instead, we subtract a sinusoidal plus a Gaussian signal contribution (as see in the periodogram Fig. 6.35) the satellite peaks are much more reduced, being compatible with the background periodogram level.

As expected, the most accurate frequency value is obtained after merging the data from both campaigns (spanning over 10 orbital cycles in total), which yields a period value of **26.8±0.2** days with a post-trial probability of $\mathbf{10^{-7}}$. The frequency error has been estimated as a propagation of the Poissonian measurement errors, using MC simulations.

In figure 6.46 we show the period obtained with MAGIC data compared to the measurements in other wavelengths. The most accurate period is reported in radio by Gregory (2002) [140] with a value of 26.496 ± 0.028. This period was estimated with GBI data from about 7 years (from 1994 to 2000) during which the instrument detected 83 outburst. The period obtained with the MAGIC date is compatible within 1.5σ with it.

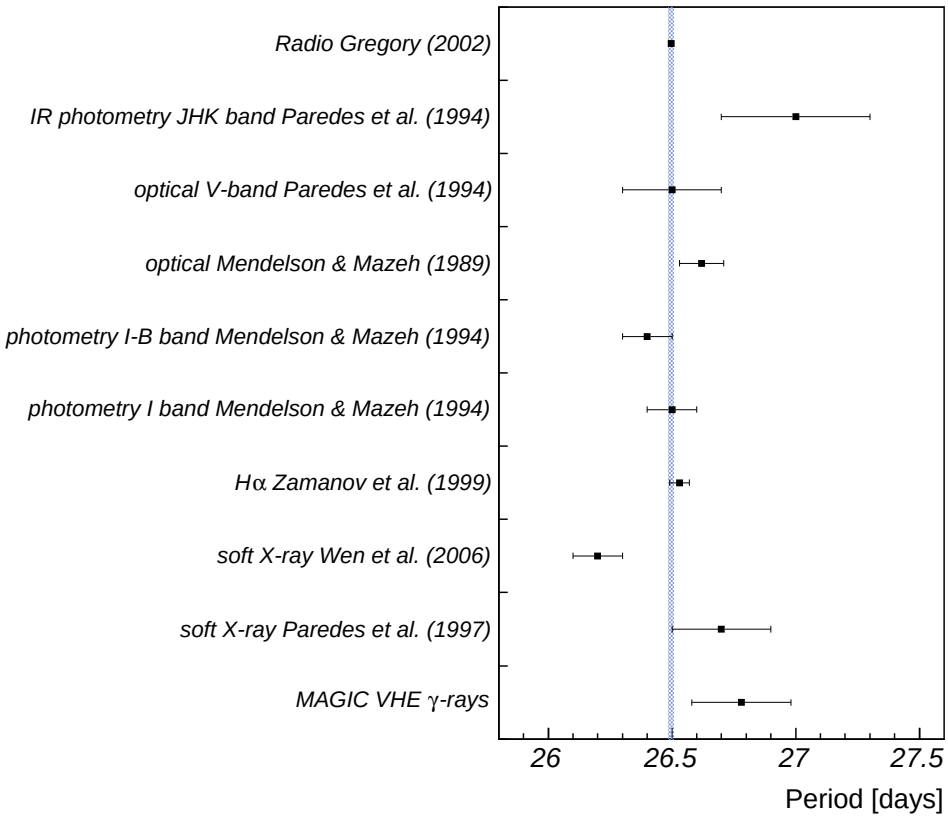

Figure 6.46: Measurements of the LSI +61°303 period measured in different wavelengths. From top to bottom: radio measurements [140], near IR and optical V-band [129], optical data [128], photometry in the I-B and I bands [204], Hα data [130] and soft X-ray data from [205] and [152]. In the last row we show the MAGIC measured period of 26.8 ± 0.2 days.

6.7 Simultaneous and follow up observations

6.7.1 Campaign I

We carried out contemporaneous radio observations of LSI +61°303 at 15 GHz (2 cm wavelength) with the Ryle Telescope [206], which forms part of the Mullard Radio Astronomy Observatory and is operated by the Cavendish Laboratory, near Cambridge. The Ryle telescope is an interferometer array of eight 13 m diameter dishes with a maximum baseline of 4.8 km. It began operation in 1972, and has been involved in numerous monitoring campaigns of variable radio sources.

The aim of this simultaneous observation is to check the possible correlation of VHE γ-rays and radio wavelengths and the radio state (active or strong, as defined in section 5.3).

The radio data cover the last orbital cycle observed by MAGIC in the first campaign: from 14 February to 8 March 2006, and are shown in Fig. 6.47. The peak of the radio outbursts had its maximum at MJD 53798.8, corresponding to an orbital phase of 0.70. The peak is then observed between 1 and 3 days after the increase observed at VHE γ-rays flux.

The radio data with fluxes between 30-70 mJy are typical for the source in its weaker state, as can be seen in Fig. 5.3 as comparison with GBI archival data at the same frequency.

Later Whipple observation on LSI +61°303 from 2004-2006 [207] covered several of the same epochs as the MAGIC detections, albeit with lower sensitivity. The Whipple observations extended 50 hours from September 2004 to February 2006. Of the six cycles covered by

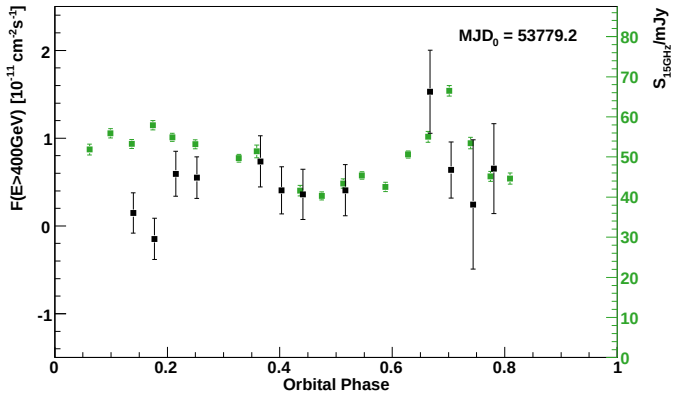

Figure 6.47: LSI +61°303 radio flux density at 15 GHz measured with the Ryle Telescope (green squares, right axis) and results from the last orbital cycle observed by MAGIC in campaign I (black dots, left axis). The MJD corresponding to orbital phase 0 is indicated.

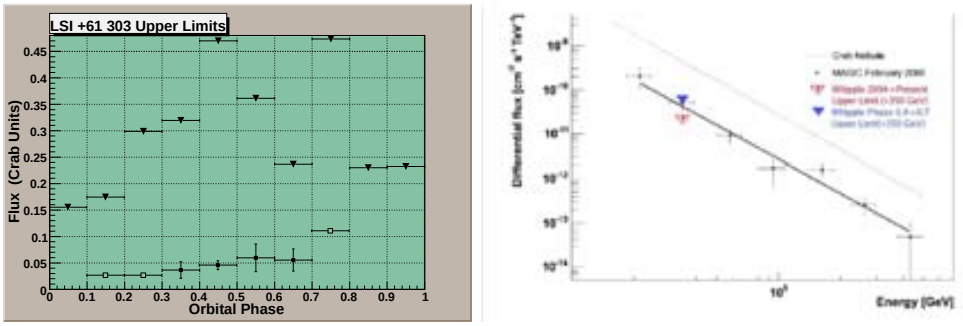

Figure 6.48: Left: 99% CL upper limits (trianlges) as measured by Whipple in terms of the Crab Nebula flux vs the LSI +61°303 orbital phase. MAGIC detections and 90% CL upper limits from campaign I, as published in [190] are aslo shown. Right: Comparison between the campaign I MAGIC spectra (in black) and upper limits for the Whipple telescope for phases 0-1 (in red) and 0.4-0.7 (in blue). From [207].

MAGIC campaign I data, Whipple had four concurrent observation cycles with no similar strong detections. Upper limits were reported for all orbital phases and are shown in Fig. 6.48 in terms of Crab Nebula flux. A total flux upper limit of 7.2% of the Crab Nebula flux was derived above 350 GeV, from observations covering the whole LSI +61°303 orbit. To compare with MAGIC data, the flux above 350 GeV in the bin phase 0.4-0.7 is estimated (with ~ 5 hours exposure) to be 18.4% of the Crab Nebula flux (solid triangle in Fig. 6.48). These upper limit are above the LSI +61°303 measurements obtained from MAGIC data in camapign I and thus consistent with the results presented in this work.

6.7.2 Campaign II

A multiwavelength campaign was carried out, aimed at shedding light on the physical processes taking place in the system. The observations include:

- radio measurements with MERLIN, e-EVN and VLBA at 5 GHz,
- X-ray with *Chandra*, and
- TeV γ-rays with MAGIC.

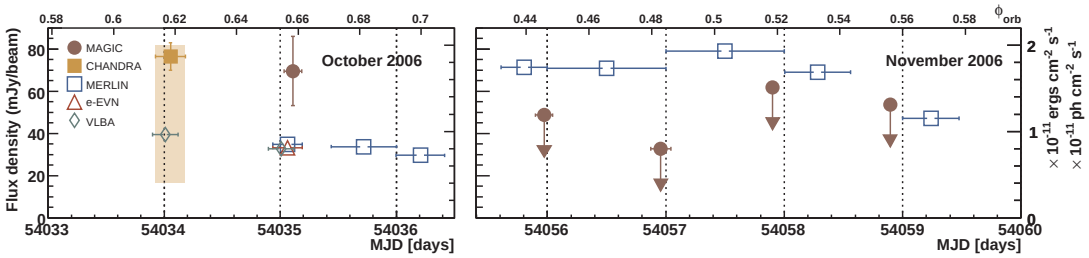

Figure 6.49: Radio, X-ray and VHE γ-ray light-curves obtained with VLBA, e-EVN, MERLIN (left-hand scale), *Chandra* (right-hand scale in 10^{-11} ergs cm^{-2} s^{-1}) and MAGIC (right-hand scale in 10^{-11} photons cm^{-2} s^{-1}) during the two observing periods (October and November 2006). The horizontal error bars show the time spanned by the different observations. The shaded area marks the range of X-ray flux values reported by [156]. The upper scale shows the orbital phase. From [208]

Results from those observations are published in [208]. The observations where scheduled for the second and third periods in the LSI +61°303 campaign II, from October 25th to November 20th, and the results are summarized in figure 6.49.

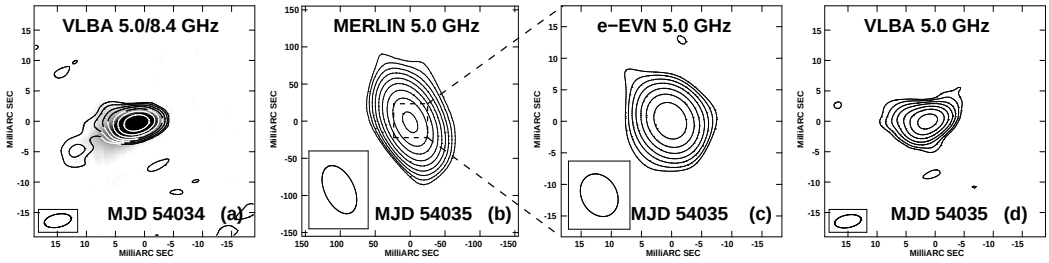

Figure 6.50: Radio images of LSI +61°303 obtained with the VLBA on 25 October 2006 (panel a) and MERLIN (panel b), e-EVN (panel c), and VLBA (panel d) on 26 October 2006. The synthesized beams of the images (bottom left corner in each panel) are 70×41 mas, 7.2×5.8 mas, and 4.6×2.1 mas for the MERLIN, e-EVN, and VLBA observations, respectively. In panel a, we also show overlaid the 8 GHz VLBA image on 2 February 2006 (grey scale) convolved with our 5 GHz VLBA beam. This date correspond to the same orbital phase $\Phi \approx 0.62$, and they show a striking similarity. From [208]

The MERLIN observations show no evidence for large angular scale structures (see Fig. 6.50), excluding the existence of persistent jets at large scales ($\sim$ 100mas). The size of the radio emitting region is no larger than $\sim$ 6 mas (12 AU). The VLBA images show a bright and unresolved component plus an extended emission to the east-southeast, with similar structure to what observed at 8.4 GHz by Dhawan et al. (2006) [115]: VLBA image on February 2006 and orbital phase $\phi = 0.62$ is shown together with the VLA image in October 2006 (same phase) in figure 6.50.

The detections at X-ray and TeV energies show particularly high flux values and one day apart, as seen in Fig. 6.49. This might point to a temporal correlation between the X-ray and the TeV emissions, and hence to the fact that both radiations are produced by the same population of particles. In the same figure, we also show the radio flux measured by MERLIN, which is about $\sim$ 30 mJy between October 26th and 28th and shows a peak later on November 18th (up to $\sim$ 79 mJy). As in the case of the campaign I, these values are typical for the source in the weak state. A hint of radio/TeV correlation, as would suggested Fig.6.47 from campaign I does not hold in general. In October 2006, the γ-ray flux reaches about 15% of the Crab Nebula flux while the radio emission is constant at about $\sim$ 35 mJy. Whereas the TeV emission in hardly significant in November 2006, where the radio flux is twice higher. This radio/TeV non-correlation points to the existence of one population of particles producing

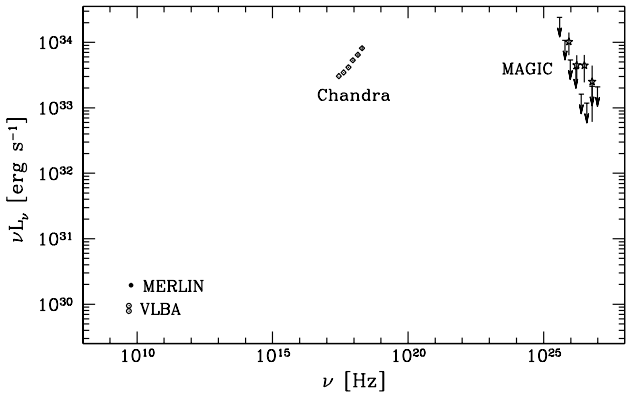

Figure 6.51: Quasi-simultaneous LSI +61°303 spectrum including radio (VLBA, open circles), X-rays (*Chandra*, squares) and VHE γ-rays (MAGIC campaign II, stars) data from the period 25-26 October 2006, along with the data from November 2006: average MERLIN flux density (filled circle) and upper limits from MAGIC (arrows). From [208]

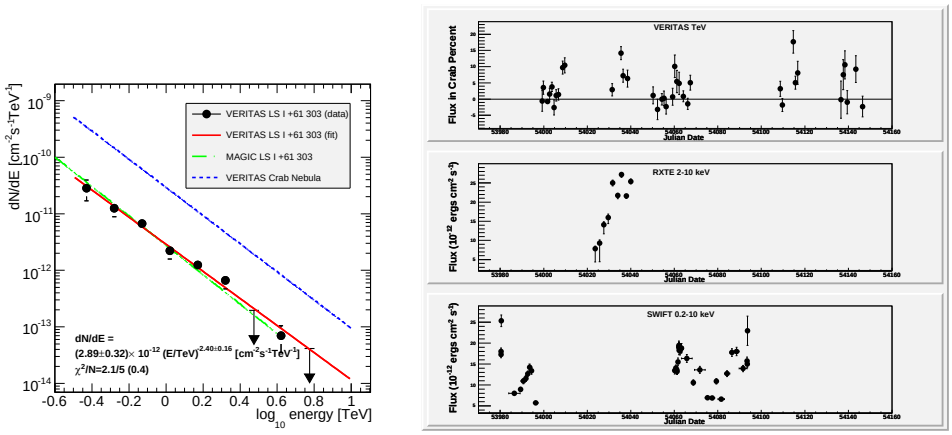

Figure 6.52: Left: Differential energy spectrum above 300 GeV for LSI +61°303 as measured by VERITAS [209] (black points and red fit) compared with LSI +61°303 campaign I as measured by MAGIC (in green). Both spectra are in good agreement. Right: VERITAS, RXTE, and Swift monitoring of LSI +61°303 over seven orbital periods. Peaks can be seen in all three data sets near dates corresponding to phase $\phi \sim 0.7$. From [210].

the radio emission and a different one producint the X-ray and TeV emissions.

A quasi-simultaneously energy spectrum is shown in figure 6.51. The X-ray emission from *Chandra* show a hard and high emission state, with a photon index of 1.53 ± 0.07 and a flux of 1.9×10^{-11} ergs cm^{-2} s^{-1}. From the 150 min observations from MAGIC on 2006/10/27, we obtained a differential spectrum (Fig. 6.14), which is also draw in the spectral energy distribution of Fig. 6.51. The average over November data give upper limits in the spectra, which are also show in the same figure.

However, given the high variability of the physical conditions of LSI +61°303 along the orbit, more simultaneous, multiwavelength data will bring further light in our understanding of the object.

LSI +61°303 was later observed (between September 2006 and February 2007) with the VERITAS array of imaging air-Čerenkov telescopes, confirming the MAGIC results [209]. The data is not strictly simultaneous with the MAGIC second campaign, although it overlaps in three orbital cycles, from September to November 2006. During those cycles, the measurements are in good agreement. The differential energy spectra is also consistent, as seen in figure 6.52, left panel.

During VERITAS campaign, monitoring in the X-ray regime was also carried out using the RXTE and Swift detectors, which offered complementary coverage of the source. Outbursts in the 0.2-10 keV band were observed by both satellites at close to the same orbital phase as the TeV peak during the 2 orbital cycles covered simultaneously in both bands [210]. Results are show in figure 6.52 (right panel). All three observation sets show elevated emission between phases 0.5 and 0.8, what points to a possible correlation between the rise time of TeV and X-ray emission in the system.

Chapter 7

Conclusions and perspectives

A new generation of ground-based VHE γ-ray telescopes are opening a new window to the universe. By ways of enhanced sensitivity, and improved angular and energy resolution, these telescopes are discovering a plethora of sources of VHE radiation.

The MAGIC telescope belongs to this generation of Čerenkov telescopes. It is optimized for VHE γ-ray astronomy with a low energy threshold. The technical contribution to MAGIC of the author has been presented. It is mainly focused on the slow control software for the camera and calibration systems. Since 2004 MAGIC is taking data regularly. In these three years the telescope has detected sources belonging to different galactic and extragalactic source populations – such as supernova remnants, pulsar wind nebulae, compact binary systems or active galactic nuclei.

LSI $+61°303$ is a high mass X-ray binary system, consisting of a massive Be star and a compact object of unknown nature (black hole or neutron star). The emission in radio, infrared, optical and X-ray is modulated with a period of ~ 26.5 days, attributed to the orbital motion. When this work was started in 2004, no X-ray binary was known to emit VHE γ-rays, although theoretical predictions for theses systems were promising. Among X-ray objects, LSI $+61°303$ is a peculiar system, which has been proposed as a possible counterpart for the high-energy COS B γ-ray source 2CG 135+01. This source was also detected by EGRET (3EG J0241+6103), but due to its poor angular resolution, the association remained unclear. The detection at GeV energies, together with the fact that radio interferometric observations suggested that relativistic jet flows were present, made LSI $+61°303$ a promising VHE γ-ray source candidate.

On this context, MAGIC observed LSI $+61°303$ in two different campaigns during 2005 and 2006. The observations lasted ~ 150 hours in total, and spanned 10 orbital cycles of the system. The analysis of the VHE data presented in this work allows us to reach the following conclusions. First we established LSI $+61°303$ as a VHE γ-ray emitter. It is the third X-ray binary which is found to emit at these energies.

The source is point-like for MAGIC, with any extension constrained to less than $0.1°$. The obtained position is (J2000): $\alpha = 2^{\mathrm{h}}40^{\mathrm{m}}34^{\mathrm{s}}$, $\delta = 61°15'25''$, in agreement with the position of LSI $+61°303$. The source is within the 95% confidence level contours of the EGRET source 3EG J0241+6103 (2CG 135+01).

This discovery triggered new observations of the source in different wavelengths. In the VHE domain, new upper limits were set by the Whipple experiment in 2007 [207]. Afterwards, the detection was confirmed by the VERITAS telescopes [209]. Also in radio and X-rays several observations were carried out in the following years.

The measured γ-ray flux from the source is found to be variable. This means that for the first time, a microquasar candidate is found to be variable at VHE γ-rays. A total of 10 orbital phases have been observed, allowing us to draw an orbital emission profile. The γ-ray flux peaks around orbital phase 0.63 and reaches a minimum near periastron passage. The maximum observed flux (above 400 GeV) corresponds to $\sim$17% of the Crab Nebula flux at the same energy. A second peak of emission at phase 0.84 reaches a similar flux level, only for one of the monitored orbital cycles.

The energy spectrum of the system have been measured between ~ 200 GeV and ~ 5 TeV. The spectral index for the phases of the emission maximum, 0.5-0.6 and 0.6-0.7, is constant over time with a value $\sim -2.7 \pm 0.3$. No evidence for a cut-off up to 5 TeV is found. There is no evidence for spectral index variations with phase or with flux level.

We looked for possible intranight variability, and found the flux to be constant within errors in 45, 60 and 75 minutes time-scales.

A search for periodicity over LSI +61°303 TeV data has been carried out. Periodicity in the VHE γ-ray flux has been established, yielding a period of 26.8 ± 0.2 days with a post-trial probability of 10^{-7}. This is the second established periodic source in the VHE band. The results implies that the flux modulation is tied to the orbital period. Any theoretical model trying to explain the behaviour of the system should accommodate the γ-ray emission profile.

The challenge is now to determine the nature of the compact object and whether the VHE γ-rays are ultimately powered by pulsar winds or relativistic jets.

In the microquasar-jet scenario, the compact object of the system accretes matter from the companion star, forming a decretion disk, and a relativistic jet may form. The mechanism behind the γ-ray production might be hadronic, leptonic or a mixture. In case of hadrons are accelerated in the jet, they may interact protons of the stellar wind; if electrons are accelerated, they can interact via inverse Compton with their own synchrotron field, or the photon field from the accretion disk, the corona or the companion star. Neutrino observations with IceCub could settle this issue in the near future.

Alternatively, relativistic particles can be injected in the surrounding medium by the wind from a young pulsar. In this case, stellar wind may contain the wind of the pulsar, and particle acceleration occurs at the termination shock. This leads to X-ray synchrotron emission and γ-ray inverse Compton emission with the stellar photons.

The modulation at VHEs is probably due to the orbital dependence of the γ-ray production or absorption processes.

This reported modulation at VHE motivate the revision of some LSI +61°303 theories. Some of them expected a VHE emission peak near periastron passage After the MAGIC observations, theories account for other mechanisms to reproduce the VHE emission, including e.g. absorption processes or focusing in detail in the system geometry.

Three other high mass X-ray binaries have been identified as VHE γ-ray emitters in the last three years: PSR B1259-63, LS 5039 and Cyg X1. Binaries are now established emitters of VHE γ-rays up to 10 TeV. With the VHE observations of this thesis, we prove that LSI +61°303 belongs also to a new class of objects. The γ-ray emission of LSI +61°303, LS 5039 and PSR B1259-63 almost dominates the source energy output, and therefore they can be named γ-ray binaries. For instance, the γ-ray luminosity of LSI +61°303 around phase 0.6 is of the same order as the average X-ray luminosity: $L_\gamma \sim L_X \sim 10^{33}$ ergs cm^{-2} s^{-1}. The spectral and temporal similarities between these binaries hint at a common scenario. MAGIC has also found evidence for VHE γ-ray emission in the black hole microquasar Cyg X1, but with a significantly different phenomenology. The emission is transient and could not be related to the orbital period. In addition, the VHE γ-ray luminosity is a fraction of 10^{-4} of the X-ray luminosity.

Future LSI +61°303 observations with MAGIC II will allow to better study the VHE emission. Since the observations will cover more orbital cycles, the stability of the γ-ray light curve could be also tested, as well as the possible modulation of the period with the radio super-orbital trend of ~ 4.5 yr. Additional tests as the behavior and stability of the spectra at shorter phase intervals could be also studied.

The increase of observational capability at VHE produced by VERITAS and CANGAROO III and the gain in sensitivity of HESS II and MAGIC II, and the planned Cerenkov Telescope Array (CTA), will allow to detect new X-binaries and establish if the variable activity is a common phenomena in these type of sources. All of this will bring more constraints to the physics of these systems.

In addition, multiwavelength (multi-particle) campaigns will also be very important to gain knowledge about these new TeV sources. A higher angular resolution radio maps may allow a clear detection of jets or a morphology unequivocally related to a wind/wind shock. The

compact object may be also identified as a pulsar through the detection of radio pulsations.

The GLAST satellite detector will cover the energy range of EGRET with improved sensitivity, field of view and angular resolution, starting on summer 2008. Its γ-ray instrument (LAT) is expected to detect the modulation of the GeV emission of LSI $+61°303$ within one year.

Appendix A

Future LSI +61°303 scheduling

In this Appendix we present the possible observation time slots on LSI +61°303 that may be scheduled form January 2008 to March 2009. We considered the observations from the MAGIC site following criteria on zenith angle and moon-light conditions. Phase of the LSI +61°303 system is also derived, as may be important for the observation schedule.

The schedule of the source LSI +61°303 have to be planned carefully. Usual conditions as zenith angle from the MAGIC site have to be considered. But if the observation is to be planned to study the phase-dependent source features, the system phase has to be examined. Also to extend the possible observation time, data conditions under moderate moon-light may be evaluated.

A software have been developed to extract, in slots of 30 minutes accuracy, the scheduling time slots of LSI +61°303 from MAGIC site, with some predefined criteria.

Figures A.1- A.3 show the possible LSI +61°303 observation times from period[1] 63 (January 2008) to period 76 (March 2009). The allowed zenith angle region to be covered by LSI +61°303 is selected between 32° and 50°. Criteria for possible moon observation is moon zenith angle more than 45° (moon above the horizon but no very high in the sky, so its light is not very strong) and angular distance between moon an the source in the range $64° < D < 115°$. Periods 65 to 68 are not drawn because during that time, there is no observation possible, accomplishing the established criteria.

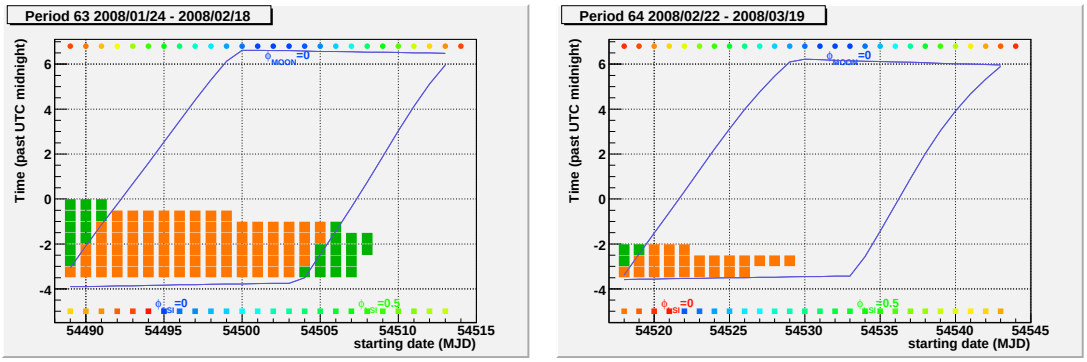

Figure A.1: Time that LSI +61°303 can be observed during MAGIC periods 63 and 64, fulfilling the observational constrains (see text for description). The orange zone is for dark time observation and the green one is for moon time. Orbital LSI +61°303 phase is given in colors at bottom band (from red to blue). Moon orbital phase is also given in colors at top of each panel.

[1] A MAGIC period is the group of days between two full moon nights.

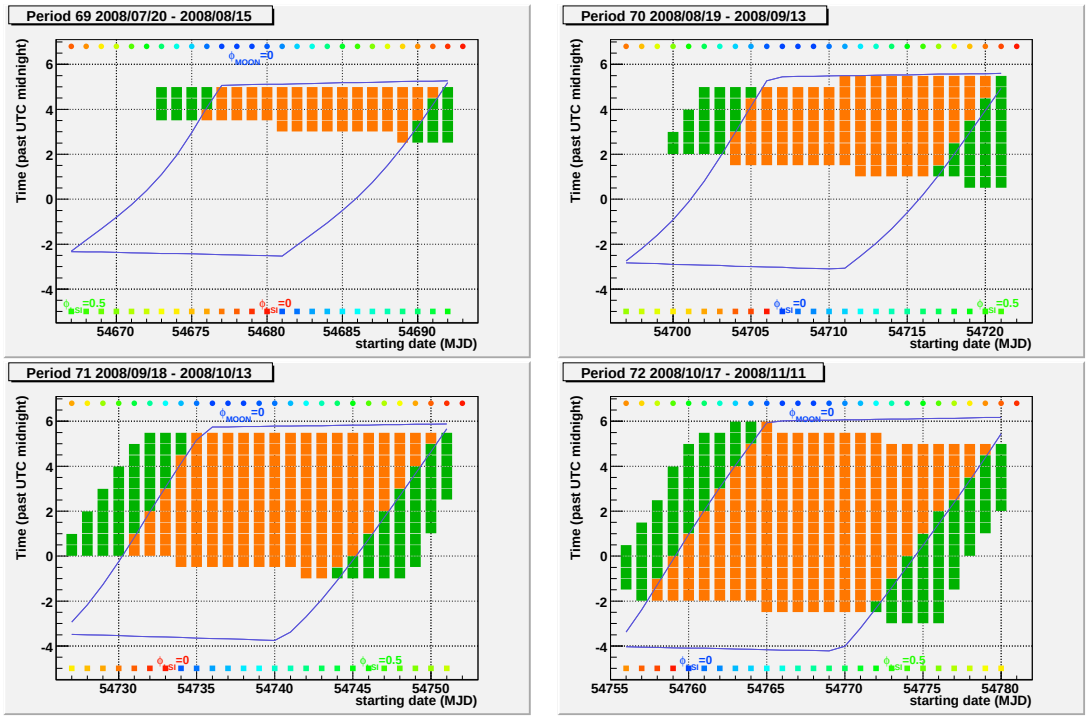

Figure A.2: Time that LSI +61°303 can be observed during MAGIC periods 69 to 72, fulfilling the observational constrains (see text for description). The orange zone is for dark time observation and the green one is for moon time. Orbital LSI +61°303 phase is given in colors at bottom band (from red to blue). Moon orbital phase is also given in colors at top of each panel.

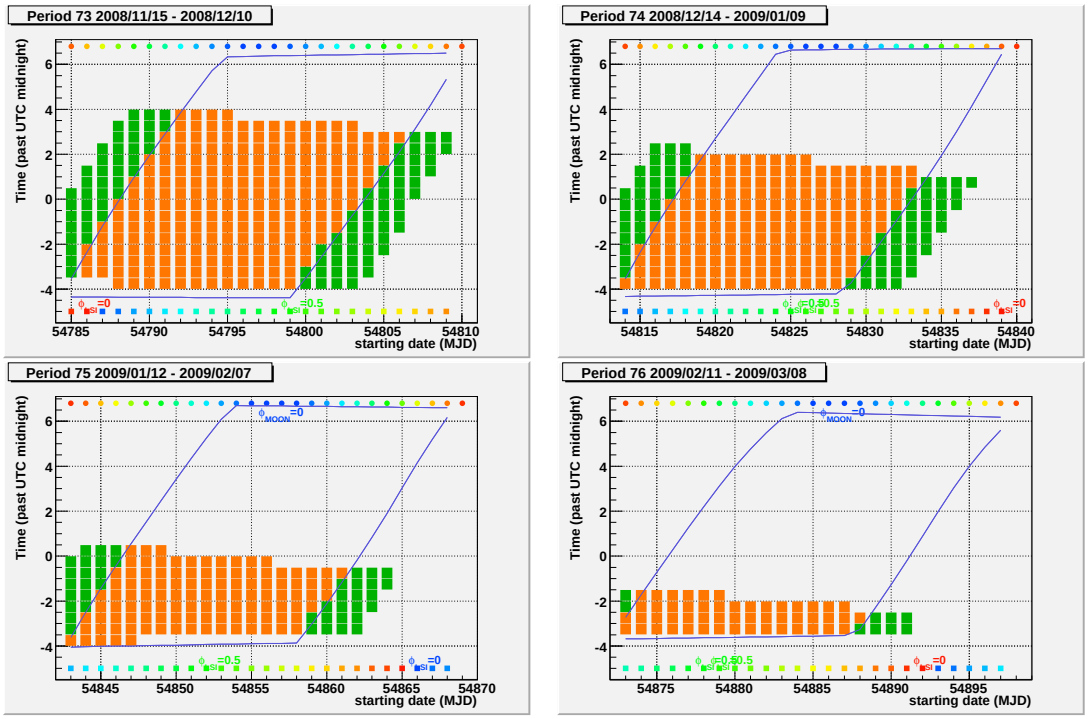

Figure A.3: Time that LSI +61°303 can be observed during MAGIC periods 73 to 76, fulfilling the observational constrains (see text for description). The orange zone is for dark time observation and the green one is for moon time. Orbital LSI +61°303 phase is given in colors at bottom band (from red to blue). Moon orbital phase is also given in colors at top of each panel.

Appendix B

Camera and calibration control: technical details

In this Appendix we summarize the Camera and Calibration Control actions. We present the commands that allow communication between it and the Central Control. We also enumerate the functions that the Camera Control can send to the subsystem drivers.

The Central Control (CeCo) computer coordinates all the telescope subsystems (DAQ, camera, AMC, $\cdots$) and communicates with all PCs via standard TCP/IP socket connections. The operator has access to all the subsystem functionalities from the CeCo program. The most important *commands* or actions that the CeCo can ask to the Camera Control (CaCo) are listed in table B.1.

Every second, the CaCo sends a report to the CeCo, which compiles all the information of each subsystem. Even if the CaCo is in stand alone mode, as long it is connected to CeCo, it starts to report the camera and calibration states. The camera report contains:

- `CAMERA-REPORT camera-status, writeyear, writemonth, writeday, writehour, writemin, writesec, writemsec comstatus, commyear, commmonth, commday, commhour, commminute, commsec, commmsec` : a subsystem identifier, status, date and time stamps and two control digits: one the report about the camera status and the second to report transmission malfunction.

- `CamCalib-state, Sentinel-state, HV.PS-state, LID-state, LV-state, COOLING-state, HV-state, DC-state, CaOS.LED-state, AMC.LED-state, Cal.CanBus-state, Cal.IO-state, Cal.LV-state, ActiveLoad-state` : we also report 14 identification numbers, one for each camera subsystem

- `DC hexcurrreport HV hexhvreport` : the DC and HV value of each pixel is sent in hexadecimal format.

- `COOL temp-wall, temp-opt-link, temp-center, temp-water, rel-hum-wall, rel-hum-center, bhigh-pressure, blow-pressure, bpump-status, brefrigerator-status, bvalve-status, bresistor-status, bfans-status` : Cooling parameters

- `LID btop-limsw-a, bbottom-limsw-a, btop-limsw-b, bbottom-limsw-b, btop-safetylimsw-a, bbottom-safetylimsw-a, btop-safetylimsw-b, bbottom-safetylimsw-b, lid-a-status, lid-b-status, motor-a-status, motor-b-status` : Lid parameters

- `HVPS hvps1, hvps2, curr1, curr2` : HV power supply parameters

- `LV voltage-pos5, voltage-pos12, voltage-neg12, voltageb-pos5, voltageb-pos12, voltageb-neg12 voltage-opt-link-pos12, voltage-opt-link-spare-pos12, curra-pos5, curra-pos12, curra-neg12, currb-pos5, currb-pos12, currb-neg12, curr-opt-link-pos12, curr-opt-link-spare-pos12, blv-ps-status, lv-temp, lv-RelativeHumidity` : Low voltage parameters

- `AUX bAux-CaOsLEDs-Off/On, bAux-AMCLEDs-Off/On` : Auxiliary parameters, which are the status of the star guider and the AMC LEDs

- `CAL cal-HV-Off/On, cal-LV-Off/On, cal-ContinuousLight-Off/On, cal-PinDiode-Off/On` : Calibration parameters

- `HOT modified` : This parameter indicates if the HV setting in the pixels have been modified by the CaCo due too high DC current.

- `ACTLOAD actloadA-V-0.1V, actloadA-curr-0.01mA, actloadB-V-0.1V, actloadB-curr-0.01mA, ps175-A-V-0.1V, ps175-A-curr-0.01mA, ps175-B-V-0.1V, ps175-B-curr-0.01mA` : voltages and currents of the active load power supplies

- `CPIX cpix-on/off` : this parameter indicates if the central pixel is or not connected

- `CHTEMP temp-OpticalReceivers, temp-ActiveLoadBox, temp-ElectRoom`: these are three temperature values measured in different position in the counting house

- `HVFIL file-name` : is the file name of the HV configuration

- `PSSEN PSsensorV1, PSsensorV2, PSsensorV3` : are the voltages measured in the camera cabinet power supply.

- `LIQ is-liq-On/Off` : is the output of a liquid sensor inside the camera

- `OVER` : this is a special last command to indicate that the report ends here.

The commands that the CaCo sends to each Subsystem Driver are listed in Tables B.2 and B.3. The common fields for different *subsystem reports* are:

```
DC-REPORT 5 2005 06 07 01 47 50 487 +00 +00 -Subsystem Contents-
```

composed by a subsystem identifier, status, date and time stamps and two control digits to report about the transmission problems and the possible subsystem malfunction. Afterwards, the specific subsystem content is reported.

More details on the individual subsystem as well as the communication with the CeCo can be found in [63, 61, 211].

CeCo to CaCo command	Description
HV002:123,1200:124,1240:...	Set one HV channel (HV001) or various HV channels (i.e, HV024)
HVALL:0000:1203:...	Set all 577 HV channels
HVFIL:HVfile.txt	Set all 577 HV according to a file
STOPR	Stop HV ramping
LDCLS/LDOPN/LDSTP	Close, open, stop Lids
LDTPN	Lid T-point
AMCON/AMCOFF	Switch ON/OFF AMC LEDs
LEDON/LEDOFF	Switch ON/OFF CaOs LEDs
DCSTA: RunNumber + ProjectName	Start a new anode DC currents run (save to file)
DCSTO	Stop a DC run
TKPED/STPED	Take or stop pedestal
CAON!/CAOFF	start and stop calibration
STACA:CalibrationScriptFile.txt	Start calibration sequence (of given type or pedestal)
STOCA	stop calibration sequence

Table B.1: Description of commands sent by the CeCo to the CaCo.

Command	Description
Camera Low Voltage	
LVOFF	Switch off low voltage
LVON!	Switch on low voltage
CPOFF	Switch off central pixel low voltage
CPON!	Switch on central pixel low voltage
Camera HV Settings (HV in V units)	
HV00N:123,1200:...	Send a HV value list of N elements: first number refers to each pixel and second refers to its HV value
HVALL:0000,1123,...	Send a HV value for all pixels in ascendant order
Camera HV Power Supply	
PSON!	Switch on power supply
SETHV	Set HV power supply to a given value (with ramping)
SETCL	Set HV limit current
STOPR	Stop HV ramping
GO2HV	Set HV power supply down in 20%
PSOFF	Switch off power supply
Camera Cooling System (RH in % and T in degrees)	
GGON!	Set the mode function when Guagua is On
STCAM	Set reference stabilization camera temperature with its variation
SETRH	Set humidity values to send and stop the flow of hot water to camera
STWAT	Set temperature values to switch on and off the water tank heater
STTFN	Set temperature values to switch on and off camera fans
STHFN	Set humidity values to switch on and off camera fans
COOFF	Force all cooling elements to be off (refrigerator, fans, resistor, pump and valve)
COLIB	Liberate all cooling system elements so that PLC control them
FNOFF	Force fans to switch off
FNON!	Force fans to switch on
FNLIB	Liberate fans so that PLC can control them
WTWLL	Set safety limits (maximum and minimum) for wall temperature
WTOPL	Set safety limits for optical transmitters temperature
WTCEN	Set safety limits for camera center temperature
WTWAT	Set safety limits for water tank temperature
WHWLL	Set safety limits for wall humidity
WHCEN	Set safety limits for camera center humidity
LIMTW	Set maximum water tank temperature for refrigerator malfunction alarm
Camera Lids	
LDOPN	Open camera lids
LDCLS	Close camera lids
LDTPN	Open camera upper lid for T-points
LDSTP	Stop lid movement
LDTMR	Send delay time between lids

Table B.2: Description of commands sent by the CeCo to each subsystem (Part I).

Command	Description
Calibration BOX	
SETPL	Set pulsed light pattern: 16 bits
SETCL	Set continuous light intensity to a given value
SETCO	Select color of the continuous light: 4-bits required (red, amber, green-blue and UV; 0000 for no-color)
HVON!	Switch on calibration HV
HVOFF	Switch off calibration HV
PDON!	Switch on pin diode
PDOFF	Switch off pin diode
Calibration I/O Card	
SETPF	Set pulse frequency
SETTF	Set train frequency
SETNP	Set number of pulses within a train
SETDL	Set delay in ns
SETVT	Set veto. 4-bits required: Pedestal, calibration, pin diode and laser
SETDM:1	Set values of digital module 1: 16-bits for module pattern
SETDM:2	Set values of digital module 2: 4-bits continuous light + 8-bits intensity + 4-bits veto
START	Start calibration run
STOPT	Stop calibration run
Auxiliary Systems	
CAOFF	Switch off the calibration LV power supply
CAON!	Switch on the calibration LV power supply
LEDOF	Switch CaOs LEDs off
LEDON	Switch CaOs LEDs on
AMCOF	Switch active mirror control LEDs off
AMCON	Switch active mirror control LEDs on
Common commands	
SETAR	Set periodic reports time (in ms)
SHUTD	Shutdown a subsystem

Table B.3: Description of commands sent by the CaCo to each subsystem (Part II).

List of Abbreviations

1ES	1st Einstein survey catalogue
2CG	2nd COS-B Gamma-ray catalog
3D	Three dimensonal space
3EG	3rd EGRET Gamma-ray catalog
Chandra	Chandra X-ray observatory
Chandra/ACIS-I	AXAF CCD Imaging Spectrometer onboard *Chandra* satellite
a.s.l.	Above the sea level
ADC	Analog-to-digital converter
AGASA	Akeno giant air shower array
AGILE	Astrorivelatore gamma ad immagini leggero
AGN	Active galactic nuclei
AMANDA	Antarctic muon and neutrino detector array, neutrino telescope
AMC	Active mirror control
ASCA	Advanced satellite for cosmology and astrophysics
ASCII	American standard code for information interchange
ASM	All-sky monitor
BeppoSAX	Beppo satellite per astronomia a raggi X
BH	Black hole
CaCo	Camera control
CACTUS	Converted atmospheric Čerenkov telescope using Solar-two
CANbus	Controller area network serial bus
CANGAROO	Collaboration of Australia and Nippon (Japan) for a gamma-ray observatory in the outback
CAT	Čerenkov Array at Themis
CCD	Charge-coupled device
CeCo	Central control
CELESTE	Cherenkov low energy sampling and timing experiment

CGRO	Compton gamma-ray observatory
CL	Confidence level
CoG	Center of gravity
COMPTEL	Compton gamma-ray observatory
CORSIKA	Cosmic ray simulations for KASCADE
COS-B	Cosmic ray Satellite (option B)
CPF	Cumulative probability function
CR	Cosmic rays
CTA	Čerenkov telescope array
Cyg	Cygnus
DAQ	Data acquisition system
DC	Direct current
DT	discriminator threshold
EAS	Extended air shower
EBL	Extragalactic background light
EGRET	Energetic gamma-ray experiment telescope
ENO	European Northern observatory
EVN	European VLBI network
FADC	Fast analog-to-digital converter
FiFo	First in, first out
FOV	Field of view
FWHM	Full width half maximum
GBI	Green Bank interferometer
GLAST	Gamma-ray large area space telescope
GRB	Gamma-ray burst
GRS	Granat satellite catalog
GUI	Graphical user interface
HE	High energy
HEGRA	High energy gamma-ray astronomy
HESS	High energy stereoscopic system
HETE-II	High energy transient explorer
HiRes	High resolution fly's eye cosmic-ray detector
HMXB	High mass X-ray binary

HR	Hardness ratio
HV	High voltage
HVPS	High voltage power supply
IACT	Imaging atmospheric Čerenkov telescope
IBIS	Imager on board the INTEGRAL satellite
IC	Inverse Compton
IceCub	IceCub neutrino observatory
IFAE	Institut de física d'altes energies
IFS	Independent Fourier spacing
IGRI	INTEGRAL soft gamma-ray imager
INTEGRAL	International gamma-ray astrophysics laboratory
IO	Input/output
IR	Infrared
KASKADE	Karlsruhe shower core and array detector
LAT	Large area telescope, gamma-ray instrument onboard GLAST
LED	Light-emitting diode
LMXB	Low mass X-ray binary
LONS	Light of the night sky
LS I	Luminous stars in the Northern hemisphere. The roman numeral in the format stands for the volume (I to VI) of the reference
LT#	Level trigger number
LV	Low voltage
M	Messier cataloge
MAGIC	Major atmospheric gamma imaging Čerenkov
MC	Monte-Carlo simulation
MERLIN	Multi-element radio-linked interferometer network
MILAGRO	Multiple institution Los Alamos gamma-ray observatory
MJD	Modified Julian date
Mkn	Markarian
MODbus	Modicon communication protocol
NFS	Network file system
NS	Neutron star
NSB	Night sky background

PC	Personal computer
PCI	Peripheral component interconnect bus
PDF	Probability density function
phe	photoelectron
PIC	Port d'informació cient/'ifica
PLC	Programmable logic controller
PMT	Photomultiplier
PSF	Point spread function
PSR	Pulsar
PWN	Pulsar wind nebula
QE	Quantum effidiency
QSO	Quasi-stellar object
RF	Random forest
RMS	Root mean square
RMSE	Root mean square error or deviation
ROSAT	Röntgen satellite
RXTE	Rossi X-ray timing explorer
SNR	Supernova remnant
STACEE	Solar tower atmospheric Čerenkov effect experiment
Swift	Swift gamma-ray burst mission
Swift/RXT	Swift X-ray telescope
TCP/IP	Transmission control protocol/Internet protocol
UV	Ultraviolet
VCSEL	Vertical cavity surface emitting laser
VERITAS	Very energetic radiation imaging telescope array system
VHE	Very high energy
VLA	Very large array
VLBA	Very long baseline array
VLBI	Very long baseline interferometry
Whipple	Fred Lawrence Whipple observatory
XMM-Newton	X-ray multi-mirror mission - Newton

List of Figures

List of Tables

Bibliography

[1] Gaisser, T. K. and Stanev, T. High-energy cosmic rays. *Nuclear Physics A*, 777:98–110, October 2006.

[2] Greisen, K. End to the Cosmic-Ray Spectrum? *Physical Review Letters*, 16:748–750, April 1966.

[3] Zatsepin, G. T. and Kuz'min, V. A. Upper Limit of the Spectrum of Cosmic Rays. *Soviet Journal of Experimental and Theoretical Physics Letters*, 4:78–+, August 1966.

[4] The Pierre Auger Collaboration. Correlation of the Highest-Energy Cosmic Rays with Nearby Extragalactic Objects. *Science*, 318:938–, November 2007.

[5] Longair, M. S. *High energy astrophysics. Vol.1: Particles, photons and their detection.* Cambridge University Press, March 1992., March 1992.

[6] Aharonian, F. A. and Atoyan, A. M. Cosmic γ-rays associated with annihilation of relativistic e^+ - e^- pairs. *Physics Letters B*, 99:301–304, February 1981.

[7] Aharonian, F. et al. Observations of 54 Active Galactic Nuclei with the HEGRA system of Cherenkov telescopes. *Astron. Astrophys.*, 421:529–537, July 2004.

[8] Teshima, M. et al. Discovery of Very High Energy γ-Rays from the Distant Flat Spectrum Radio Quasar 3C 279 with the MAGIC Telescope. In *Proceedings of the 30th International Cosmics Rays Conference, Merida, Mexico*, July 2007.

[9] Waxman, E. Cosmological Gamma-Ray Bursts and the Highest Energy Cosmic Rays. *Physical Review Letters*, 75:386–389, July 1995.

[10] Rees, M. J. and Meszaros, P. Relativistic fireballs - Energy conversion and time-scales. *Mon. Not. Roy. Astron. Soc.*, 258:41P–43P, September 1992.

[11] Hurley, K. et al. Detection of a Gamma-Ray Burst of Very Long Duration and Very High Energy. *Nature*, 372:652–+, December 1994.

[12] Albert, J. et al. MAGIC upper limits on the high energy emission from GRBs. *Astrophys. J.*, 667:358–366, September 2007.

[13] Albert, J. et al. Observation of VHE γ-rays from Cassiopeia A with the MAGIC telescope. *Astron. Astrophys.*, 474:937–940, November 2007.

[14] Aharonian, F. et al. Primary particle acceleration above 100 TeV in the shell-type supernova remnant RX J1713.7-3946 with deep HESS observations. *Astron. Astrophys.*, 464:235–243, March 2007.

[15] Aharonian, F. et al. H.E.S.S. Observations of the Supernova Remnant RX J0852.0-4622: Shell-Type Morphology and Spectrum of a Widely Extended Very High Energy Gamma-Ray Source. *Astrophys. J.*, 661:236–249, May 2007.

[16] Oña-Wilhelmi, E. and others. First pulsar observations with the MAGIC Telescope. In *Proceedings of the 29th International Cosmics Rays Conference, Pune, India* [212], pages 247–250.

[17] Albert, J. et al. Constraints on the Steady and Pulsed Very High Energy Gamma-Ray Emission from Observations of PSR B1951+32/CTB 80 with the MAGIC Telescope. *Astrophys. J.*, 669:1143–1149, November 2007.

[18] Albert, J. et al. Very High Energy γ-Ray Radiation from the Stellar Mass Black Hole Binary Cygnus X-1. *Astrophys. J. Letters*, 665:L51–L54, August 2007.

[19] Aharonian, F. et al. 3.9 day orbital modulation in the TeV γ-ray flux and spectrum from the X-ray binary LS 5039. *Astron. Astrophys.*, 460:743–749, December 2006.

[20] Aharonian, F. et al. Detection of extended very-high-energy γ-ray emission towards the young stellar cluster Westerlund 2. *Astron. Astrophys.*, 467:1075–1080, June 2007.

[21] Tsuchiya, K. et al. Detection of Sub-TeV γ-Rays from the Galactic Center Direction by CANGAROO-II. *Astrophys. J. Letters*, 606:L115–L118, May 2004.

[22] Aharonian, F. et al. Very high energy gamma rays from the direction of Sagittarius A*. *Astron. Astrophys.*, 425:L13–L17, October 2004.

[23] Kosack, K. and others. TeV γ-ray observations of the galactic center. *Astrophys. J.*, 608:L97–L100, 2004.

[24] Albert, J. et al. Observation of γ-rays from the galactic center with the MAGIC telescope. *Astrophys. J.*, 638:L101–L104, 2006.

[25] Aharonian, F. et al. An unidentified TeV source in the vicinity of Cygnus OB2. *Astron. Astrophys.*, 393:L37–L40, October 2002.

[26] Albert, J. et al. MAGIC Observations of the Unidentified γ-Ray Source TeV J2032+4130. *Astrophys. J. Letters*, 675:L25–L28, March 2008.

[27] Aharonian, F. et al. HESS very-high-energy gamma-ray sources without identified counterparts. *Astron. Astrophys.*, 477:353–363, January 2008.

[28] Hunter, S. D. et al. EGRET Observations of the Diffuse γ-Ray Emission from the Galactic Plane. *Astrophys. J.*, 481:205–+, May 1997.

[29] Aharonian, F. et al. Discovery of very-high-energy γ-rays from the galactic centre ridge. *Nature*, 439:695–698, February 2006.

[30] Elsässer, D. and Mannheim, K. MAGIC and the search for signatures of supersymmetric dark matter. *New Astronomy Review*, 49:297–301, May 2005.

[31] Albert, J. et al. Upper limit for gamma-ray emission above 140 GeV from the dwarf spheroidal galaxy Draco. *ArXiv e-prints*, 711, November 2007.

[32] Albert, J., for the MAGIC Collaboration, Ellis, J., Mavromatos, N. E., Nanopoulos, D. V., Sakharov, A. S., and Sarkisyan, E. K. G. Probing Quantum Gravity using Photons from a Mkn 501 Flare Observed by MAGIC. *ArXiv e-prints*, 708, August 2007.

[33] Blanch, O. *Study of the Gamma Ray Horizon with MAGIC as a new method to perform cosmological measurements*. PhD thesis, Universitat Autònoma de Barcelona, 2004.

[34] Hartman, R. C. et al. The Third EGRET Catalog of High-Energy γ-Ray Sources. *Astrophys. J. Suppl.*, 123:79–202, July 1999.

[35] Gaisser, T. K. *Cosmic rays and particle physics*. Cambridge and New York, Cambridge University Press, 1990.

[36] Schmidt, F. CORSIKA shower images. http://www.ast.leeds.ac.uk/∼fs/ . *University of Leeds*, 2007.

[37] Berger, M. J. and Seltzer, S. M. Tables of Energy Losses and Ranges of Electrons and Positrons. NASA SP-3012. *NASA Special Publication*, 3012, 1964.

[38] Falcke, H. et al. Detection and imaging of atmospheric radio flashes from cosmic ray air showers. *Nature*, 435:313–316, May 2005.

[39] Čerenkov, P. A. Visible Emission of Clean Liquids by Action of γ Radiation. *Doklady Akad. Nauk SSSR*, 451:451, 1934.

[40] Mazin, D. *A study of VHE γ-ray emission from AGNs and constraints on the extragalactic background light*. PhD thesis, Technische Universitaet Muenchen, 2007.

[41] Yao, W. M. and others. Review of particle physics. *J. Phys.*, G33:1–1232, 2006.

[42] Wagner, R. M. *Measurement of VHE γ-ray emission from four blazars using the MAGIC telescope and a comparative blazar study*. PhD thesis, Technische Universitaet Muenchen, 2006.

[43] Barrio, J. A. and others. The MAGIC Telescope – Design Study for the Construction of a 17 m Cherenkov Telescope for Gamma Astronomy above 10 GeV. *MPI Institute Report*, 1998. MPI-PhE/98-05.

[44] de Naurois, M. et al. Status and Current Sensitivity of the CELESTE Experiment. In F. A. Aharonian and H. J. Völk, editors, *American Institute of Physics Conference Series*, volume 558 of *American Institute of Physics Conference Series*, pages 540–+, 2001.

[45] Gingrich, D. M. et al. The STACEE Ground-Based Gamma-Ray Detector. *IEEE Transactions on Nuclear Science*, 52:2977–2985, December 2005.

[46] Jarvis, A. et al. Gamma-Ray Burst Follow-up Observations with STACEE During 2003-2007. In *Proceedings of the 30^{th} International Cosmics Rays Conference, Merida, Mexico*, July 2007.

[47] Kildea, J. et al. The Whipple Observatory 10-m γ-ray telescope, 1997-2006. *Astropart. Phys.*, 28:182–195, 2007.

[48] Daum, A. et al. First Results on the Performance of the HEGRA IACT Array. *Astroparticle Physics*, 8:1–2, December 1997.

[49] Punch, M. et al. Detection of TeV photons from the active galaxy Markarian 421. *Nature*, 358:477–+, August 1992.

[50] Maier, G. et al. VERITAS: Status and Latest Results. In *Proceedings of the 30^{th} International Cosmics Rays Conference, Merida, Mexico*, July 2007.

[51] Hinton, J. Gamma-ray Astronomy. In *Proceedings of the 30^{th} International Cosmics Rays Conference, Merida, Mexico*, July 2007.

[52] Bradbury, S. M. and others. The MAGIC telescope project based on a 17-m diameter parabolic solar concentrator. In Ed. Cresti M., editor, *Proceedings of the Workshop:Towards a Major Atmospheric Cherenkov Detector IV, Padova, Italy*, page 277, 1995.

[53] Cortina, J. et al. Technical Performance of the MAGIC Telescope. In *Proceedings of the 29th International Cosmics Rays Conference, Pune, India* [212].

[54] Riegel, B., Bretz, T., Dorner, D., and Wagner, R. A tracking monitor for the MAGIC Telescope. In *Proceedings of the 29th International Cosmics Rays Conference, Pune, India* [212], pages 215–218.

[55] Davies, J. M. and Cotton, E. S. Design of the quartermaster solar furnace. *J. Solar Energy Science and Engineering*, 1:16, 1957.

[56] Tonello, N. *Study of the VHE γ-ray emission from the Active Galactic Nucleus 1ES 1959 +650*. PhD thesis, Technische Universitaet Muenchen, 2006.

[57] Garczarczyk, M. *First observations of the GRB prompt and early afterglow emission phase at $\sim$100 GeV energy regime with the 17 m diameter MAGIC imaging atmospheric Čerenkov telescope*. PhD thesis, Technische Universitaet Muenchen, 2007.

[58] Paneque, D., Gebauer, J., Lorenz, E., Martinez, M., Mase, K., and Mirzoyan, R. A Method to Enhance the Sensitivity of Photomultipliers for Air Cherenkov Telescopes. *NIM*, A504:109–115, 2003.

[59] Ostankov, A. et al. A study of the new hemispherical 6-dynodes PMT from electron tubes. *NIM A*, 442, Issue 1-3:117–123, 2000.

[60] Goebel, F., Bartko, H., Carmona, E., et al. Upgrade of the MAGIC Telescope with a Multiplexed Fiber-Optic 2 GSamples/s FADC Data Acquisition System. In *Proceedings of the 30th International Cosmics Rays Conference, Merida, Mexico*, July 2007.

[61] Flix, J. *Observations of γ-rays from the Galactic Center with the MAGIC Telescope*. PhD thesis, Universitat Autònoma de Barcelona, 2006.

[62] López, J. *Measurement of the invariance of the speed of light observing the active galactic nucleus Mkn421 with the MAGIC Telescpe*. PhD thesis, Universitat Autònoma de Barcelona, 2006.

[63] Domingo-Santamaría, E. *γ-ray emission from regions of star formation: Therory and observations with the MAGIC Telescope*. PhD thesis, Universitat Autònoma de Barcelona, 2006.

[64] Albert, J. et al. Signal reconstruction for the MAGIC telescope. *NIM*, A548:464, 2006.

[65] Bartko, H, Gaug, M., Moralejo, A., and Sidro, N. FADC pulse reconstruction using a digital filter for the MAGIC telescope. In Ed. Cresti M., editor, *Proceedings of the Workshop:Towards a Major Atmospheric Cherenkov Detector VII, Palaiseau, France*, 2005.

[66] James, F., Cousins, R., and Cowan, G. Statistics. *Phys. Lett.*, B592, 1:289–291, 2004.

[67] Press, W. et al. *Numerical Recipes in C++*. Cambridge University Press, 2nd edition, 2002.

[68] Papoulis, A. *Signal analysis*. McGraw-Hill, New York, 1977.

[69] Cleland, W. and Stern, E. Signal processing considerations for liquid ionization calorimeters in a high rate environment. *Nuclear Instruments and Methods in Physics Research A*, 338:467–497, January 1994.

[70] Bartko, H, Gaug, M., Moralejo, A., and Sidro, N. *Comparison of Signal Reconstruction Algorithms for the MAGIC Telescope*, 2005. MAGIC-TDAS 05-03.

[71] Gaug, M. *Calibration of the MAGIC Telescope and Observation of Gamma Ray Bursts*. PhD thesis, Universitat Autònoma de Barcelona, 2006.

[72] Albert, J. et al. VHE γ-Ray Observation of the Crab Nebula and its Pulsar with the MAGIC Telescope. *Astrophys. J.*, 674:1037–1055, February 2008.

[73] Tescaro, D. Timing Analysis of the MAGIC Telescope Data after the Installation of the Ultra-fast 2 GSamples/s FADC Readout. Master's thesis, Universitat Autònoma de Barcelona, 2007.

[74] Aliu, E. *VHE γ-ray observations of Northern sky pulsar wind nebulae with the MAGIC telescope*. PhD thesis, Universitat Autònoma de Barcelona, 2007.

[75] Hillas, A. M. Cherenkov light emission of extensive air showers produced by primary γ-rays and by nuclei. In *Proceedings of the 19th International Cosmics Rays Conference, La Jolla, USA*, volume 3, page 445, 1985.

[76] Majumdar, P., Moralejo, A., Bigongiari, C., Blach, O., and Sobczynska, D. Monte Carlo simulation for the MAGIC telescope. In *Proceedings of the 29th International Cosmics Rays Conference, Pune, India* [212], pages 203–206.

[77] Heck, D., Schatz, G., Thouw, T., Knapp, J., and Capdevielle, J. N. *CORSIKA: A Monte Carlo code to simulate extensive air showers*. Forschungszent. Karlsruhe GmbH., 1st edition, 1998. FZKA-6019.

[78] Sobczynska, D. *MMCS from CORSIKA 6.014*, 2002. MAGIC-TDAS 02-10.

[79] Moralejo, A. *The reflection simulation program V.05*, 2002. MAGIC-TDAS 02-05.

[80] Blanch, O. and Moralejo, A. *How to use the Camera simulation program 0.7*, 2003. MAGIC-TDAS 03-06.

[81] Fegan, D. γ/hadron separation at TeV energies. *Journal of Physics G Nuclear Physics*, 23:1013–1060, September 1997.

[82] Albert, J. et al. Implementation of the Random Forest Method for the Imaging Atmospheric Cherenkov Telescope MAGIC. *ArXiv e-prints*, 2007.

[83] Fomin, V. P. et al. New methods of atmospheric Cherenkov imaging for γ-ray astronomy. 1: The False source method. *Astropart. Phys.*, 2:137–150, 1994.

[84] Lessard, R. W., Buckley, J. H., Connaughton, V., and Le Bohec, S. A new analysis method for reconstructing the arrival direction of TeV γ-rays using a single imaging atmospheric Cherenkov telescope. *Astropart. Phys.*, 15:1–18, 2001.

[85] Domingo-Santamaria, E., Flix, J., Rico, J., Scalzotto, V., and Wittek, W. The DISP analysis method for point-like or extended gamma source searches/studies with the MAGIC telescope. In *Proceedings of the 29th International Cosmics Rays Conference, Pune, India* [212], pages 363–366.

[86] Kranich, D. and Stark, L. S. A new method to determine the arrival direction of individual air showers with a single air Cherenkov telescope. In *Proceedings of the 28th International Cosmics Rays Conference, Tsukuba, Japan*, July 2003.

[87] Wittek, W. *Transformations between the sky, the local and the camera reference systems*, 2005. MAGIC-TDAS 05-07.

[88] Li, T.-P. and Ma, Y.-Q. Analysis methods for results in γ-ray astronomy. *Astrophys. J.*, 272:317–324, 1983.

[89] Helene, O. Upper Limit of Peak Area. *Nucl. Instr. Meth.*, 212:319, 1983.

[90] Feldman, G. J. and Cousins, R. D. A Unified approach to the classical statistical analysis of small signals. *Phys. Rev.*, D57:3873–3889, 1998.

[91] Rolke, W. A. and Lopez, A. M. Confidence intervals and upper bounds for small signals in the presence of background noise. *Nucl. Instrum. Meth.*, A458:745–758, 2001.

[92] Rolke, W. A., Lopez, A. M., and Conrad, J. Confidence Intervals with Frequentist Treatment of Statistical and Systematic Uncertainties. *Nucl. Instrum. Meth.*, A551:493–503, 2005.

[93] Wittek, W. *Determination of the effective observation time*, 2002. MAGIC-TDAS 02-02.

[94] Albert, J. et al. Unfolding of differential energy spectra in the MAGIC experiment. *Nucl. Instrum. Meth.*, A583:494–506, 2007.

[95] Barkto, H. *Observations of galactic sources of VHE γ-rays with the MAGIC Telescope*. PhD thesis, Technische Universitaet Muenchen, 2006.

[96] Armada, A. Characterization and some applications of the anode current monitoring system of the MAGIC telescope. Master's thesis, Universitat Autònoma de Barcelona, 2005.

[97] de Oña, E. and Rico, J. and Cortina, J. and Sidro, N. and Firpo, R. *Observations under moonlight and twilight with MAGIC*, 2005. MAGIC-TDAS 06-09.

[98] Albert, J. et al. Very high energy gamma-ray observations during moonlight and twilight with the MAGIC telescope. *ArXiv Astrophysics e-prints*, February 2007.

[99] Wagner, R. and others. Observations of the Crab nebula with the MAGIC telescope. In *Proceedings of the 29th International Cosmics Rays Conference, Pune, India* [212], pages 163–166.

[100] Elterman, L. Parameters for attenuation in the atmospheric windows for fifteen wavelengths. *Applied Optics IP*, 3:745–+, June 1964.

[101] Bernlohr, K. Impact of atmospheric parameters on the atmospheric Cherenkov technique. *Astropart. Phys.*, 12:255–268, 2000.

[102] Otte, A. N. *Observation of VHE γ-rays form the vicinity of magnetized neutron stars and development of new photon-detectors for future ground based γ-ray detectors*. PhD thesis, Technische Universitaet Muenchen, 2007.

[103] Deloye, C. J. The Connection Between Low-Mass X-ray Binaries and (Millisecond) Pulsars: A Binary Evolution Perspective. *ArXiv e-prints*, 710, September 2007.

[104] Patterson, J. The evolution of cataclysmic and low-mass X-ray binaries. *Astrophys. J. Suppl.*, 54:443–493, April 1984.

[105] Kalogera, V. and Webbink, R. F. Formation of Low-Mass X-Ray Binaries. II. Common Envelope Evolution of Primordial Binaries with Extreme Mass Ratios. *Astrophys. J.*, 493:351–+, January 1998.

[106] Tauris, T. M. and van den Heuvel, P. J. Formation and Evolution of Compact Stellar X-ray Sources. *ArXiv*, March 2003.

[107] Liu, Q. Z., van Paradijs, J., and van den Heuvel, E.P.J. Catalogue of high-mass X-ray binaries in the Galaxy (Fourth edition). *Astron. Astrophys.*, 455:1165, 2006.

[108] Liu, Q. Z., van Paradijs, J., and van den Heuvel, E.P.J. A catalogue of low-mass X-ray binaries in the Galaxy, LMC, and SMC (Fourth edition). *Astron. Astrophys.*, 469:807, 2007.

[109] Paredes, J.M. VHE γ-rays from galactic X-ray binary systems. In *Proceedings of the High Energy Phenomena in Relativistic Outflows, Dublin, Ireland*, September 2007.

[110] Mirabel, I. F., Rodriguez, L. F., Cordier, B., Paul, J., and Lebrun, F. A double-sided radio jet from the compact Galactic Centre annihilator 1E140.7 - 2942. *Nature*, 358:215–217, July 1992.

[111] Bosch-Ramon, V. and Paredes, J. M. Microquasars as High-energy γ-ray Sources. In *Proceedings of the The Fifth Microquasar Workshop, China, 2004*, page 133, 2005.

[112] Hutchings, J. B. and Crampton, D. Spectroscopy of the unique degenerate binary star LSI +61°303. *Publications Astronomical Society of the Pacific*, 93:486–489, August 1981.

[113] Frail, D. A. and Hjellming, R. M. Distance and total column density to the periodic radio star LSI +61°303. *Astronomical Journal*, 101:2126–2130, June 1991.

[114] Steele, I. A. and Negueruela, I. and Coe, M. J. and Roche, P. The distances to the X-ray binaries LSI +61°303 and A0535+262. *Mon. Not. Roy. Astron. Soc.*, 297:L5+, June 1998.

[115] Dhawan, V., Mioduszewski, A., and Rupen, M. LSI +61°303 is a Be-Pulsar binary, not a Microquasar. In *Proceedings of the VI Microquasar Workshop: Microquasars and Beyond. Sep 2006, Italy., p.52.1*, 2006.

[116] Casares, J., Ribas, I., Paredes, J. M., Marti, J., and Allende Prieto, C. Orbital Parameters of the Microquasar LSI +61°303. *Mon. Not. Roy. Astron. Soc.*, 360:1091–1104, 2005.

[117] Grundstrom, E. D. et al. Joint Hα and X-Ray Observations of Massive X-Ray Binaries. II. The Be X-Ray Binary and Microquasar LSI +61°303. *Astrophys. J.*, 656:437–443, February 2007.

[118] Harmanec, P. Stellar masses and radii based on modern binary data. *Bulletin of the Astronomical Institutes of Czechoslovakia*, 39:329–345, December 1988.

[119] Rhoades, C. E. and Ruffini, R. Maximum mass of a neutron star. *Physical Review Letters*, 32:324–327, 1974.

[120] Massi, M., Ribó, M., Paredes, J. M., Garrington, S. T., Peracaula, M., and Martí, J. Hints for a fast precessing relativistic radio jet in LSI +61°303. *Astron. Astrophys.*, 414:L1–L4, January 2004.

[121] Hutchings, J. B., Nemec, J. M., and Cassidy, J. Further studies of stellar rotation from Copernicus satellite data. *Publications Astronomical Society of the Pacific*, 91:313–318, June 1979.

[122] Porter, J. M. On the rotational velocities of Be and Be-shell stars. *Mon. Not. Roy. Astron. Soc.*, 280:L31–L35, June 1996.

[123] Zdziarski, A. A., Neronov, A., and Chernyakova, M. A compact pulsar wind nebula model of the γ-ray loud binary LSI +61°303. *ArXiv e-prints*, 802, February 2008.

[124] Tauris, T.M. and van der Heuvel, E.P.J. *Compact stellar X-ray sources*. Academic Press, New York, 1972.

[125] Zhang, F., Li, X.-D., and Wang, Z.-R. Where Are the Be/Black Hole Binaries? *Astrophys. J.*, 603:663–668, March 2004.

[126] Podsiadlowski, P., Rappaport, S., and Han, Z. On the formation and evolution of black hole binaries. *Mon. Not. Roy. Astron. Soc.*, 341:385–404, May 2003.

[127] Waters, L. B. F. M., van den Heuvel, E. P. J., Taylor, A. R., Habets, G. M. H. J., and Persi, P. Evidence for low-velocity winds in Be/X-ray binaries. *Astron. Astrophys.*, 198:200–210, June 1988.

[128] Mendelson, H. and Mazeh, T. Discovery of a 26.5-day optical periodicity of LSI +61°303. *Mon. Not. Roy. Astron. Soc.*, 239:733–740, August 1989.

[129] Paredes, J. M. et al. Photometric and Hα observations of LSI +61°303: detection of a $\sim$26 day V and JHK band modulation. *Astron. Astrophys.*, 288:519–528, August 1994.

[130] Zamanov, R. K., Martí, J., Paredes, J. M., Fabregat, J., Ribó, M., and Tarasov, A. E. Evidence of Hα periodicities in LSI +61°303. *Astron. Astrophys.*, 351:543–550, November 1999.

[131] Liu, Q.Z. and Yan, J.Z. An additional Hα emission component in LSI +61°303: Further evidence for the Hα emission related to the neutron star. *New Astronomy*, pages 130–137, November 2005.

[132] Zamanov, R. K., Stoyanov, K. A., and Tomov, N. A. Halpha Observations of the Galactic Microquasar LSI +61°303. *Informational Bulletin on Variable Stars*, 5776:1–+, June 2007.

[133] Zamanov, R. and Martí, J. First correlation between compact object and circumstellar disk in the Be/X-ray binaries. *Astron. Astrophys.*, 358:L55–L58, June 2000.

[134] Okazaki, A. T. On the confinement of one-armed oscillations in discs of Be stars. *Astron. Astrophys.*, 318:548–560, February 1997.

[135] Huang, S.-S. Profiles of Emission Lines in be Stars. *Astrophys. J.*, 171:549–+, February 1972.

[136] Okazaki, A. T. and Negueruela, I. A natural explanation for periodic X-ray outbursts in Be/X-ray binaries. *Astron. Astrophys.*, 377:161–174, October 2001.

[137] Marti, J. and Paredes, J. M. Modelling of LSI +61°303 from near infrared data. *Astron. Astrophys.*, 298:151–+, June 1995.

[138] Marlborough, J. M., Zijlstra, J.-W., and Waters, L. B. F. M. A study of the infrared spectrum of ψ Persei. I. A parameter study of the disc model. *Astron. Astrophys.*, 321:867–876, May 1997.

[139] Gregory, P. C. and Taylor, A. R. New highly variable radio source, possible counterpart of big γ-ray source CG135+1. *Nature*, 272:704–706, April 1978.

[140] Gregory, P. C. Bayesian Analysis of Radio Observations of the Be X-Ray Binary LSI +61°303. *Astrophys. J.*, 575:427–434, August 2002.

[141] Gregory, P. C., Xu, H.-J., Backhouse, C. J., and Reid, A. Four-year modulation of periodic radio outbursts from LSI +61°303. *Astrophys. J.*, 339:1054–1058, April 1989.

[142] Gregory, P. C. Bayesian Periodic Signal Detection. I. Analysis of 20 Years of Radio Flux Measurements of the X-Ray Binary LSI +61°303. *Astrophys. J.*, 520:361–375, July 1999.

[143] Gregory, P. C., Peracaula, M., and Taylor, A. R. Bayesian Periodic Signal Detection. II. Discovery of Periodic Phase Modulation in LSI +61°303 Radio Outbursts. *Astrophys. J.*, 520:376–390, July 1999.

[144] Paredes, J. M., Estalella, R., and Rius, A. Observation at 3.6 CM wavelength of the radio light curve of LSI +61°303. *Astron. Astrophys.*, 232:377–380, June 1990.

[145] Peracaula, M., Marti, J., and Paredes, J. M. Short term radio variability and polarization properties of LSI +61°303. *Astron. Astrophys.*, 328:283–289, December 1997.

[146] Bignami, G. F., Caraveo, P. A., Lamb, R. C., Markert, T. H., and Paul, J. A. Einstein X-ray identification of the variable radio star LSI +61°303. *Astrophys. J. Letters*, 247:L85–L88, July 1981.

[147] Goldoni, P. and Mereghetti, S. X-ray observations of the peculiar Be star LSI +61°303. *Astron. Astrophys.*, 299:751–+, July 1995.

[148] Taylor, A. R., Young, G., Peracaula, M., Kenny, H. T., and Gregory, P. C. An X-ray outburst. from the radio emitting X-ray binary LSI +61°303. *Astron. Astrophys.*, 305:817–824, January 1996.

[149] Greiner, J. and Rau, A. The X-ray spectrum of LSI +61°303. *Astron. Astrophys.*, 375:145–148, August 2001.

[150] Leahy, D. A., Harrison, F. A., and Yoshida, A. The ASCA X-Ray Spectrum of the Unusual Binary LSI +61°303. *Astrophys. J.*, 475:823–+, February 1997.

[151] Harrison, F. A., Ray, P. S., Leahy, D. A., Waltman, E. B., and Pooley, G. G. Simultaneous X-Ray and Radio Monitoring of the Unusual Binary LSI +61°303: Measurements of the Light Curve and High-Energy Spectrum. *Astrophys. J.*, 528:454–461, January 2000.

[152] Paredes, J. M., Marti, J., Peracaula, M., and Ribo, M. Evidence of X-ray periodicity in LSI +61°303. *Astron. Astrophys.*, 320:L25–L28, April 1997.

[153] Hermsen, W. and Kuiper, L. INTEGRAL deep observation of LSI +61°303. In *Proceedings of the 1st Glast Symposium, Stanford University, USA*, February 2007.

[154] Chernyakova, M., Neronov, A., and Walter, R. INTEGRAL and XMM-Newton observations of LSI +61°303. *Mon. Not. Roy. Astron. Soc.*, 372:1585–1592, November 2006.

[155] Tavani, M. and Kniffen, D. and Mattox, J. R. and Paredes, J. M. and Foster, R. The Variable γ-Ray Source 2CG 135+01. *Astrophys. J.*, 497:L89+, April 1998.

[156] Sidoli, L., Pellizzoni, A., Vercellone, S., Moroni, M., Mereghetti, S., and Tavani, M. XMM-Newton observation of a spectral state transition in the peculiar radio/X-ray/γ-ray source LSI +61°303. *Astron. Astrophys.*, 459:901–907, December 2006.

[157] Esposito, P., Caraveo, P. A., Pellizzoni, A., de Luca, A., Gehrels, N., and Marelli, M. A. Swift/XRT monitoring of five orbital cycles of LSI +61°303. *Astron. Astrophys.*, 474:575–578, November 2007.

[158] Paredes, J. M., Ribó, M., Bosch-Ramon, V., West, J. R., Butt, Y. M., Torres, D. F., and Martí, J. Chandra Observations of the γ-Ray Binary LSI +61°303: Extended X-Ray Structure? *Astrophys. J. Letters*, 664:L39–L42, July 2007.

[159] Lestrade, J.-F., Niell, A. E., Preston, R. A., and Mutel, R. L. Mark III very long baseline interferometry positions of eight stellar systems and astrometric comparisons. *Astronomical Journal*, 96:1746–1754, November 1988.

[160] Massi, M., Ribó, M., Paredes, J. M., Peracaula, M., and Estalella, R. One-sided jet at milliarcsecond scales in LSI +61°303. *Astron. Astrophys.*, 376:217–223, September 2001.

[161] Massi, M., Paredes, J. M., Estalella, R., and Felli, M. High resolution radio map of the X-ray binary LSI +61°303. *Astron. Astrophys.*, 269:249–254, March 1993.

[162] Hermsen, W. et al. New high energy γ-ray sources observed by COS B. *Nature*, 269:494–+, October 1977.

[163] Kniffen, D. A. et al. EGRET Observations of the γ-Ray Source 2CG 135+01. *Astrophys. J.*, 486:126–+, September 1997.

[164] Wallace, P. M. et al. A Systematic Search for Short-Term Variability of EGRET Sources. *Astrophys. J.*, 540:184–191, September 2000.

[165] Massi, M., Ribó, M., Paredes, J. M., Garrington, S. T., Peracaula, M., and Martí, J. The γ-ray emitting microquasar LSI +61°303. In F. A. Aharonian, H. J. Völk, and D. Horns, editors, *High Energy Gamma-Ray Astronomy*, volume 745 of *American Institute of Physics Conference Series*, pages 311–316, February 2005.

[166] Massi, M. LSI +61°303 in the context of microquasars. *Astron. Astrophys.*, 422:267–270, July 2004.

[167] van Dijk, R. et al. COMPTEL detection of the high-energy γ-ray source 2CG 135+01. *Astron. Astrophys.*, 315:485–492, November 1996.

[168] Hall, T. A. et al. Search for TeV Emissions from Pulsars in Binary Systems. *Astrophys. J.*, 583:853–860, February 2003.

[169] Fegan, S. J. et al. A survey of unidentified EGRET sources at very high energies. *Astrophys. J.*, 624:638–655, 2005.

[170] Mirabel, I. F. Very energetic γ-rays from microquasars and binary pulsars. *Science*, 312:1759–1760, 2006.

[171] Massi, M. Introduction to Astrophysics of Microquasars. *ArXiv Astrophysics e-prints*, June 2005. Habilitationsschrift, Friedrich-Wilhelms-Universität Bonn.

[172] Fender, R. Relativistic Outflows from X-ray Binaries ('Microquasars'). In A. W. Guthmann, M. Georganopoulos, A. Marcowith, and K. Manolakou, editors, *Relativistic Flows in Astrophysics*, volume 589 of *Lecture Notes in Physics, Berlin Springer Verlag*, pages 101–+, 2002.

[173] Mirabel, I. F., Dhawan, V., Chaty, S., Rodriguez, L. F., Marti, J., Robinson, C. R., Swank, J., and Geballe, T. Accretion instabilities and jet formation in GRS 1915+105. *Astron. Astroph.*, 330:L9–L12, February 1998.

[174] Bosch-Ramon, V., Paredes, J. M., Romero, G. E., and Ribó, M. The radio to TeV orbital variability of the microquasar LSI +61°303. *Astron. Astrophys.*, 459:L25–L28, November 2006.

[175] Gupta, S. and Böttcher, M. A Time-dependent Leptonic Model for Microquasar Jets: Application to LSI +61°303. *Astrophys. J. Letters*, 650:L123–L126, October 2006.

[176] Dermer, C. D. and Böttcher, M. γ Rays from Compton Scattering in the Jets of Microquasars: Application to LS 5039. *Astrophys. J.*, 643:1081–1097, June 2006.

[177] Bednarek, W. Inverse Compton $e^{+/-}$ pair cascade model for the γ-ray production in massive binary LSI +61°303. *Mon. Not. Roy. Astron. Soc.*, 371:1737–1743, October 2006.

[178] Bednarek, W. Propagation of very high energy γ-rays inside massive binaries LS 5039 and LSI +61°303. *Mon. Not. Roy. Astron. Soc.*, 368:579–591, May 2006.

[179] Romero, G. E., Christiansen, H. R., and Orellana, M. Hadronic High-Energy γ-Ray Emission from the Microquasar LSI +61°303. *Astrophys. J.*, 632:1093–1098, October 2005.

[180] Orellana, M. and Romero, G. E. High-energy γ-ray emission from the inner jet of LSI +61°303: the hadronic contribution revisited. *Astrophys. Space Sci.*, 309:333–338, June 2007.

[181] Torres, D. F. and Halzen, F. LSI +61°303 as a potential neutrino source on the light of MAGIC results. *Astroparticle Physics*, 27:500–508, July 2007.

[182] Maraschi, L. and Treves, A. A model for LSI +61°303. *Mon. Not. Roy. Astron. Soc.*, 194:1P–5P, January 1981.

[183] Protheroe, R. J. and Stanev, T. Constraints on models of Cygnus X-3 from high-energy gamma-ray absorption at source. *Astrophys. J.*, 322:838–841, November 1987.

[184] Moskalenko, I. V. TeV emission from close binaries. *Space Science Reviews*, 72:593–627, May 1995.

[185] Dubus, G. γ-ray binaries: pulsars in disguise? *Astron. Astrophys.*, 456:801–817, September 2006.

[186] Sierpowska-Bartosik, A. and Torres, D. F. Pulsar wind model of close massive gamma-ray binaries: The influence of geometry in the pulsar wind zone processes. *ArXiv e-prints*, 801, January 2008.

[187] Romero, G. E., Okazaki, A. T., Orellana, M., and Owocki, S. P. Accretion vs. colliding wind models for the γ-ray binary LSI +61°303: an assessment. *Astron. Astrophys.*, 474:15–22, October 2007.

[188] Bogovalov, S. V. et al. Modeling interaction of relativistic and nonrelativistic winds in binary system PSR 1259-63/SS2883. I.Hydrodynamical limit. *ArXiv e-prints*, 710, October 2007.

[189] Aharonian, F. et al. Discovery of the binary pulsar PSR B1259-63 in very-high-energy gamma rays around periastron with HESS. *Astron. Astrophys.*, 442:1–10, October 2005.

[190] Albert, J. et al. Variable very high energy γ-ray emission from the microquasar LSI +61°303. *Science*, 312:1771–1773, 2006.

[191] Albert, J. et al. Periodic VHE γ-ray emission from LSI +61°303 observed with the MAGIC telescope. *in Prep.*, 2008.

[192] Bosch-Ramon, V. and Paredes, J. M. Gamma-ray emission from microquasars: A numerical model for LSI +61°303. *Astron. Astrophys.*, 425:1069–1074, 2004.

[193] Moralejo, A. *Monte Carlo estimate of flux sensitivity of MAGIC for point-like sources*, 2004. MAGIC-TDAS 04-04.

[194] Albert, J. et al. Systematic search for VHE γ-ray emission from X-ray bright high-frequency BL Lac objects. *Accepted for Astrophys. J.*, 2008.

[195] Strickman, M. S. and others. A Multiwavelength Investigation of the Relationship between 2CG 135+1 and LSI +61°303. *Astrophys. J.*, 497:419, April 1998.

[196] Tavani, M. et al. Monitoring the γ-ray source 2CG 135+1 and the radio star LSI +61°303. *Astronomy and Astrophysics Suppl.*, 120:C243, December 1996.

[197] Lomb, N. R. Least - squares frequency analysis of unequally spaced data. *Astrophys. Space Sci.*, 39:447–462, 1976.

[198] Scargle, J. D. Studies in astronomical time series analysis. 2. Statistical aspects of spectral analysis of unevenly spaced data. *Astrophys. J.*, 263:835–853, 1982.

[199] Mardia, K. V. *Statistics of Directional Data*. Academic Press, New York, 1972.

[200] Kranich, D. *Temporal and spectral characteristics of the active galactic nucleus Mkn 501 during a phase of high activity in the TeV range*. PhD thesis, Technische Universitaet Muenchen, 2001.

[201] Schwarzenberg-Czerny, A. The distribution of empirical periodograms: Lomb-Scargle and PDM spectra. *Mon. Not. Roy. Astron. Soc.*, 301:831–840, December 1998.

[202] Frescura, F. A. M. and Engelbrecht, C. A. and Frank, B. S. Significance Tests for Periodogram Peaks. *ArXiv e-prints*, 706, June 2007.

[203] Akerlof, C. et al. Application of cubic splines to the spectral analysis of unequally spaced data. *Astrophys. J.*, 436:787–794, December 1994.

[204] Mendelson, H. and Mazeh, T. Further Photometry of LSI +61°303. *Mon. Not. Roy. Astron. Soc.*, 267:1–+, March 1994.

[205] Wen, L., Levine, A. M., Corbet, R. H. D., and Bradt, H. V. A Systematic Search for Periodicities in RXTE ASM Data. *Astrophys. J. Suppl.*, 163:372–392, April 2006.

[206] Ryle, M. The 5-km Radio Telescope at Cambridge. *Nature*, 239:435–+, October 1972.

[207] Smith, A. et al. Whipple telescope observations of LSI +61°303: 2004-2006. *Astrophysics and Space Science*, 309:299–303, June 2007.

[208] Albert, J. et al. Multi-wavelength (radio, X-ray and γ-ray) observations of the γ-ray binary LSI +61°303. *ArXiv e-prints*, 801, January 2008.

[209] Acciari, V. A. et al. VERITAS Observations of the gamma-Ray Binary LSI +61°303. *ArXiv e-prints*, 802, February 2008.

[210] Smith, A. et al. TeV and X-ray Monitoring of LSI +61°303 with VERITAS, Swift, and RXTE. In *Proceedings of the 30th International Cosmics Rays Conference, Merida, Mexico*, July 2007.

[211] Cortina, J. and others. *The Control System of the MAGIC Telescope*, 2007. MAGIC-TDAS 00-07.

[212] *Proceedings of the 29th International Cosmics Rays Conference, Pune, India*, August 2005.

Agraïments

En primer lugar, quisiera agradecer a Juan Cortina y Javi Rico su dedicación. Es mucho lo que he aprendido con ellos. Mucho. Ambos implicados y atentos, más no se puede pedir. Gracias por vuestra paciencia. Sois estupendos!

Tanto Enrique Fernández como Manel Martínez me dieron la oportunidad de trabajar en el IFAE y en MAGIC, donde me acogieron muy amablemente. Gracias por vuestros consejos.

I would like to take this opportunity to thank all the members of the tribunal, who kindly accepted the revision of this work: professors Eckart Lorentz, Ramon Miquel, Josep M. Paredes, Xavier Barcons and Mathieu de Naurois.

As a member of the MAGIC collaboration, I am grateful to all of the 150 collaborators, without whose effort, this work would not have been possible. Thanks for the dynamic and creative work environment. In particular, I would like to thank Tobias: Danke für die gute Zusammenarbeit. And also to Daniel Kranich, for the useful discussions. Y un saludo para Florian, porque, hace mucho ya, me descubrió MAGIC en una charla de la DPG.

No puedo olvidar aquí el apoyo de Diego Torres: muchas gracias por las charlas juntos. Gracias por tu sensatez.

Durante mi temporada de clases en la UAB, contar con Manuel Delfino fue una gran suerte.

Tampoc puc oblidar els consells de Jordi Vidal, que hem va iniciar en el món de la física.

Durant els quatre anys que he estat a l'IFAE, he passat moments molt bons i he conegut una gent fantàstica. En especial recorde a Oscar, Pepe, Markus i els meus ex-companys de despatx Eva i Javi. Ha segut un plaer treballar amb vosaltres. I no només treballar, clar, també viatjar junts, fer soparets... I després vingueren Manel, Diego, Roberta... I per suposat el Roger (un plaer compartir depatx amb tu) i la Neus (ánimo niña!).

Con especial buen rollo recuerdo el paso de Emma por el IFAE. Gracias otra vez chiquilla. Debo también mucho a Abelardo, siempre dispuesto a contestar cualquier duda; y perdona por el 'solo una preguntita' que luego era un bug de dos días. Also very kind with me was Daniel Mazin (Danke!).

Pero la vida no es solo trabajar (aunque escribiendo una tesis, a veces lo parce). Así que ha sido un placer salir con Ana, Enol, Carlos, Ester, Sigrid, Jose... Lo pasé en grande con vosotros en el cine, escalando o saliendo a merendar chocolate *amb melidros*! Nuestra estancia en Barcelona fue más agradable gracias a la acogida de los Mañas, esa gran trupe. Y por los respiros que permiten nuestras escapadas a Alicante: Piedad, Toni y Clara, me haceis sentir como en casa. Y prometo a David y a Vicente y al resto, que no me pierdo por nada la proxima salida al Mas del Corb!

I també ens hem anat escapant a Castelló, on Raquel i Jose sempre han tingun un moment per quedar i no permetre que es gelés la nostra amistat en la distància. Així com Lledo i Joan (besitos als dos) i Anna, Mireia i Carles (ànim doctorandos) i la resta de grup: *xa*, que mos feu passar molt bons ratos!

Gràcies especials a Gabriel, pel teu suport incondicional. I per aguantar-me, i per la teua paciència infinita i per fer-me eixir de casa enmig de la desesperació de la tesi. I per cuidar-me i estimar-me tant. És un plaer caminar amb tu.

I finalment, però no per açò menys important, vull dedicar aquest treball a la meva familia. Un record especial per a la tia Rosé. I un abraç molt fort per Araceli i Ana. El meu germà Xavier: per a mi el millor periodista de la ràdio. I els meus pares, Araceli i Jose Juan, que m'han prestat des de sempre tot l'afecte i la confiança. Us vull.